Catalytic Activity and Photophysical Properties of Biomolecules Immobilized on Mesoporous Silica

Ikemoto, Hideki; Chi, Qijin; Ulstrup, Jens

Publication date:
2012

Document Version
Publisher's PDF, also known as Version of record

Citation (APA):
Ikemoto, H., Chi, Q., & Ulstrup, J. (2012). Catalytic Activity and Photophysical Properties of Biomolecules Immobilized on Mesoporous Silica. Kgs. Lyngby: Technical University of Denmark (DTU).

Catalytic Activity and Photophyscial Properties of Biomolecules Immobilized on Mesoporous Silica

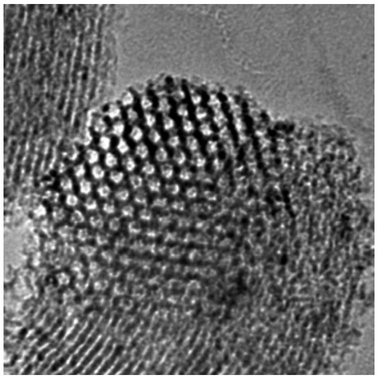

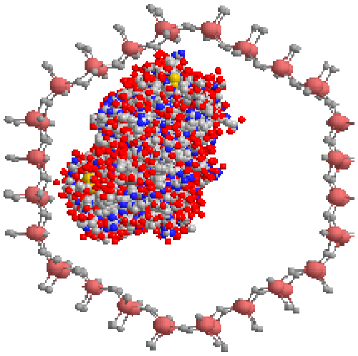

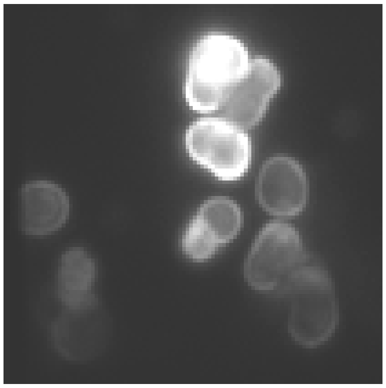

Ph.D. Thesis
by Hideki Ikemoto
Department of Chemistry
Technical University of Denmark
2011

Preface

This thesis is submitted to Department of Chemistry, Technical University of Denmark in partial fulfilment of the requirements for the degree of Ph.D. The research work was carried out at Department of Chemistry under the supervision of Professor Jens Ulstrup and Associate professor Qijin Chi. The project was supported by the Danish Research Council for Technology and Production Sciences.

Hideki Ikemoto, November, 2011.

Acknowledgements

I would like first to thank my two supervisors, Jens Ulstrup and Qijin Chi, for their instructions, guidance, regular-base meetings and extensive discussion to keep my Ph.D. study and the research project on the right track. In the past three years, I have enjoyed working in the Nanochemistry group at Department of Chemistry. Many thanks go to all the group members for their help and collaboration.

Partial work of the thesis was conducted at the Department of Chemical Physics, Lund University during an external research stay. I would like to thank Professor Tönu Pullerits for his kindness and supervision. There, I was lucky to have the chance to work together with a wonderful Ph.D. student, Sumera Tubasum. Her cooperation and help were crucial for a successful external research. I am also grateful to Professor Marie Wahlgren at Department of Food Technology, Lund university for the ellipsometry experiments.

I would like to thank many people at DTU, particularly at Deparrtment of Chemistry. I should especially mention: senior laboratory technician Bodil F. Holten for her help in the nitrogen adsorption experiments; laboratory technician Brian Dideriksen for IR measurements; Assistant Professor Susanne L. Mossin for the measurements of EPR spectra; Associate Professor Kenny Ståhl for help with the XRD experiments; Professor Robert Madsen for providing facilities for chemical synthesis; and laboratory technician Lise-Lotte Jespersen for help with the laboratory work generally. Special thanks goes to engineer Helge Kildahl Rasmussen at DTU Physics for his assistance with the XRD measurements, and the staff at the Center of Electron Nanoscopy (CEN) for offering the advanced SEM and TEM facilities, especially Dr. Takeshi Kasama for his assistance in the TEM measurements. I appreciate the help of Dr. Jens Wenzel Andreasen at DTU Risø in the SAXS measurements. Without their help, I could not have accomplished this interdisciplinary research project.

Finally, I would like to thank my family for their support and patience during my PhD study.

Abstract

Mesoporous silicas, based on Santa Barbara Amorphous-15 (SBA-15), with different morphology, structure, pore size and functional groups have been synthesized. Two metalloenzymes and a photosynthetic membrane protein were immobilized on or confined in the pores of the mesoporous silicas to prepare hybrid materials used for further study.

One metalloenzyme, horseradish peroxidase (HRP), was immobilized on rod-shaped SBA-15 by physical adsorption. The catalytic activity of free and immobilized enzyme was first compared at room temperature. Details of the enzyme kinetics including the apparent Michaelis constant (K_M) and maximum rate (V_{max}) were determined. Both thermal stability and the stability toward the denaturing agents guanidinium chloride and urea, of free and immobilized enzymes were compared next. The thermal stability of the immobilized enzyme is significantly improved in comparison with free HRP. The catalytic kinetics is slowed down notably, but V_{max} is much more robust to heat than for the free enzyme. The stability resistance of the enzyme toward the denaturing agents depends on the chemical nature of the denaturing agents and interactions between enzyme and silica nanopore walls. Guanidinium chloride showed similar attenuation of the catalytic activity of immobilized and free enzyme. In contrast, immobilized HRP was much more resistant to urea than the free enzyme. The different behavior of free and immobilized enzyme is most likely due to different hydrogen bonding of water and increased hydration strength of the protein inside the nanopores.

A copper-containing enzyme, galactose oxidase (GAOX), was immobilized on SBA-15 with a hexagonally ordered pore structure, or on mesocellular foam (MCF)-type mesoporous silica with a cage-like pore structure. Physical adsorption of this enzyme on the SBA-15 with a pore diameter comparable to the size of GAOX keeps enzyme stably immobilized with no enzyme leaching detected. Catalysis by immobilized GAOX was ca. 30 % less efficient than for the free enzyme. Immobilized enzyme did not show improved thermal stability compared to free GAOX. When GAOX was immobilized on the MCF-type mesoporous silica with cage-like mesopores interconnected by smaller openings (the opening comparable to the size of GAOX), significant leaching of enzyme was observed. Covalent attachment of GAOX was found to prevent leaching of the enzyme.

Light harvesting complex 2 (LH2) from purple photosynthetic bacteria was immobilized on SBA-15 with hexagonally ordered cylindrical pores or on MCF-type mesoporous silica with disordered cage-like mesopores. To identify the location of LH2, spherical particles with small or large pores were tested for the adsorption of LH2. LH2 was adsorbed to the particles with large pores, while little LH2 was adsorbed to the particles with small pores. Subsequent observation with fluorescence microscopy confirmed that LH2 is adsorbed in the pores of mesoporous silica. The conjugates of LH2 and mesoporous silica were studied by steady state fluorescence measurements from ambient to cryogenic temperatures and also by time resolved fluorescence spectroscopy at room temperature. Fluorescence spectra of the LH2-silica conjugates suspended in solution measured at room temperature were found to be almost the same as those of free LH2. Fluorescence spectra of the LH2-silica conjugates in a film form were measured from room temperature down to 77 K and compared with the spectra of LH2 alone in a film form. Temperature dependent bandwidth change and peak position shift were observed. The immediate difference between the samples was small, but systematic differences in the temperature-dependent patterns of the spectral band widths and band maximum positions were found by detailed bandshape analysis. Lifetime measurements brought other interesting results. Free LH2 and LH2 confined in disordered cage-like mesopores showed monoexponential fluorescence decay. In contrast, LH2 confined in hexagonally ordered cylindrical pores showed biexponential fluorescence decay. The data are under further scrutiny for proper interpretation.

Dansk Resume

Mesoporøse silicapartikler baseret på Santa Barbara Amorphous-15 (SBA-15), med varierende morfologi, struktur, porestørrelse og funktionelle grupper er blevet syntetiseret. To metalloenzymer og et fotosyntetisk membranproteinkompleks er blevet immobiliseret på partiklernes overflade eller i deres poresystem og de resulterende hybrider anvendt til videre studier.

Det ene metalloenzym, peberrodsperoxidase (HRP), blev immobiliseret ved physisorption på stavformet SBA-15. Den katalytiske aktivitet af det frie og immobiliserede enzym ved stuetemperatur blev først sammenlignet og detaljer i enzymkinetikken, den tilsyneladende Michaelis konstant (K_M) og maksimale reaktionshastighed (V_{max}) bestemt. Både termisk stabilitet og stabilitet over for to denatureringsreagenser, guanidiniumchlorid og urinstof (urea) for frie og immobilizerede enzymer blev dernæst sammenlignet. Termisk stabilitet af det immobiliserede enzym HRP er stærkt forbedret sammenlignet med det frie enzym Den katalytiske hastighed er nedsat, men V_{max} er langt mere varmerobust end for det frie enzym. Enzymstabilitet over for kemisk denaturering afhænger af denatureringsreagensets kemiske natur og vekselvirkning med både enzym og nanoporevægge. Guanidiniumchlorid viste næsten ens nedsættelse af den katalytiske aktivitet af fri og immobiliseret enzym. Til forskel herfra var immobiliseret HRP langt mere modstandsdygtigt over for urea end det frie enzym. Disse forskellige mønstre kan korreleres med vands forskellige hydrogenbindingsmønstre og proteinsolvatisering i silicananoporerne sammenlignet med den frie vandige opløsning.

Som sammenligning blev kobberenzymet galactose oxidase (GAOX) immobiliseret på SBA-15 med hexagonalt ordnet porestruktur og på cellulær “skum-struktureret (MCF)-type mesoporøs silica med kavitetslignende porestruktur. Enzymudslip kunne ikke detekteres efter physisorption af enzymet på SBA-15 med hexagonalt ordnede porer med en porediameter sammenlignelig med GAOX’s størrelse. Immobiliseret GAOX aktivitet

var ca. 30 % mindre end det frie enzyms. Det immobiliserede enzym viste ikke øget termisk stabilitet sammenlignet med det frie enzym, snarere tværtimod. GAOX immobilisering på MCF-type mesoporøs silica med kavitetslignende mesopore forbundet med snævrere åbninger (sammenlignelige med GAOX's størrelse), kunne ikke opretholdes, men førte til betydeligt enzymudslip. Kovalent GAOX-binding kunne fastholde enzymet uden udslip.

Det lysabsorberende (Light harvesting) kompleks 2 (LH2) fra fotosyntetiske purpurbakterier blev endelig immobiliseret på SBA-15 med hexagonalt ordnede cylindriske porer og på MCF-type mesoporøs silica with uordnede kavitets-lignende mesoporer. LH2 kunne adsorberes på partikler med vide porer, men ikke på partikler med snævre porer. Efterfølgende fluorescensmikroskopi bekræftede, at LH2 adsorberes inde i de mesoporøse partikelporer. Hybriderne af LH2 og mesoporøs silica blev yderligere undersøgt med steady state fluorescens målinger fra stuetemperatur til kryogene temperaturer og desuden ved tidsopløst fluorescensspektroskopi ved stuetemperatur. Fluorescensspektre af LH2-silica hybriderne suspenderet i opløsning ved stuetemperatur var umiddelbart næsten identiske med spektrene for fri LH2 i opløsning. Fluorescensspektre af LH2-silica hybriderne på filmform fra stuetemperatur ned til 77 ^{o}K kunne optages og sammenlignes med spektre for det frie LH2 ligeledes på filmform. Spektrene udviste temperaturafhængig båndbredde og maksimumforskydning De umiddelbare visuelle spektralforskelle mellem fri og immobiliseret LH2 var små, men efter numerisk spetralanalyse fandtes tydelige forskelle i temperaturmønstrene for både båndbredder og fluorescensmaksima. Fluorescenslevetider gav andre interessante observationer. Fri LH2 og LH2 i uordnede kavitetslignende mesoporer viste monoexponentielt fluorescenshenfald. I modsætning hertil viste LH2 immobiliseret i hexagonalt ordnede cylindriske porer biexponentielt fluorescenshenfald. Disse data er under yderligere behandling.

List of Abbreviations

BChl a	Bacteriochlorophylls a
BET	Brunauer-Emmett-Teller
BJH	Barrett-Joyner-Halenda
Car	Carotenoid
CW	Continuous wave
GAOX	Galactose oxidase
HRP	Horseradish peroxidase
LDAO	Lauryl dimethylamine N-oxide
LH2	Light harvesting complex 2
MCF	Mesostructured cellular foam
MCM-41	Mobil Composition of Matter no. 41
MCM-48	Mobil Composition of Matter no. 48
PEO	Poly(ethylene oxide)
PPO	Poly(propylene oxide)
PSD	Pore size distribution
SEM	Scanning electron microscopy
SBA-15	Santa Barbara Amorphous-15
STP	Standard temperature and pressure (273.15 K and 760 torr).
TEM	Transmission electron microscopy
TEOS	Tetraethyl orthosilicate
TMB	1,3,5-trimethylbenzene
K_M	Michaelis constant
V_{max}	Maximum velocity of a reaction

Table of contents

1. General introduction 1

2. Mesoporous silica 9

3. Basics of enzyme catalytic kinetics 39

4. Fluorescence spectroscopy 47

5. Experimental Methods and Techniques 55

6. Synthesis and characterization of mesoporous silica 75

8. Catalytic activity of galactose oxidase immobilized on SBA-15 mesoporous silica 127

9. Photophysical properties of light harvesting complex 2 confined in SBA-15 151

10. Concluding summary 187

Appendix 191

Publications and Presentations 205

1. General introduction

This Ph.D. dissertation aims to summarize the study of three biological entities (i.e., two metalloenzymes and a large membrane-spanning protein complex) immobilized on mesoporous silica. In more general term, the silica/protein systems studied are hybrid materials consisting of proteins (biological materials) and inorganic porous material. In this chapter, we first give a brief introduction to porous materials and hybrid materials.

1.1 Porous materials

Porous materials can be found around us as often as we can imagine. Examples in nature include bone, wood, sponge and cork [1]. In our daily life, porous materials are used for a wide range of purposes including as desiccants, membranes, construction materials, and insulation. By the IUPAC definition, porous materials are classified according to the pore size in diameter (d) into microporous ($d < 2$ nm), mesoporous ($2 \text{ nm} < d < 50$ nm), and macroporous materials ($d > 50$ nm). Figure 1-1 illustrates schematically some examples referred to this classification. Porous materials have been used in a variety of fields such as for catalysis, immobilization of molecules, and chemical micro-reactors. Zeolites are a classical example of microporous materials and have been extensively investigated. One of the most recently developed new microporous materials is MOFs (Metal Organic Frameworks). MOFs are porous crystalline solids where metal atoms are joined together by organic linkers. Since the pores of microporous materials are restricted in size, applications are limited especially in terms of biological application. Macroporous materials have low surface areas and due to their large pores, their potential as a host material is also limited. A typical example of macroporous material with a broad pore size distribution is active charcoal.

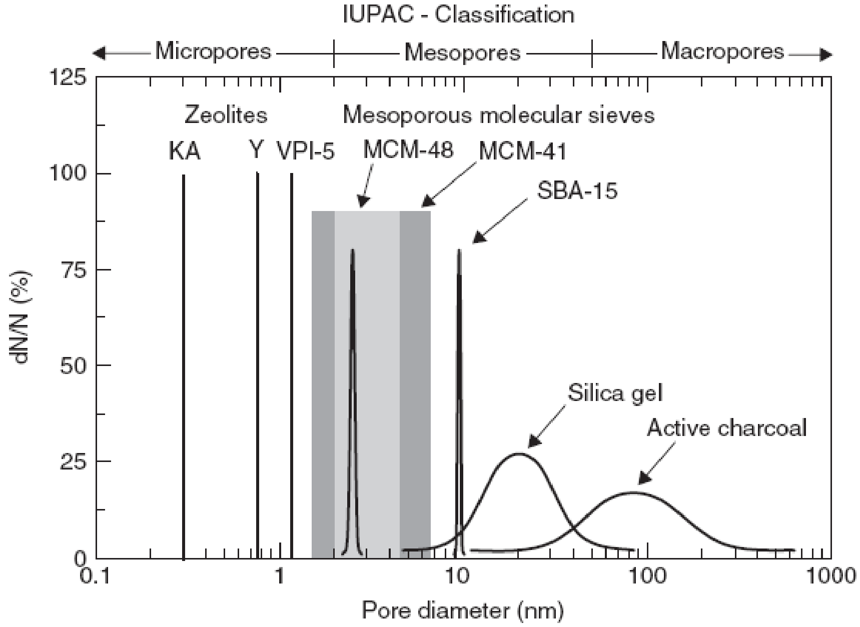

Figure 1.1: Some examples of microporous, mesoporous, and macroporous materials [2]. Silica gel and active charcoal have a broad pore size distribution and wide pore diameters, while zeolites and mesoporous molecular sieves such as MCM-48 (Mobil Composition of Matter no. 48) and SBA-15 have a narrow pore size distribution and much smaller pore diameters.

Mesoporous materials are, however an important class of the porous materials when considering the application of porous materials in biological fields since biological molecules such as proteins are also in the mesoscale range. Examples of mesoporous materials include ordered mesoporous silica, aerogels and Vycor glass [1]. After the first reports of mesoporous silica in the early 1990s [3][4][5], research on mesoporous materials have significantly increased. Following mesoporous silica, a variety of mesoporous materials such as carbon, transition metal oxides, and metals have recently been developed [6].

1.2 Hybrid materials

Hybrid materials combine organic and inorganic components. Organic-inorganic composites have been continuously developed since the mid-20th century [7]. The sol–gel process, one of the important processes used in the preparation of hybrid materials, was first invented in the 1930s [8]. The term "hybrid" organic-inorganic materials has become popular since the 1990s, and research in hybrid organic- or bio-inorganic materials has increasingly expanded in the last two decades [7]. Two new types of interesting materials first developed in the 1990s have offered effective frameworks for preparing new hybrid materials [7]. One is ordered mesoporous materials, and the other one is MOFs as mentioned above. The hybrid materials are classified into two classes depending on the nature of the interaction forces at the interface between organic and inorganic components. Surface interaction plays an important role in determining the overall properties of hybrid materials. For example, weak interaction between the inorganic and organic components may cause dynamic changes in the material over long time, possibly resulting in phase separation and even aggregation of the components in the final material [8]. Class I materials are hybrid materials in which the two phases interact each other relatively weakly, through non-covalent forces such as van der Waals forces, hydrogen bonds and other electrostatic forces. In class II hybrid materials, the components interact strongly and in some cases they are linked by covalent bonding.

As well known, biological molecules are often susceptible to environmental changes. In contrast, inorganic materials are robust and have high mechanical and thermal strength. The combination of inorganic materials and biological molecules are thus expected to extend applications of biological molecules beyond their natural conditions. Examples of bio-inorganic hybrid materials include hydroxyapatite–collagen composites (class I material), assembly of magnetite with dextran (class II material), and layered clay minerals-chitosan nanocomposites (class I material) [9]. One of the major biohybrid materials is silica or silicate based materials. There are two approaches to prepare biohybrids based on silica or silicates [10]. One is a molecular assembly approach and the other a block assembly approach. In the molecular assembly approach, biomolecules (e.g, proteins) are directly encapsulated during the growth of the matrix through the sol-gel process. In the block assembly approach, natural or synthetic silicates such as sepiolite, laponite, or pre-prepared mesoporous silica are mixed with protein solutions, and proteins are adsorbed in the pores or channels. The prepared biohybrids by the latter often show high stability and allow biological components to be recycled.

1.3 Organization of the thesis

Following the general introduction in Chapter 1, Chapter 2 provides first the background and relevant knowledge of mesoporous silica including synthesis mechanisms, synthesis under different conditions, and pore size and morphological control. A brief description of applications of mesoporous silica is then offered. Adsorption of proteins, and different immobilization methods of enzymes on mesoporous silica are further described, followed by a short section about confinement effects.

Chapters 3 and 4 give the basics of enzyme kinetics and fluorescence spectroscopy, respectively. The contents are focused on these issues directly related to the experiments described in the later chapters. Chapter 5 briefly introduces the experimental techniques used.

Chapter 6 describes the details of the materials used in the Chapters 7-9. Characterization of the materials is described from practical aspects. In addition to commonly used rod-shaped SBA-15, silica particles with enlarged pore size and spherical particles are also described.

Chapters 7-9 describe the main results of the thesis. Chapters 7 and 8 concern the study of metalloenzymes immobilized on mesoporous silica. Chapter 7 describes immobilization of horseradish peroxidase (HRP) on mesoporous silica, SBA-15. Catalytic kinetics and enzyme stability were investigated in detail. Chapter 8 describes, galactose oxidase (GAOX) immobilized on mesoporous silicas with different structure and pore size. Different immobilization methods were used. The catalytic activity and thermal stability were studied. Chapter 9 presents the study of the photosynthetic light harvesting complex 2 (LH2) entrapped in mesoporous silica. The steady-state fluorescence properties of the conjugate of LH2 and mesoporous silica were investigated in detail under various temperatures ranging from room temperature to cryogenic temperatures and also by time-resolved measurements. Chapter 10 presents overall conclusions of the study.

The references cited are listed at the end of each chapter.

References

[1] U. Schubert and N. Hüsing. *Synthesis of Inorganic Materials.* Wiley, Weinheim, 2005.

[2] M. Hartmann and D. Jung. Immobilization of Proteins and Enzymes, Mesoporous Supports. In *Encyclopedia of Industrial Biotechnology: Bioprocess, Bioseparation, and Cell Technology Vol. 7.,* pages 1–30. New York: John Wiley & Sons; 2009.

[3] T. Yanagisawa, T. Shimizu, K. Kuroda and C. Kato. The Preparation of Alkyltriinethylaininonium–Kaneinite Complexes and Their Conversion to Microporous Materials. *Bull. Chem. Soc. Jpn.*, 63:988-992, 1990.

[4] C. T. Kresge, M. E. Leonowicz, W. J. Roth, J. C. Vartuli and J. S. Beck. Ordered Mesoporous Molecular Sieves Synthesized by a Liquid-Crystal Template Mechanism. *Nature* 359:710-712, 1992.

[5] J. S. Beck, J. C. Vartuli, W. J. Roth, M. E. Leonowicz, C. T. Kresge, K. D. Schmitt, C. T. W. Chu, D. H. Olson, E. W. Sheppard, S. B. McCullen, J. B. Higgins and J. L. Schlenker. A New Family of Mesoporous Molecular Sieves Prepared with Liquid Crystal Templates. *J. Am. Chem. Soc.*, 114:10834-10843, 1992.

[6] Y. Yamauchi, N. Suzuki, L. Radhakrishnan, and L. Wang. Breakthrough and Future: Nanoscale Controls of Compositions, Morphologies, and Mesochannel Orientations Toward Advanced Mesoporous Materials. *The Chemical Record*. 9:321–339, 2009.

[7] C. Sanchez, P. Belleville, M. Popalld and L. Nicole. Applications of Advanced Hybrid Organic–Inorganic Nanomaterials: from Laboratory to Market. *Chem. Soc. Rev.*, 40: 696–753, 2011.

[8] G. Kickelbick. Introduction to Hybrid Materials, chapter 1. In *Hybrid Materials: Synthesis, Characterization, and Applications*, page 3. Willey VCH Verlag GbmH, 2007. Editor: G. Kickelbick.

[9] E. Ruiz-Hitzky, K. Ariga, and Y. Lvov. Bio-inorganic Hybrid Nanomaterials: Strategies, Syntheses, Characterization and Applications, Wiley-VCH: Weinheim, Germany, 2008.

[10] E. Ruiz-Hitzky, P. Aranda, M. Dardera and M. Ogawa. Hybrid and Biohybrid Silicate Based Materials: Molecular vs. Block-Assembling Bottom–up Processes. *Chem. Soc. Rev.*, 40:801–828, 2011.

2. Mesoporous silica

2.1 Brief introduction

In the early 1990s, two groups reported independently the synthesis of mesoporous silica. Kuroda's group reported Folded Sheets Mesoporous Materials (FSM) [1]. Researchers at Mobil Research and Development Corporation reported a new family of molecular sieves called M41S [2][3]. Kuroda's group prepared mesoporous silica by first intercalation of hexadecycltrimethylammonium cation into the layered silicate kanemite ($NaHSi_2O_5 \cdot 3H_2O$) and then removal of the template. The researchers from Mobil used cationic surfactant as a template molecule and prepared M41S family members (MCM-41, MCM-48, MCM-50) where the surfactant is organized in a different phase. MCM-41 has honeycomb arrays of pores with diameters from 2 -10 nm. MCM-48 has a cubic structure where the three-dimensional channels are interconnected. Although a patent application filed in 1969 already described the preparation of silica, which has all the properties of MCM-41, this discovery was not recognized at that time [4]. However, after the reports in the early 1990s a large amount of research has been conducted based on a variety of mesoporous silica. Huo et al [5] synthesized mesoporous silica, denoted as SBA-1 (Santa Barbara Material No. 1), with a 3D cubic mesostructure in acidic media. Later, mesoporous silica with large pores, SBA-15, was reported [6]. SBA-15 has two-dimensional hexagonally arranged pore structure with thick pore walls where the main pores are interconnected with micropores.

For the synthesis of SBA-15, amphillic triblock copolymer, poly(ethylene oxide)-poly-(propylene oxide)-poly(ethylene oxide), $PEO_{20}PPO_{70}PEO_{20}$, was used as a structure-directing agent in acidic solutions. By using different templates and adjusting synthesis conditions such as temperature, aging time, or by addition of swelling agent, the pore size of SBA-15 can be tuned in the range of 5 to 30 nm.

Schmidt-Winkel et al. reported the preparation of MCF (mesostructured cellular foam) type materials [7]. Addition of a large amount of swelling agent, 1,3,5-trimethylbenzene (TMB), in the synthesis of SBA-15 induces transformation to mesostructured cellular foams. The material has a three-dimensional, continuous, large pore mesostructure where cells are interconnected with uniform windows or openings (cage-like mesopores that are interconnected).

Mesoporous silica can be used as a template for the synthesis of mesoporous carbon. The mesoporous carbon is prepared by filling the pores of the template mesoporous silica with a precursor for carbon and then removing the template silica. Ryoo et al. first reported the synthesis of mesoporous carbon, CMK-1 (Carbon Molecular Sieve from KAIST), using mesoporous silica MCM-48 as a template and sucrose as a carbon source [8]. SBA-15 was used as a template for the synthesis of mesoporous carbon, CMK-3 [9].

2.2 Synthesis of mesoporous silica

2.2.1 General procedure

In general, the synthesis of mesoporous silica needs several steps. *First*, a homogenous solution of a surfactant as a template molecule is prepared to which a specific silicate precursor is added. The commonly used silicate precursors include sodium silicate (Na_2SiO_3), alkoxysilanes such as tetramethyl orthosilicate (TMOS), and tetraethyl orthosilicate (TEOS). The mixed solution is *then* subjected to hydrothermal treatment (so-called aging). *Finally*, the template molecules are removed. Synthesis of mesoporous silica is thus based on the combination of surfactant chemistry and traditional sol-gel chemistry, with surfactant molecules serving as templates. According to molecular charges, surfactants are classified into cationic, anionic, non-ionic, and zwitterionic surfactants. Amphiphilic surfactants containing a hydrophilic head group and a hydrophobic tail (such as quaternary cationic surfactants, $C_nH_{2n+1}(CH_3)_3N^+X^-$ where n = 12-16, X = Br or Cl) were used from the early development of mesoporous silica [3]. It is well known that surfactants form micelles when their concentration exceeds a certain value, called the critical micellar concentration (CMC). Micelles take particular forms, normally spherical but cylindrical at higher concentration. If the concentration is increased further, a liquid crystal phase is formed starting with hexagonal close-packed arrangement, followed by cubic and lamellar structures. The inorganic framework is formed through the sol-gel processing. The chemical reactions during the sol-gel processing are summarized schematically in Eq. (2.1). Hydrolysis of inorganic species $Si(OR)_4$ produces $Si(OH)_{4-n}$ and ROH, and condensation of either $Si(OR)_4$ or $Si(OH)_{4-n}$ produces siloxane bonds [10].

Hydrolysis:

$$\equiv Si{-}OR + H_2O \longrightarrow \equiv Si{-}OH + ROH$$

Condensation:

(2.1)

$$\equiv Si{-}OH + \equiv Si{-}OR \longrightarrow \equiv Si{-}O{-}Si \equiv + ROH$$

$$\equiv Si{-}OH + \equiv Si{-}OH \longrightarrow \equiv Si{-}O{-}Si \equiv + H_2O$$

Note: Each “–“ of the “≡” represents an alkoxide group (OR) or a hydroxyl group (OH).

The sol-gel process starts from alkoxide precursors, $Si(OR)_4$. As shown in Fig. 2.1, hydrolysis and condensation reactions allow polymerization of the precursors, resulting in the formation of sols. Sols are then aggregated to generate gel networks. Solution pH affects the rates of both hydrolysis and condensation reactions. The hydrolysis rate is faster than the condensation in the acidic solutions, whereas the opposite kinetics is observed under strong basic conditions (i.e., the condensation reaction is faster than hydrolysis).

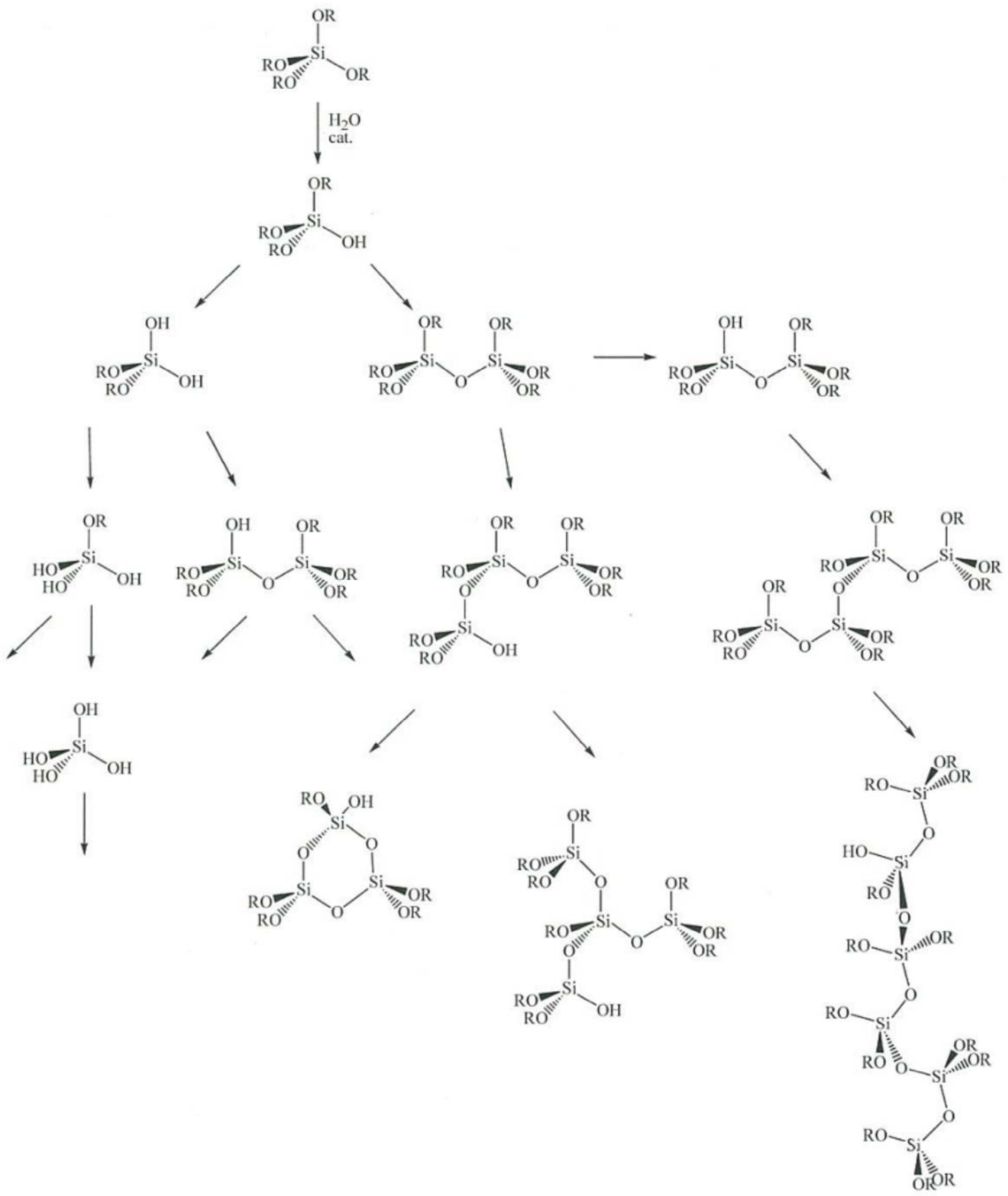

Figure 2.1: Initial events during the sol-gel processing. The sol-gel process starts from alkoxide precursors, Si(OR)$_4$. Hydration and condensation result in the formation of sols. Note that in principle each intermediate can undergo both hydrolysis and condensation. From Schubert et al [10].

2.2.2 Formation mechanisms and pathways

Much research has been devoted to elucidating the formation mechanisms of mesoporous silica. In the case of MCM-41, researchers at the Mobil company have proposed two possible mechanisms: (I) a liquid crystal templating (LCT) mechanism and (II) a cooperative mechanism [2][3]. According to the LCT mechanism, hexagonal arrays of cylindrical micelles first form (liquid crystalline phase). Silicates then surround the hexagonal arrays and are polymerized under templating, leading to the ordered mesostructures observed. The template molecules are removed normally by calcination (i.e., the heating of the crude product to a certain temperature high enough but below its melting point, so that thermal decomposition or phase transition of the template molecules occurs but not melting or fusing [10]). In the cooperative mechanism, precursor silicate species are first linked to surfactant molecules and are then together organized into the hexagonal array of cylindrical surfactant-silicate rods. Monnier *et al.* [11] introduced a new concept termed "charge density matching" at the interfaces between the surfactant and the silicate. The charge density of the silicate would determine the assembly and packing of the surfactant molecules. If silica oligomers have high charge density, surfactant molecules are required to have high charge density too. Such a charge density matching induces surfactant molecules to take a configuration with a low curvature at the silica/surfactant interface. The authors suggested that MCM-41 could be formed from a lamellar phase to a hexagonal phase through charge density matching. However, the proposed mechanism is not generally valid since a large number of different synthesis routes are reported and even MCM-41 can be synthesized by other routes [12].

Later, Firouzi *et al.* proposed an alternative model based on the cooperative formation mechanism [13]. Cooperative interaction between inorganic and organic species could lead to a variety of structures. For example, electrostatic interactions between surfactant and silicate molecules result in the formation of a silicatropic liquid crystal (SLC) mesophase which has long-range order. The ordering is governed by charge density and molecular packing. More specifically (Fig. 2.2), in the surfactant solution, surfactants form spherical or cylindrical micelles depending on the concentration and the surfactant anions, Br^- and OH^- compensate the charge of the surfactant molecules. At high pH, silicate precursor solution contains multiply charged silicate anions such as D4R (double four-ring) oligomers (Fig. 2.2A). After mixing the two solutions, halide ions are subjected to ion-exchange with silicate oligomers to form silicate-surfactant aggregates (Fig. 2.2B). Multidentate interactions of silicate oligomers with surfactants result in screening of electrostatic repulsion between aggregates among other effects. The screening of electrostatic repulsion in turn induces self-assembly of the SLC mesophase (Fig. 2.2C).

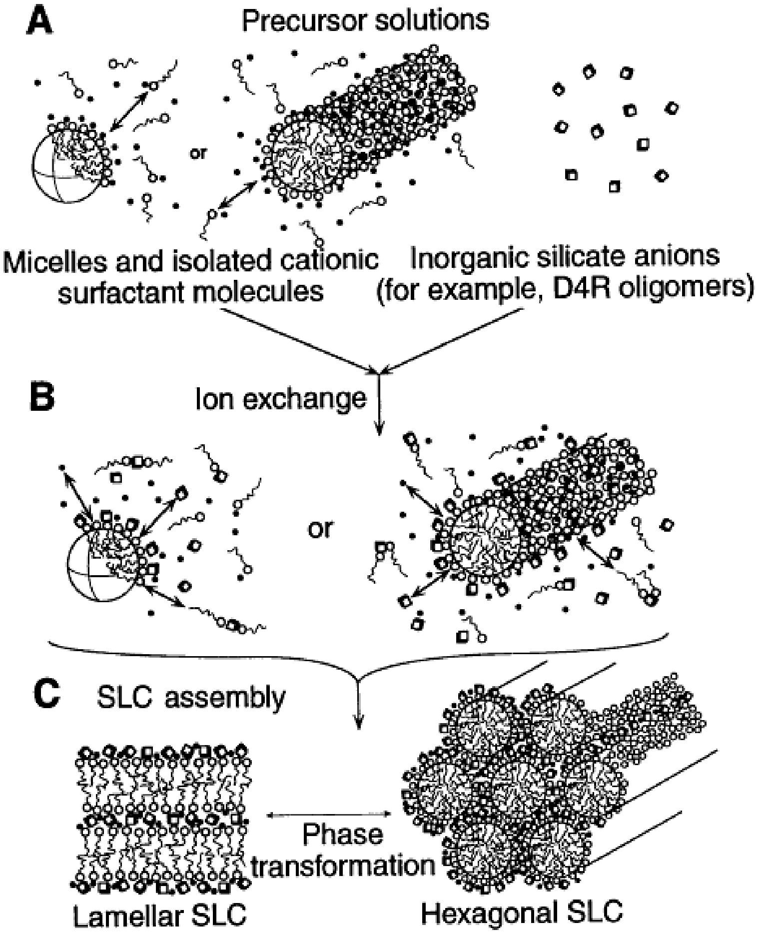

Figure 2.2: Schematic diagram of the “surfactant-silica” cooperative organization mechanism. (A) In the organic precursor solution, micelles and single surfactant molecules are in equilibrium. The surfactant halide counterions (Br^- or Cl^-) are preadsorbed on the surfactant cation head. The inorganic precursor solution contains multiply charged silicate anions. (B) After mixing the two precursor solutions, silicate anions ion-exchange with Br- or Cl-, (C) resulting in the formation of the final SLC phase. From Firouzi et al [13].

Huo et. al proposed a more general formation mechanism of surfactant and inorganic composite, based on the inorganic–organic interactions [14]**.** There are several possible routes to form mesoporous materials in terms of inorganic-organic interaction, including S^+I^-, $S^+X^-I^+$, S^-I^+ and $S^-M^+I^-$ (electrostatic interaction) and S^0I^0 and $S^0(XI)^0$ (hydrogen bonding), where S and I represent surfactant (S^0, non-ionic surfactant) and inorganic framework, respectively, while X and M represent the corresponding counter ions [15].

Ordered mesoporous silica can be prepared using cationic, anionic, or non-ionic surfactants. When cationic quaternary ammonium surfactants are used as a template and the reaction takes place in the basic solution (where the silica species are present as anions), the surfactant directly interacts with anionic inorganic species (S^+I^-, Fig. 2.3 a). Examples include the synthesis of MCM-41 and MCM-48 ([2] [3]). The synthesis also can be performed under the acidic condition below pH ≈ 2 (the isoelectric point of the Si-OH bearing inorganic species is pH ≈ 2 [16]). Under this condition, the silica species are positively charged. Since the surfactant and inorganic species have the same charges, counter ions X^- (usually halide ions, Cl^- or Br^-) are involved ($S^+X^-I^+$, Fig. 2.3 b). When anionic surfactants are used as a template and the reaction takes place in the basic solution, an organoalkoxysilane with a positively charged functional group (e.g. 3-aminopropyltrimethoxysilane) is used to ensure charge matching, in addition to TEOS as a silica source (S^-I^+, Fig. 2.3 c) [17]. In the synthesis of mesoporous silica using non-ionic surfactants under neutral conditions, the attractive interactions are mediated mainly through hydrogen bonds (S^0I^0, Fig. 2.3 d). SBA-15 is synthesized under a strongly acidic condition using a non-ionic surfactant, poly(ethylene oxide)-poly-(propylene oxide)-poly(ethylene oxide), $PEO_{20}PPO_{70}PEO_{20}$. In this case, the interaction between the surfactant and the inorganic framework is mediated through double-layer hydrogen bonding ($(S^0H^+)(X^-I^+)$, Fig. 2.3 e) [18].

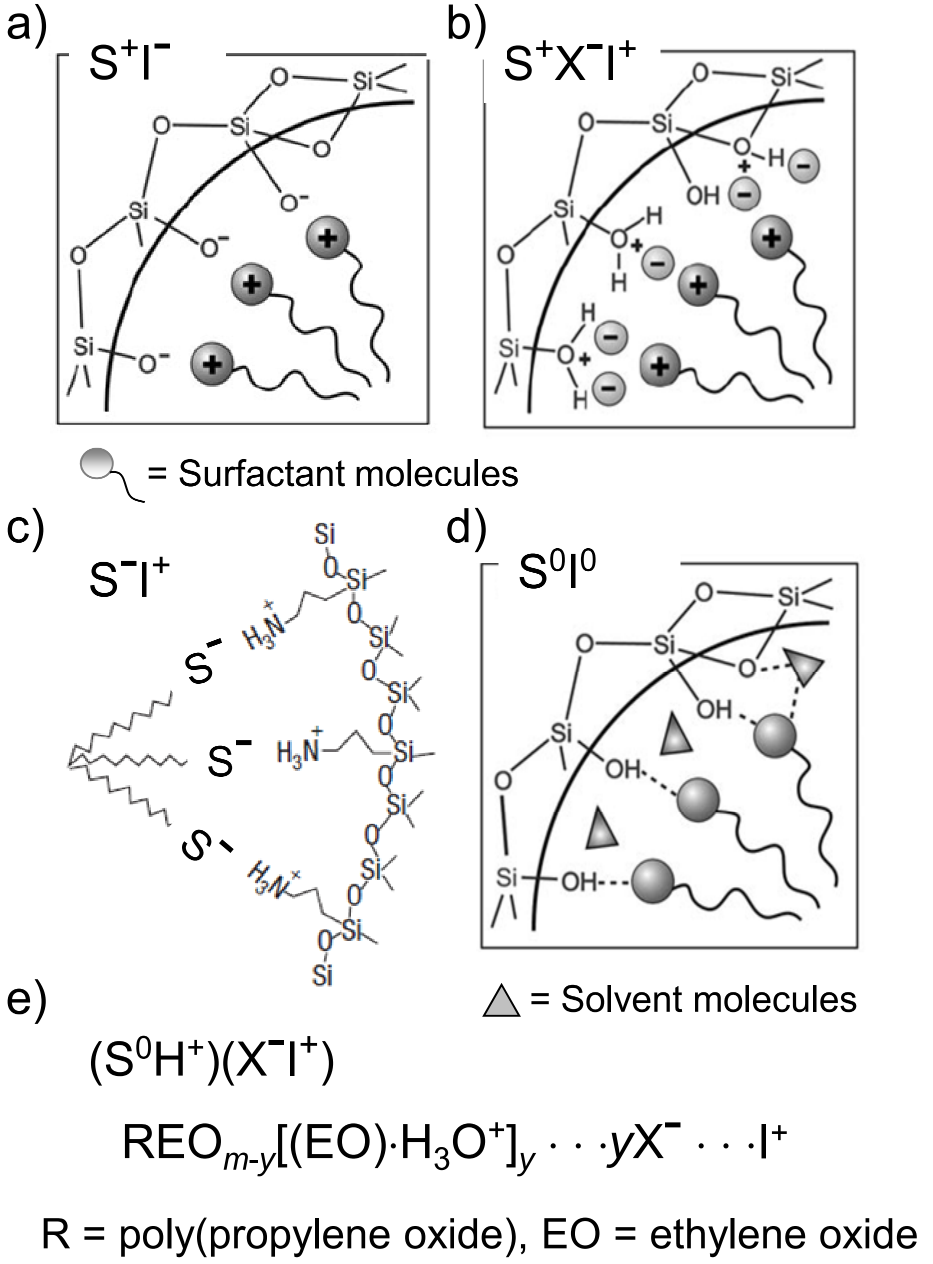

Figure 2.3: Schematic representation of the different types of silica-surfactant interfaces. S represents the surfactant molecule and I, the inorganic framework. X represents the corresponding counterions. Dashed lines indicate hydrogen bonding interactions. Note that in e), the part "$REO_{m-y}[(EO)$" corresponds to S^0. For a detailed explanation, see the text. Images are obtained from [16][17][19].

One of the most studied mesoporous silicas is SBA-15. In the synthesis of this material, poly(ethylene oxide)-poly-(propylene oxide)-poly(ethylene oxide) block copolymers

(Pluronic P123, $PEO_{20}PPO_{70}PEO_{20}$) is normally used as the template. The $Si(OEt)_4$ is supposed to be hydrolysed and polymerized in the hydrophilic domains in the liquid crystal, dominated by the well-organized mesopores, but SBA-15 also contains disordered micropores. Ruthstein *et al* studied the formation mechanism of SBA-15 [20]. Unfavorable micropores are formed due to the fact that some PEO chains penetrate in the silica wall. A dynamic silica network containing water and PEO is formed within the first 2 h. During this period, hexagonal order is established [20]. Flodström et al. studied the formation dynamics of SBA-15 using 1H NMR spectroscopy and TEM [21]. NMR and TEM observations suggest the following sequential events: *firstly*, silicates are adsorbed onto globular micelles. *Secondly*, the globular micelles are converted into flocs (Note: When a sol is colloidally unstable, the formation of aggregates is called coagulation or flocculation. The flocculation implies the formation of a loose or open network which may or may not separate macroscopically. The loose structure formed in this way is called a floc [22]). *Third*, the flocs are precipitated. The structure of the flocs changes when micelle-micelle coalescence occurs to generate cylindrical hexagonally packed micelles. More recently, Sundblom *et al.* [23] have proposed a formation mechanism of mesostructured silica using non-ionic surfactant Pluronic P123. First, silica and Pluronic aggregates. The incorporation of silica into the PEO part results in further growth of micellar aggregates. Second, the interaction of silica/Pluronic micelles causes phase separation and particles grow. Finally, particles reorganize to form the hexagonal mesostructure.

2.2.3 Effects of different experimental conditions

Various parameters, in particular solution pH and temperature, significantly affect the formation of mesoporous silica**.** Mesoporous silica can be synthesized under basic or acidic condition. The M41S family of molecular sieves was synthesized in basic pH by using cetyl trimethyl ammonium bromide (CTAB) [2], whereas Stucky *et al*. synthesized SBA materials in acid media [6]. pH affects the charge of inorganic precursors and the rate of hydrolysis and condensation of silica precursors as described above. In the acidic pH range, inorganic precursors are protonated to form $(S^0H^+)(X^-I^+)$ in the synthesis of SBA-15 [19]. In basic solution, negatively charged inorganic precursors interact with positively charged surfactant to form (S^+I^-) in the synthesis of MCM-41 [14]. The control of hydrolysis and condensation rate is important to obtain well-ordered mesoporous silica. The hydrolysis rate is faster than the condensation rate in the acidic pH range, while the condensation rate is faster than the hydrolysis rate at basic pH. Kim et al. synthesized ordered silica/block copolymer (PEO-PPO-PEO) mesostructured composites over a wide range of pH by controlling the rate of hydrolysis relative to that of condensation of silica species using fluoride and TMOS [24]. Fluoride is a catalyst for hydrolysis and polymerization of silica species [24]. Well ordered hexagonal mesoporous silica materials were obtained at acidic pH (up to pH 4) without fluoride, but above pH 4, disordered products were obtained. Above pH 4, the condensation is relatively rapid compared to the rate of hydrolysis. This leads to the incomplete hydrolysis and condensation of the partially hydrolysed silica species. The resulting silica oligomers may contain the organic moieties due to incomplete hydrolysis. The presence of such residual organic moieties results in weaker interaction between the hydrophilic EO (ethylene oxide) moieties and the silica oligomers, leading to poorly ordered materials [24]. High temperature accelerates condensation of silica precursors. The condensation of silanol groups and deprotonated silanol groups (negatively charged inorganic precursors) forms siloxane linkages to liberate hydroxide ions and reduce the interfacial charge density. To match charge density, the surfactant phase is transformed to an alternative phase, for example from the lamellar phase to the cylindrical phase.

2.2.4 Control of pore diameter and morphology

Control of pore size and morphology is one of the most important aspects for applications of mesoporous silica. For example, as will be described in later chapters, size matching of pore size and enzyme dimension is crucial to avoid leaching. Proper morphology may be needed when mesoporous silica is used as a carrier for intra-cellular drug delivery. There are three ways to control pore size: 1) Adjustment of chain length of amphiphilic surfactants, 2) use of swelling agents, and 3) control of synthesis conditions such as temperature. These key factors will change the packing parameters of the amphiphile. Larger amphiphiles lead to larger micelles, resulting in larger pore size. For example, by increasing the surfactant chain length from C8 to C22, the pore diameter for MCM-41 increases from 1.6 to 4.2 nm [25]. Swelling agents such as TMB and triisopropylbenzene [26] have been used to obtain the materials with large pores. Hydrophobic swelling agents enter into the hydrophobic region of the micelle, resulting in the expansion of the micelles. The pore size of SBA-15 was increased up to 30 nm by using the proper ratio of TMB: surfactant [19]. Adjustment of aging temperature and time also enable increasing the pore size. Higher temperature makes the PEO blocks more hydrophobic and PEO partially dehydrated, which leads to increased hydrophobic domain volumes and results in the increase of pore size [27]. Increase in the pore size of SBA-15 was also observed [28] by increasing the hydrothermal time. Several factors affect the morphology of the final product, including co-surfactants, co-solvents and inorganic salts [29]. Large-pore SBA-15 microspheres were synthesized by the addition of inorganic salts and mesitylene (TMB) [30]. Recently, Lee obtained SBA-15 with various morphologies without using additives but by changing the initial temperature, stirring speed, and micelle packing parameters [31].

2.3 Applications of mesoporous silica

Ordered mesoporous silica is characterized by high specific surface area, pore volumes, well-defined pore structure, and narrow pore size distribution. Mesoporous silica can be prepared in a variety of forms such as particles and films. These features make it possible to use mesoporous silica in a variety of fields such as in catalysis, optics, energy, environment, biotechnology, and life science (Fig. 2.4). Mesoporous silica can be efficiently used for the adsorption of toxic substances due to reasons such as high surface area, large volume, and possibility of functionalization with a variety of functional groups [32]. Tunable pore size, narrow pore size distribution, and well-defined pore structure could lead to another application of mesoporous silica serving as a scaffold for guest compounds or as a container for nanoparticles. For instance, confinement of ammonia borane (NH_3BH_3) in MCM-41 results in a significant enhancement in hydrogen storage [33].

Fig. 2.4 Schematic illustration of some examples for promising applications of mesoporous silica. (Biosensor); FDH: formaldehyde dehydrogenase, FSM8.0: A folded-sheet mesoporous silica material having honeycomb structures with ordered cylindrical channels of 8.0-nm diameter, P123-M: An alumina membrane comprising surfactant (Pluronic P123)-templated silica nanochannels with a channel diameter of 8.0 nm within the columnar alumina pores [34]. (Separation); M-C8TE: MCM-41 modified with n-octyltrimethoxysilane and endcapped with hexamethyldisilazane [35]. Images are obtained from [36] (Catalysis); [34] (Biosensor); [33] (Hydrogen storage); [37] (Drug delivery); and [35] (Separation).

The narrow pore size distribution allows selective adsorption of biomolecules. Mesoporous silica can therefore be used as a support for chromatography [38].

Mesoporous silica is used as a controlled drug-release device [37] for medical applications. In addition, recent studies of mesoporous silica for use in the proteomics termed "*Mesopore* Protein Digestion" could open new approaches to proteomics. The new approach relies on the fact that enzyme (e.g., trypsin) is concentrated in mesoporous silica particles to promote rapid digestion of protein and high through-put treatment of samples, which is a remarkable advantage compared to conventional treatment [39].

2.4 Immobilization of proteins on mesoporous silica

2.4.1 Adsorption of proteins onto solid surfaces

Interaction of proteins with solid surfaces is involved in food science [40], nanotechnology [41], and biotechnology. Adsorption of proteins depends strongly on the surface properties of both proteins and solids as well as on solution conditions [42]. The surface properties of individual proteins differ widely and are often heterogeneous, which makes it very challenging to precisely evaluate how proteins adsorb onto different solid surfaces. However, in general proteins adsorb more strongly onto a hydrophobic surface. Proteins adsorb to hydrophobic surfaces through the hydrophobic patches on the surface of the protein. Protein adsorbs to hydrophilic surfaces through the interaction of the charged or polar functional groups on the surface of the protein with the hydrophilic surfaces [43].

Adsorption of proteins on a flat surface can be studied, for example, by ellipsometry. Elwing et al. studied the adsorption of protein and surfactant on glass with a gradient in wet ability by ellipsometry [44]. The gradient was generated by modifying the glass with dichlorodimethylsilane. The adsorbed amount of negatively charged proteins increased towards the hydrophobic end of the gradient. An unmodified glass (hydrophilic part) is negatively charged at physiological pH. It is therefore difficult to separate the effect caused by hydrophobic interactions and electrostatic interactions. In the present study, the adsorption of a photosynthetic membrane protein and a surfactant to a flat silica surface was studied by *in situ* ellipsometry (see Chapter 9).

Sigal et al. studied the effect of surface wet ability on the nonspecific adsorption of proteins to uncharged self-assembled monolayers (SAM) of alkanethiolates on gold [45]. SAMs of alkanethiolates on gold are excellent model systems to study the effects of surface properties because well-defined surfaces are needed for the study of protein adsorption. SAM modified metal electrodes are used for protein film voltammetry (PFV) [46]. PFV is, further a technique for studying redox enzyme mechanisms. A redox protein is adsorbed to an electrode and addressed by a variety of electrochemical techniques [47] [48].

Surface curvature affects the conformation of adsorbed proteins. Vertegel et al. [49] studied how the surface curvature (positive curvature) of silica nanoparticles affects the structure and activity of adsorbed lysozyme. Loss in α-helix content upon adsorption was observed and found to depend on the size of the nanoparticle. Large particle size (less curved surface) induced more protein unfolding and thus larger loss in activity. Roach et al. [50] investigated the effect of the surface curvature on the adsorption of bovine serum albumin (BSA) and bovine fibrinogen (Fg) onto silica spheres. Albumin, a globular protein, became greatly disordered upon adsorption to spheres with large size (less curved surface). In contrast, fibrinogen, a rodlike protein, lost its secondary structures to a larger extent when adsorbed on particles with a high surface curvature.

A major factor governing protein adsorption is the surface energy [42]. Adsorption of proteins can be either exothermic or endothermic [51]. Katiyar et al. [51] investigated adsorption of bovine serum albumin (BSA) and lysozyme on SBA-15 using flow microcalorimetry. For a relatively soft protein (BSA), it was estimated that secondary adsorption of BSA occurred through the specific sites created by the conformational changes of adsorbed BSA molecules during the primary adsorption process. In contrast, for a relatively robust protein such as lysozyme, secondary adsorption did not take place.

Organization and orientation of proteins at the surface affect properties such as immunological and enzymatic activity of proteins adsorbed [42]. Lei *et al.* [52] showed higher activity of organophosphorous hydrolase (OPH) immobilized in functionalized mesoporous silica than the activity of free enzyme. In another paper [53], the authors concluded, from molecular dynamics simulations, that part of the reason for the enhanced activity may be attributed to the conformational change induced upon adsorption where the entrance to the active site of OPH is exposed against pore wall and fully accessible to the substrate compared to free OPH.

2.4.2 Immobilization of enzymes onto mesoporous silica

In general, enzyme immobilization can be achieved in several ways. These include direct binding to a pre-fabricated support, encapsulation or entrapment in organic or inorganic polymer matrices, and cross-linking of enzyme molecules (carrier-free) [54]. The binding to a pre-fabricated support (support binding) can be physical, ionic, or covalent. The difference between support binding and encapsulation is not completely distinguishable [54]. In this thesis, support binding is defined as the binding of an enzyme to a prefabricated support, while encapsulation is defined as the inclusion of an enzyme in a polymer network such as a silica sol-gel. Carrier-free cross-linking of dissolved enzyme molecules can be achieved via the reaction of surface NH_2 groups with a cross-linker, producing insoluble cross-linked enzymes.

When we discuss the immobilization of enzymes (and also other proteins) onto mesoporous silica, the location of the enzymes, which could be outside of the particle or the inside of the pores, is an important issue. In this Section, we address possibility of enzyme immobilization on both outside of the particle and inside the pore of mesoporous silica.

Immobilization of enzymes onto mesoporous silica is performed, in most cases, by binding to a pre-fabricated support. As mentioned above, the support binding can be induced by physical adsorption, electrostatic interaction, and covalent linking. Each of the immobilization methods is further detailed below.

Immobilization via physical adsorption. Enzymes can be immobilized onto mesoporous silica by physical adsorption such as by Van der Waals forces, hydrogen bonding and hydrophobic interactions. The binding force is normally weak because no chemical bonds are formed. As a consequence, leaching of adsorbed enzyme may occur during the use of the conjugate such as in catalysis.

Immobilization through electrostatic interaction. Electrostatic interaction is commonly used to immobilize enzymes onto the pores of silica. By controlling solution pH, the charge of the pore wall and net charge of the proteins can be adjusted. Acidic silica walls can be obtained by doping aluminium in the silica network during the synthesis in which Si sites are replaced by Al atoms [55]. The presence of aluminium was found to enhance the adsorption of heme protein cytochrome *c* (cyt *c*) [56]. The pore wall can be tuned to be positively charged by introducing amine groups, to which negatively charged enzymes are able to bind. Although ionic binding is slightly stronger than hydrophobic forces (about 3% stronger in water) [57], leaching may still occur.

Immobilization through covalent binding. To prevent leaching, enzymes can be immobilized on the silica wall by forming a covalent chemical bond. Covalent binding is strong, but the enzyme conformation may be modified during the process of immobilization. There are several ways to immobilize enzymes onto amino-functionalized silica walls via covalent binding (Fig. 2.5).

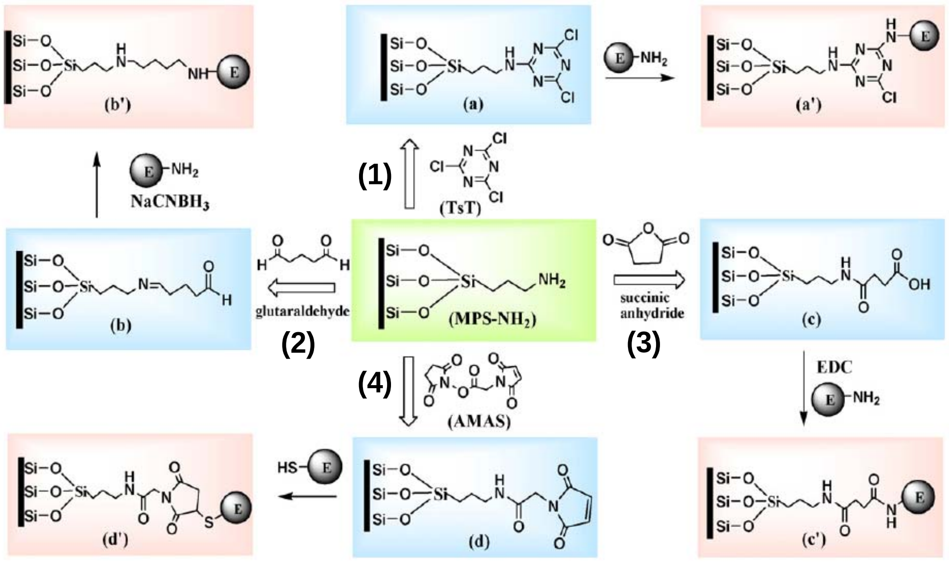

Figure 2.5: Several routes for covalent binding of enzymes to amino-functionalized silica wall. (1) Cyanuric chloride or trichloro-s-triazine (TsT), (a) and (a'); (2) glutaraldehyde, (b) and (b'); (3) succinic anhydride and 1-ethyl-3-(3-dimethylaminopropyl) carbodiimide (EDC), (c) and (c'); (4) N-(a-maleimidoacetoxy) succinimide ester (AMAS), (d) and (d') From Lee et al [58].

In general, the covalent attachment is performed through the following steps [59]:

1. Grafting the functional groups (e.g., amino groups in Fig. 2.5) onto the silica wall
2. Derivatization with a cross-linking agent such as glutaraldehyde or cyanuric chloride
3. Covalent binding of enzyme molecules.

The immobilized enzyme obtained through covalent binding is stable. α-Chymotrypsin, immobilized onto mesoporous silica via covalent binding exhibited improved thermal stability and enhanced activity in organic solvents compared to free enzyme [60]. The authors argued that the enhanced stability and activity are most likely caused by the large curvature of the pores, which provide multiple sites for attachment of the enzyme.

2.4.3 Key factors determining protein adsorption onto mesoporous silica

Several factors such as pH, ionic strength, and size of pore and proteins affect the adsorption of proteins onto mesoporous silica. Below, we summarize briefly how each factor affects the adsorption of proteins.

Effect of pH on protein adsorption. Solution pH affects the adsorption of proteins onto mesoporous silica since both the surface net charge of the proteins and the charge state of the silica wall depend on solution pH. The isoelectric point (pI) of proteins is the pH at which the net surface charge is zero. When pH of the solution is below the pI of a protein, the surface net charge of the protein is positive, and when pH of the solution is above the pI of the protein, the surface net charge is negative. These principles also apply to the silica pore wall. Silica surfaces are negatively charged at pH >2. Different types of mesoporous silica have slightly different isoelectric points. Deere et. al [61] reported pI of MCM-41 as 3.6 and Hudson et al. [62] reported pI of SBA-15 and MSE (an organosilicate) as ~3.7 ± 0.3 and ~4.8 ± 0.3, respectively. When we select solution pH for adsorption of proteins, it is desirable to choose the pH at which proteins and silica wall have opposite charges. Deere et. al [61] investigated adsorption of pepsin (pI < 1) to cyano-modified silicate. When solution pH is 6.5, both pepsin and the silicate are negatively charged. No adsorption of protein was observed. Hudson et al. [62] investigated the effect of pH on the adsorption of horse heart cyt *c* (pI: 10.7) on SBA-15. At pH = 10, higher loading of cyt *c* was observed. At pH close to pI, lateral repulsion between protein molecules is reduced, thereby allowing close packing of the proteins onto the surface of the pore. Vinu et al. [63] investigated adsorption of lysozyme (pI~11). Maximum loading was obtained at pH 10.5 very close to pI. At solution pH close to pI, ionic interaction is also minimized and hydrophobic interaction could play more important roles [64].

Effect of ionic strength. The ionic strength of the solution will significantly affect the adsorption of proteins if the adsorption is dominated by electrostatic interactions. Deere et al. [61] studied the effect of ionic strength on the adsorption of cyt *c* on cyano-modified silicate. The amount of adsorbed cyt *c* decreased with increasing ionic strength. Hudson et al. [62] investigated the effect of ionic strength on the adsorption of cyt *c* and xylanase (an enzyme widely used in paper production) on SBA-15 by increasing the ionic strength of the initial protein solution and found that if the ionic strength is higher than 0.5 M, almost no adsorption took place.

Size of protein and pore size of mesoporous silica. Matching of the hydrodynamic diameter of protein with pore size is important to achieve adsorption of proteins into the pores. Diaz and Balkus [65] investigated the adsorption of proteins using MCM-41. There was a clear trend in the amount adsorbed with respect to the molecular mass of proteins (Fig. 2.6). When MCM-41 with a pore diameter smaller than the size of HRP is used, the amount of adsorbed protein was significantly lower. The size of HRP (4.0 x 4.4 x 6.8 nm^3) is here too large to enter the pore (pore size of 4 nm).

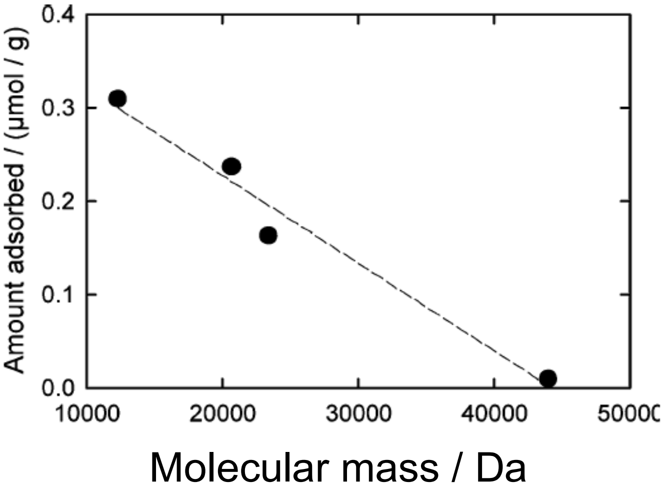

Figure 2.6: Effect of enzyme size on the immobilization efficiency of MCM-41 host with a pore diameter of 4 nm). The adsorbed amount of horseradish peroxidase, HRP, (Molecular mass: 44,000 Da) is significantly lower compared to other proteins, cytochrome c (12,400 Da), papain (20,700 Da) and trypsin (23,400 Da), suggesting that HRP detected was adsorbed on the outer surface of MCM-41 host. From Hartmann [64].

Size matching is also important in order to prevent leaching of proteins. If the pore diameter is too large compared to the size of proteins, leaching can occur depending on the immobilization method used. From the enzyme activity, however, small pores cause diffusion limitation.

2.4.4 Confinement of proteins in mesoporous silica

How confinement of molecules in the pore affects the properties of the guest molecules is of great interest from both fundamental aspects and from application points of view such as in biosensor function. Before discussing proteins confined in mesoporous silica, the properties of water confined in mesoporous silica will be briefly discussed because water surrounds protein molecules in the solution as a hydration shell and strongly affects the properties of the proteins [66]. In addition, interfacial water plays an important role in nature [67]. The properties of water confined in mesoporous silica have been investigated experimentally as well as by molecular dynamics simulations. Yamaguchi et al. [68] studied the microscopic structure and dynamic properties of water and other liquids in MCM-41 by in situ FTIR, X-ray diffraction and quasielastic neutron scattering techniques. The authors reported that hydrogen bonded structures of water and methanol in the pores are distorted compared with bulk solvent, i.e., less hydrogen bonds formed among water molecules or methanol molecules in the pores, due to strong interaction with the hydrophilic surface of MCM-41. Lerbret et al. studied water confined in cylindrical pores by molecular dynamics simulations and found strong interaction of interfacial water molecules with the silica pore surface. The mean number of hydrogen bonds formed by a water molecule with another water molecule decreases near the pore surface. This arises from the distortion of the water hydrogen bond network (HBN) near the pore surface. It was also found that the tetrahedral structure of water is distorted near the pore surface [69].

Confinement of macromolecules such as proteins brings about excluded volume effects. Both excluded volume effects and the water structure change are two major factors to affect the stability of proteins confined in a nanoscale environment [58]. Proteins in a pore comparable to their size may not be able to assume certain states, e.g. unfolded states, due to excluded volume effects in that way obtaining an increased structural stability. Ravindra et. al [70] showed, for example, that the thermal stability of RNase A confined in MCM-48 is enhanced with an increased unfolding temperature. They attributed the increased stability to limited conformational space and increased hydration strength. In the present study, horseradish peroxidase (HRP) in SBA-15 was more resistant to a denaturing agent, urea, than free HRP, but the confined HRP did not show enhanced resistance to another denaturing agent, guanidinium chloride. The different behavior of free and immobilized enzyme is most likely due to different hydrogen bonding patterns of water and increased hydration strength of the protein inside the nanopores.

References

[1] T. Yanagisawa, T. Shimizu, K. Kuroda and C. Kato. The Preparation of Alkyltriinethylaininonium–Kaneinite Complexes and Their Conversion to Microporous Materials. *Bull. Chem. Soc. Jpn.*, 63:988-992, 1990.

[2] C. T. Kresge, M. E. Leonowicz, W. J. Roth, J. C. Vartuli and J. S. Beck. Ordered Mesoporous Molecular Sieves Synthesized by a Liquid-Crystal Template Mechanism. *Nature* 359:710-712, 1992.

[3] J. S. Beck, J. C. Vartuli, W. J. Roth, M. E. Leonowicz, C. T. Kresge, K. D. Schmitt, C. T. W. Chu, D. H. Olson, E. W. Sheppard, S. B. McCullen, J. B. Higgins and J. L. Schlenker. A New Family of Mesoporous Molecular Sieves Prepared with Liquid Crystal Templates. *J. Am. Chem. Soc.*, 114:10834-10843, 1992.

[4] F. Di Renzo, H. Cambon and R. Dutartre. A 28-year-old synthesis of micelle-templated mesoporous silica. *Microporous Mater.,* 10: 283-286, 1997.

[5] Q. Huo, D. I. Margolese, U. Cielsa, P. Feng, T. E. Gier, P. Sieger, R. Leon, P. M. Petroff, F. Schuth and G. D. Stucky. Generalized Synthesis of Periodic Surfactant/Inorganic Composite Materials. *Nature*, 368:317-321, 1994.

[6] D. Zhao, J. Feng, Q. Huo, N. Melosh, G. H. Fredrickson, B. F. Chmelka, and G. D. Stucky. Triblock Copolymer Syntheses of Mesoporous Silica with Periodic 50 to 300 Angstrom Pores. *Science*, 279: 548-552, 1998.

[7] P. Schmidt-Winkel, W. W. Lukens, D. Zhao, P. Yang, B. F. Chmelka and G. D. Stucky. Mesocellular Siliceous Foams with Uniformly Sized Cells and Windows. *J. Am. Chem. Soc.*, 121:254-255, 1999.

[8] R. Ryoo, S. H. Joo, and S. Jun. Synthesis of Highly Ordered Carbon Molecular Sieves via Template-Mediated Structural Transformation, *J. Phys. Chem. B*, 103: 7743-7746, 1999.

[9] S. Jun, S. H. Joo, R. Ryoo, M. Kruk, M. Jaroniec, Z. Liu, T. Ohsuna and O. Terasaki. Synthesis of New Nanoporous Carbon with Hexagonally Ordered Mesostructure, *J. Am. Chem. Soc.*, 122:10712-0713, 2000.

[10] U. Schubert and N. Hüsing. *Synthesis of Inorganic Materials.* Wiley, Weinheim, 2005.

[11] A. Monnier, F. Schuth, Q. Huo, D. Kumar, D. Margolese, R. S. Maxwell, G. D. Stucky, M. Krishnamurty, P. Petroff, A. Firouzi, M. Janicke and B.F. Chmelka. Cooperative Formation of Inorganic-Organic Interfaces in the Synthesis of Silicate Mesostructures. *Science*, 261:1299-1303, 1993.

[12] R. Xu, W. Pang, J. Yu, Q. Huo, and J. Chen. Synthesis, Structure, and Characterization of Mesoporous Materials, chapter 8. In *Chemistry of Zeolites and Related Porous Materials: Synthesis and Structure.,* Online. John Wiley & Sons (Asia) Pte Ltd. 2010.

[13] A. Firouzi, D. Kumar, L. M. Bull, T. Besier, P. Sieger, Q. Huo, S. A. Walker, J. A. Zasadzinski, C. Glinka, J. Nicol, D. Margolese, G. D. Stucky and B. F. Chmelka. Cooperative Organization of Inorganic-Surfactant and Biomimetic Assemblies. *Science*, 267:1138-1143, 1995.

[14] Q. Huo, D.I. Margolese, U. Ciesla, P. Feng, T.E. Gier, P. Sieger, R. Leon, PM Petroff, F. Schuth, G.D. Stucky. Generalized Synthesis of Periodic Surfactant/Inorganic Composite Materials. *Nature* 368:317-321, 1994.

[15] G.J. de A.A. Soler-Illia, C. Sanchez, B. Lebeau and J. Patarin. Chemical Strategies to Design Textured Materials: from Microporous and Mesoporous Oxides to Nanonetworks and Hierarchical Structures. *Chem. Rev.*, 102:4093-4138, 2002.

[16] F. Hoffmann, M. Cornelius, J. Morell, and M. Fröba. Silica-Based Mesoporous Organic–Inorganic Hybrid Materials. *Angew. Chem. Int. Ed.*, 45:3216-3251, 2006.

[17] S. Che, A. E. Garcia-Bennett, T. Yokoi, K. Sakamoto, H. Kunieda, O. Terasaki and T. Tatsumi. A Novel Anionic Surfactant Templating Route for Synthesizing Mesoporous Silica with Unique Structure. *Nature Materials*, 2:801-805, 2003.

[18] Y. Wan and D. Zhao. On the Controllable Soft-Templating Approach to Mesoporous Silicates. *Chem. Rev.*, 107:2821–2860, 2007.

[19] D. Zhao, Q. Huo, J. Feng, B.F. Chmelka and G.D. Stucky, Nonionic Triblock and Star Diblock Copolymer and Oligomeric. *J. Am. Chem. Soc.*, 120: 6024-6036, 1998.

[20] S. Ruthstein, V. Frydman, S. Kababya, M. Landau, and D. Goldfarb. Study of the Formation of the Mesoporous Material SBA-15 by EPR Spectroscopy. *J. Phys. Chem. B*, 107:1739, 2003.

[21] K. Flodström, H. Wennerström, and V. Alfredsson. Mechanism of Mesoporous Silica Formation. A Time-Resolved NMR and TEM Study of Silica-Block Copolymer Aggregation. *Langmuir*, 20: 680-688, 2004.

[22] http://goldbook.iupac.org/C01117.html, Web page, October 26, 2011.

[23] A. Sundblom, C. L. P. Oliveira, J. S. Pedersen and A. E. C. Palmqvist. On the Formation Mechanism of Pluronic-Templated Mesostructured Silica. *J. Phys. Chem. C*, 114: 3483-3492, 2010.

[24] J. M. Kim, Y.-J. Han, B. F. Chmelka and G. D. Stucky. One-step synthesis of ordered mesocomposites with non-ionic amphiphilic block copolymers: implications of isoelectric point, hydrolysis rate and fluoride. *Chem. Commun.*, 2437-2438, 2000.

[25] S. K. Jana, A. Mochizuki and S. Namba, Progress in Pore-Size Control of Mesoporous MCM-41 Molecular Sieve Using Surfactant Having Different Alkyl Chain Lengths and Various Organic Auxiliary Chemicals. *Catalysis Surveys from Asia*, 8:1-13, 2004.

[26] L. Cao, T. Man and M. Kruk**,** Synthesis of Ultra-Large-Pore SBA-15 Silica with Two-Dimensional Hexagonal Structure Using Triisopropylbenzene As Micelle Expander. *Chem. Mater.*, 21:1144-1153, 2009.

[27] A. Galarneau, H. Cambon, F. Di Renzo, and F. Fajula. True Microporosity and Surface Area of Mesoporous SBA-15 Silicas as a Function of Synthesis Temperature. *Langmuir*, 17:8328-8335, 2001.

[28] P. F. Fulvio, S. Pikus and M. Jaroniec. Tailoring Properties of SBA-15 Materials by Controlling Conditions of Hydrothermal Synthesis. *J. Mater. Chem.*, 15:5049-5053, 2005.

[29] D. Zhao, J. Sun, Q. Li, and G. D. Stucky. Morphological Control of Highly Ordered Mesoporous Silica SBA-15. *Chem. Mater.*, 12:275-279, 2000.

[30] L. Wang, T. Qi, Y. Zhang, J. Chu. Morphosynthesis Route to Large-Pore SBA-15 Microspheres. *Microporous Mesoporous Mater.*, 91:156-160, 2006.

[31] H. I. Lee, J. H. Kim, G. D. Stucky, Y. Shi, C. Pak and J. M. Kim, Morphology-Selective Synthesis of Mesoporous SBA-15 Particles. *Mater. Chem.*, 20:8483-8487, 2010.

[32] Z. Wu and D. Zhao. Ordered Mesoporous Materials as Adsorbents. *Chem. Commun.*, 47:3332–3338, 2011.

[33] H. Kim, A. Karkamkar, T. Autrey, P. Chupas, and T. Proffen. Determination of Structure and Phase Transition of Light Element Nanocomposites in Mesoporous Silica: Case study of NH_3BH_3 in MCM-41. *J. Am. Chem. Soc.* 131:13749–13755, 2009.

[34] T. Shimomuraa, T. Itoh, T. Sumiya, F. Mizukami, and M. Ono. Electrochemical Biosensor for the Detection of Formaldehyde Based on Enzyme Immobilization in Mesoporous Silica Materials. *Sens. Actuators, B*, 135:268–275, 2008.

[35] T. Yasmin and K. Müller. Synthesis and Surface Modification of Mesoporous MCM-41 Silica Materials. *J. Chromatogr. A*, 1217:3362–3374, 2010.

[36] S. Boujday, J. Blanchard, R. Villanneau, J. Krafft, C. Geantet, C. Louis, M. Breysse, and A. Proust. Polyoxomolybdate-Stabilized Ru(0) Nanoparticles Deposited on Mesoporous Silica as Catalysts for Aromatic Hydrogenation. *ChemPhysChem*. 8:2636–2642, 2007.

[37] I. Slowing, B. G. Trewyn, and V. S.-Y. Lin. Mesoporous Silica Nanoparticles for Intracellular Delivery of Membrane-Impermeable Proteins. *J. Am. Chem. Soc.*, 129: 8845–8849, 2007.

[38] A. Katiyar and N. G. Pinto. Visualization of Size-Selective Protein Separations on Spherical Mesoporous Silicates. *Small*. 2:644-648, 2006.

[39] R. Savino, F. Casadonte and R. Terracciano. *In Mesopore* Protein Digestion: A New Forthcoming Strategy in Proteomics. *Molecules*. 16:5938-5962, 2011.

[40] S.R. Euston. Computer Simulation of Proteins: Adsorption, Gelation and Self-Association. *Curr. Opin. Colloid Interface Sci.*, 9:321-327, 2004.

[41] P. Asuri, S. S. Bale, S. S. Karajanagi, and R. S. Kane. The Protein–Nanomaterial Interface. *Curr Opin Biotechnol.*, 17:562–568, 2006.

[42] M. Wahlgren and T. Arnebrant. Protein Adsorption to Solid Surfaces. *Trends Biotechnol.*, 9:201-8, 1991.

[43] R. A. Latour, Jr. Biomaterials: Protein–Surface Interactions. In *Encyclopedia of Biomaterials and Biomedical Engineering*. Taylor & Francis, 2005.

[44] H. Elwing, S. Welin, A. Askendal, U. Nilsson, and I. LundstrÖm. A Wettability Gradient Method for Studies of Macromolecular Interactions at the Liquid/Solid Interface. *J. Colloid Interface Sci.*, 119:203-210, 1987.

[45] G. B. Sigal, M. Mrksich, and G. M. Whitesides. Effect of Surface Wettability on the Adsorption of Proteins and Detergents. *J. Am. Chem. Soc.* 120:3464-3473, 1998**.**

[46] J. N. Butt and F. A. Armstrong. Voltammetry of Adsorbed Redox Enzymes: Mechanisms in the Potential Dimension, chapter 4. In *Bioinorganic Electrochemistry*, pages 91–128. Springer, Dordrecht, 2008. Editors: O. Hammerich and J. Ulstrup.

[47] J. D. Gwyer, J. Zhang, J. N. Butt, and J. Ulstrup. Voltammetry and In Situ Scanning Tunneling Microscopy of Cytochrome c Nitrite Reductase on Au(111) Electrodes. *Biophys. J.*, 91:3897–3906, 2006.

[48] A. G. Hansen, A. Boisen, J. U. Nielsen, H. Wackerbarth, I. Chorkendorff, Jens E. T. Andersen, Jingdong Zhang, and Jens Ulstrup. Adsorption and Interfacial Electron

Transfer of *Saccharomyces Cerevisiae* Yeast Cytochrome *c* Monolayers on Au(111) Electrodes. *Langmuir*, 19:3419-3427, 2003.

[49] A. Vertegel, R. W. Siegel, and J. S. Dordick. Silica Nanoparticle Size Influences the Structure and Enzymatic Activity of Adsorbed Lysozyme. *Langmuir,* 20: 6800-6807, 2004.

[50] P. Roach, D. Farrar, and C. C. Perry. Surface Tailoring for Controlled Protein Adsorption: Effect of Topography at the Nanometer Scale and Chemistry, *J. Am. Chem. Soc*., 128:3939-3945, 2006.

[51] A. Katiyar, S.W. Thiel, V.V. Guliants and N.G. Pinto. Investigation of the Mechanism of Protein Adsorption on Ordered Mesoporous Silica Using Flow Microcalorimetry. *J. Chromatogr. A*, 1217:1583-1588, 2010.

[52] A. Lei, Y. Shin, J.K. Magnuson, G.E. Fryxell, L.L. Lasure, D.C. Elliott, J. Liu, and E.J. Ackerman. Characterization of Functionalized Nanoporous Supports for Protein Confinement. *Nanotechnology*, 17:5531-5538, 2006.

[53] D. E. B. Gomes, R. D. Lins, P. G. Pascutti, C. Lei, and T. A. Soares. The Role of Nonbonded Interactions in the Conformational Dynamics of Organophosphorous Hydrolase Adsorbed onto Functionalized Mesoporous Silica Surfaces. *J. Phys. Chem. B*, 114:531–540, 2010.

[54] R. A. Sheldon, Enzyme Immobilization: The Quest for Optimum Performance. *Adv. Synth. Catal.*, 349:1289-1307, 2007.

[55] A. Dragoi, E. Dumitriu, C. Guimon, and A. Auroux. Acidic and Adsorptive Properties of SBA-15 Modified by Aluminum Incorporation. *Microporous Mesoporous Mater.*, 121:7–17, 2009.

[56] C.H. Lee, J. Lang, C.W. Yen, P.C. Shih, T.S. Lin, C.Y. Mou, Enhancing Stability and Oxidation Activity of Cytochrome *c* by Immobilization in the Nanochannels of Mesoporous Aluminosilicates. *J. Phys. Chem. B*, 109: 12277-12286, 2005.

[57] M. Matsui, Y. Kiyozumi, T. Yamamoto, Y. Mizushina, F. Mizukami, and K. Sakaguchi. Selective Adsorption of Biopolymers on Zeolites, Matsui, *Chem.-Eur. J. 7*: 1555, 2001.

[58] A. H. Lee, T. S. Lin and C. Y. Mou. Mesoporous Materials for Encapsulating Enzymes. *Nano Today*, 4:165-179, 2009.

[59] A. Ispas, I. Sokolov, and S. Andreescu. Enzyme-Functionalized Mesoporous Silica for Bioanalytical Applications. *Analytical and Bioanalytical Chemistry*, 393:543-554, 2009.

[60] P. Wang, S. Dai, S. D. Waezsada, A. Y. Tsao, and B. H. Davison. Enzyme Stabilization by Covalent Binding in Nanoporous Sol-Gel Glass for Nonaqueous Biocatalysis. *Biotechnol. Bioeng.*, 74:249-255. 2001.

[61] J. Deere, E. Magner, J. G. Wall, and B. K. Hodnett, Mechanistic and Structural Features of Protein Adsorption onto Mesoporous Silicates, *J. Phys. Chem. B*, 106:7340-7347, 2002.

[62] S. Hudson, E. Magner, J. Cooney, and B. K. Hodnett, Methodology for the Immobilization of Enzymes onto Mesoporous Materials. *J. Phys. Chem. B*, 109:19496–19506, 2005.

[63] A. Vinu, V. Murugesan, O. Tangermann, and M. Hartmann, Adsorption of Cytochrome *c* on Mesoporous Molecular Sieves: Influence of pH, Pore Diameter, and Aluminum Incorporation. *Chem. Mater.*, 16: 3056–3065, 2004.

[64] M. Hartmann. Ordered Mesoporous Materials for Bioadsorption and Biocatalysis. *Chem. Mater.*, 17: 4577-4593, 2005.

[65] J. F. Diaz and K. J. Balkus. Enzyme Immobilization in MCM-41 Molecular Sieve. *J. Mol. Catal. B*, 2:115-126, 1996.

[66] A. Franks. Protein Hydration, chapter 12. In *Protein Biotechnology*, pages 437-465. Humana Press, New Jersey, 1993. Editor: F. Franks.

[67] P. Ball. Water as a Biomolecule. *ChemPhysChem*. 9:2677-2685, 2008.

[68] T. Yamaguchi, K. Yoshida, P. Smirnov, T. Takamuku, S. Kittaka, S. Takahara, Y. Kuroda, and M.-C. Bellissent-Funel. Structure and Dynamic Properties of Liquids Confined in MCM-41 Mesopores. *Eur. Phys. J.* Special Topics 141:19–27, 2007.

[69] A. Lerbret, G. Lelong, P. E. Mason, M-L. Saboungi and J. W. Brady. Water Confined in Cylindrical Pores: A Molecular Dynamics Study. *Food Biophys.*, 6:233–240, 2011.

[70] R. Ravindra, S. Zhao, H. Gies, and R. Winter. Protein Encapsulation in Mesoporous Silicate: The Effects of Confinement on Protein Stability, Hydration, and Volumetric Properties. *J. Am. Chem. Soc.*, 126:12224–12225, 2004.

3. Basics of enzyme catalytic kinetics

3.1 Enzyme

Enzymes catalyze chemical reactions, by which the reaction rate is enhanced usually very strongly and highly selectively, compared with the same reaction in the absence of enzyme. Typically, the rate of a reaction is limited by a highest energy state, called the transition state (Fig. 3.1). The rate enhancement by the enzyme is achieved by lowering the activation-barrier between the substrate and the product.

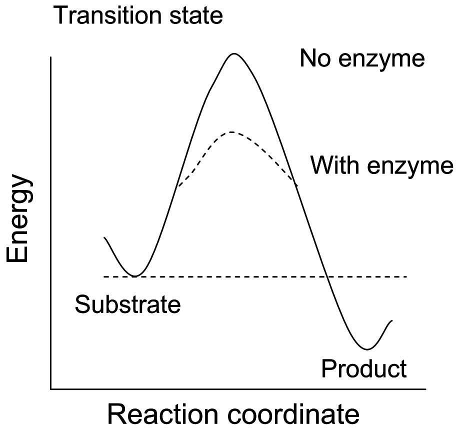

Figure 3.1: Diagram of energetics of a reaction. Enzymes act by lowering the activation barrier for the catalyzed reaction.

When we study the enzyme (e.g. reaction mechanism, function), the enzyme of interest must be purified because crude extracts contain other enzymes and contaminants that may affect the catalytic reaction.

3.2 Steady state kinetics [1] [2]

In the simplest enzyme mechanism, an enzyme (E) binds a substrate (S) during the catalysis and forms an enzyme-substrate (ES) complex. The complex then decomposes to products (P) and enzyme:

$$\mathrm{E} + \mathrm{S} \underset{k_{-1}}{\overset{k_1}{\rightleftharpoons}} \mathrm{ES} \xrightarrow{k_2} \mathrm{P} + \mathrm{E} \tag{3.1}$$

The velocity of the reaction is:

$$v = \frac{d[\mathrm{P}]}{dt} = k_2[\mathrm{ES}] \tag{3.2}$$

The production rate of ES is the difference between the generation and the disappearance of the ES complex:

$$\frac{d[\mathrm{ES}]}{dt} = k_1[\mathrm{E}][\mathrm{S}] - k_{-1}[\mathrm{ES}] - k_2[\mathrm{ES}] \tag{3.3}$$

When we use this equation, assumption of steady state is commonly involved. That is, it is assumed that the concentration of enzyme-substrate complex [ES] remains constant, that is,

$$\frac{d[\mathrm{ES}]}{dt} = 0 \tag{3.4}$$

The steady state considerations apply broadly over wide time ranges, but obviously not for the stages at the beginning and towards the end of the reaction. The total concentration of the enzyme, $[\mathrm{E}]_\mathrm{T}$, is measurable and can be described as:

$$[\mathrm{E}]_\mathrm{T} = [\mathrm{E}] + [\mathrm{ES}] \tag{3.5}$$

From eqs. (3.3), (3.4) and (3.5), we obtain under steady-state conditions

$$k_1([\mathrm{E}]_\mathrm{T} - [\mathrm{ES}])[\mathrm{S}] = (k_{-1} + k_2)[\mathrm{ES}] \tag{3.6}$$

Rearrangement of this equation gives:

$$[\mathrm{ES}](k_{-1} + k_2 + k_1[\mathrm{S}]) = k_1[\mathrm{E}]_\mathrm{T}[\mathrm{S}] \tag{3.7}$$

Dividing both sides by k_1 and solving for [ES] gives:

$$[\mathrm{ES}] = \frac{[\mathrm{E}]_\mathrm{T}[\mathrm{S}]}{K_M + [\mathrm{S}]} \tag{3.8}$$

where $K_M = \frac{k_{-1} + k_2}{k_1}$ is the Michaelis constant.

The initial velocity (v_0) of the reaction can be expressed from (3.2) as:

$$v_0 = \left(\frac{d[\mathrm{P}]}{dt}\right)_{t=0} = k_2[\mathrm{ES}] = \frac{k_2[\mathrm{E}]_\mathrm{T}[\mathrm{S}]}{K_M + [\mathrm{S}]} \tag{3.9}$$

The maximum velocity of a reaction, $V_{\max}$, occurs at high concentration of substrate, where enzyme is saturated with substrate. Therefore, from eq. (3.2),

$$V_{\max} = k_2\,[\mathrm{E}]_\mathrm{T} \tag{3.10}$$

i.e. $V_{\max}$ is independent of the substrate concentration. Combining eqs. (3.9) and (3.10), we obtain the Michaelis-Menten equation:

$$v_0 = \frac{V_{\max}[\mathrm{S}]}{K_M + [\mathrm{S}]} \tag{3.11}$$

K_M has two meanings. One is the substrate concentration at which initial velocity is half of the maximum velocity, $V_{\max}$. At this concentration, half of the enzyme is bound to substrate.

Secondly, K_M is approximately the dissociation constant of the enzyme-substrate complex. As noted, $K_M = \frac{k_{-1} + k_2}{k_1}$. When $k_{-1} >> k_2$, $K_M = k_{-1}/ k_1$, i.e. dissociation constant. Large K_M therefore means lower enzyme affinity for the substrate, and small value means higher affinity to substrate.

V_{max} can be used to obtain the turnover number, k_{cat}, of an enzyme, which is derived from eq. (3.10).

$$k_{cat} = k_2 = \frac{V_{max}}{[E]_T} \tag{3.12}$$

k_{cat} is the number of reaction events that each active site of an enzyme catalyzes per unit time. When $[S] << K_M$, little ES is formed. $[E]_T = [E]$. (3.9) can then be rewritten as

$$v_0 \approx \left(\frac{k_2}{K_M} \right) [E]_T [S] \approx \left(\frac{k_{cat}}{K_M} \right) [E][S] \tag{3.13}$$

i.e. the rate is first order at the low substrate concentrations. k_{cat}/K_M is thus the apparent second-order rate constant of the reaction and can be used as a measure of the catalytic efficiency of an enzyme.

3.3 Determination of catalytic constants

3.3.1 Determination from initial velocity measurement

To determine catalytic constants, in general, the initial velocity is measured over a range of substrate concentrations. When two or more substrates are involved in the enzyme reaction, the concentration of one substrate must be fixed. Several methods are available to estimate catalytic constants. In this thesis, two methods were used, namely (1) transformation of data to linear form and use of linear regression; (2) direct nonlinear curve fitting of the Michaelis-Menten form, e.q. (3.11). The method (1) uses the reciprocal of eq. (3.11):

$$\frac{1}{v_0} = \frac{1}{V_{\max}} + \frac{K_M}{V_{\max}} \frac{1}{[\mathrm{S}]} \tag{3.14}$$

This linear equation with respect to 1/ v_0 and 1/[S] is called a Lineweaver-Burk plot (Fig. 3.2).

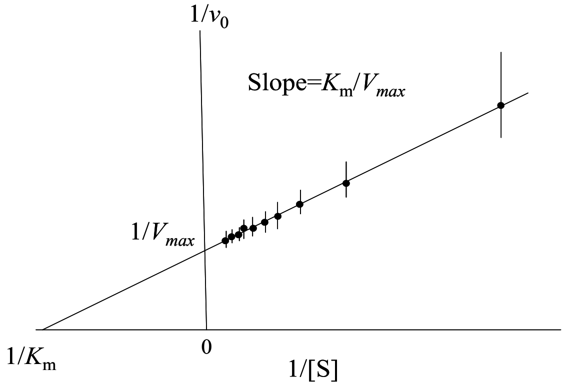

Figure 3.2: A Lineweaver-Burk or double-reciprocal plot with error bars. The plot was redrawn from the figure in Voet et al [2]. The data points and error bars are shown approximately from those in the original figure. At small [S], i.e. large 1/[S], the error effect is large. At large [S], the data points are crowded.

The Lineweaver-Burk plot or double-reciprocal plot is sensitive to errors. For small [S], small errors in v_0 leads to large errors in 1/[v_0]. The data points at high [S] tend to be crowded to the left side of the plot. To determine the catalytic constants more accurately, the nonlinear curve fitting method, i.e. method (2) would be a better approach.

3.3.2 Determination from progress curve

The progress curve (Fig. 3.3) of a reaction can also be used for the determination of catalytic constants from a single substrate concentration. To do so, Michaelis-Menten equation, eq. (3.11) is modified as below.

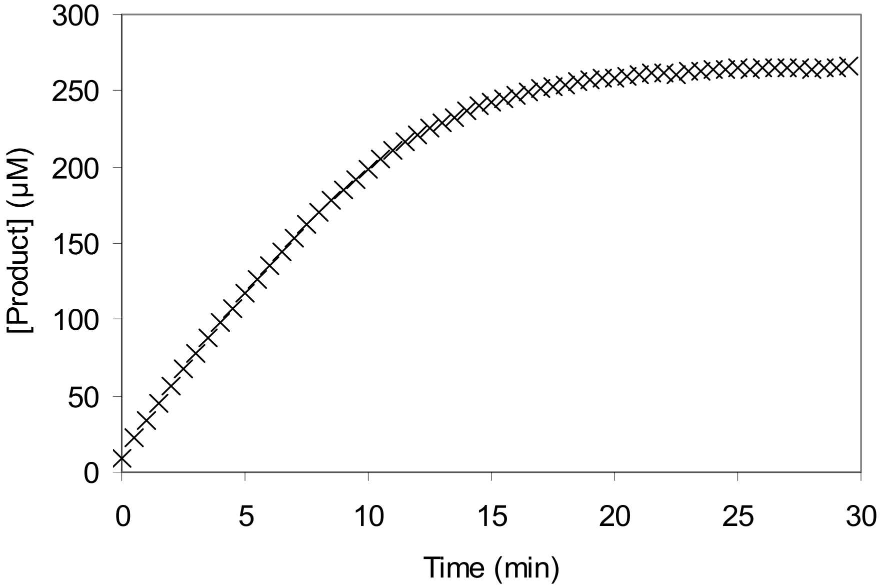

Figure 3.3: Changes in product (P) concentration as a function of time. Product (N-antipyryl-p-benzoquinoneimine) is formed in the oxidation of phenol by H_2O_2. The data of Figure 7.7 in Chapter 7 was redrawn by converting the absorbance into product concentration.

From the Michaelis-Menten kinetic equation,

$$v_0 = -\frac{dS}{dt} = \frac{V_{\max}[S]}{K_M + [S]} \tag{3.15}$$

Integration from $S=S_0$ to $S=S$ and from $t=0$ to $t=t$ gives:

$$-(S - S_0) - K_M \ln\frac{S}{S_0} = V_{\max} t \tag{3.16}$$

If we follow P rather than S and notice that $[S_0] = [P_\infty]$, then $[S] = [S_0] - [P] = [P_\infty] - [P]$

Insertion of these equivalents into eq. (3.16) gives

$$t = \frac{1}{V_{\max}} \cdot [P] - \frac{K_M}{V_{\max}} \ln \frac{[P_\infty] - [P]}{[P_\infty]} \tag{3.17}$$

eq. (3.17) is the correlation between P and t. This equation can be converted to the linear form:

$$\frac{[\mathrm{P}]}{t} = V_{\max} - K_M \frac{\ln \dfrac{[\mathrm{P}]_\infty}{[\mathrm{P}]_\infty - [\mathrm{P}]}}{t} \tag{3.18}$$

[P]/t plotted against ln ($[P]_\infty/([P]_\infty - [P])$)/t thus gives a straight line with a slope of $-K_M$ and the intercept gives V_{max}. This allows using the reaction progress curve experimentally measured for the approximate quantitative analysis of kinetic data with less work than that required for the determination by the initial rate measurements. We shall exploit both the Lineweaver-Burk/Michaelis-Menten and the direct time progress curve in the data analysis in chapters 7 and 8.

References

[1] G. Marangoni. *Enzyme Kinetics. A Modern Approach*. John Wiley & Sons, Inc., Hoboken, New Jersey, 2003.

[2] D. Voet and J. G. Voet, *Biochemisty*, pages 351-354. John Wiley & Sons, Inc., 2nd edition, 1995.

4. Fluorescence spectroscopy

Fluorescence spectroscopy of proteins (the light-harvesting protein complex of photosynthetic purple bacteria) confined in mesoporous SBA-15 silica pores was part of the present study. We provide here a brief overview of the key concepts used.

4.1 Absorption of light

When a molecule absorbs photons, the energy of the molecule increases and the molecule is promoted to an excited state. The lowest energy state of a molecule is called the ground state. The absorbance of a sample is defined:

$$A(\lambda) = \log_{10} \frac{I_\lambda^0}{I_\lambda} \tag{4.1}$$

Where I_λ^0 and I_λ are the intensity of the incident light and transmitted light, respectively. In most cases, the relationship between absorbance of a sample, molar absorption coefficient (ε, L mol^{-1}cm^{-1}), and the concentration of the absorbing species (c, in mol/l) follows the Lambert–Beer Law:

$$A(\lambda) = \log_{10} \frac{I_\lambda^0}{I_\lambda} = \varepsilon c l \tag{4.2}$$

where l is the light path length (in cm) of the solution absorbing the light.

4.2 Fluorescence

Absorption of light causes the molecule to be excited from a ground state to, the first singlet (S_1) or second excited singlet state (S_2) [1]. This is illustrated by the Jablonski diagram (Fig. 4.1) [1]. Singlet states are the states in which the spins are opposite in both the ground and excited states. The transition between the two states is rapid and takes place in about 10^{-15} s [1]. The motion of the electrons is much faster than that of the nuclei. The nuclei are therefore not displaced during the transition. This is called the Franck–Condon principle [1].

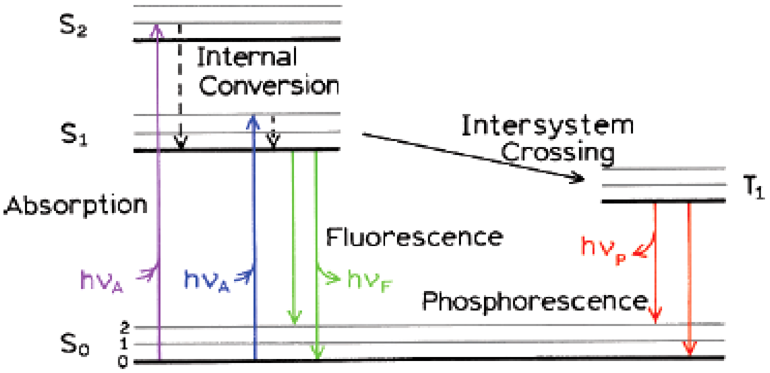

Figure 4.1: Jablonski diagram. The transitions between different electronic and vibrational states are shown as vertical lines. After light absorption, a fluorophore is excited to higher S_1 or S_2 levels. The molecule relaxes to the lowest S_1 state (internal conversion). A radiative transition from S_1 state to S_0 results in fluorescence. Molecules in the S_1 state can also undergo a conversion to the first triplet state, T_1 (intersystem crossing). A radiative transition from T_1 to S_0 results in phosphorescence. From Lakowicz [1].

When a molecule absorbs light and reaches the higher energetic S_1 or S_2 level, the molecule will subsequently dissipate the energy and relax to the lowest S_0 state (Fig. 4.1). This is called internal conversion. The internal conversion is a non-radiative transition and completed within 10^{-12} s or so. A radiative transition from S_1 state to S_0 results instead in fluorescence. Intersystem crossing is another non-radiative transition between the singlet state (S_1) and the first triplet state (T_1). A radiative transition from T_1 to S_0 is called phosphorescence, which is “forbidden”, but can still be observed due to spin-orbit coupling [2]. The rate constant of triplet emission is much smaller than that of fluorescence and phosphorescence, i.e. a slow process. As shown in the Jablonski diagram (Fig. 4.1), the energy of absorption is higher than that of fluorescence due to the non-radiative loss of energy. Fluorescence therefore occurs at longer wavelength than that of absorption. This phenomenon is called Stokes shift.

4.3 Excited state lifetime and quantum yield

Suppose that a sample containing a fluorophore is excited with a short pulse of light. This results in a certain number of molecules (n_0) of the fluorophore to be in an excited state. The decay of excited molecules is expressed by the kinetic equation:

$$\frac{dn(t)}{dt} = (\Gamma + k_{\mathrm{nr}})\, n(t) \tag{4.3}$$

where $n(t)$ is the number of molecules excited at time t, Γ is the emissive rate of the fluorophore, and k_{nr} is the rate of non-radiative decay. Integration of this equation gives

$$n(t) = n_0 \exp\left(-\frac{t}{\tau}\right) \tag{4.4}$$

where τ, the life time, is given by

$$\tau = \frac{1}{\Gamma + k_{\mathrm{nr}}} \tag{4.5}$$

In the experiment, instead of the number of excited molecules, fluorescence intensity is measured, which is proportional to $n(t)$. (4.4) can be rewritten as

$$I(t) = I_0 \exp\left(-\frac{t}{\tau}\right) \tag{4.6}$$

where I_0 is the fluorescence intensity at $t = 0$.

The fluorescence lifetime can be determined by fitting assumed decay models to experimental data.

The lifetime of a fluorophore in the absence of non-radiative decay is called intrinsic or natural lifetime, defined as:

$$\tau_n = \frac{1}{\Gamma} \tag{4.7}$$

The radiative decay, Γ, can be calculated using the Strickler–Berg relation [1] [3]. Between the fluorescence and absorption spectra:

$$\begin{aligned} \Gamma &\cong 2.88 \times 10^9 n^2 \frac{\int F(\bar{v}) d\bar{v}}{\int F(\bar{v}) d\bar{v} / \bar{v}^3} \int \frac{\varepsilon(\bar{v})}{\bar{v}} d\bar{v} \\ &= 2.88 \times 10^9 n^2 < \bar{v}^{-3} >^{-1} \int \frac{\varepsilon(\bar{v}) d\bar{v}}{\bar{v}} \end{aligned} \tag{4.8}$$

where $F(\bar{v})$ is the emission spectrum plotted on the wavenumber scale, $\varepsilon(\bar{v})$ is the molar absorption coefficient, and n the refractive index of the medium.

The efficiency of the fluorescence process, i.e. the fluorescence quantum yield, is the number of photons emitted relative to the number of photons absorbed. The quantum yield, *Q*, is given by:

$$Q = \frac{\Gamma}{\Gamma + k_{\mathrm{nr}}} \tag{4.9}$$

The natural lifetime, τ_n, can be calculated from the τ / Q correlation. The value obtained sometimes differs from that calculated from the absorption and emission spectra using eq. (4.8). The discrepancy arises from unknown and known factors such as secondary processes caused by fluorophores located next to quenching groups [1].

4.4 Environmental factors affecting fluorescence

The emission of fluorescence is influenced by a number of environmental factors such as solvent polarity, viscosity and, pH, pressure, temperature, and the presence of ions. Solvent effects rooted in strong electronic-vibrational coupling are the primary cause of the Stokes shift. Solvents with different polarity give rise to emission with different maximum frequencies. As noted, when the absorbed light is emitted as fluorescence, the wavelength of the emitted fluorescence is longer than the wavelength of the absorbed light, because vibrational energy is lost during the dynamic process of fluorescence emission (Fig. 4.2), and the fluorophore is accommodated in a vibrationally excited state of the electronic ground S_1-State after fluorescence. The dipole moment of the excited state (μ_E) is, further higher than that of the ground state (μ_G) [1]. This causes the solvent molecules to reorient to a relaxed state of minimal energy. The excited fluorophore thus loses energy by solvent relaxation and the emitted fluorescence is therefore centred at wavelengths longer than that for absorbed light. If the solvent relaxation time is shorter than the fluorescence lifetime, fluorescence will be emitted as shown in Fig. 4.2. Among other factors, the rate of solvent relaxation depends on the polarity (dielectric permittivity) and viscosity of the solvent. The more polar the solvent, the larger the

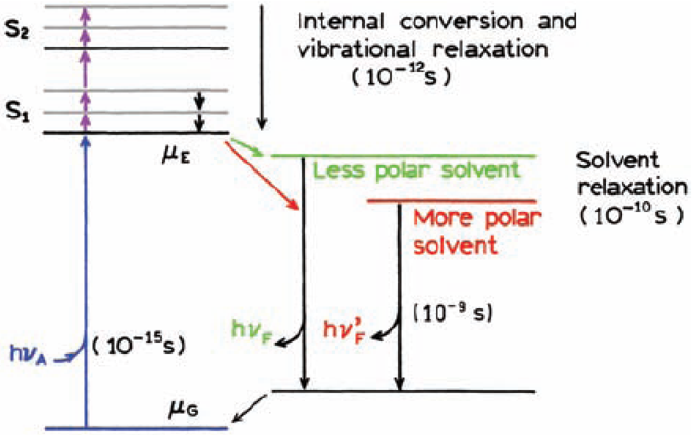

Figure 4.2: Jablonski diagram for fluorescence with solvent relaxation. The fluorophore is excited to S_1. If the fluorophore is excited to S_2, it rapidly decays to the S_1 state due to internal conversion. The excited fluorophore loses energy by solvent relaxation. The stronger the solvent polarity, the lower the emission energies. From Lakowicz [1].

energy loss. The solvent effects thus enable extracting information about the local environment of the fluorescent probe.

When the temperature is decreased, non-radiative processes such as collision with solvent molecules are less efficient. The quantum yield and excited state lifetime therefore increase. At low temperatures, the solvent also becomes more viscous. The solvent relaxation time therefore increases. If the solvent relaxation time, $k_{s,}$ is longer than the lifetime of the fluorophore, emission from vibrationally excited Franck–Condon (F) states is expected (Fig. 4.3). If the solvent relaxation is faster than the lifetime of the fluorophore, emission from the vibrationally fully relaxed state (R) will be observed. When the solvent relaxation is comparable to the fluorescence lifetime, emission both from F states and from solvent relaxation take place. In this case the spectrum both evolves in time and becomes broadened because of the contribution from both the F and R states and from intermediate, partially vibrationally relaxed states.

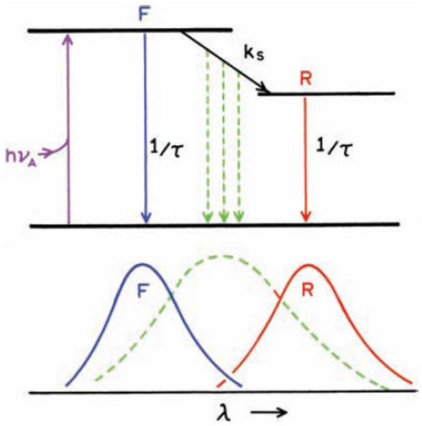

Figure 4.3: Jablonski diagram explaining solvent relaxation. After excitation, the fluorophore is initially in the vibrationally excited Franck–Condon (F) state. If the solvent relaxation time, k_s, is slower than the decay rate, $1/\tau$, emission from the state F is expected. Emission from the relaxed state (R) will be observed, if $k_s > 1/\tau$.. If the solvent relaxation is comparable to the fluorescence lifetime, an intermediate emission spectrum (---) will be observed. From Lakowicz [1].

The fluorescence bandshape of the fluorophore offers in principle detailed information about electronic-vibrational interaction, the nature of the local solvent environment and the nature of the local and solvent vibrational motion (classical reorganization or reorganization by nuclear tunneling) [4]. Fluorescence spectroscopy and bandshape analysis of mesoporous silica pore-confined proteins are parts of the present study (see Chapter 9). Fluorescence bandshape analysis requires at least a few elements of further theoretical concepts and formalism. These are provided in Appendix 6.

References

[1] J. R. Lakowicz. *Principles of Fluorescence Spectroscopy.* Springer, 3rd edition, 2006.

[2] B. Valeur. Molecular Fluorescence: Principles and Applications. Wiley-VCH Verlag GmbH, 2001.

[3] S.J. Strickler and R.A. Berg. Relationship between Absorption Intensity and Fluorescence Lifetime of Molecule. *J. Chem. Phys.* 37:814–822, 1962.

[4] A. M. Kuznetsov and J. Ulstrup. Electron Transfer in Chemistry and Biology : An Introduction to the Theory. Wiley, 1 edition, 1999.

5. Experimental Methods and Techniques

This chapter briefly describes major experimental methods and techniques used for the characterization of mesoporous silica materials and for enzyme activity and fluorescence measurements.

5.1 Methods for characterization of mesoporous silica

5.1.1 Powder X-ray diffraction (XRD)

X-ray diffraction is based on the interaction of a monochromatic X-ray beam with matter and has been widely used to determine the structures of various specimens. In particular, this technique has served as common means for structural characterization of nanomaterials. We here start the description from the XRD principles. Figure 5.1 depicts a side view of layers in a simplified lattice. Two X-ray beams impinge on a crystalline material at an angle θ and are reflected. When the *Bragg*'s law (eq. 5.1) is satisfied, the reflected beams are in phase and interfere constructively.

$$n\lambda = 2d\sin\theta \tag{5.1}$$

where λ is the wavelength, d is the distance between the layers, and n is an integer. By varying the angle (θ), the conditions required by the *Bragg*'s law can be satisfied by different *d*-spacings. Plotting the angular positions and intensities of the reflected beams produces a pattern, which is characteristic of the sample. Although the silica wall of the mesoporous silica is amorphous, characteristic peaks are still observed at small angles of 2θ = 0.6°-5.0°. This is due to the ordered pores of mesoporous silica. The contrast between the silica wall and pores is enhanced at certain angles.

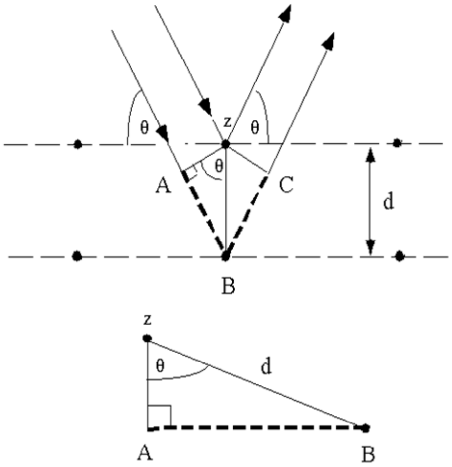

Figure 5.1: Diffraction of x-rays by crystal planes [1]. “d” is the distance between the layers. The lower beam travels the extra distance (AB + BC) = 2d sinθ where AB = d sinθ from the bottom image.

5.1.2 Nitrogen adsorption–desorption

5.1.2.1 Adsorption isotherms

The surface area, pore size, and total pore volume of mesoporous materials can be estimated from the nitrogen adsorption/desorption measurements. The adsorption/desorption of a gas (adsorbate) on a porous material (adsorbent) provides comprehensive information regarding textural properties of the adsorbent such as surface area, pore size, total pore volume, and pore geometry. The gas can be adsorbed either physically (physisorption) or chemically (chemisorptions). If the main purpose is to estimate surface area, pore size and pore volume of porous materials, physical adsorption is favoured [2]. The reasons include: (a) physical adsorption allows multilayered adsorption of gas, (b) pores can be fully filled to precisely determine pore volume, (c) physical adsorption is reversible, and (d) physically adsorbed molecules are not restricted to specific sites, but instead they cover the entire surface (good for surface area determination). Van der Waals and dispersion forces are main driving forces for physical adsorption [2]. The gas used to obtain textural properties of porous materials needs to be inert, and nitrogen is thus commonly used. The amount of gas adsorbed on an adsorbent is proportional to the amount of the sample and depends on the temperature (T), the pressure (p) of the vapor and the nature of the gas and the adsorbent used. The quantity of gas adsorbed in terms of moles per gram solid (n) is expressed as follows [3]:

$$n = f\,(p,\, T,\, \text{gas, solid}) \tag{5.2}$$

For a given gas, solid material, and temperature, (5.2) is simplified to

$$n = f\,(p)_{\,T,\ \text{gas, solid}} \tag{5.3}$$

An alternative form is:

$$n = f\,(p/\,p^{\circ})_{\,T,\ \text{gas, solid}} \tag{5.4}$$

where p° is the saturation pressure, this equation is more useful if the temperature is below the critical temperature of the gas [4]. The relation between the amount adsorbed and the equilibrium pressure of the gas at a fixed temperature is known as the adsorption isotherm. The normal measurement process is: a known amount of gas is transferred to the sample tube; after equilibrium is established, the pressure is measured. The amount of adsorbed gas can thus be calculated using the general gas equation (PV/T = constant). The adsorption isotherm is the function of a relative pressure (P/P_0) at a given temperature, where P represents the equilibrium pressure and P_0 the saturation pressure. The saturation pressure (P_0) is defined as the saturated equilibrium vapor pressure displayed by the pure adsorptive (Note: the gas, capable of being adsorbed, is called the *adsorptive*. The material in the adsorbed state is called the *adsorbate* [2].) in the sample cell immersed in a coolant such as liquid nitrogen (see Fig.5.2) [2]. Typically, the nitrogen adsorption measurements are carried out at the liquid nitrogen temperature (77K at 760 torr).

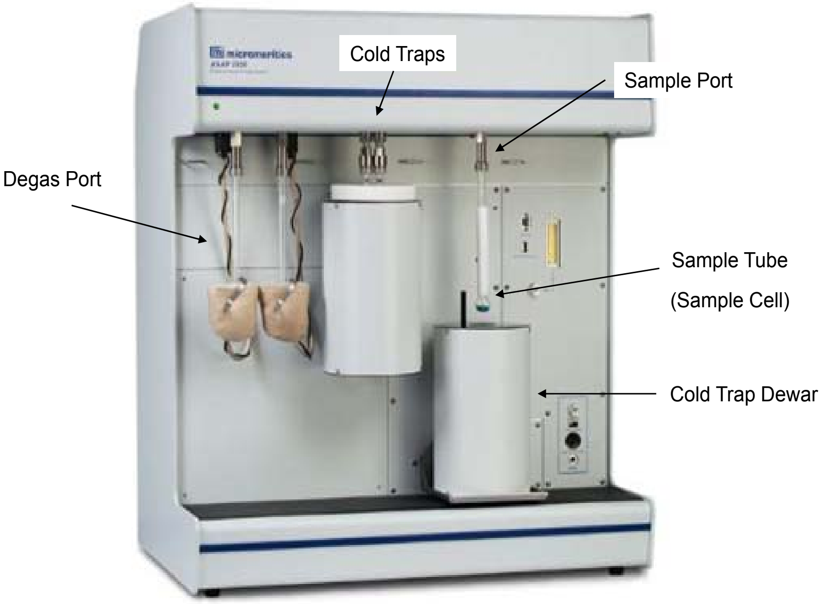

Figure 5.2: Micromeritics’ ASAP® 2020 Accelerated Surface Area and Porosimetry Analyzer [4]. The sample is first outgassed on the degass port and then transferred to the sample port. The sample tube (cell) is immersed in the cold trap dewar that contains a coolant and the measurement is then started. All the adsorption measurements are carried out at 77K if liquid nitrogen is used as the coolant.

There are six types of adsorption isotherms that have been observed, as illustrated in Fig. 5.3. Type I occurs when the adsorbent is microporous material, because micropores can be quickly filled fully with gas molecules at low pressure. Type II is obtained when the adsorbent is nonporous or macroporous material. Monolayer adsorption of gas molecules is accomplished at point B, followed by multilayer adsorption. When the interaction between the adsorbate and adsorbent is weak, types III and V could be observed but they are not common. Type IV isotherms are shown by mesoporous materials. The detail will be described below. As a special case, type VI isotherm shows adsorption following a step-wise multilayer adsorption processes. This type of adsorption commonly occurs at a uniform and non-porous surface [2].

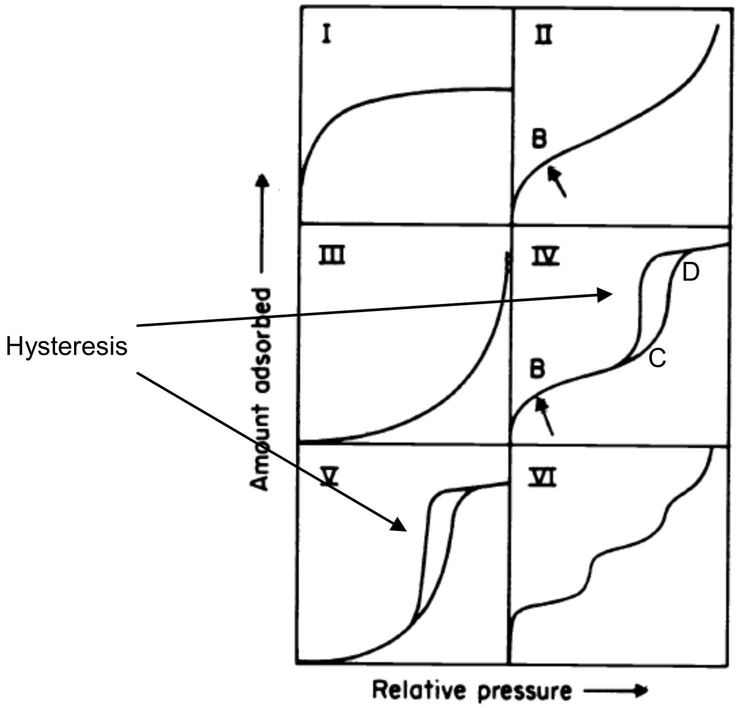

Figure 5.3: Types of adsorption isotherm. Point B, the beginning of the linear part, indicates that monolayer coverage is complete and multilayer adsorption is about to begin. Mesoporous material falls in type IV. Capillary condensation occurs between the points C and D. For details of each type, see text. From Sing et al [5].

5.1.2.2 Assessment of mesoporous materials with micropores

The adsorption behavior of gas molecules to a macropore is considered to be similar to that for gas molecules adsorbed onto a flat surface. In case of micropores, the adsorption behavior is mainly determined by the interaction between adsorbate and adsorbent. For mesopores, the situation becomes more complicated. In addition to the interaction between a gas molecule and adsorbent, the interaction between gas molecules causes the gas to be condensed into liquid-like phase in pores (capillary condensation) [2]. In the type IV isotherm (Fig. 5.3), after a steep increase at low relative pressures due to monolayer adsorption, the isotherm becomes linear (point B), indicating the stage at which monolayer coverage is completed and multilayer adsorption initiated. Using the low-pressure part of the isotherm, the specific surface area can be calculated by the Brunauer-Emmett-Teller (BET) equation [6]:

$$\frac{P}{V(P_0-P)}=\frac{1}{V_mC}+\frac{(C-1)}{V_mC}\cdot\frac{P}{P_0} \tag{5.5}$$

where V is the volume adsorbed at the pressure P, P_0 is the saturation pressure, C is a constant, and V_m is the monolayer capacity (the volume of gas adsorbed when the entire adsorbent surface is covered with a complete monolayer). The specific surface area calculated by the BET equation (S_{BET}) includes both the surface area of inside the pore and that of the outside of the particles.

At point B, multilayer adsorption commences and after reaching a critical film thickness (point C), the volume of gas adsorbed increases steeply due to capillary condensation within the mesopores at higher relative pressures. A characteristic feature of the type IV isotherm is its hysteresis loop, which is associated with capillary condensation. After the sharp increase (point D), the adsorbed amount reaches a plateau region where pores are filled with liquid and separated from the bulk phase by a hemispherical meniscus. The total specific pore volume is defined as the volume of liquid at a pre-determined relative pressure (usually at P/P_0=0.95). The adsorbed amount of gas (V_{gas} cm^3) at the pre-determined relative pressure is converted to the volume of liquid (V_{L} cm^3) using a density conversion factor of 0.0015468 (in the case of nitrogen) [7], which is obtained by the following relation:

$$V_L=\frac{V_{gas}}{22.4\times10^3}\times34.6 \tag{5.6}$$

where 22.4×10^3 $\mathrm{cm}^3\ \mathrm{mol}^{-1}$ is the molar volume of gas and 34.6 $\mathrm{cm}^3\ \mathrm{mol}^{-1}$ is the molar volume of liquid nitrogen at 77 K [2]. When the pressure is reduced, pore evaporation occurs at a pressure lower than the pore condensation pressure, resulting in sharp drop of the isotherm curve. At the point where hysteresis closes, multilayers of adsorbed nitrogen can be found. The reason why hysteresis occurs is a matter of debate. Three models are proposed: (1) independent (single) pore model, (2) network model, and (3) disordered porous material model [2] (For details, see p. 45-49 of ref. [2]). The hysteresis loop is classified into 4 types (Fig. 5.4). The shape of the hysteresis gives information about the pore geometry, pore connectivity, etc [2]. Type H1 is associated with porous material containing cylindrical pores or agglomerates of compacts (compacted solid under pressure) of approximately uniform spheres [2] (Note: agglomerate is defined as an assemblage of particles rigidly joined together [5]). The materials with type H2 hysteresis have often disordered pores [2]. The isotherm of type H3 hysteresis does not show limiting adsorption at a high relative pressure. Aggregates of plate-like particles, which form a slit-shaped capillary, give rise to type H3 hysteresis. Type H4 hysteresis is also associated with a slit-shaped pore. The isotherm with type H4 hysteresis indicates microporosity (the type I isotherm shape).

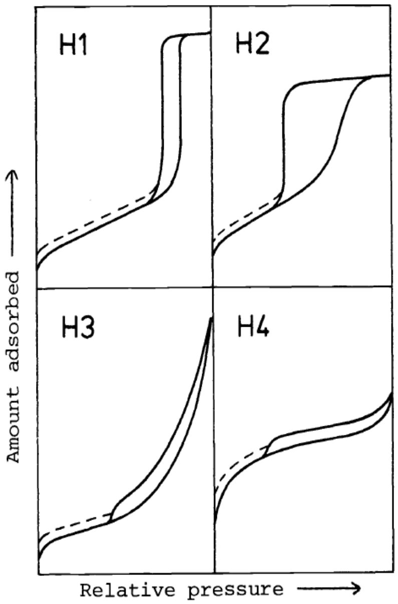

Figure 5.4: Types of hysteresis loops. Two extreme cases are shown as H1 and H4. In H1, the two branches are almost vertical and parallel. In H4, the branches are almost horizontal and parallel. Types H2 and H3 are considered as intermediates of H1 and H4. Types H1 and H2 were observed in the present study. See text about the detail of each type. From Sing et al [5].

Mesoporous silica, SBA-15, has mesopores and micropores which penetrate the silica walls between the primary mesopores. The micropore volume can be calculated using the α_s plot method [2]. The α_s plot method is an empirical approach. The isotherm measured for porous material is compared with a standard isotherm for the adsorption on a non-porous reference material. First, the reference (standard) isotherm is constructed. The amount of adsorbed nitrogen by the reference sample (V_{ads}) is normalized by the amount adsorbed at a relative pressure of 0.4 ($V_{ads}^{0.4}$) and converted into the dimensionless quantity, $V_{\text{ads}}/V_{ads}^{0.4}$. This is defined as α_s. The reduced isotherm for the non-porous reference adsorbent, called the standard α_s curve (α_s versus P/P_0), is thus obtained (e.g. Fig. 5.5).

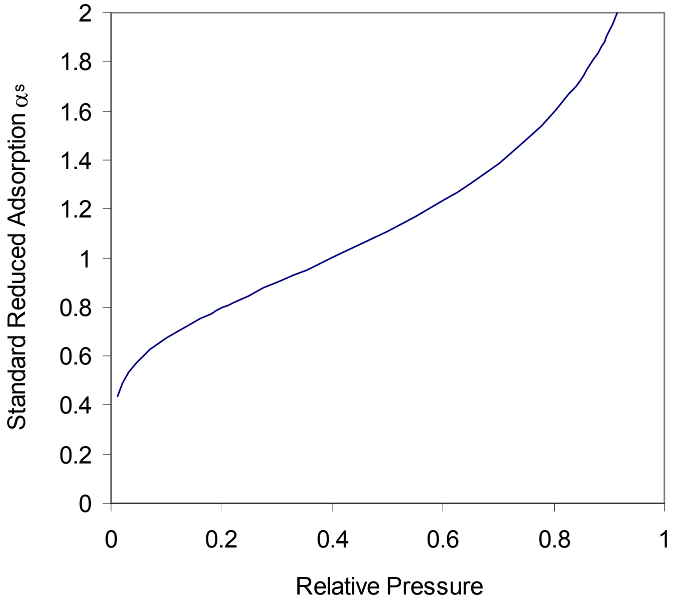

Figure 5.5: Standard α_s curve for macroporous silica LiChrospher Si-1000. The standard reduced nitrogen isotherm data for LiChrospher Si-1000 was replotted from Jaroniec et al [8].

The experimental isotherm of a test sample is then redrawn as an α_s plot (Fig. 5.6), i.e., a plot of the volume of gas adsorbed by the test sample as a function of α_s. The horizontal axis (P/P_0) of the experimental isotherm is converted to α_s using the standard α_s curve (Fig. 5.5). The micropore volume can be estimated by extrapolating the linear part of the α_s plot to the y-axis. An intercept of zero means that no detectable amounts of micropores are present in the test sample (e.g. typical MCM-41, see Figure 3 of ref. [8]).

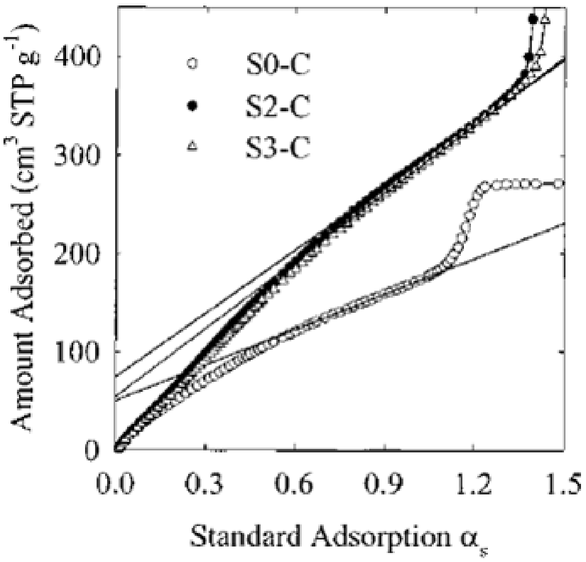

Figure 5.6: α_s plot for calcined SBA-15 samples [9]. The intercept of the ordinate indicates the micropore volume. S0-C, S2-C, and S3-C are the samples obtained under different conditions (with or without aging or at different temperatures).

In the case of capillary condensation in cylindrical pores, the meniscus of the condensed adsorbate is assumed to be hemispherical and a correlation between pore diameter and pore condensation pressure is provided by the Kelvin equation [10]:

$$r = \frac{2\gamma V_L}{RT \ln[(P_0 / P)]} \quad \text{or} \quad \ln P / P_0 = \frac{-2\gamma V_L}{rRT} \tag{5.7}$$

where r is the pore radius, R the gas constant, γ the surface tension of the liquid, and V_L the molar volume of the condensed liquid. The Kelvin equation relates the equilibrium vapor pressure exerted from the meniscus of the pore liquid to the equilibrium pressure of the same liquid on a planar surface [2].

The Kelvin equation does not take into account the interaction force between fluid and wall; multilayer adsorbed film formation is therefore neglected. To take formation of multilayer adsorbed film into account, the Kelvin equation needs to be modified by introducing the term $t(P/P_0)$ [10]:

$$r = \frac{2\gamma V_L}{RT \ln[(P_0 / P)]} + t(P / P_0) \tag{5.8}$$

where t is the film thickness (thickness of the adsorbed multilayer). The t(P/P$_0$) is obtained from the adsorption data of the same adsorbate on a non-porous sample with a similar surface to that of a test sample. A pore filled with condensed liquid consists of adsorbed layer and core (Fig. 5.7). The core refers to the diameter at which all condensed liquid evaporates at the critical pressure. The relationship between the core radius and the critical pressure follows the Kelvin equation, eq. 5.7. The modified Kelvin equation (eq. 5.8) indicates that the pore diameter, r, is the sum of the radius of the core and the multilayer thickness t(P/P$_0$).

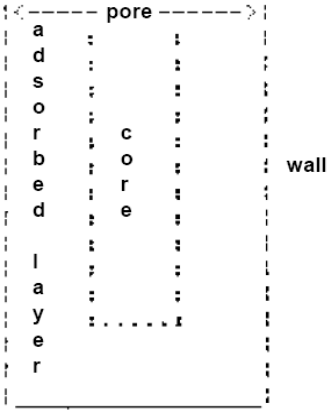

Figure 5.7: A pore filled with condensed liquid consisting of adsorption layer and core [7]. The radius of the core is determined by the Kelvin equation, eq. (5.7).

The pore size and Pore Size Distribution (PSD) are broadly determined by the Barrett-Joyner-Halenda (BJH) method [11]. The BJH method is a classical macroscopic method and is based on the modified Kelvin equation (eq. 5.8). Fig. 5.8 shows an example of the nitrogen adsorption isotherm and its tabular form of part of the desorption branch. Each data pair of "relative pressure" and "quantity adsorbed" is named as (Pr$_1$, Va$_1$), (Pr$_2$, Va$_2$), … where Va represents a volume adsorbed at a relative pressure (Pr). In the BJH method, the amount of adsorbate lost in a desorption step, say, (Pr$_3$, Va$_3$) to (Pr$_4$, Va$_4$), is related to the average size of the pores emptied in the step based on the notion that the desorption consists of desorption from multilayers and from the evaporation of condensed liquid of the core [7].

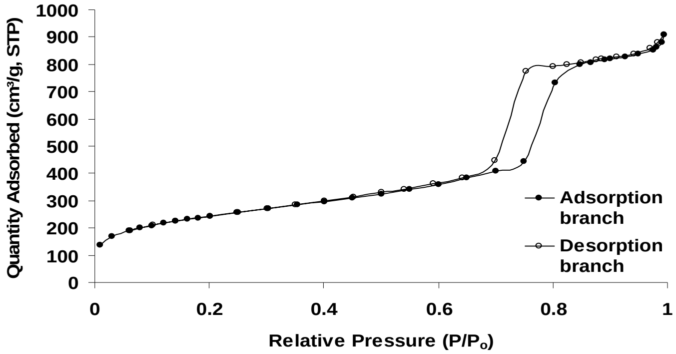

Relative Pressure (P/P_0)	Quantity Adsorbed (cm³/g STP)	
0.994485	907.5675	(Pr_1, Va_1)
0.983899	879.646	(Pr_2, Va_2)
0.970651	859.4397	(Pr_3, Va_3)
0.940704	839.7229	(Pr_4, Va_4)
0.91204	828.7387	(Pr_5, Va_5)
0.885574	820.0493	
0.876125	816.4978	
0.849833	807.1302	
0.82558	799.1918	

Figure 5.8: An example of the nitrogen adsorption isotherm (left) and part of the tabular form of the desorption branch (right). STP: standard temperature and pressure (273.15 K and 760 torr). The data were taken from chapter 6.

The development of ordered mesoporous silica such as MCM-41 made it possible to test the validity of the Kelvin equation and modifications to be made. Kruk *et al* proposed the Kruk-Jaroniec-Sayari (KJS) method [9]. The KJS method uses a corrected form of the Kelvin equation to calculate pore size distributions by means of the BJH method. The authors used the nitrogen adsorption data of a series of MCM-41 materials to establish accurate relations for the statistical film thickness as a function of pressure and for the pore diameter as a function of the capillary condensation pressure.

Modern, microscopic models for pore size analysis have been developed over the last decades. One of such models is the nonlocal density functional theory (NLDFT) model. The NLDFT method is based on statistical mechanics and assumes a model solid structure and pore geometry. The adsorbate is regarded as an inhomogeneous fluid and characterized by density profiles across the pore [12]. After the development of ordered mesoporous silica in the 1990s, it became possible to test such models against reliable experiments. It has been reported that the NLDFT method evaluates pore size and PSD more accurately than other methods such as the BJH method [13]. The BJH method has several problems or limitations when applied to narrow mesopores [2]. For example, the BJH method does not take into account the influence of solid-fluid interactions on capillary condensation [13]. As noted above, the thickness of the adsorbed multilayer, $t(P/P_0)$, in the modified Kelvin equation is obtained from the adsorption data of the same adsorbate on a non-porous sample with a similar surface to that of a test sample. When the pore diameter is less than 10 nm, the thickness, $t(P/P_0)$, obtained using a non-porous sample, does not reflect the real thickness of the adsorbed multilayer due to the presence of curvature effects [2]. In contrast, the NLDFT method correctly describes local fluid structure near curved solid walls on a microscopic level and also correctly captures the thermodynamics of the confined fluid, which is altered compared to that of bulk fluid [2].

5.1.3 Electron microscopy

Electron microscopy was used to characterize the size and morphology of the mesoporous target silica particles. The following overview is very brief. For detailed overviews of scanning and transmission electron microscopies, see ref. 14.

In the electron microscope, electrons are generated and accelerated through a large potential difference in the electron gun. The accelerated electrons with high energy hit a specimen. The interaction of the electrons with the specimen produces scattered or diffracted electrons (Fig. 5.9). These electrons are used to obtain scanning electron microscopy (SEM) images or diffraction patterns. The transmitted electrons are used to obtain transmission electron microscopy (TEM) images.

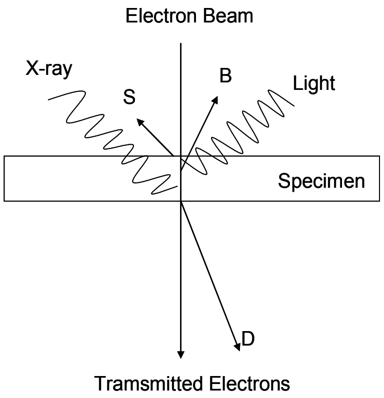

Figure 5.9: Interaction of electron beam with a specimen. S: Secondary electrons, B: Backscattered electrons, D: Diffracted electrons. When an electron beam hits the specimen, the interaction of the electron beam with the specimen causes electron radiation (secondary electrons and backscattered electrons) and electromagnetic radiation (e.g. X rays and light).

SEM is mainly used to study surface features of the material. The electron beam is scanned across the specimen. As noted, the primary electrons that interact with the specimen produce secondary and backscattered electrons. The secondary electrons are electrons with energies below about 50 eV that escape from the specimen [14]. The backscattered electrons are incident electrons that leave the surface with a high energy close to the initial energy. Both the secondary electrons and the backscattered electrons can be collected by a detector, but the secondary electrons are the ones mainly used. The electrons collected are amplified and displayed on a screen. Charging of the specimen (a build up of excess electrons on the surface of the sample) degrades the images. To prevent problems caused by charging, non-conducting materials are coated with a thin conducting layer of gold or carbon.

Surface information such as the morphology of the material can be obtained from SEM. TEM is used to obtain high resolution images, giving local information. The transmitted electrons are focused with an objective lens, pass further through the lens for magnification and are then projected onto a phosphorescent screen. Images are recorded with a camera such as CCD mounted under the screen. The brighter area in the TEM image indicates that more electrons have passed through the specimen, while the darker area indicates that fewer electrons have passed through the sample.

5.2 Instrumental methods for enzyme activity measurements

The activity of HRP was measured by following product formation with a UV-Visible spectrophotometer (Chapter 7). The activity of galactose oxidase was measured by following dioxygen consumption with a dioxygen sensor (Chapter 8).

5.2.1 UV-Visible spectrophotometry

A single-beam UV-Visible spectrophotometer was used (HP8453, Hewlett Packard) to measure absorbance of a solution. HP8453 is a photodiode array spectrophotometer (Fig. 5.10). The light source is a combination of a deuterium lamp for ultraviolet light and a tungsten lamp for visible light. The light passes through the sample to the slit. Light is dispersed by a dispersion device, a holographic grating for HP8453, onto a diode array.

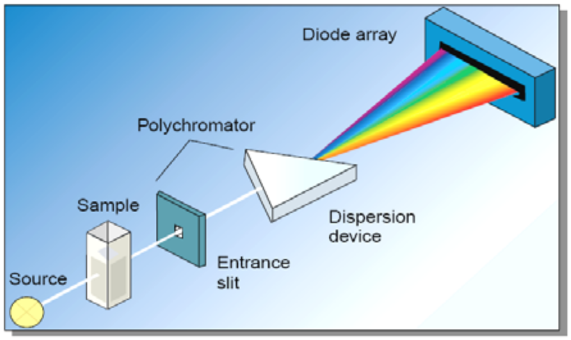

Figure 5.10: Optical layout for photodiode array spectrophotometer. The sample is irradiated with white light. After passing through the sample, the light is dispersed by a dispersion monochromator (polychromator) onto the diode array. From Upstone [15].

As described in Chapter 4, the absorbance is proportional to the concentration of the light-absorbing substance in the sample (eq. (4.2)). By following the absorbance change, the rate of product formation can be obtained.

5.2.2 Oxygen sensor

The catalytic activity of galactose oxidase was followed by monitoring the dioxygen consumption using a YSI 5300A Biological Oxygen Monitor system (Fig. 5.11). The system consists of a monitor, a bath, a dioxygen probe (sensor), and other accessories. The bath is connected to a constant temperature circulator to maintain constant temperature of the bath.

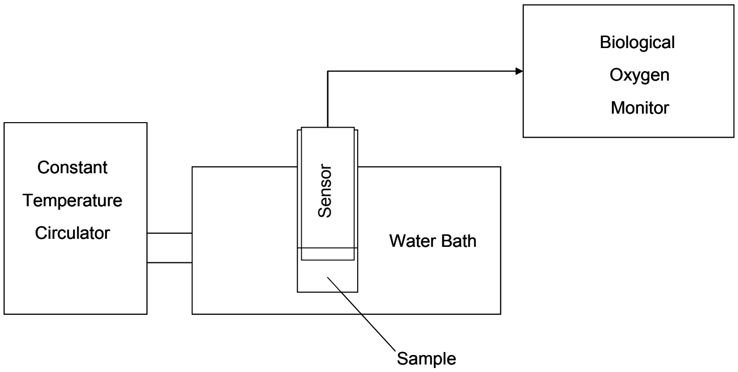

Figure 5.11: Schematic diagram of dioxygen monitoring system. The dioxygen probe (sensor) is inserted into the chamber containing a sample. The chamber is maintained at a constant temperature by the water bath, which is connected to the constant temperature circulator. The monitor displays %AIR based on 100 % AIR corresponding to the concentration of dissolved dioxygen in air-saturated distilled water.

The dioxygen probe is mounted into a plunger, which is fitted to a glass sample chamber (Fig. 5.12 (a)). The temperature of the sample chamber is maintained at a constant bath temperature. The dioxygen in the solution is monitored by a Clark-type electrode (Fig. 5.12 (b)). The electrode consists of a platinum cathode and a silver anode. The whole electrode is covered with a Teflon membrane that holds a KCl solution. When a polarizing voltage is applied to the electrode, dioxygen at the probe is reduced at the cathode which produces a current. The current is proportional to the dioxygen concentration. The current change with time therefore monitors the rate of the consumption of oxygen. If the dioxygen pressure outside the membrane increases, more dioxygen diffuses through the membrane, resulting in increased current at the electrode.

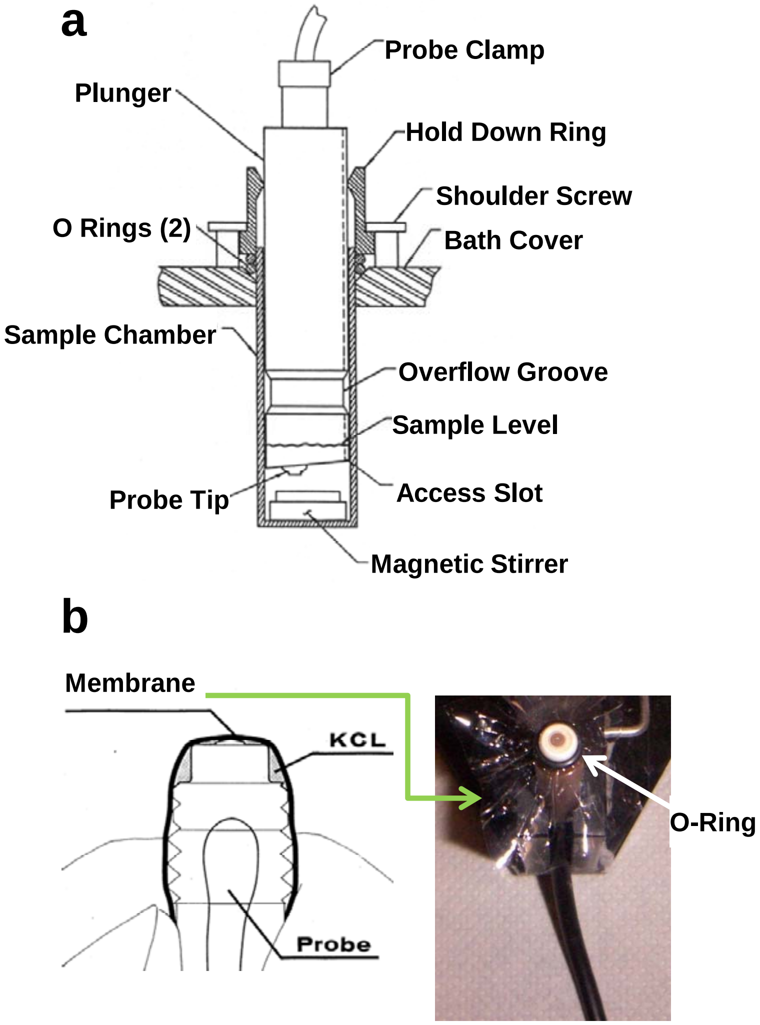

Figure 5.12: (a) Schematic diagram of sample chamber assembly. From Operations Manual [16]. (b) Dioxygen probe covered with a membrane. The Teflon membrane fastened with an o-ring holds a KCl solution.

5.3 Fluorescence measurements

5.3.1 Steady state spectrofluorometry

The steady state fluorescence measurements were carried out at Department of Chemical Physics at Lund University. A SPEX 1681 0.22 m spectrofluorometer was used in the measurement of steady-state fluorescence at room temperature in the initial period of my external stay at Lund University. This is a commonly used instrument type in spectrofluorimetry. Due to instrument failure, the steady-state fluorescence spectra at room temperature were, however, obtained using the configuration (laser excitation source + spectrometer with CCD) described in Appendix 1 in the latter period of the external stay. A layout for general spectrofluorometer principle is shown schematically in Fig. 5.13, including a light source, monochromators, a sample holder, and photomultiplier tubes (PM). A xenon arc lamp is commonly used as light source, which gives radiation in the ultraviolet, visible, and near-infrared wavelength ranges. There are two monochromators, one for selecting the excitation wavelength and the other one for selecting the emission wavelength. The light with a wavelength for excitation is selected by the excitation monochromator. The passed light hits the sample. A fluorescence cuvette with a translucent wall is used. Emitted light enters the emission monochromator, where a desired wavelength is selected and detected by a photomultiplier (PM).

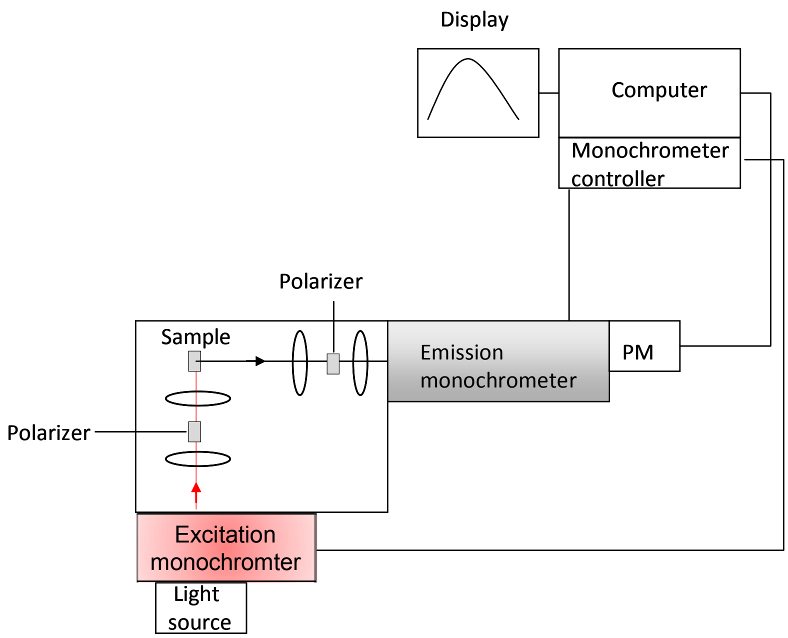

Figure 5.13: Schematic diagram of a spectrofluorometer. Red line represents the excitation beam and the black line the emission. Fluorescence is collected at right angles with respect to the incident beam, passes through an emission monochromator, and is detected by a photomultiplier (PM).

Further instrument description and fluorescence data for mesoporous silica containing protein complex and subsequent bandshape analysis are detailed in Chapter 9.

References

[1] http://www.bmsc.washington.edu/people/merritt/bc530/bragg/. Web page, October 26, 2011.

[2] S. Lowell, J. Shields, M.A. Thomas and M. Thommes, *Characterization of Porous solids and Powders: Surface Area, Porosity and Density*, Kluwer Academic Publishers, 2004.

[3] S. J. Gregg and K. S. W. Sing. *Adsorption, Surface Area and Porosity*, Academic Press: London, 1982.

[4] http://www.micromeritics.com/Product-Showcase/ASAP-2020-Physisorption.aspx. Web page, October 26, 2011.

[5] K. S. W. Sing, R. A. W. Haul, L. Moscou, R. A. Pierotti, J. Rouquerol, and T. Siemieniewska. Reporting Physisorption Data for Gas/Solid Systems with Special Reference to the Determination of Surface Area and Porosity. *Pure Appl. Chem.* 57: 603-619, 1985.

[6] S. Brunauer, P. H. Emmett, and E. Teller. Adsorption of Gases in Multimolecular Layers. *J. Am. Chem. Soc.*, 60:309–319, 1938.

[7] ASAP 2020 Accelerated Surface Area and Porosimetry System Operator’s Manual V3.01, May 2006.

[8] M. Jaroniec, M. Kruk, and J. P. Olivier. Standard Nitrogen Adsorption Data for Characterization of Nanoporous Silicas. *Langmuir*. 15:5410-5413, 1999.

[9] M. Kruk and M. Jaroniec. Characterization of the Porous Structure of SBA-15. *Chem. Mater.*, 12:1961–1968, 2000.

[10] M. Kruk, M. Jaroniec and A. Sayari. Application of Large Pore MCM-41 Molecular Sieves to Improve Pore Size Analysis Using Nitrogen Adsorption Measurements. *Langmuir*, 13:6267–6273, 1997.

[11] E. P. Barrett, L. G. Joyner and P. P. Halenda. The Determination of Pore Volume and Area Distributions in Porous Substances. I. Computations from Nitrogen Isotherms. *J. Am. Chem. Soc.*, *73*:373–380, 1951.

[12] K. Sing. The Use of Nitrogen Adsorption for the Characterisation of Porous Materials. *Colloids Surf., A: Physicochemical and Engineering Aspects*. 187–188:3–9, 2001.

[13] P. I. Ravikovitch and A. V. Neimark, Characterization of Micro- and Mesoporosity in SBA-15 Materials from Adsorption Data by the NLDFT Method. *J. Phys. Chem. B*, 105: 6817-6823, 2001.

[14] P. J. Goodhew, J. Humphreys and R. Beanland, *Electron Microscopy and Analysis*, Taylor & Francis, London, 2001.

[15] S. L. Upstone. Ultraviolet/Visible Light Absorption Spectrophotometry in Clinical Chemistry. In *Encyclopedia of Analytical Chemistry*, pages 1699–1714. Ó John Wiley & Sons Ltd, Chichester, 2000. Editor: R.A. Meyers.

[16] YSI 5300A Biological Oxygen Monitor System Operations Manual, YSI *incorporated*, May 2002.

6. Synthesis and characterization of mesoporous silica

Synthesis and characterization of mesoporous silica are summarized in this chapter. This chapter also serves as an introduction to the materials used in chapters 7-9. *First*, we describe preparation and characterization of rod-shaped SBA-15 and SBA-15 with expanded pores, followed by those for spherical SBA-15, for which two synthesis methods were used. *Finally*, the results on functionalization of the SBA-15 pore wall with amino or methyl groups are presented. Some contents of this chapter will be re-addressed briefly in Chapters 7-9.

6.1 Rod-shaped SBA-15

6.1.1 Synthesis

The SBA-15 mesoporous silica was synthesized by adopting the procedure of Fulvio et al [1] with modifications. Typically, 4.00 g poly-(ethylene oxide)–poly(propylene oxide)–poly(ethylene oxide) triblock copolymer (PEO_{20}–PPO_{70}–PEO_{20}; Pluronic 123) was added to 144 mL of 1.7 M HCl solution, and the mixture was stirred for 4 hours at 40 °C. Next, Tetraethyl orthosilicate (TEOS) was added dropwise (mass ratio of TEOS/P123 = 2) to the solution and the polymer–TEOS synthesis mixture further stirred for 2 hours. The resulting gel was incubated at 100 °C for 24 hours under static conditions. The final product was filtered, washed with water three times, and dried at 80 °C overnight. The as-synthesized sample was calcined in air at 500 °C for 6 hours with a ramp rate of ca. 1 °C/min.

6.1.2 Characterization

The SBA-15 particles were characterized in detail by XRD, SEM, TEM, and N_2 adsorption/desorption experiments.

6.1.2.1 X-ray diffraction

X-ray diffraction (XRD) patterns of the mesoporous silica materials were collected on a PANalytical's X'Pert PRO X-ray diffractometer using Cu Kα as radiation. The measurements were conducted at the Center for Electron Nanoscopy (CEN) of DTU (DTU CEN). The diffractograms were recorded in the 2θ range of 0.6° to 5°. Low angle X-ray diffraction was used to examine pore order of the synthesized particles. Figure 6.1 shows a XRD pattern for calcined SBA-15. Three reflections at 2θ = 0.86, 1.49, and 1.69° were consistently observed in the powder XRD patterns with d-spacing of 102.8 Å, 60.0 Å, and 52.0 Å, respectively. The reciprocal spacing ratio is about 1: $\sqrt{3}$: 2. The three

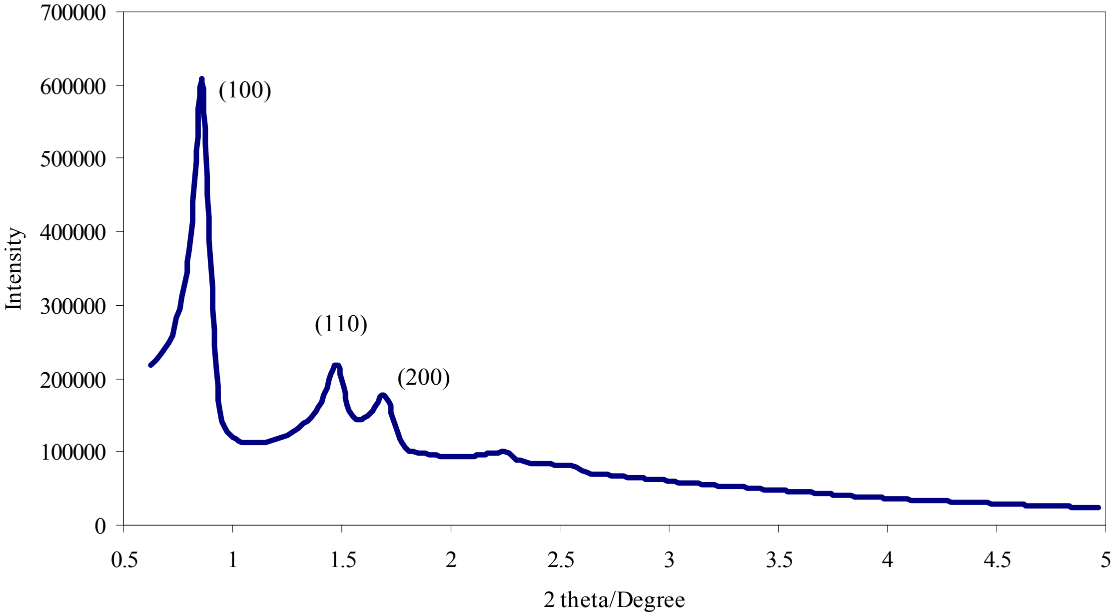

Figure 6.1: Powder XRD patterns of calcined rod-shaped SBA-15. The three peaks at 2θ = 0.86, 1.49, and 1.69° can be indexed as (100), (110), and (200) reflections associated with *p6mm* hexagonal symmetry.

peaks can thus be indexed to (100), (110), and (200) reflections [2], respectively, indicating that as expected the SBA-15 particles contains the pores with hexagonally (space group *p6mm*) ordered structures.

6.1.2.2 SEM images

SEM images were obtained using a Helios EBS3 instrument. These data were also recorded at DTU CEN. Silica particles for SEM observations were first coated with gold by sputtering. The SBA-15 synthesized is rod-shaped. The size of the SBA-15 particle is several hundred nanometers in diameter and around 1 μm in length (Fig. 6.2). As noted from the images, the SBA-15 particles tend to agglomerate.

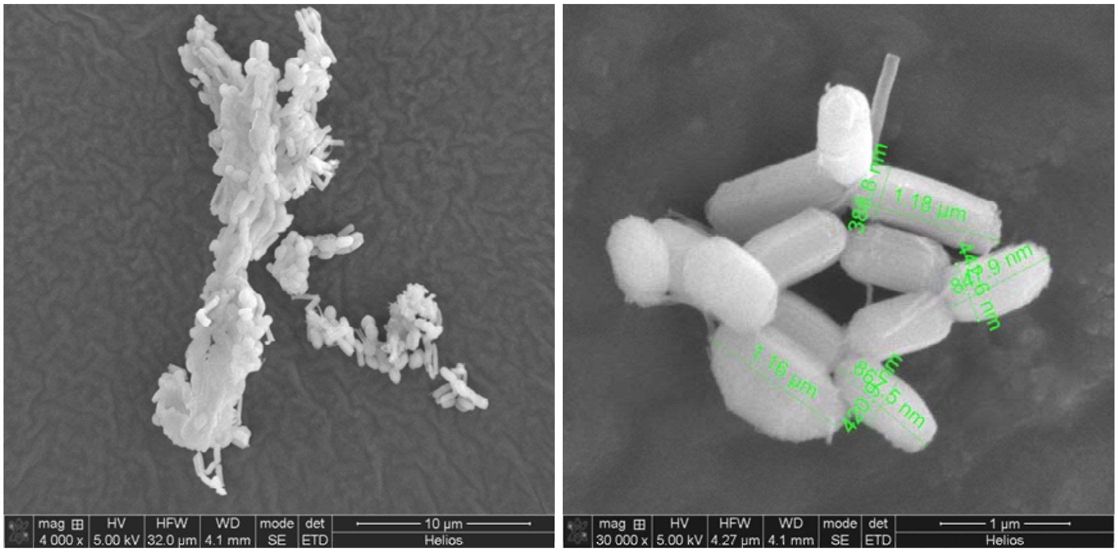

Figure 6.2: SEM images of calcined rod-shaped SBA-15 obtained on a Helios EBS3 instrument at different magnifications. The SEM images reveal that the rod-shaped SBA-15 particles are aggregated. Scale bars: 10 μm (left) and 1 μm (right).

6.1.2.3 TEM images

TEM images were obtained using a Tecnai T20 instrument operated at 200 kV at DTU CEN. High-resolution TEM images (Fig. 6.3 (a)-(d)) show the structural details of this material. The particle size of the material is several hundred nanometers in diameter and around 1 μm in length. The parallel strips in Fig. 6.3 (b) are the projections of hexagonal cylindrical pores from the side. The ordered channels are oriented along the long axis of the rod. The cylindrical pores are arranged in an ordered hexagonal array. Some particles were connected (Fig. 6.3 (c)). It is noted that some channels have a curved shape (e.g., U-shape, see Fig. 6.3 (d)). The existence of U-shaped pores should not be ignored if we

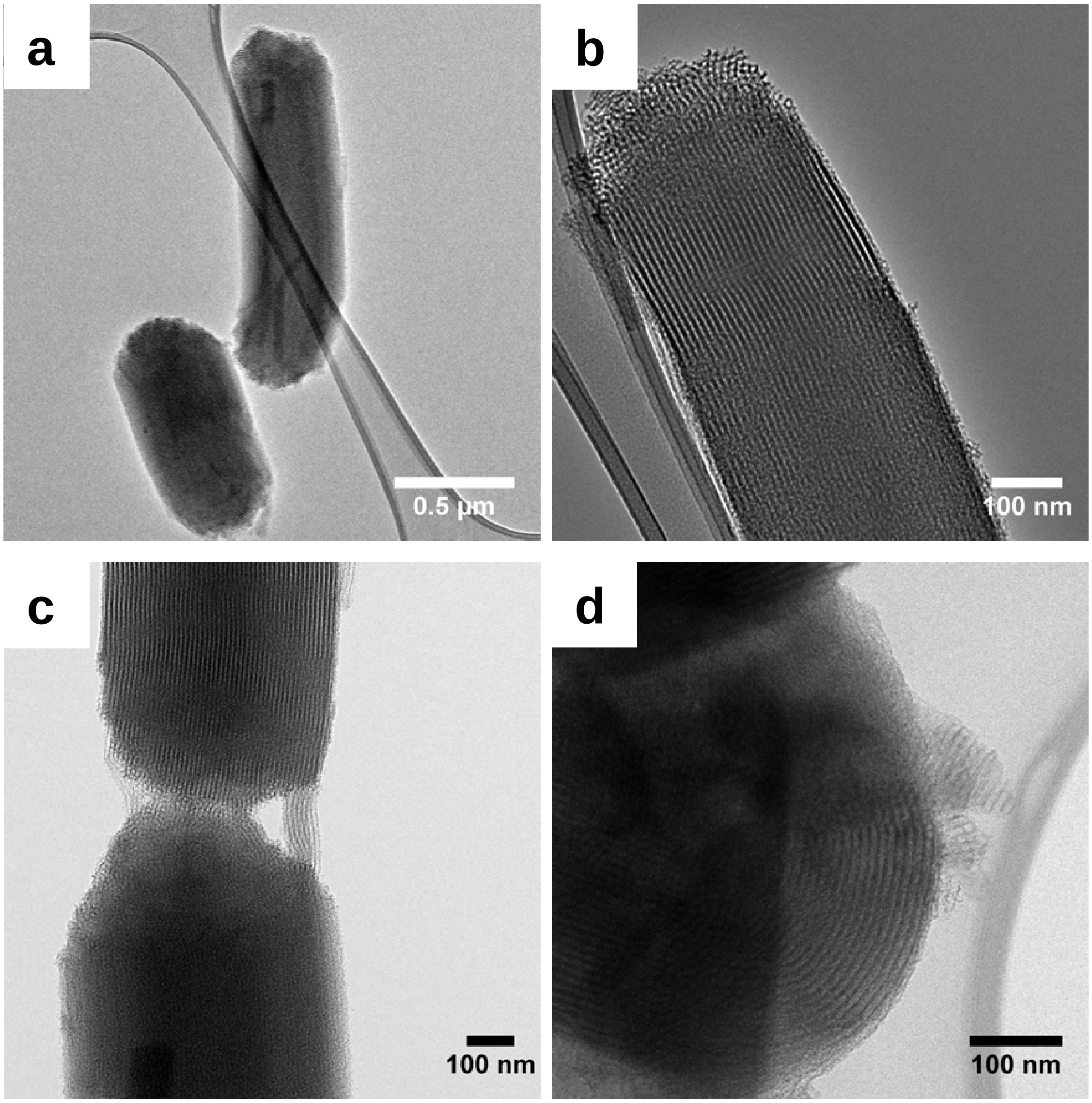

Figure 6.3: High-resolution TEM images of rod-shaped SBA-15. Scale bars: (a) 500 nm, (b) to (d) 100 nm. The images were obtained with a Gatan charge-coupled device (CCD) camera on a Tecnai T20 instrument operated at 200 kV.

discuss diffusion paths of species in the pores. The assumption that the particle length is the same as the diffusion path length through mesopores could lead to underestimate diffusion path length, since the presence of U-shape pores means that the total length of the pore channel can be twice the length of the particle.

6.1.2.4 Nitrogen adsorption and desorption

Nitrogen adsorption/desorption isotherms were obtained at 77 K using a Micromeritics ASAP 2020 system. The measurements were carried out at the Centre for Catalysis and Sustainable Chemistry, DTU Chemistry with the help from Bodil Fliis Holten. Theoretical aspects related to the N_2 adsorption/desorption in mesoporous materials are described in Chapter 5. Experimentally, the calcined SBA-15 samples were degassed at 200 °C for 2 h under vacuum. Figure 6.4 shows a typical nitrogen adsorption/desorption isotherm for rod-shaped SBA-15. The isotherm is a Type IV isotherm with relatively narrow hysteresis loop of H1 type (c.f. chapter 5). The isotherm shows a sharp step of

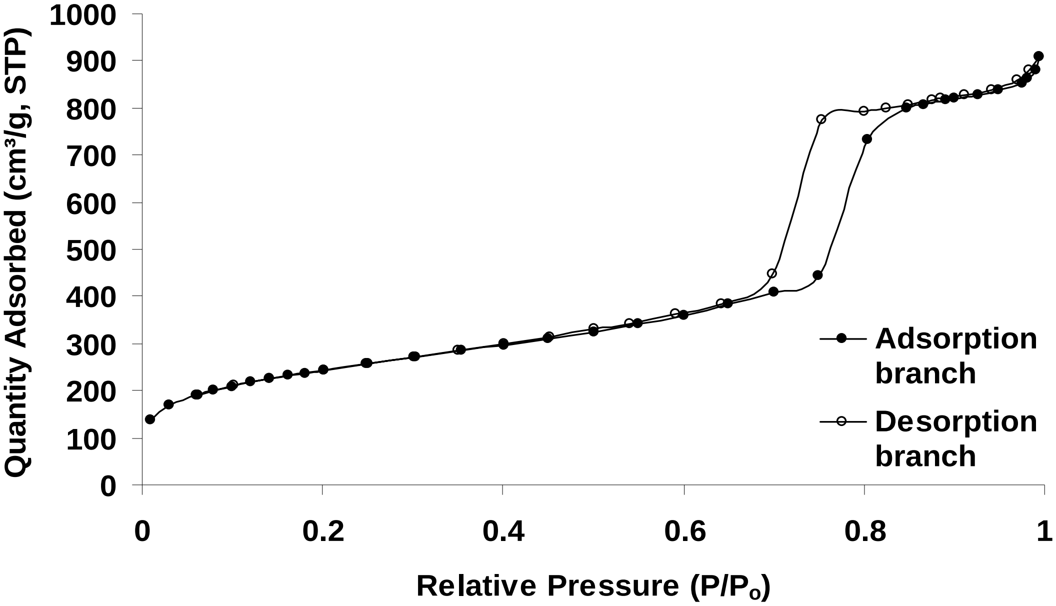

Figure 6.4: Nitrogen isotherm for rod-shaped SBA-15. The material shows a type IV isotherm (Section 5.1.2), indicating that the material has a mesoporous structure. The pore volume was determined from the gas adsorbed at the P/P_0 of 0.95. STP: standard temperature and pressure (273.15 K and 760 torr).

capillary condensation at a relative pressure from around 0.75 to 0.85. This sharp step of capillary condensation indicates that the pores are uniform.

The structural properties of the particles are summarized in Table 6.1. The specific surface area (S_{BET}) of the sample, which includes both the surface area inside the pore and that of the outside of the particles, was calculated using the BET method (Chapter 5, Section 5.1.2) from the adsorption data in a relative pressure range from 0.06 to 0.2. The total pore volume (V_{tot}) was calculated from the amount of gas adsorbed at a relative pressure of 0.95. The pore size distribution (PSD) and pore size was initially calculated from the desorption branch using the BJH method. The BJH pore diameter, which is defined as the position of the maximum of the PSD, is 7.6 nm. Theoretically, the desorption branch should be used for the calculation of pore size distribution [3]. However, it is reported that the BJH method could underestimate the pore size [4]. As described in Chapter 5, the pore diameter of conventional SBA-15 with cylindrical pore structure can be accurately determined by NLDFT method [4]. It seems that the software associated with the Micromeritics ASAP 2020 system does not provide a proper model for NLDFT analysis of the PSD. Instead, an instrument manufacturer named Quantachrome has developed the software for NLDFT analysis applicable to SBA-15. In most literature, when pore size is determined by NLDFT, the instrument used is from Quantachrome. For example, one report uses the instrument from Micromeritics and analyzes the isotherm data by the software from Quantachrome [5].

As an alternative to the NLDFT method, in the later stage of this PhD programme, pore size distributions were evaluated from the adsorption branch using the BJH method with the statistical film thickness curve for macroporous silica [6]. The maximum of the resulting PSD is defined as the BJH pore diameter, w_{BJH}. As described in the previous chapters, SBA-15 contains both mesopores and micropores which penetrate the silica walls between the primary mesopores. The PSD (Fig. 6.5) shows the micropores around 2 nm in diameter. The micropore volume, V_{mi}, was determined by the α_s plot method (Chapter 5 Section 5.1.2). For hexagonally ordered mesoporous silica, the size of the primary mesopores, w_d, can be calculated from the following geometrical relation using XRD unit cell parameter and mesopore volume [7].

$$w_{\mathrm{d}} = cd\left(\frac{\rho V_{\mathrm{p}}}{1+\rho V_{\mathrm{p}}}\right)^{1/2} \tag{6.1}$$

where w_d is the size of the primary mesopores, d is the (100) interplanar spacing obtained from XRD measurements, ρ is the density of the pore walls (ρ = 2.2 g/cm^3), c is a constant (c = 1.213), and V_p is the primary mesopore volume. Equation (6. 1) is valid for materials with structures that can be approximated as an infinite array of cylindrical pores arranged in a hexagonal fashion.

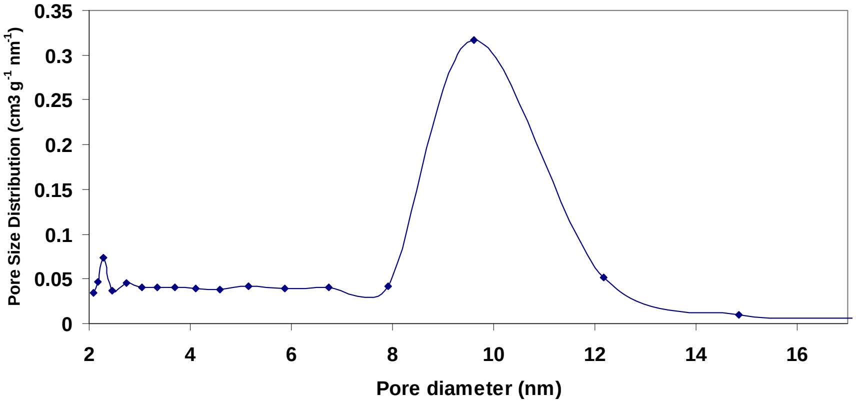

Figure 6.5: Pore size distribution for rod-shaped SBA-15 determined from the adsorption branch. In addition to mesopores, smaller pores at about 2 nm are also detected.

Table 6.1: Physical Characteristics of Rod-shaped SBA-15.

Sample	d (nm)	S_{BET} (m²/g)	V_{tot} (cm³/g)	V_p (cm³/g)	V_{mi} (cm³/g)	w_{BJH} (nm)	w_d (nm)	w_t (nm)
SBA-15	10.3	872	1.34	1.05	0.05	9.6	10.4	1.5

d = XRD (100) interplanar spacing, S_{BET}: Total surface area, V_{tot}: Total pore volume, V_p: Primary mesopore volume, V_{mi}: micropore volume, w_{BJH}: BJH pore diameter, w_d: pore diameter determined by eq. (6.1), w_t : wall thickness calculated by the difference between a and w_d, where a is the unit cell parameter, determined by a = 2(d(100)/√3).

6.2 SBA-15 with expanded pores

As described in Section 2.2.4, one of the methods to synthesize particles with large pores is the use of a swelling agent. In the present work, TMB was used to prepare SBA-15 with larger pores. The sample, denoted as SBA-15-TMB, was synthesized using a similar procedure documented in the literature [8].

6.2.1 Synthesis

About 4 g Pluronic P123 was added to 120 mL 2 M HCl solution and the solution was stirred for 4 hours at 40 °C (until Pluronic P123 completely dissolved). 6 g mesitylene (TMB) and 8.5 g TEOS were then added dropwise under stirring and the polymer–TEOS synthesis mixture was subjected to continuous stirring for ca. 18 hours. The resulting gel was kept at 100 °C for 24 hours under static conditions.

6.2.2 Characterization

Figure 6.6 shows the powder XRD pattern of the sample obtained. No peak is found. The sample is expected to have large-size pores. With the increase of the interplanar distance, the peak is shifted to a smaller angle. The peak may appear at very small angles (e.g. $2\theta \leq 0.5^{\circ}$), but it is beyond the detection limit for the instrument used. If the sample has an ordered hexagonal pore structure, the peaks corresponding to (110) and (200) should be found above $2\theta = 0.6^{\circ}$. This is obviously not the case, a clear indication that the synthesized SBA-15-TMB lacks ordered hexagonal pore structure.

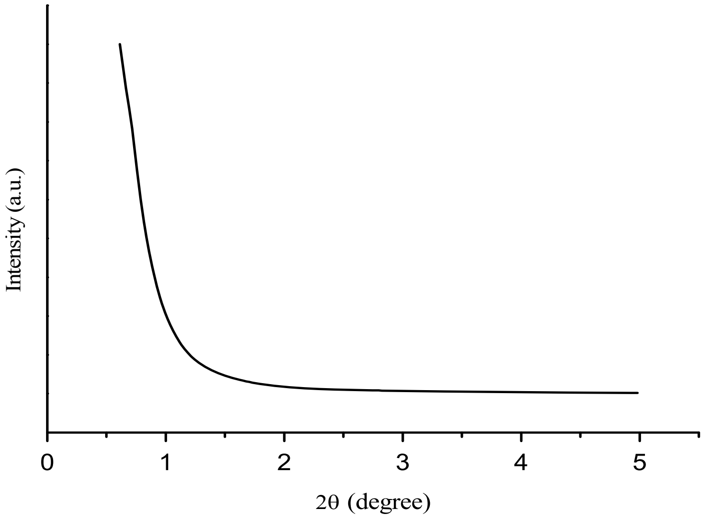

Figure 6.6: Powder XRD patterns of SBA-15-TMB. There is no peak above 2θ = 0.6°, indicating that the material does not have a hexagonal structure. The detection limit for the instrument used is around 2θ = 0.6°.

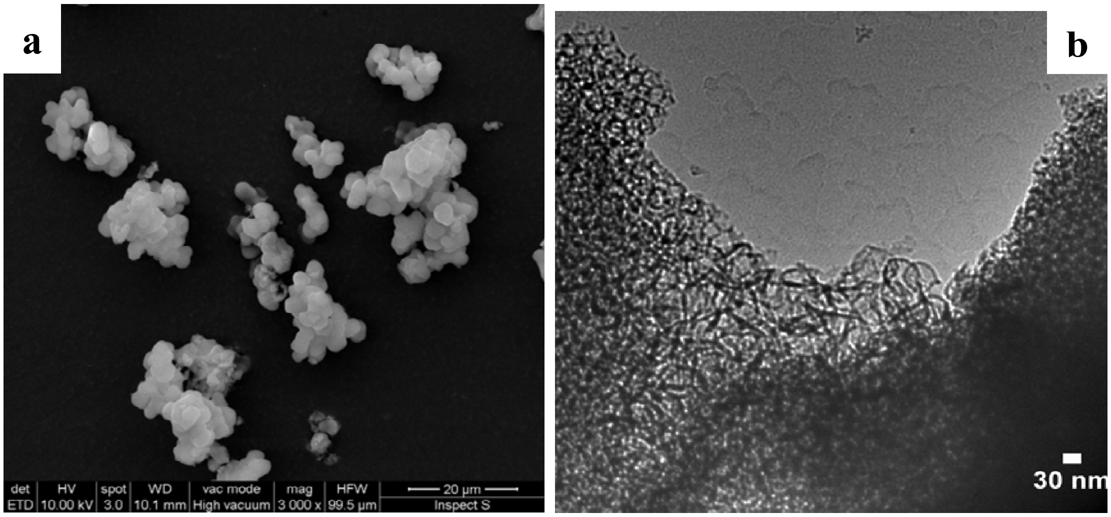

Figure 6.7: SEM (a) and TEM (b) micrographs of SBA-15-TMB. The SEM image indicates that SBA-15-TMB does not have a well-defined morphology. The TEM image (b) shows the edge part of the material. In the top left corner, a disordered foam pore structure can be seen. In addition to mesopores, roughly spherical macropores (> 50 nm) are also visible. Scale bars: (a) 20 µm and (b) 30 nm.

Figure 6.7 shows SEM (a) and TEM (b) images of SBA-15-TMB. As shown in Fig. 6.7 (a), the SEM image suggests that the sample has agglomerated structures but lacks well-defined morphology. In the TEM image (Fig. 6.7 (b)), large pores are visible, which are formed by the use of the swelling agent during the synthesis. In the TEM observation, part of the material was not observable because thick material prevented the penetration of the electron beam. The image shows only the edge part of the material.

From the XRD pattern and TEM images, we conclude that the synthesized SBA-15-TMB contains larger but disordered pores. This is dramatically different from the rod-shaped SBA-15 which contains smaller but highly ordered pores.

TMB was used in the synthesis to obtain SBA-15 with expanded pores. The synthesis recipe of SBA-15-TMB is similar to that of siliceous mesostructured cellular foams (mesocellular foam, MCF). The main difference is the timing when tetraethyl orthosilicate (TEOS) is added to the reaction mixture. In the synthesis of SBA-15-TMB, TMB and TEOS were simultaneously added to the reaction mixture. In the synthesis of MCF, TEOS is added at least 45 min after the addition of TMB [9]. Zhao *et al.* first reported the synthesis of SBA-15 in 1998 and claimed this material having 2D hexagonal pores up to 30 nm [10]. However, subsequent work showed that when the TMB/P123 ratio exceeds 0.2, phase transformation occurs and the material only has a foamlike (mesocellular foam, MCF) structure. In the present synthesis, a TMB/P123 ratio of ca.1.5 was used. MCF consists of spherical cells (pores) connected by windows (smaller openings). It is formed from copolymer/TMB microemulsions as a template [11][12]. If the material is synthesized without fluoride, the MCF formed resembles arrays of close-packed spheres that are interconnected by smaller windows (Fig. 6.8, left). If the material is synthesized with fluoride, the MCF formed exhibits a strutlike structure (Fig. 6.8, right) [9].

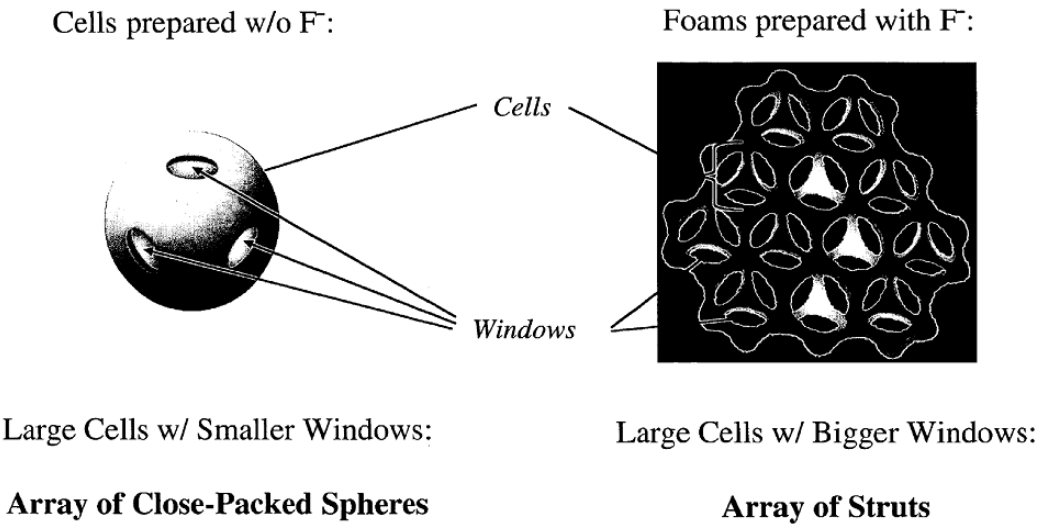

Figure 6.8: Schematic illustrations of the structures of mesocellular foams (MCFs). The openings correspond to windows. (Left) If the material is synthesized without fluoride, the MCF formed resembles arrays of close-packed spheres that are interconnected by smaller windows. (Right) If the material is synthesized with fluoride, the MCF formed resembles a lattice of struts. From Schmidt-Winkel et al [9]. It should be noted that the image is presented here to explain the structure of mesocellular foam. In the image (right), the cells are arranged in an ordered way, but the pores of actual SBA-TMB are considered to be disordered from the results of the XRD pattern and the TEM image.

A recent study by Chen *et al* [13] has shown that pre-hydrolysis of TEOS is crucial to obtain the particles with 2D hexagonally ordered pores when TMB is used as a swelling agent. However, the method can only prepare the mesoporous material with the pore diameter up to 12 nm [13].

Figure 6.9 shows the nitrogen isotherm data. The amount of N_2 adsorbed is much larger compared to that of rod-shaped SBA-15 (Fig. 6.4), indicating that the material has a large pore volume.

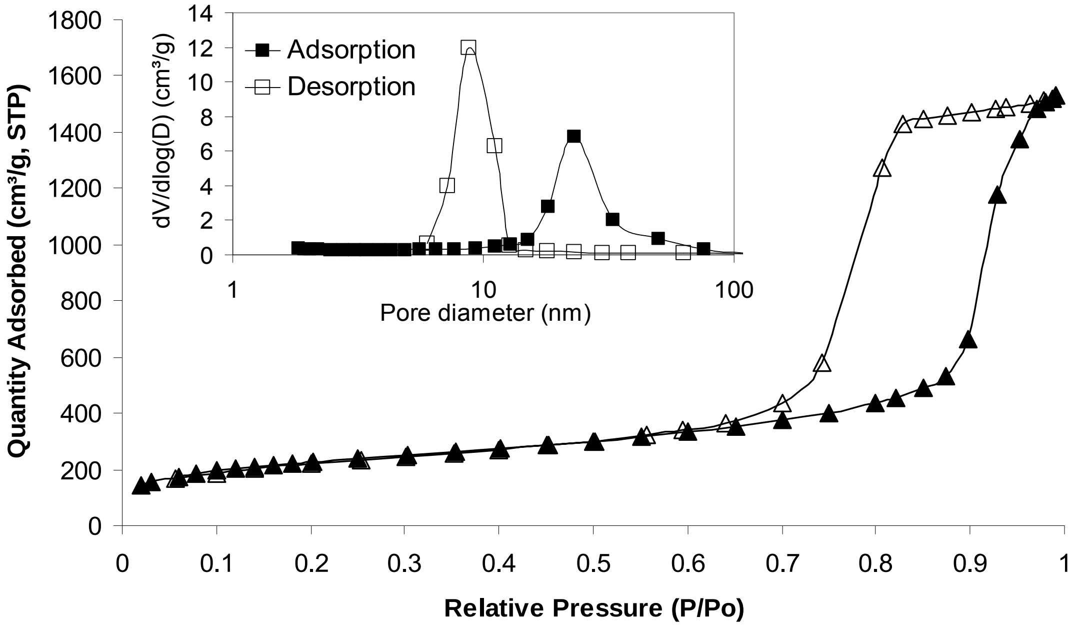

Figure 6.9: Nitrogen adsorption isotherm for calcined SBA-15-TMB. The isotherm is type IV, which is typical for mesoporous material (Section 5.1.2). The sharp rise at a relative pressure (P/P0) of 0.9 indicates that capillary condensation occurs. The occurrence of capillary condensation at high P/P_0 indicates that the SBA-15-TMB has a large pore diameter. The inset shows the pore size distribution (PSD). The filled and open squares represent the PSD determined from the adsorption branch of the isotherm and that determined from the desorption branch of the isotherm, respectively.

As noted, the synthesis recipe of SBA-15-TMB is similar to that of MCF. The TEM images have shown that at least part of the SBA-15-TMB has a foam pore structure. From these facts, SBA-15-TMB appears to have a MCF-like structure. The TEM image (Fig. 6.7 (b)) revealed only the edge part of the material due to the thick sample and information about the pore shape of a majority of the pores of the SBA-15-TMB was not obtained. Since MCF has spherical pores, the pore shape of the SBA-15-TMB is most likely to be spherical. The nitrogen adsorption isotherm further confirms this assumption. The nitrogen adsorption isotherm is similar to that of MCF (Fig. 2 (a) of Schmidt-Winkel et al [12]). MCF has ink-bottle-type pores. The size of the bottleneck (corresponding to the “window” in Fig. 6.8) can be determined from the desorption branch of the isotherm [14], while the size of the body of the ink bottle (corresponding to “cell” in Fig. 6.8) can be determined from the adsorption branch.

The SBA-15-TMB had a total surface area of 810 m^2 g^{-1} and a total pore volume of 2.12 cm^3 g^{-1}. The inset in Fig. 6.9 shows the pore size distribution. The BJH pore diameter determined from the adsorption branch was 23 nm, but the value estimated from the desorption branch is only 8.8 nm. As noted, SBA-15-TMB is most likely to have a MCF-like structure. The pore diameter of MCF is more precisely determined by the modified Broekhoff-de Boer (BdB) method, called, BdB-FHH method where FHH refers to Frenkel-Halsey-Hill form of the isotherm [14]. However, the BdB-FHH method is not easily available in the common software. Instead, the BJH method [15] was used for the pore size determination. MCF consists of spherical cells connected by windows. The BJH pore diameters determined from the adsorption and desorption branches correspond to the diameter of the "cell" and the diameter of the window, respectively. It should be noted that the BJH method could underestimate the pore size by ca. 20% compared to the BdB-FHH method [14].

In summary, the synthesized SBA-15-TMB has a foam-like structure consisting of large spherical disordered pores (cells) with a BJH pore diameter of ca. 23 nm, and the pores are interconnected by smaller openings of ca. 8.8 nm.

6.3 Synthesis of SBA-15 spherical particles

In some applications such as chromatographic applications of the mesoporous particles, controlling the morphology is important. Spherical particles were also synthesized in the present study. As described in section 2.2.4, the morphology of mesoporous silica can be controlled in several ways. Two methods were used to prepare spherical particles. The first method involves use of the co-surfactant, Cetyl Trimethyl Ammonium Bromide (CTAB). In the second method, an inorganic salt, KCl, was used. In addition, mesitylene or trimethylbenzene (TMB) was used as a swelling agent to obtain the particles with large pores.

6.3.1 Synthesis

In the first method, the synthesis was performed following a reported procedure [16]: A solution of N-cetyl-N,N;N-trimethylammounium bromide in H_2O (20 mL) was added to a solution of Pluronic P123 (3.10 g) in 1.5 M aqueous HCl (45.9 mL). After the addition of ethanol (7.8 mL), the mixture was stirred vigorously and TEOS (10 mL) was added dropwise. Following further stirring for 2 h at room temperature, the mixture was transferred to a bottle and kept at 75°C for 24 h and then at 80 °C for 48 h. The product was obtained by filtration, washed with H_2O (50 mL), and dried at room temperature. Calcination was performed at 500°C for 6 h. In the second method (use of KCl), the synthesis was performed following another procedure described in the literature [17]: 4.0 g Pluronic P123 and 6.08 g KCl were dissolved in 120 g H_2O and 23.6 g concentrated HCl at room temperature until the solution became transparent. 3.0 g mesitylene (TMB) was then added and the solution was stirred for 2 h. After that, 8.5 g TEOS was added dropwise and the solution was further stirred vigorously for about 10 min. The mixture was then kept under static condition at 35 °C for 24 h and another 24 h at 100 °C. The resultant precipitates were filtered, washed, and dried at 60°C.

6.3.2 Characterization

Based on the pore size of the synthesized particles, the spherical particles synthesized by the first method (use of co-surfactant) are called “SBA-sph-s”, and those synthesized by the second method (use of KCl) are called “SBA-sph-l”.

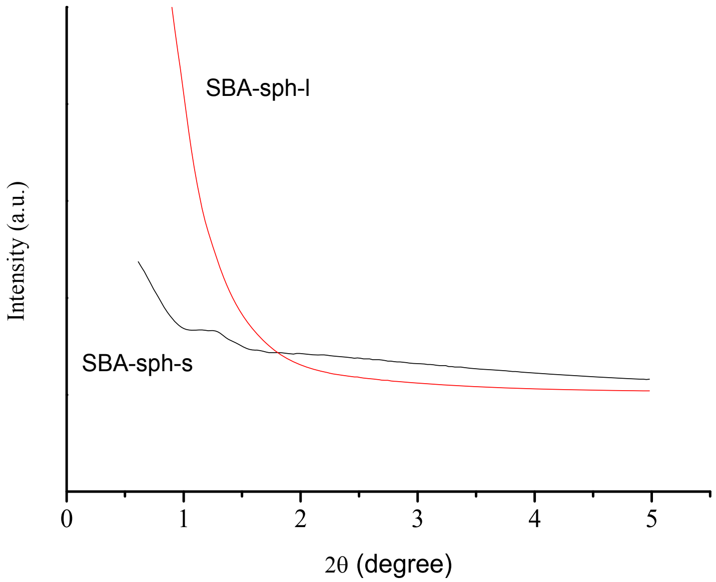

Figure 6.10: Powder XRD patterns of spherical SBA-15 samples, SBA-sph-s and SBA-sph-l. SBA-sph-s shows a single weak peak, indicating that pores are less ordered and tend to be randomly arranged. No peak is found above 2θ = 0.6° for SBA-sph-l, indicating that the material does not have a hexagonal structure. Detection limit for the instrument used is around 2θ = 0.6°.

Figure 6.10 shows powder XRD patterns of the two samples. SBA-sph-s gives rise to a single weak peak, indicating that pores are partially ordered but largely randomly arranged. No peak was detected for SBA-sph-l. SBA-sph-l is expected to have large-size pores. As described in Section 6.2.2, the peak may be found at the angles $2\theta \leq 0.5^{o}$, but it is beyond the detection limit for the instrument used. If the sample pore structure is ordered hexagonally, the peaks corresponding to (110) and (200) should be observed, the results shown in Fig. 6.10 thus strongly suggest that the sample does not have an ordered hexagonal pore structure.

Figure 6.11 (a) and (b) show SEM images of SBA-sph-s. The SBA-sph-s particles are spherical with the sizes in the range of 4-6 μm. For the spherical silica particles with large pore (SBA-sph-l), the morphology of some particles is non-spherical and of irregular shape (Fig. 6.11 (c) and (d)). The particle size with spherical shape is 2 to 5 μm. The particles were ground to break grain boundaries before the adsorption experiments.

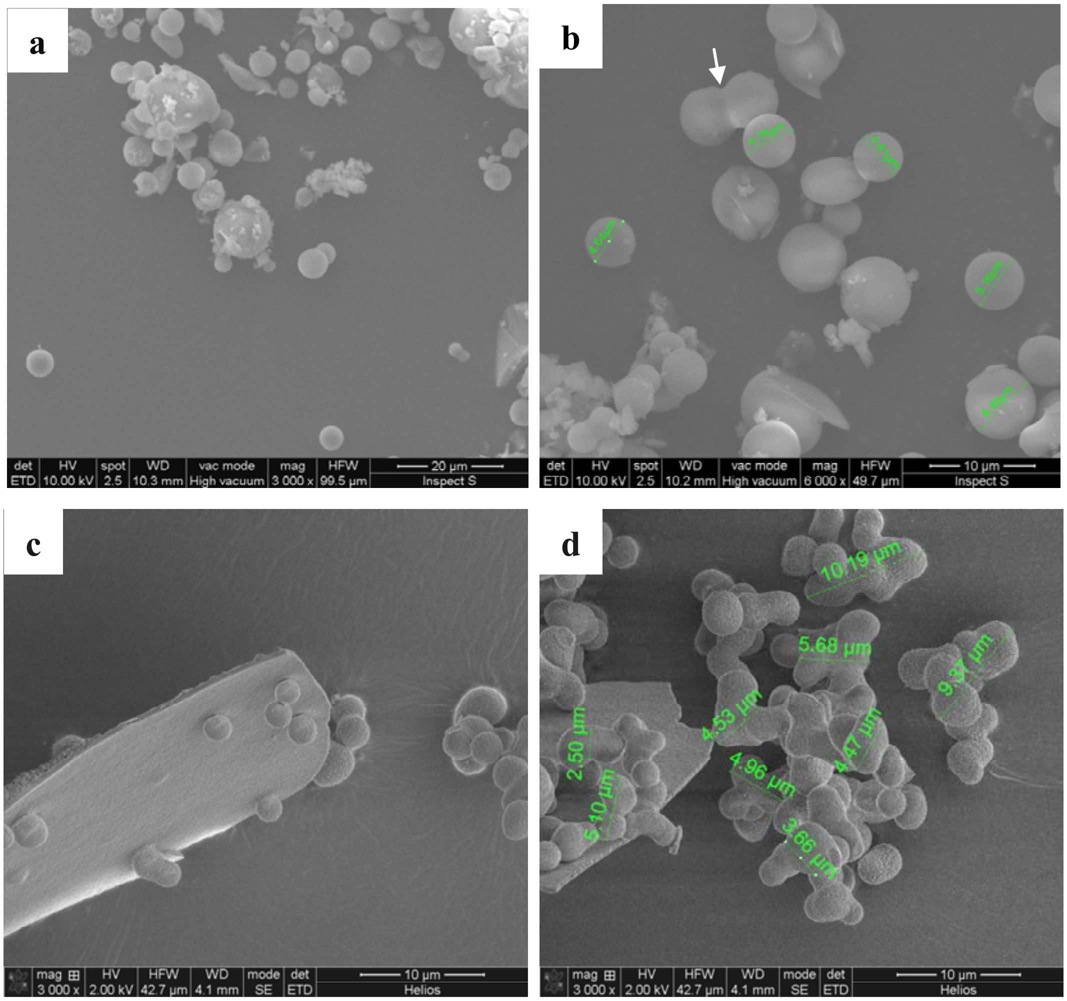

Figure 6.11: Examples of SEM micrographs of spherical SBA-15 particles synthesized. (a) and (b) SBA-sph-s, and (c) and (d) SBA-sph-l. The SEM images of SBA-sph-s ((a), (b) and other images not shown) reveal that some particles are in the form of “dimers” or “trimers” that are made of two or three spherical particles (arrow in image (b)). The SEM image of SBA-sph-l (d) shows irregular particles which appear to be the fusion of two or three particles. SEM images were obtained using an Inspect S (images (a) and (b)) or Helios EBS3 instrument (images (c) and (d)). Note: the long object in (c) is considered to be dust. Scale bars: (a) 20 µm, (b) to (d) 10 µm.

Large mesopores are visible in the TEM images of SBA-sph-l (Fig. 6.12). The overall structure consists of spherical pores (cells) separated by silica wall where pores are disordered. The material looks like clusters of soap bubbles (foam-like structure).

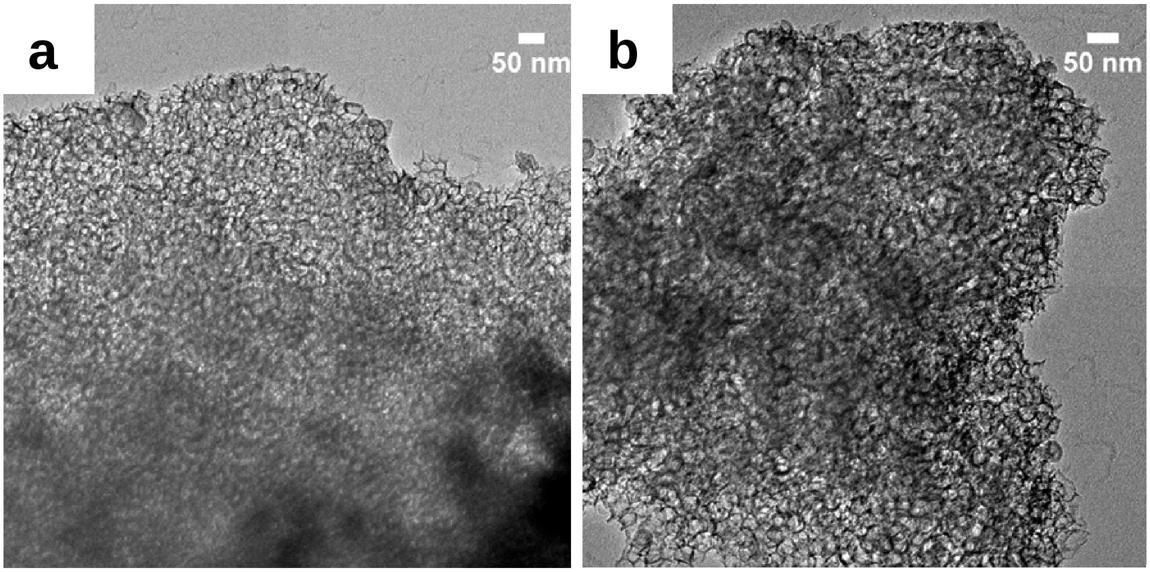

Figure 6.12: TEM images of spherical SBA-15, SBA-sph-l. Scale bars: (a) and (b) 50 nm. Spheroid shape of the pores (cells) is visible. The pores are disordered and the SBA-sph-l has a foam-like structure.

Fig. 6.13 shows the nitrogen adsorption isotherms of spherical SBA-15 samples. The adsorption branch of the SBA-sph-s is less sharp compared to the well-ordered sample with narrow pore size distribution (see Fig. 6.4). The hysteresis in the nitrogen adsorption and desorption isotherms of SBA-sph-l is also significantly larger. The isotherm also suggests that the desorption of nitrogen proceeds via two steps. The desorption at a relative pressure of around 0.45-0.5 appears to be caused by the instability of the meniscus of the condensed nitrogen in the pores [18].

In the synthesis of SBA-sph-l, TMB was used with a TMB/P123 ratio of 0.75. The synthesis recipe of SBA-sph-l is similar to that of siliceous mesostructured cellular foams (mesocellular foam, MCF) except that KCl was used. During the synthesis TMB was added in both cases and, after stirring for a certain time, tetraethyl orthosilicate (TEOS) was added. Specifically, in the synthesis of SBA-sph-l, TEOS was added after stirring for 2h following the addition of TMB. In the synthesis of MCF, TEOS was added at least 45 min after the addition of TMB [9]. The TEM images have shown that SBA-sph-l has a foam-like structure. The nitrogen adsorption isotherm of SBA-sph-l has similar features to those for MCF [14] such as the sharp rise at a high relative pressure (P/P_0) and large

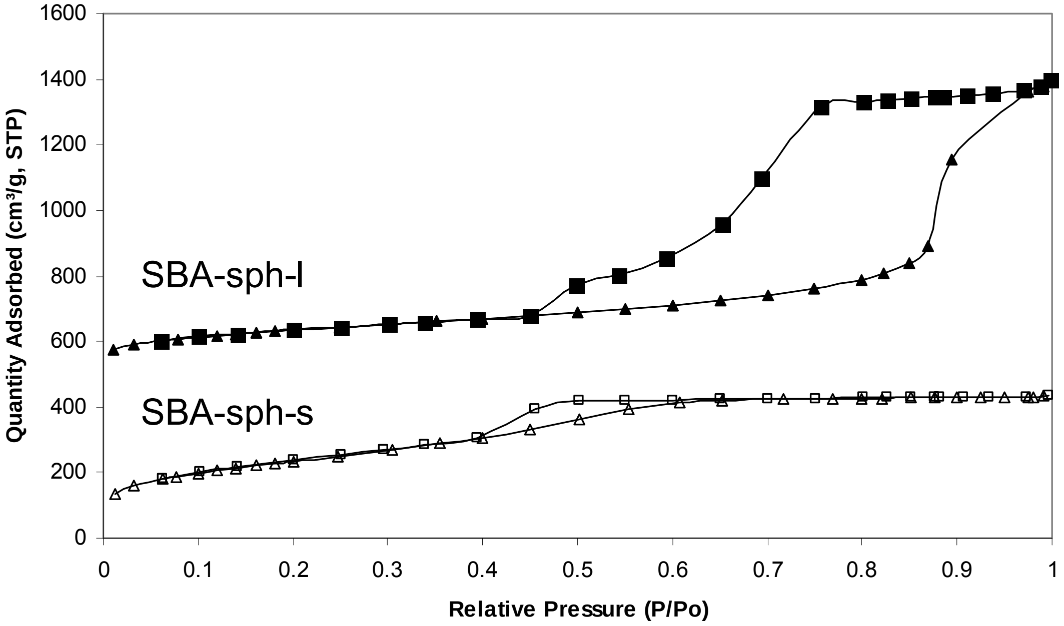

Figure 6.13: Nitrogen adsorption isotherms for calcined SBA-sph-s (open) and SBA-sph-l (closed). The adsorption isotherm for SBA-sph-l is shifted by 500 cm^3 g^{-1} STP. Both samples exhibit type IV isotherms.

hysteresis. SBA-sph-l also has a MCF-like structure, i.e., a three-dimensional pore structure consisting of large spherical pores (cells) interconnected by windows of smaller openings.

The structural properties of the samples based on the nitrogen adsorption isotherm are summarized in Table 6.2. The pore diameter (D_p) corresponds to the diameter of the "cell" and D_w represents the diameter of the window. As noted in Section 6.2, the BJH method could underestimate the pore size by ca. 20%, compared to the more precise BdB-FHH method [14].

Table 6.2: Physical Characteristics of two sphere-shaped SBA-15 samples.

Sample	S_{BET} (m^2/g)	V_{tot} (cm^3/g)	D_p (nm)	D_w (nm)
SBA-sph-s	853	0.67	3.7^a	-
SBA-sph-l	491	1.34	17.3^a	5.8^c

SBET: Total surface area, V_{tot}: Total pore volume, D_p: Pore diameter, D_w: Window diameter, a: Determined by the BJH method from the adsorption branch, b: Determined by the BJH method from the desorption branch.

In summary, the results obtained from the XRD, TEM, and N_2 adsorption/desorption experiments show that, SBA-sph-s has a less ordered structure with small-size pores, while SBA-sph-l has a foam-like structure consisting of large spherical disordered pores (cells) interconnected by smaller openings.

6.4 Functionalization of mesoporous silica

The surfaces of mesoporous silica can be functionalized specifically for facilitating immobilization of biomolecules. Compared to unfunctionalized surfaces, specific functionalization could improve the interactions between the silica walls and protein molecules, for example through stronger electrostatic binding. Surface functionalization also allows chemically covalent binding of enzymes onto the silica wall, which is expected to improve stability by preventing enzyme leaching from the pores. Furthermore, the chemical properties of the pores can be changed, for instance from hydrophilic to hydrophobic by the functionalization of silica walls. In the present study, SBA-15 was functionalized by introducing amino groups or methyl groups into the pore walls with the aim to further investigate the nature of the interactions between protein molecules and the pore walls. The functionalized SBA-15 materials were characterized by infrared spectroscopy.

6.4.1 Functionalization of SBA-15 with amino groups

6.4.1.1 Procedure

Amino groups were introduced to the pore walls of SBA-15 by chemical functionalization using a similar procedure as documented [19]. In a typical procedure, 200 mg calcined mesoporous silica was dispersed in 12 mL dried toluene. After the addition of 0.137 ml (equivalent to 130.17 mg) 3-aminopropyltrimethoxysilane (APTMS, Sigma-Aldrich;), the suspension was refluxed for 3 h. The modified product was recovered by filtration, washed with 40 mL ethanol, and incubated at 80 °C for 1 h.

6.4.1.2 IR analysis

IR measurements were carried out with the assistance from Brian Dideriksen at Department of Chemistry, DTU. Representative FTIR spectra for SBA-15 before and after functionalization are compared in Fig. 6.14. The FTIR spectrum of SBA-15 before functionalization shows absorption bands in the 3700-3000 cm^{-1} and around 1640 cm^{-1} corresponding to the O-H stretching and bending modes, respectively, of the silanol groups of the silica particles and/or adsorbed water [20][21]. After functionalization, the intensity of the band around 3400 cm^{-1} is decreased and a new peak appears at 2928 cm^{-1}, corresponding to the C-H stretching mode [22]. This peak is attributed to the C-H stretching mode of the methylene groups in the $–Si(CH_2)_3NH_2$ (APTMS, 3-aminopropyltrimethoxysilane, moieties) bound onto the surface of silica [23]. The absorption of the N-H (primary amine) bending vibration is at 1560 cm^{-1} [22]. However, there is no detectable peak around 1560 cm^{-1} in the spectrum. Nonetheless, the overall results suggest that SBA-15 was functionalized with NH_2 groups.

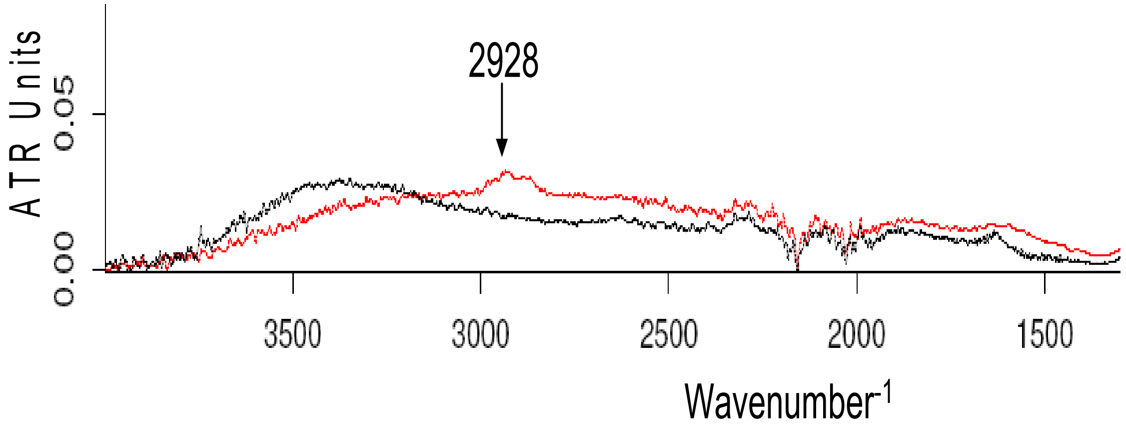

Figure 6.14: FT-IR spectra of SBA-15 before (black line) and after (red line) functionalization with amino groups. A new peak corresponding to the C-H stretching mode [22] appears at 2928 cm^{-1} after the functionalization with amino groups.

6.4.2 Functionalization of SBA-15 with methyl groups

6.4.2.1 Procedure

The SBA-15 particles (0.75g) were first dried at 150 ºC for 2 h and then dissolved in dry toluene (25 mL) at 70 ºC under an N_2 atmosphere. $(CH_3)_3SiCl$ (5 mL) was added to the solution under stirring. After further stirring for 24 h, the mixture was filtered and the residue dried in vacuum at 90 ºC for at least 8 h [24].

6.4.2.2 IR analysis

Figure 6.15 shows FTIR spectrum after methyl group functionalization. The peak at 2965 cm^{-1} is attributed to the C-H bond [25], indicating that the sample was functionalized with $-CH_3$ groups. The modified SBA-15 particles were used in the study of galactose oxidase described in Chapter 8.

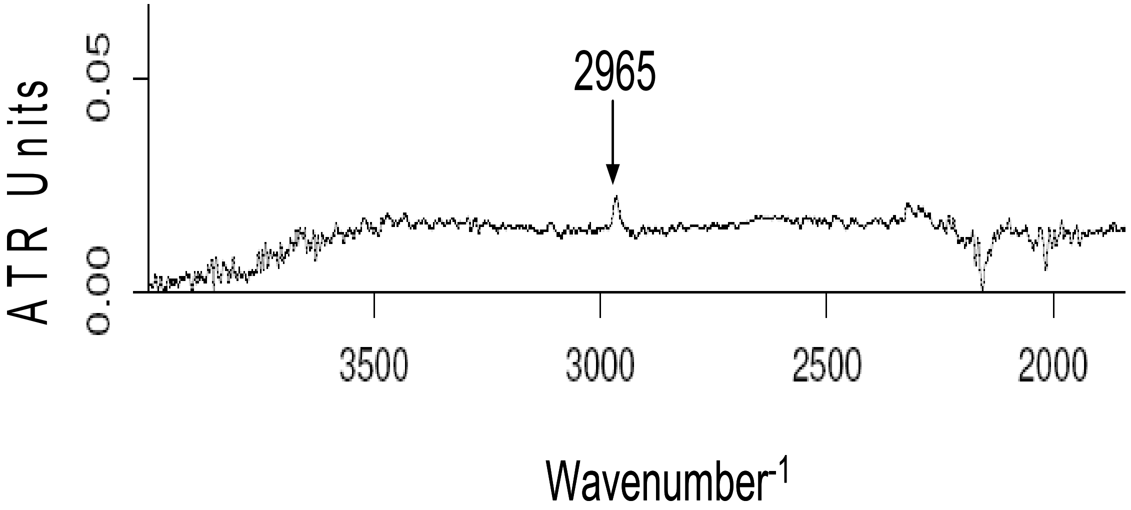

Figure 6.15: FT-IR spectrum of SBA-15 after methyl group functionalization. The peak at 2965 cm-1 is attributed to alkyl C-H stretching [25].

References

[1] P. F. Fulvio, S. Pikusb and M. Jaroniec. Tailoring Properties of SBA-15 Materials by Controlling Conditions of Hydrothermal Synthesis. *J. Mater. Chem.*, 15:5049–5053, 2005.

[2] A.-H. Lu, D. Zhao and Y. Wan. Nanocasting: *A Versatile Strategy for Creating Nanostructured Porous Materials*. RSC Nanoscience & Nanotechnology No. 11, The Royal Society of Chemistry, Cambridge, 2010.

[3] S. Lowell, J. Shields, M.A. Thomas & M. Thommes, *Characterization of Porous solids and Powders: Surface Area, Porosity and Density*, Kluwer Academic Publishers, 2004.

[4] P. I. Ravikovitch and A. V. Neimark, Characterization of Micro- and Mesoporosity in SBA-15 Materials from Adsorption Data by the NLDFT Method. *J. Phys. Chem. B*, 105: 6817-6823, 2001.

[5] J. Puputti, H. Jin, J. Rosenholm, H. Jiang, and M. Lindén, The Use of an Impure Inorganic Precursor for the Synthesis of Highly Siliceous Mesoporous Materials under Acidic Conditions. *Microporous Mesoporous Mater.*, 126: 272–275, 2009.

[6] M. Jaroniec, M. Kruk, and J. P. Olivier. Standard Nitrogen Adsorption Data for Characterization of Nanoporous Silicas. *Langmuir*. 15:5410-5413, 1999.

[7] M. Kruk, M. Jaroniec and A. Sayari. Application of Large Pore MCM-41 Molecular Sieves To Improve Pore Size Analysis Using Nitrogen Adsorption Measurements. *Langmuir*. 13:6267-6273, 1997.

[8] C. Lei, Y. Shin, J.K. Magnuson, G.E. Fryxell, L.L. Lasure, D.C. Elliott, J. Liu, and E.J. Ackerman. Characterization of Functionalized Nanoporous Supports for Protein Confinement. *Nanotechnology*, 17, 5531-5538, 2006.

[9] P. Schmidt-Winkel, W. W. Lukens, D. Zhao, P. Yang, B. F. Chmelka and G. D. Stucky. Mesocellular Siliceous Foams with Uniformly Sized Cells and Windows. *J. Am. Chem. Soc.*, 121:254-255, 1999.

[10] D. Zhao, J. Feng, Q. Huo, N. Melosh, G. H. Fredrickson, B. F. Chmelka, and G. D. Stucky. Triblock Copolymer Syntheses of Mesoporous Silica with Periodic 50 to 300 Angstrom Pores. *Science*, 279: 548-552, 1998.

[11] P. Schmidt-Winkel, C. J. Glinka, and G. D. Stucky. Microemulsion Templates for Mesoporous Silica. *Langmuir*. 16: 356–361, 2000.

[12] P. Schmidt-Winkel, W. W. Lukens, P. Yang, D. I. Margolese, J. S. Lettow, J. Y. Ying and G. D. Stucky. Microemulsion Templating of Siliceous Mesostructured Cellular Foams with Well-Defined Ultralarge Mesopores. *Chem. Mater,.* 12:686-696, 2000.

[13] S.-Y. Chen, Y.-T. Chen, J.-J. Lee and S. Cheng. Tuning Pore Diameter of Platelet SBA-15 Materials with Short Mesochannels for Enzyme Adsorption. *J. Mater. Chem.*, 21: 5693-5703, 2011.

[14] W. W. Lukens, P. Schmidt-Winkel, D. Y. Zhao, J. Feng and G. D. Stucky, Evaluating Pore Sizes in Mesoporous Materials: A Simplified Standard Adsorption Method and a Simplified Broekhoff−de Boer Method. *Langmuir*, 15:5403, 1999.

[15] E. P. Barrett, L. G. Joyner and P. P. Halenda. The Determination of Pore Volume and Area Distributions in Porous Substances. I. Computations from Nitrogen Isotherms. *J. Am. Chem. Soc.*, *73*:373–380, 1951.

[16] N. Gartmann and D. Brühwiler. Controlling and Imaging the Functional-Group Distribution on Mesoporous Silica. *Angew. Chem. Int. Ed.*, 48:6354 –6356, 2009.

[17] L. Wang, T. Qi, Y. Zhang, and J. Chu. Morphosynthesis Route to Large-Pore SBA-15 Microspheres. *Microporous Mesoporous Mater.*, 91:156-160, 2006.

[18] W. W. Lukens, Jr., P. Yang, and G. D. Stucky. Synthesis of Mesocellular Silica Foams with Tunable Window and Cell Dimensions. *Chem. Mater.*, 13:28–34, 2001.

[19] H. Ritter and D. Brühwiler, Accessibility of Amino Groups in Postsynthetically Modified Mesoporous Silica. *J. Phys. Chem. C.* 113:10667–10674, 2009.

[20] L. D. Pérez, J. F. López, V. H. Orozco, T. Kyu, and B. L. López. Effect of the Chemical Characteristics of Mesoporous Silica MCM-41 on Morphological, Thermal, and Rheological Properties of Composites Based on Polystyrene. *J. Appl. Polym. Sci.*, 111:2229–2237, 2009.

[21] D. J. N. Subagyono, Z. Liang, G. P. Knowles and A. L. Chaffee. Amine Modified Mesocellular Siliceous Foam (MCF) as a Sorbent for CO_2. *Chem. Eng. Res. Des.*, 89:1647–1657, 2011.

[22] E. I. Basaldella and M. S. Legnoverd. Functionalized Silica Matrices for Controlled Delivery of Cephalexin. *J Sol-Gel Sci Technol.*, 56:191-196, 2010.

[23] I. Shimizu, H. Okabayashi, K. Taga, E. Nishio, and C. J. O'Connor. Diffuse Reflectance Infrared Fourier Transform Spectral Study of the Thermal and Adsorbed-Water Effects of a 3-Aminopropyltriethoxysilane Layer Modified onto the Surface of Silica Gel. *Vibrational Spectroscopy*, 14:113–123, 1997.

[24] L. Li, J.-L. Shi, L.-X. Zhang, L.-M. Xiong, J.-N. Yan. A Novel and Simple In-Situ Reduction Route for the Synthesis of an Ultra-thin Metal Nanocoating in the Channel of Mesoporous Silica Materials. *Adv. Mater.*, 16:1079-1082, 2004.

[25] L.-X. Zhang, J.-L. Shi, J. Yu, Z.-L. Hua, X.-G. Zhao, M.-L. Ruan. A New In-Situ Reduction Route for the Synthesis of Pt Nanoclusters in the Channels of Mesoporous Silica SBA-15. *Advanced Materials*. 14:1510–1513, 2002.

7. Catalytic kinetics and stability of horseradish peroxidase immobilized on mesoporous silica, SBA-15

Chapters 7-9 present the major results of the work, i.e., electronic and kinetic properties of three proteins confined in the pores of the mesoporous silica particles compared with the free solute proteins. Three protein systems have been studied. Two of them are redox metalloenzymes, i.e., the heme enzyme horseradish peroxidase (HRP), chapter 7, and the copper enzyme galactose oxidase, chapter 8. Focus here was on the changes in enzyme catalytic kinetics and the enzyme stability in pore confinement upon exposure to a temperature excursion or addition of denaturing agents. The third system, chapter 9, is the large photosynthetic light-harvesting protein complex (LH2). In the third system, the study was focused on structural and electronic changes of LH2 invoked by nanoscale confinement.

This chapter describes immobilization and functional characterization of the redox enzyme horseradish peroxidase (HRP) in SBA-15 mesoporous silica. The catalytic activity of free HRP in solution and immobilized enzyme in the pores was systematically compared at room temperature. In the context of enzyme kinetics, interesting details including the apparent Michaelis constant (K_M) and maximum rate (V_{max}) were determined. Comparison of thermal stability and the stability resistance to the denaturing agents guanidinium chloride and urea, of free and immobilized enzymes was further featured.

7.1 Brief introduction

HRP belongs to the plant peroxidases superfamily [1]. The plant peroxidase superfamily includes the peroxidases of both prokaryotic and eukaryotic origins. These peroxidases are divided into three classes according to the enzyme primary structures [1]. With this classification, HRP belongs to class III (higher plant peroxidases targeted for the secretory pathway) [2]. HRP is a single chain polypeptide containing four disulfide bridges, with a molecular mass of ca. 44 kDa. HRP also contains a single heme group as redox center and a calcium binding site proximal or distal to the heme group (Fig. 7.1). There are at least seven isomers of HRP [3], among which HRP C from horseradish root is a dominant type [1]. HRP has an average dimension of 6.8 nm × 4.4 nm × 4.0 nm in solution [4] [5]. HRP was chosen for this study because it is well characterized structurally, which allows us to focus on the investigation of the catalytic properties of the immobilized enzyme.

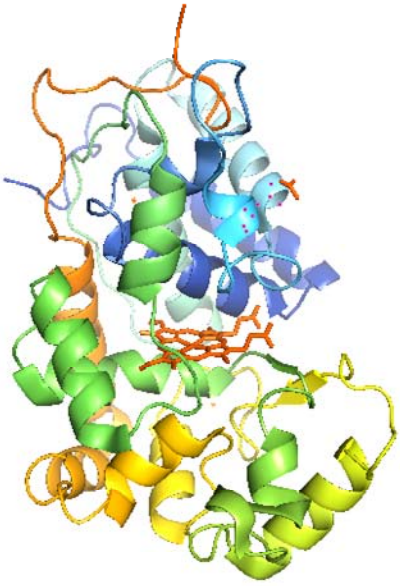

Figure 7.1: Three-dimensional structure of horseradish peroxidase C. The heme group in the middle is coloured in orange. PDB code: 1H5A [5].

Preliminary studies of HRP immobilization on different types of mesoporous silica materials were previously reported. For example, Takahashi et al. [6] investigated the catalytic activity of HRP adsorbed on MCM-41, FSM-16 and SBA-15 and found that both surface character and pore size are crucial to achieve high catalytic activity. In another study by Chouyyok et al. [7], three types of mesoporous silica (MCM-41, SBA-15, and MCF) were used, and the effects of pH on HRP immobilization and catalytic activity investigated. The largest loading amount of this enzyme was achieved for MCF, and maximum catalytic activity for the enzyme confined in this material was observed at pH 6. However, a detailed kinetic study of immobilized HRP has not been carried out. In the present study, the enzyme kinetic constants were obtained by different methods and compared with those for the free enzyme. The stability of the enzyme immobilized in mesoporous silica was also investigated using two commonly used denaturing agents, guanidium chloride and urea.

7. 2 Experimental Section

7.2.1 Chemicals

Horseradish peroxidase P8250-5KU Type II (EC number: 1.11.1.7, 150-250 units/mg solid, Sigma-Aldrich), urea (minimum, 99.5%), tetraethyl orthosilicate (98% (GC), Aldrich), poly(ethylene glycol)-*block*-poly(propylene glycol)-*block*-poly(ethylene glycol) (denoted as Pluronic® P-123, Sigma-Aldrich), 4-aminoantipyrine (≥ 98.0%, Sigma-Aldrich), phenol (≥ 99.5%, Sigma-Aldrich), and 30% hydrogen peroxide (Fluka) were used as received. The precise H_2O_2 concentration was determined by MnO_4^- titration. Other agents used were at least of analytical grade. High-quality Milli-Q water (18.2 MΩ·cm) was used throughout.

7.2.2 Experimental details

Synthesis and characterization of silica particles. The synthesis procedure and characterization of rod-shaped SBA-15 are described in Section 6.1. Silica particles for SEM were coated with gold to 3.0 nm thickness by sputtering. To prepare TEM specimens, a lacey carbon grid was put into the powder a few times. This ensured that the particles would stick to the grid.

Immobilization of HRP in SBA-15. HRP solution (2.5 ml, 0.5 mg ml^{-1}) was added to 125 mg SBA-15 placed in a centrifuge tube. The mixture was stirred at 4 °C for 48 h. The loading of HRP into the nanopores was monitored by UV-vis spectra at 409 nm after centrifugation using a UV-vis spectrophotometer (HP8453, Hewlett Packard) until no apparent decrease in absorbance was detected in the supernatant. The suspension was then centrifuged and washed several times with phosphate buffer (pH 7.4) until no free enzyme in the supernatant could be detected. The total amount of HRP immobilized was estimated from absorbance changes to be ca. 7.1 mg per gram SBA-15. The HRP-SBA-15 conjugated material (in solid-state form) was dried and stored at 4 °C.

Staining of HRP with gold nanoparticles and sample preparation. It was attempted to stain HRP with nanogold® following the procedure of Chenghong *et al.* [8]. Specifically, 0.3 or 0.5 mg of the enzyme–SBA-15 or SBA-15 (control) suspension was washed twice with 60 μl H_2O, and resuspended in 60 μl H_2O. The washed and resuspended enzyme–SBA-15 or SBA-15 alone was mixed with 20 μl of the negatively charged gold nanoparticle solution (NCGN, diameter: 1.4 nm, 30 μM of gold, from Nanoprobes, Inc.) and the mixture was stirred at 1400 min^{-1} at room temperature for 12 min. The resulting enzyme–SBA-15 or SBA-15 incubated with NCGN was centrifuged, washed twice with 60 μl H_2O, and finally resuspended in 60 μl H_2O. A few drops of the suspension were applied on a holy carbon film coated Cu grid.

Assays of Enzyme Activity. The catalytic activity of free and immobilized enzyme was determined using a modified reported colorimetric procedure [9]. For the free enzyme, a solution containing 2.4 mM 4-aminoantipyrine (4-AAP), 86 mM phenol, 0.077 to 1.5 mM hydrogen peroxide, and 25 mM phosphate buffer (pH 7.4) in a total volume of 1.21 ml was prepared in a cuvette, and 40 μL 0.01 mg ml^{-1} HRP added and mixed. The absorbance at 510 nm was monitored to determine the initial reaction rates. For the immobilized enzyme, 13.6 mg HRP-containing SBA-15 was mixed with 12.5 ml solution containing 2.4 mM 4-AAP, 86 mM phenol, 0.077 to 1.5 mM hydrogen peroxide, and 25 mM phosphate buffer (pH 7.4). The samples (1 ml) were centrifuged at given intervals to remove the particles, and the corresponding absorbance of the supernatant at 510 nm recorded. The extinction coefficient used for calculation is 7100 M^{-1} cm^{-1} [10]. Full time records were also performed to obtain kinetic constants at given substrate concentrations.

Evaluations of Thermal Stability. The thermal stability of HRP immobilized in SBA-15 was examined by adding 13.6 mg HRP immobilized SBA-15 to 2.2 ml 100 mM phosphate buffer (pH 7.4) and then heating the mixture at 70 °C for 30 min. The solution was left in air for cooling down to room temperature, and the catalytic activity then determined. The free enzyme, 40 μL HRP (0.01 mg mL^{-1}) solution, was treated similarly.

Stability in the Presence of Denaturing Agents. Free or immobilized HRP was incubated for 22-28 h in the solutions containing various denaturant concentrations. Catalytic activity in the denaturant solutions was determined after incubation, as described above.

7.3 Results

7.3.1 Synthesis of SBA-15 and immobilization of HRP

SBA-15 synthesized by the slightly modified reported procedure [11] was characterized by SEM, TEM, and XRD. The characterization is detailed in Section 6.1. Figure 7.2 shows XRD patterns of SBA-15 used. Three reflections were readily observed in the powder XRD pattern at $2\theta = 0.86$, 1.49, and 1.69° for the calcined material. The three peaks correspond to (100), (110), and (200) reflections, respectively, indicating that the particles have hexagonally (space group *p6mm*) ordered pore structures.

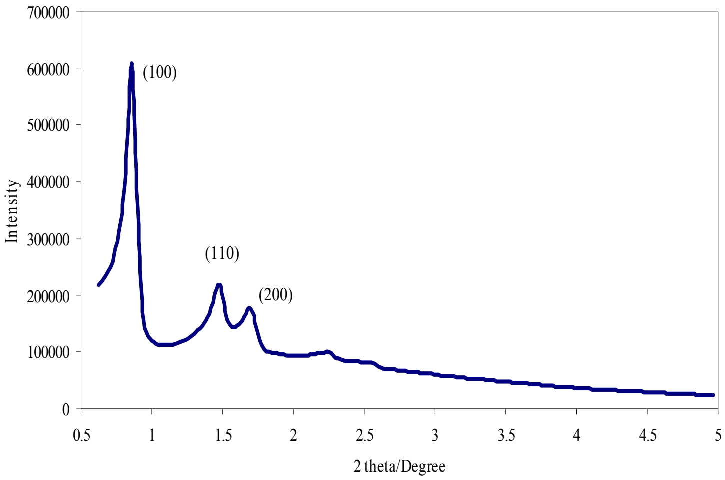

Figure 7.2: Powder XRD patterns of calcined SBA-15. The three peaks at 2θ = 0.86, 1.49, and 1.69° can be indexed as (100), (110), and (200) reflections associated with p6mm hexagonal symmetry.

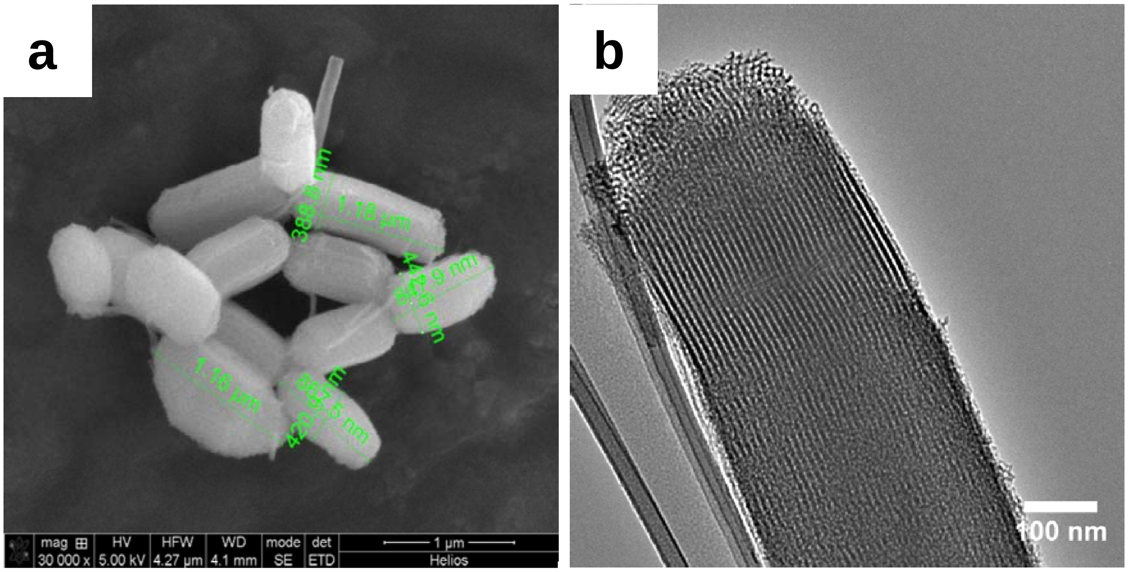

Figure 7.3: SEM and TEM images of rod-shaped SBA-15. The SEM image (a) reveals that the rod-shaped SBA-15 particles are aggregated. The parallel strips in the TEM image (b) are the projections of hexagonal cylindrical pores from the side. The ordered channels are oriented along the long axis of the rod. Scale bars: (a) 1 µm and (b) 100 nm.

The average particle size was several hundred nanometers in diameter and 1 µm in length (Fig. 7.3). The BJH (Barrett-Joyner-Halenda) pore diameter of calcined SBA-15 determined from the adsorption branch of the nitrogen adsorption isotherm is 9.6 nm, suitable to accommodate HRP (6.8 nm × 4.4 nm × 4.0 nm in solution [4][5]). Pore surface area and pore volume determined from nitrogen adsorption experiments were 872 m^2g^{-1} and 1.3 cm^3 g^{-1}, respectively.

Immobilization of HRP was achieved by suspending nanoporous material in HPR solution (pH 7.4). The isoelectric point of HRP is 8.9 and the HRP molecules thus positively charged in the buffer solution used. The silanol groups inside the nanopores are deprotonated at pH 7.4. Electrostatic interactions between HRP molecules and the inner nanopore walls are thus crucial if not exclusive in enzyme immobilization.

7.3.2 TEM observation of enzyme on SBA-15

An attempt by TEM was made to investigate how the HRP is distributed on the SBA-15 particles. To obtain TEM images of enzyme on SBA-15, staining of HRP was attempted. The HRP on SBA-15 is considered to be positively charged and thus negatively charged gold nanoparticles (NCGNs, diameter: 1.4 nm) were used to stain the enzyme. Enzyme-free SBA-15 was used as a control sample. A few black spots, considered to be gold nanoparticles, were found on the sample (black arrows) for stained samples (Fig. 7.4 (a)). In about half the cases (at ca. 50% of the places examined by TEM), it was difficult to identify clear black spots (Fig. 7.4 (b)), and also difficult to find clear differences between the sample and the control (e.g. control: Fig. 7.4 (d)). It was therefore concluded that the enzyme was not stained with NCGNs successfully. However, more black spots were found for the enzyme–SBA-15 sample than for the enzyme-free SBA-15. Energy-dispersive X-ray (EDX) analysis was run on the place where black spots were contained, but the signals from gold are not completely certain. The particle contains ca. 0.24% (wt) Au at maximum. It was therefore concluded that it was impossible to identify the Au peak due to the trace amount of Au even if gold nanoparticles were located inside the particles. The results of the TEM examination appear to suggest that the pore size was not large enough for the gold nanoparticles to enter the pore and attach to the enzyme.

However, recently reported TEM images [8] show that immobilized protein inside the pores can be stained with gold nanoparticles to display dark spots. There are several differences in the present study compared to those data in the literature. *First*, the pore size is different (30 nm for the reported study vs. 9.6 nm in the present case). *Secondly*, electrostatic charges are opposite. While the gold nanoparticles in the reported study are

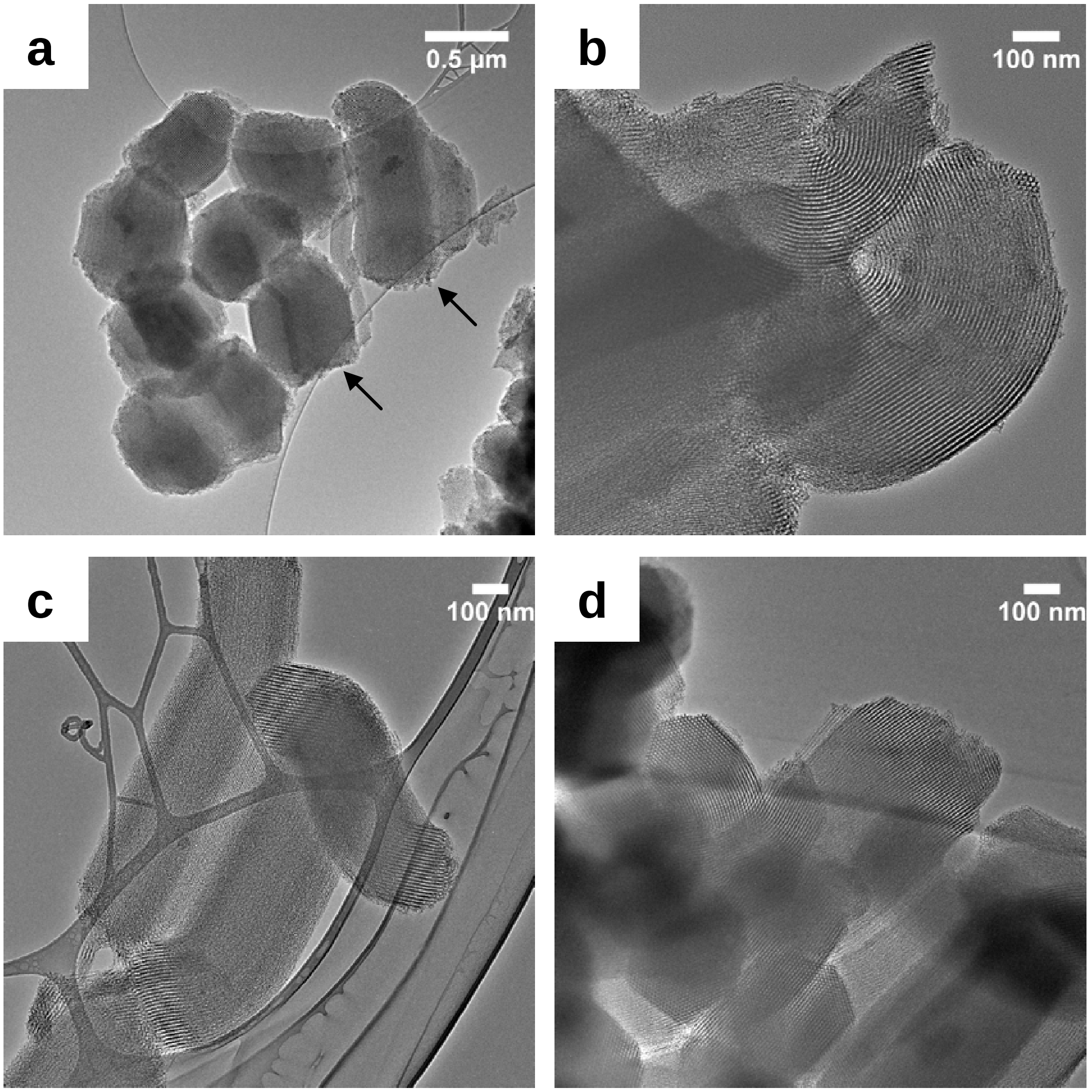

Figure 7.4: TEM micrographs after the attempt of staining HRP with NCGN; (a) and (b) enzyme–SBA-15, and (c) and (d) enzyme-free SBA-15.

positively charged, the gold nanoparticles used in the present case are negatively charged. Since the pore walls are also negatively charged, gold nanoparticles could thus be prevented from entering the pores by electrostatic repulsion.

The attempts for staining HRP with AuNPs were carried out as part of the project in the PhD course “Electron Microscopy and Analysis for Materials Research” at DTU CEN. In the report, I wrote that “Ultramicrotome treatment may be one possible future task to identify the distribution of enzyme or protein distribution.” An ultramicrotome is an instrument for cutting a specimen embedded in resin into many sections. These sections can then be used for reconstruction of a three-dimensional TEM image of the particle. Further study along with the line could not, unfortunately, be performed due to time limit in the PhD study. Recently, 3D distribution of lysozyme adsorbed onto SBA-15 was published [12]. In this article, an immunogold staining method was used and 3D images were reconstructed from ultrathin sections.

7.3.3 Catalytic activity of free and SBA-15 immobilized HRP at room temperature

The catalytic activity of the immobilized HRP and the effect of the H_2O_2 concentration were first investigated. A similar investigation of the freely dissolved enzyme as a reference was also carried out. The initial velocity was determined from the absorbance change at 510 nm. Figure 7.5 shows an example of absorbance-time relations at a H_2O_2 concentration of 1.2 mM. The exact amount of accessible active enzyme immobilized could not be determined. Direct clues to the accessibility issue and to the amount of pore-confined enzyme that retains activity are in fact quite elusive, but irreversibly bound inhibitors may offer a way if appropriate inhibitors are available. For example, the active site of immobilized lipase can be titrated by using irreversible inhibitors [13]. The inhibitor irreversibly binds to the active site of the enzyme to produce a product. The released product can be determined spectrophotometrically, thus allowing active site titration. This issue will be discussed in Section 7.4. However, the concentration of accessible HRP in the immobilized state is expected to be significantly higher than that of free HRP in solution because the amount of enzyme used in the activity assays is 7.7 and 0.38 μg mL^{-1} for the immobilized and free states, respectively. Even so, the initial rate of product formation is much lower for the immobilized enzyme than for the free enzyme. If the product is adsorbed onto the SBA-15 surface and is not able to enter the reaction mixture, less amount of product is detected than actually formed, resulting in a lower initial rate. However, separate adsorption experiments did not detect any adsorbed product.

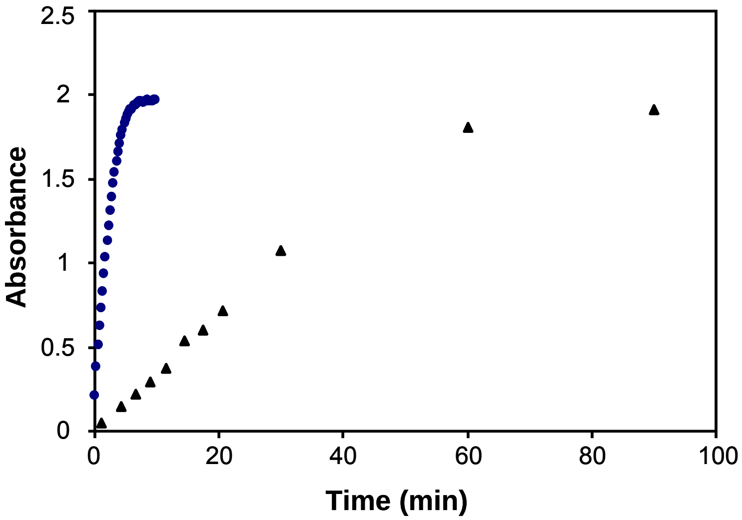

Figure 7.5: Time courses of product (N-antipyryl-p-benzoquinoneimine, APBQ) formation in the oxidation of phenol by H_2O_2. Free or immobilized enzyme was mixed with a solution containing 2.4 mM 4-AAP, 86 mM phenol, 1.2 mM hydrogen peroxide and 25 mM phosphate buffer (pH 7.4). Filled circles and triangles show the response from free and immobilized enzyme, respectively.

The Michaelis constant (K_M) and the maximum rate constant (V_max) were determined from Lineweaver-Burk or directly from Michaelis-Menten plots (Appendix 2). The use of these frames in their simplest form raises questions regarding the mechanism of the assay reaction. The reaction is certainly more complicated than inherent in straightforward use of Lineweaver-Burk or Michaelis-Menten analysis and involves two substrate molecules eq. (7.2) [9]. Lineweaver-Burk or Michaelis-Menten analysis or equivalent analysis directly of the time evolution of the process at each given substrate concentration, however, still offers applicable operational frames with reference to the dominating assay process (see eq. (7.2)), as well as for the analysis of the temperature and denaturation effects on free and pore-confined enzyme.

$$PhOH + Am\text{-}NH_2 + 2H_2O_2 \rightarrow APBQ + 4H_2O \tag{7.1}$$

The main reservation is then that the catalytic constants K_M and V_{max} are composite quantities and acquire the status of "apparent". The "apparent" K_M values of free and immobilized HRP from the former plots were 0.47 ± 0.06 and 0.35 ± 0.03 mM, respectively, and the apparent V_{max} values 160 ± 20 and 9.3 ± 0.7 μM min^{-1}. Similar values were obtained by the latter method (using an Excel solver program), giving V_{max} of free and immobilized HRP of 120 ± 10 and 8.6 ± 0.2 μM min^{-1}, respectively, and K_M = 0.27 ± 0.03 and 0.31 ± 0.01 mM.

Table 7.1: Comparison of Apparent Catalytic Constants of Free and Immobilized HPR at Room Temperature.

HRP Status	K_M(mM)			$10^3 V_{max}$ (mM min^{-1})			K_M/V_{max} (min)		
	a	b	c	a	b	c	a	b	c
Free	**0.47 ± 0.06**	**0.27 ± 0.03**	**0.65**	**160 ± 20**	**120 ± 10**	**150**	**3.4 ± 0.6**	**2.3 ± 0.1**	**4.3**
Immobilized	**0.35 ± 0.03**	**0.31 ± 0.01**	**N/A**	**9.3 ± 0.7**	**8.6 ± 0.2**	**N/A**	**37.8 ± 0.7**	**36 ± 3**	**N/A**

[a] Obtained from the Lineweaver-Burk plots. [b] Obtained from the Michaelis-Menten method.
[c] The values reported in ref. [14] .

Table 7.1 summarizes the catalytic constants obtained. V_{max} of immobilized HRP is significantly lower than that of free HRP. Several reasons for this are suggested. The active site of some of the enzyme molecules adsorbed in the SBA-15 pores may not be accessible. The conformation of some of the enzyme molecules may also have been changed by electrostatic interaction with the silica surface. Diffusion constraints are other possible reasons. Recently, Jaladi et al. investigated the effects of diffusion resistance on the activity of an immobilized enzyme (*Burkholderia cepacia* lipase) [15]. The enzyme immobilized in SBA-15 with 5.5 nm pores showed only 20-30% of the catalytic activity for free lipase. The enzyme was, however, more catalytically active in SBA-15 with large pore diameter (24 nm), most likely because of fewer diffusion limitations [15]. TEM further revealed that some particles were connected end-to-end (Fig. 7.3 (c)), which would make it even more difficult for substrates to reach the enzyme or for the products to escape from the pores to the outside. The detailed reaction scheme (Figure 7.6) shows that the substrate H_2O_2 is involved not only in the enzymatic reaction but also in enzyme-independent product formation. Diffusion thus significantly affects the rate of product formation by immobilized HRP. It is known that the catalytic activity of HRP is inhibited by high concentration of hydrogen peroxide [9]. Diffusion resistance would alleviate the inhibition of the immobilized enzyme because the local concentration of hydrogen peroxide in the pores would not be as high as in the bulk solution.

$$
\begin{aligned}
&E + \underline{H_2O_2} \xrightarrow{k_1} E_1 + H_2O \\
&E_1 + PhOH \xrightarrow{k_2} E_2 + PhO\cdot \\
&E_2 + PhOH \xrightarrow{k_3} E + PhO\cdot + H_2O \\
&PhO\cdot + Am\text{-}NH_2 \leftrightharpoons PhOH + Am\text{-}NH\cdot \\
&PhO\cdot + Am\text{-}NH\cdot \rightarrow Am\text{-}NH\text{-}OPh \\
&Am\text{-}NH\text{-}OPh + \underline{H_2O_2} \rightarrow Dye + 2H_2O
\end{aligned}
\tag{7.2}
$$

Figure 7.6: Reaction scheme of oxidation of phenol catalyzed by peroxidase. The native enzyme (E) is oxidized by H_2O_2 to an active intermediate enzymatic form (E_1). E_1 accepts phenol (PhOH) and carries out oxidation to produce a free radical (PhO•). The enzyme turns into the E_2 state. E_2 oxidizes a second molecule of phenol to release another free radical (PhO•). The enzyme returns to its native state to complete the cycle. The phenoxy radicals (PhO•) react with 4-aminoantipyrine (Am-NH_2) and H_2O_2 to generate the dye (color generation). From Nicell et al [9].

7.3.4 Thermal stability

The stability of immobilized HRP to heat was investigated next. After incubation at 70 ºC for 30 min, the catalytic activity was determined after cooling to room temperature. The initial rate of product formation has decreased to 73% after the free enzyme had been incubated at 70 ºC, indicating that the enzyme has denatured extensively (Fig. 7.7). In contrast, the initial rates of product formation catalyzed by immobilized enzyme are about the same before and after incubation at 70 ºC (Fig. 7.8). These results indicate that immobilized enzyme improves the thermal stability significantly, holding promise for exploiting the enzyme at elevated temperatures where the free enzyme is too unstable.

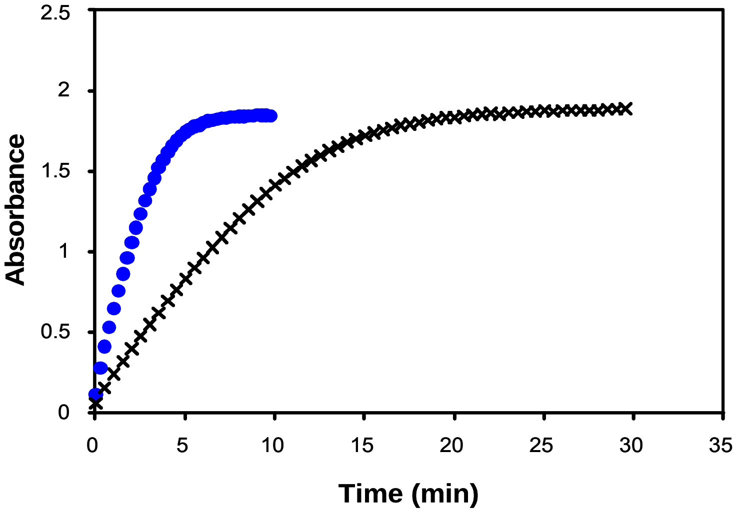

Figure 7.7: Time course of product (N-antipyryl-p-benzoquinoneimine) formation in the oxidation of phenol by H_2O_2 before (filled circle) and after (cross) incubation of free enzyme at 70°C. Free HRP was incubated at 70°C for 30 min and then left for cooling to room temperature. $[H_2O_2] = 0.6$ mM.

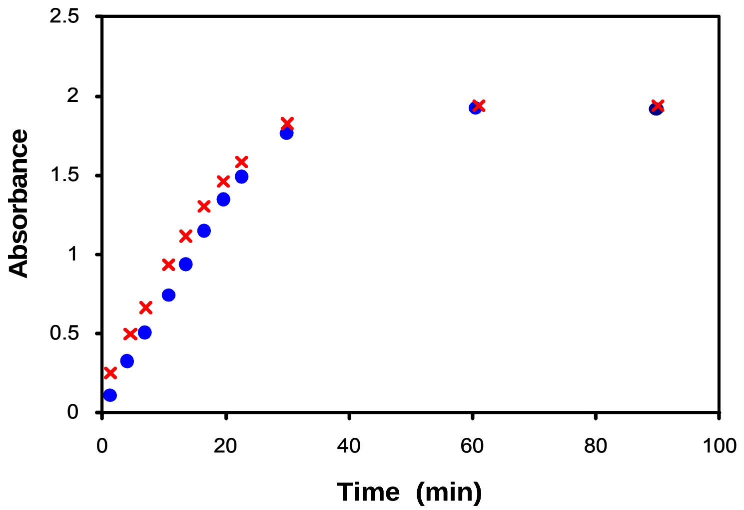

Figure 7.8: Time course of product formation in phenol oxidation by H_2O_2 before (filled circle, blue) and after (cross, red) treatment of immobilized enzyme at 70°C. 13.6 mg HRP-containing SBA-15 was added to 2.2 ml of 100 mM phosphate buffer (pH 7.4) and incubated at 70°C for 30 min, followed by cooling to room temperature. The catalytic activity was determined at room temperature. $[H_2O_2] = 0.6$ mM.

7.3.5 Stability in the presence of denaturing agents

The stability of the immobilized enzyme against guanidinium chloride (GdmCl) and urea was, finally, investigated. Immobilized enzyme behaved in much the same way on GdmCl addition as the free enzyme (Fig. 7.9). Significant activity decrease is noted at 1 to 2 M GdmCl, followed by further strong decrease at [GdmCl] > 4 M. The plateau suggests unfolding in a two-step process.

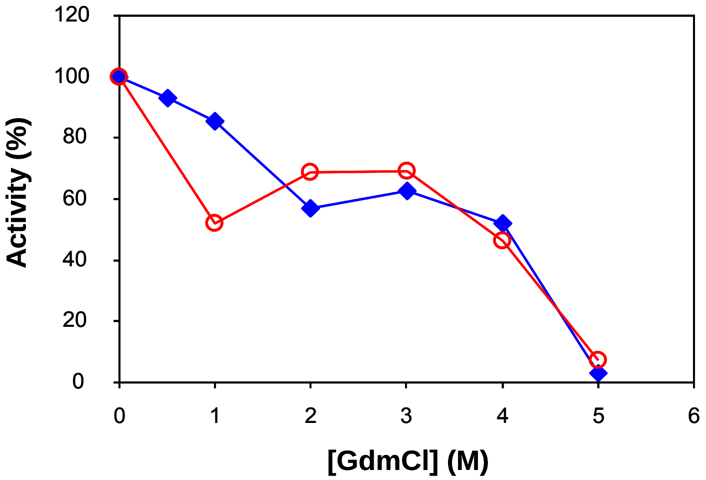

Figure 7.9: Comparison of retained activity of free (filled squares) and immobilized (open circles) enzyme after incubation with GdmCl. 0.27 μM free HRP was incubated with GdmCl in various concentrations for 22-28 hours. For immobilized enzyme, 13.6 mg HRP-immobilized-SBA-15 was incubated in solution containing varying concentrations of GdmCl also for 22-28 hours. The activity of the enzyme was determined by monitoring product (N-antipyryl-p-benzoquinoneimine) formation in the oxidation of phenol by H_2O_2. $[H_2O_2]$ = 0.6 mM.

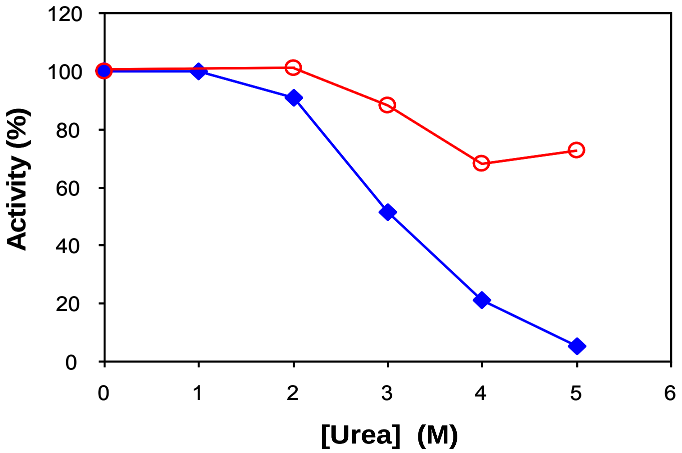

Figure 7.10: Comparison of retained activity of free (filled squares, blue) and immobilized enzyme (open circles, red) after urea incubation. 0.27 μM free HRP was incubated in urea solutions of various concentrations for 22-28 hours. For immobilized enzyme, 13.6 mg HRP-immobilized-SBA-15 was incubated in solutions containing varying concentrations of urea also for 22-28 hours. The activity of the enzyme was determined by monitoring product formation in the oxidation of phenol by H2O2. $[H_2O_2]$ = 0.6 mM.

In contrast, immobilized HRP incubated with urea showed strongly improved resistance to denaturation (Fig. 7.10). The immobilized enzyme has retained 80% activity, even at 5 M urea, where the activity of the free enzyme has dropped to < 10%. The immobilized enzyme still retains 16% activity after treatment with 10 M urea. This difference can be at least partially associated with recognized differences between the patterns of interaction of the protein and its solvation sphere with GdmCl or urea (Section 7.4).

The urea-induced denaturation of free and immobilized HRP can again be framed by the Lineweaver-Burk or Michaelis-Menten formalism (Chapter 3). Time-evolved free or immobilized HRP catalytic data framing offer other analysis based on a single substrate concentration value. Such analysis is useful for immediate comparative data assessment such as those of free and immobilized HRP or HRP catalytic activity after subjection to temperature excursions or exposure to denaturing agents. Approximate relations between the reaction time (t) and the product concentration ([P]) are given in the following equations, obtained by integration of the Michaelis-Menten scheme with respect to time

$$\frac{t}{[P]} = \frac{2}{V_{\max}} + \frac{K_M}{V_{\max}} \frac{1}{[P]} \ln \frac{[S_0]}{[S]_0 - 2[P]} \tag{7.3}$$

Eq. 7.3 can be recast as:

$$\frac{2[P]}{t} = V_{\max} - \frac{K_M}{t} \ln \frac{[S_0]}{[S]_0 - 2[P]} \tag{7.4}$$

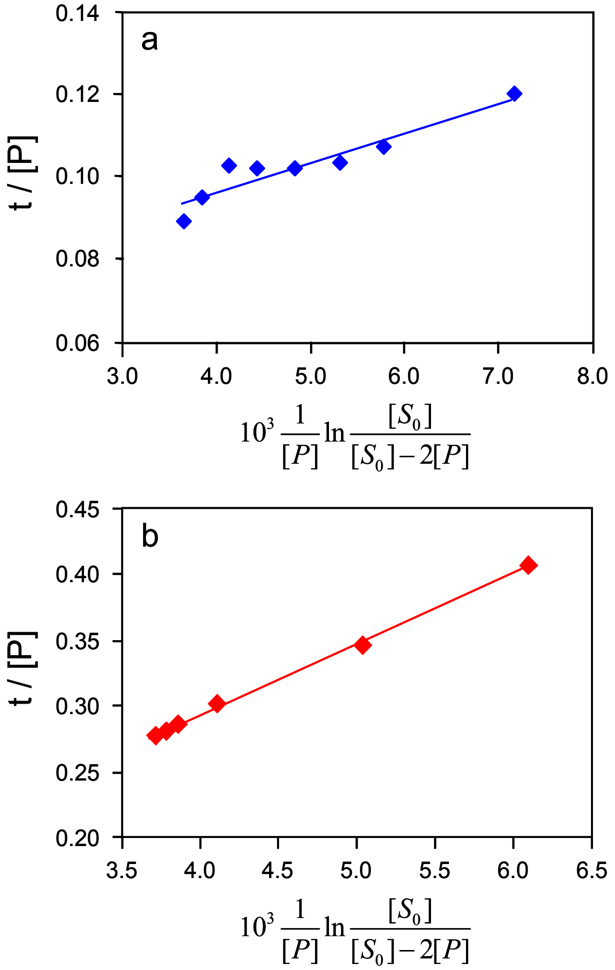

Figure 7.11: Plots of the catalytic curves of immobilized HRP in (a) the absence and (b) presence of 4 M urea treatment. The filled squares are experimental data and the solid lines fits according to eq. 7.3. Experimental conditions as for Figure 7.10.

Equations 7.3 and 7.4 are the basis for the analysis of single concentration-based data, for example, shown in Fig. 7.11.

Figure 7.11 shows examples of fits of eq. 7.3 to the catalytic data for immobilized HRP in the absence of urea and in the presence of 4 M urea. Similar single-kinetic-curve fits could be achieved using eq. 7.4 and applied to all reaction conditions, temperature dependence, and the effects of denaturing agents on either free or immobilized enzyme over substantial parts of the time courses. Table 7.2 summarizes the kinetic constants that give the best fits to the data. The following is noted:

(1) The free enzyme without treatment by heat or denaturing agents gives similar K_M/V_{max} in Lineweaver-Burk and Michaelis-Menten analysis, whereas K_M and V_{max} individually vary by a factor of two to three because of the different kind of data analysis. Observed effects of temperature or denaturation effects must therefore exceed this difference to be significant.

(2) The significant drop in V_{max} but largely unchanged K_M on enzyme immobilization is re-encountered, but there is a factor of three to four or so difference in V_{max} determined by the two approaches, whereas the differences in K_M are much smaller. The difference in the ratio K_M/V_{max} is therefore also significant.

(3) Both K_M and V_{max} have decreased after heat exposure, with the decrease of V_{max} being by far the largest, a factor of four to five or so. K_M, V_{max}, and K_M/V_{max} are, however, all unchanged in the immobilized form. Immobilization thus leads to notable heat stabilization.

(4) K_M for the free enzyme is largely unchanged from pure buffer when the reaction medium is 4 M GdmCl, whereas V_{max} has dropped significantly, by a factor of 8 or so. K_M appears to increase twice and V_{max} appears to drop to half its value in the immobilized state compared with the free enzyme in 4 M GdmCl. In view of the limitations associated with single-curve time analysis, these deviations are at the limit of being insignificant.

(5) The effects of urea addition are more pronounced (Fig. 7.11). V_{max} of the free enzyme has dropped to only 12% in 4 M urea, whereas K_M is largely unaffected. The drops shown by the immobilized enzyme is, however, only less than half the value of the immobilized enzyme in the absence of urea, again with K_M largely unaffected. Immobilization thus significantly stabilizes the enzyme toward denaturation in urea, primarily through more robust V_{max}.

Table 7.2: Apparent Catalytic Constants of Free and Immobilized HRP without (W/O) and with Subjection to Treatments of Heating or Denaturing Agent.

HRP Status		K_M (mM)				$10^3 V_{max}$ (mM min^{-1})				K_M / V_{max} (min)			
		W/O	Heat	GdmCl [c]	Urea [c]	W/O	Heat	GdmCl	Urea	W/O	Heat	GdmCl	Urea
Free	a	1	0.5	0.6	0.6	500	90	50	60	2.3 (± 0.1)	5.5 (± 0.1)	12.1 (± 0.2)	9.8 (± 0.1)
	b	0.70 (± 0.01)	0.39 (± 0.01)	0.53 (± 0.01)	0.48 (± 0.01)	400	80	50	50	2	5	10	9
Confined	a	0.2	0.3	1	0.3	30	30	30	20	7 (± 1)	8 (± 1)	54 (± 1)	18 (± 1)
	b	0.25 (± 0.06)	0.41 (± 0.06)	1.30 (± 0.1)	0.24 (± 0.05)	30	40	20	20	10	10	50	20

[a] Obtained from the fits of the experimental data using eq.(7.3). [b] Obtained from the fits of the experimental data using eq.(7.4). [c] The concentration of GdmCl and urea is 4 M. Note: The slope is more accurately determined than the intercept. For a, the slope, K_M/V_{max}, is expressed in 2 digits (±error). Other values are expressed in 1 digit without error. For b, the slope, K_M is expressed in 2 digits (±error), other values in 1 digit without error.

7.4 Discussion

Enzymes confined in mesoporous silica can be compared with enzymes in other "nanocage" or microreactor environments. Enzyme activity in reverse micelles (RMs) has been addressed comprehensively, mostly with observed significant activity decrease compared with free enzyme in aqueous buffer. Biswas and associates observed, for example that R-chymotrypsin activity drops two orders of magnitude in RM compared with aqueous buffer [16]. Strongly decreased enzyme activity was also found in activity and solvation dynamics studies of R-chymotrypsin and other hydrolytic enzyme activity (Subtilisin Carlsberg) as well as of other enzymes in the "crowded environment" of a range of RMs [17]-[21]. The observed confinement effects were assigned to a combination of volume exclusion (macromolecular "crowding") [22], changed protein folding, and complex formation with the electrostatically charged micellar head groups. All of these effects are undoubtedly also important for mesoporous silica-confined HRP, even though binding modes (electrostatic and via hydrogen bonds) are different. As a first physical origin of the observed modified catalytic effects, confinement and interaction of the enzyme with pore walls and other surfaces can affect the folding state of the enzyme. As shown by Sarkar et. al [19], RM binding of cytochrome *c* affects both the degree of compactness and the local segment mobility of the protein. In the present study, HRP is considered to interact with the silica walls through a hydration layer. The folding issue in this environment can be illuminated by recent studies of protein encapsulation in sol-gel glasses [23]. A protein (apomyoglobin) encapsulated in unmodified hydrophilic silica glass is unfolded, whereas the protein encapsulated in organically modified hydrophobic silica glass retains folding. HRP in the present study was immobilized on unmodified silica pore walls. HRP in this environment could therefore be partially unfolded by interaction with the hydrophilic silica walls, slowing down the catalytic reaction. Partial orientation blocking of the enzyme active site by adsorption to the pore walls is part of these scenarios [24], but it is notable that K_M is largely unaffected by the confinement. The nature of this quantity as a substrate binding constant would, however, be overall less sensitive to the conformational changes imposed by the confinement than the catalytic rate constant V_{max}.

Unfavorable partitioning of the substrate or product among protein binding and binding to the confining walls has, secondly, been forwarded as a confinement effect on the enzyme activity [17]. The affinity (adsorption) of the product to the pore walls was not considered in the present study, but adsorption of the product to SBA-15 was not observed. The adsorption of the product to SBA-15 was tested by stirring a mixture containing SBA-15 particles and the product (N-antipyryl-p-benzoquinoneimine) in a buffer solution for 2 hours. After 2 hours, the decrease of N-antipyryl-p-benzoquinoneimine in the solution was not detected (data not shown). Crowding, however, reduces the (substrate/product) molecular diffusion rates, which can differ greatly from bulk values [25]. As noted, the study by Jaladi et al. [15] showed that the effective substrate diffusivity in 5.5 nm pores is one order of magnitude smaller than that in 24 nm pores and two orders of magnitude smaller than that in free solution. Diffusional resistance is therefore also likely to contribute to the slow reaction rate of immobilized compared with free HRP.

The rigidity of the enzyme environment, the enzyme structural flexibility, or both are finally a cause of reduced enzyme activity [26]. Hydrogen bond strengthening and strengthened protein hydration were suggested as one of the causes of retarded R-chymotrypsin activity in RMs [17], whereas Sarkar and associates suggested [19] that bulk-like water is less available in RMs with small radius than in RMs with larger radius. The pore-confined structural aqueous environmental rigidity in the present study is not directly known, but the environment in the close vicinity of the surface of HRP is considered to be rigid, as evidenced from the increased hydration strength of other proteins in narrow mesopores based on pressure perturbation and differential scanning calorimetry [27] and from partial ordering of water at the surface of confined space, as addressed by NMR spectral techniques [28]. The rigid environment in the close vicinity of the surface of HRP may therefore have affected both protein folding and surface binding as well as caused slow dissociation of the substrate and product at the catalytic site.

The different behavior of HRP on GdmCl and urea addition may be attributed to a combination of different hydrogen bond properties of water and increased hydration strength of the protein inside the mesopores. The precise denaturing mechanisms of GdmCl and urea are still elusive [29]. One view is based on direct contact between denaturing agents and proteins; another one on modification of the hydrogen bond patterns of water solvation [30]. Camilloni et al. have illustrated this difference by addressing different unfolding mechanisms caused by GdmCl and urea using molecular dynamics simulation [30]. Urea was found to interact directly with protein in the denaturation process, and water surrounding the protein is pulled away. In contrast, GdmCl does not perturb the water solvation structure around the protein. Other recent NMR studies have addressed the hydrogen bonding properties of water in the confined space inside mesoporous silica ([28] and [31]) where water in SBA-15 is strongly adsorbed and the hydrogen bonds strengthened compared with water in bulk solution. These observations offer clues to the different effects of GdmCl and urea on the enzyme activity in the confined space. In contrast with urea in bulk solution, urea in the confined pore space cannot replace the water near the pore wall. This water segment is also part of the hydration shell of the enzyme. As a consequence, the residual activity of immobilized enzyme after urea addition is not affected as strongly as that of free enzyme. In contrast, GdmCl acts directly on the protein without perturbation of the water structure. The catalytic activity of immobilized enzyme therefore follows more closely the trend of the free enzyme.

References

[1] N. C. Veitch, Horseradish Peroxidase: A Modern View of a Classic Enzyme. *Phytochemistry*. 65:249-259, 2004.

[2] M. Gajhede, Horseradish Peroxidase. In *Handbook of Metalloproteins,* Online. John Wiley & Sons, Ltd., 2006.

[3] Sigma-Aldrich. http://www.sigmaaldrich.com/catalog/ProductDetail.do?N4=P8250|SIGMA&N5=SEARCH_CONCAT_PNO|BRAND_KEY&F=SPEC&lang=en_US. Web page, July 17th 2011.

[4] E. Wang, H. Wang, and Z. Li, Protein Structural Characterization by Scanning Tunneling Microscopy with Electrochemistry. *Anal. Sci.*, 16:205-209, 2000.

[5] G. I. Berglund, G. H. Carlsson, A. T. Smith, H. Szöke, A. Henriksen and J. Hajdu. The Catalytic Pathway of Horseradish Peroxidase at High Resolution. *Nature*, 417:463-468, 2002.

[6] H. Takahashi, B. Li, T. Sasaki, C. Miyazaki, T. Kajino, and S. Inagaki. Catalytic Activity in Organic Solvents and Stability of Immobilized Enzymes Depend on the Pore Size and Surface Characteristics of Mesoporous Silica. *Chem. Mater.*, 12:3301–3305, 2000.

[7] W. Chouyyok, J. Panpranot, C. Thanachayanant, and S. Prichanont. Effects of pH and Pore Characters of Mesoporous Silicas on Horseradish Peroxidase Immobilization. *J. Mol. Catal. B: Enzym.*, 56, 246-252, 2009.

[8] L. Chenghong, S. Yongsoon, K. M. Jon, F. Glen, L. L. Linda, C. E. Douglas, L. Jun, and E. J. Ackerman. Characterization of Functionalized Nanoporous Supports for Protein Confinement. *Nanotechnology*, 17**:**5531–5538, 2006.

[9] J. A. Nicell and H. Wright. A model of Peroxidase Activity with Inhibition by Hydrogen Peroxide. *Enzyme Microb. Technol.*, 21:302–310, 1997.

[10] I. D. Buchanan, and J. Nicell. Model Development for Horseradish Peroxidase Catalyzed Removal of Aqueous Phenol. *Biotechnol. Bioeng.*, 54:251-261, 1997.

[11] P. F. Fulvio, S. Pikus and M. Jaroniec, Tailoring Properties of SBA-15 Materials by Controlling Conditions of Hydrothermal Synthesis. *J. Mater. Chem.*, 15:5049–5053, 2005.

[12] M. Piras, A. Salis, M. Piludu, D. Sterib and M. Monduzzi. 3D vision of Human Lysozyme Adsorbed onto a SBA-15 Nanostructured Matrix. *Chem. Commun.*, 47:7338–7340, 2011.

[13] D. Rotticci, T. Norin, K. Hult, and M. Martinelle. An Active-Site Titration Method for Lipases. Biochim. Biophys. Acta, 1483:132-140, 2000.

[14] A. C. Patel, S. Li, J. Yuan, and Y. Wei. In situ Encapsulation of Horseradish Peroxidase in Electrospun Porous Silica Fibers for Potential Biosensor Applications. *Nano Lett.*, 6:1042–1046, 2006.

[15] H. Jaladi, A. Katiyar, S. W. Thiel, V. V. Guliants, and N. G. Pinto. Effect of Pore Diffusional Resistance on Biocatalytic Activity of *Burkholderia Cepacia*. *Chem. Eng. Sci.*, 64:1474-1479, 2009.

[16] R. Biswas and S. K. Pal. Caging Enzyme Function: α-Chymotrypsin in Reverse Micelle. *Chem. Phys. Lett.*, 387:221–226, 2004.

[17] R. Sarkar, M. Ghosh, A. K. Shaw, and S. K. Pal. Ultrafast Surface Solvation Dynamics and Functionality of an Enzyme α-Chymotrypsin upon Interfacial Binding to a Cationic Micelle. *J. Photochem. Photobiol., B.*, 79:67–78, 2005.

[18] P. Majumder, R. Sarkar, A. K. Shaw, A. Chakraborty, and S. K. Pal. Ultrafast Dynamics in a Nanocage of Enzymes: Solvation and Fluorescence Resonance Energy Transfer in Reverse Micelles**.** *J. Colloid Interface Sci.***,** 290**:**462**-**474**,** 2005**.**

[19] R. Sarkar, A. K. Shaw, S. S. Narayanan, F. Dias, A. Monkman, and S. K. Pal. Direct Observation of Protein Folding in Nanoenvironments Using a Molecular Ruler**.** *Biophys. Chem.***,** 123**:**40–48**,** 2006**.**

[20] A. K. Shaw and S. K. Pal. Activity of Subtilisin Carlsberg in Macromolecular Crowding. *J. Photochem. Photobiol., B*., 86:199–206, 2007.

[21] A. K. Shaw, R. Sarkar, D. Banerjee, S. Hintschich, A. Monkman, and S. K. Pal. Direct Observation of Protein Residue Solvation Dynamics. *J. Photochem. Photobiol. A*., 185:76–85, 2007.

[22] D. D. L. Minh, C. Chang, J. Trylska, V. Tozzini, and J. A. McCammon. The Influence of Macromolecular Crowding on HIV-1 Protease Internal Dynamics. *J. Am. Chem. Soc.*, 128:6006–6007, 2006.

[23] B. Menaa, Y. Miyagawa, M. Takahashi, M. Herrero, V. Rives, F. Menaa, and D. K. Eggers. Bioencapsulation of Apomyoglobin in Nanoporous Organosilica Sol-Gel Glasses: Influence of the Siloxane Network on the Conformation and Stability of a Model Protein. *Biopolymers*, 91:895–906, 2009.

[24] D. E. B. Gomes, R. D. Lins, P. G. Pascutti, C. Lei, and T. A. Soares. The Role of Nonbonded Interactions in the Conformational Dynamics of Organophosphorous

Hydrolase Adsorbed onto Functionalized Mesoporous Silica Surfaces. *J. Phys. Chem. B*, 114:531–540, 2010.

[25] R. J. Ellis. Macromolecular Crowding: Obvious but Underappreciated. *Trends Biochem. Sci.*, 26:597–604, 2001.

[26] H. Frauenfelder, P. W. Fenimore, and B. H. McMahon. Hydration, Slaving and Protein Function. *Biophys. Chem.*, 98:35–48, 2002.

[27] R. Ravindra, S. Zhao, H. Gies, and R. Winter. Protein Encapsulation in Mesoporous Silicate: The Effects of Confinement on Protein Stability, Hydration, and Volumetric Properties. *J. Am. Chem. Soc.*, 126:12224-12225, 2004.

[28] G. Buntkowsky, H. Breitzke, A. Adamczyk, F. Roelofs, T. Emmler, E. Gedat, B. Gru¨nberg, Y. Xu, H. Limbach, I. Shenderovich, A. Vyalikh, and G. Findenegg. Structural and Dynamical Properties of Guest Molecules Confined in Mesoporous Silica Materials Revealed by NMR. *Phys. Chem. Chem. Phys.*, 9:4843–4853, 2007.

[29] J. L. England and G. Haran. Role of Solvation Effects in Protein Denaturation: From Thermodynamics to Single Molecules and Back. *Annu. Rev. Phys. Chem*. 62:257–77, 2011.

[30] C. Camilloni, A. Guerini Rocco, I. Eberini, E. Gianazza, R. A. Broglia, and G. Tiana. Urea and Guanidinium Chloride Denature Protein L in Different Ways in Molecular Dynamics Simulations. *Biophys. J.*, 94:4654–4661, 2008.

[31] B. Grünberg, T. Emmler, E. Gedat, I. Shenderovich, G. H. Findenegg, H. Limbach, and G. Buntkowsky. Hydrogen Bonding of Water Confined in Mesoporous Silica MCM-41 and SBA-15 Studied by 1H Solid-State NMR. *Chem.-Eur. J.*, 10:5689-5696, 2004.

8. Catalytic activity of galactose oxidase immobilized on SBA-15 mesoporous silica

In this chapter, galactose oxidase from *Dactylium dendroides* was immobilized on mesoporous silica, SBA-15 with different pore sizes. Galactose oxidase is a metalloenzyme which has been extensively studied since 1950s [1]. Galactose oxidase can be used for the determination of galactose or lactose concentrations in complex biological fluids. Galactose activity measurements are of interest in the preliminary diagnosis of galactosemia and galactose intolerance [2]. For analytical applications, galactose oxidase has been immobilized on different supports including macroporous silica support [3-5]. However, there are no reports on the immobilization of galactose oxidase on porous silica with mesopore size (8 to 30 nm).

8.1 Introduction to galactose oxidase

Galactose oxidase (GAOX) is a free radical metalloenzyme and catalyzes two-electron oxidation of a primary alcohol to aldehyde concomitant with two-electron reduction of dioxygen to hydrogen peroxide [6]. The enzymatic reaction can be written as:

$$RCH_2OH + O_2 \rightarrow RCHO + H_2O_2 \qquad (8.1)$$

Figure 8.1 shows the active site region of galactose oxidase. Copper is coordinated to two tyrosines (Tyr272 and Tyr495), two histidines (H496 and H581) and a water molecule. Tyr272, Tyr495, His496, His581, and solvent constitute the inner coordination sphere. The sulfur of Cys 228 forms a bond with Tyr 272 (thioether bond). A Tyr 272 radical, $Tyr^{\bullet}272$ serves as the second redox site. Trp290 stacks over the sulphur of Cys 228. The second-coordination sphere residue Trp290 has an important role in the generation and reactivity of the tyrosyl radical $Tyr^{\bullet}272$, and therefore in the catalysis [7].

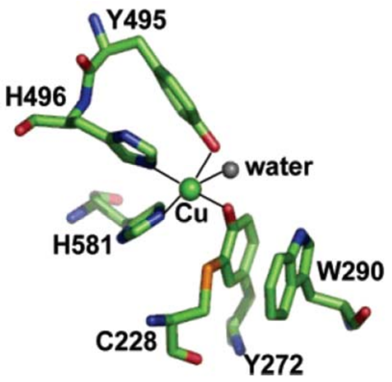

Figure 8.1: The active site region of galactose oxidase at pH 7.0. The solid lines represent the ligand bonds to the copper (green sphere). Copper is coordinated to a tyrosyl radical (Tyr•272), two histidines (H496 and H581), a tyrosine (Tyr495), and a water molecule. C228–Y272 thioether bond and the so-called "stacking tryptophan", Trp290 are also shown. From Rogers et al [7].

The oxidation state of galactose oxidase takes three forms (Fig. 8.2). The fully oxidized form (Fig. 8.2A) is the active form of the enzyme. The oxidized form is stable in the absence of reducing agents [6], but reacts readily with electron donors and is reduced to a non-radical inactive form (Fig. 8.2B). This form is also called semi-reduced form. Further reduction leads to the fully reduced form (Fig. 8.2C). In most enzyme samples, GAOX is a mixture of the active and inactive forms. Activation of the enzyme can be achieved by one-electron oxidants such as $K_3[Fe(CN)_6]$ which facilitates the removal of one electron, generating a tyrosyl radical ($Tyr^{\bullet}272$) [8].

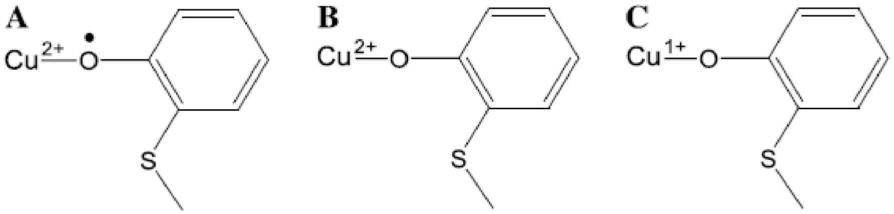

Figure 8.2: The three oxidation states of galactose oxidase. From ref. [6].

The enzymatic reaction (eq. 8.1) can be divided into two-half reactions. The following mechanism is proposed (Fig. 8.3). In the first-half reaction (Fig. 8.3 (A)), the bound substrate (RCH_2OH) is first deprotonated and then oxidized by proton-coupled electron transfer (PCET) to copper, generating the enzyme in fully reduced form (Fig. 8.2C). In the second half reaction (Fig. 8.3 (B)), electron transfer from Cu(I) to dioxygen *first* forms superoxide. The superoxide species *then* accepts a proton to generate hydroperoxide and Tyr$^{\bullet}$272. *Finally*, a proton is transferred to metal-bound hydroperoxide and the oxidized enzyme (Fig. 8.2A) is regenerated to complete a reaction cycle.

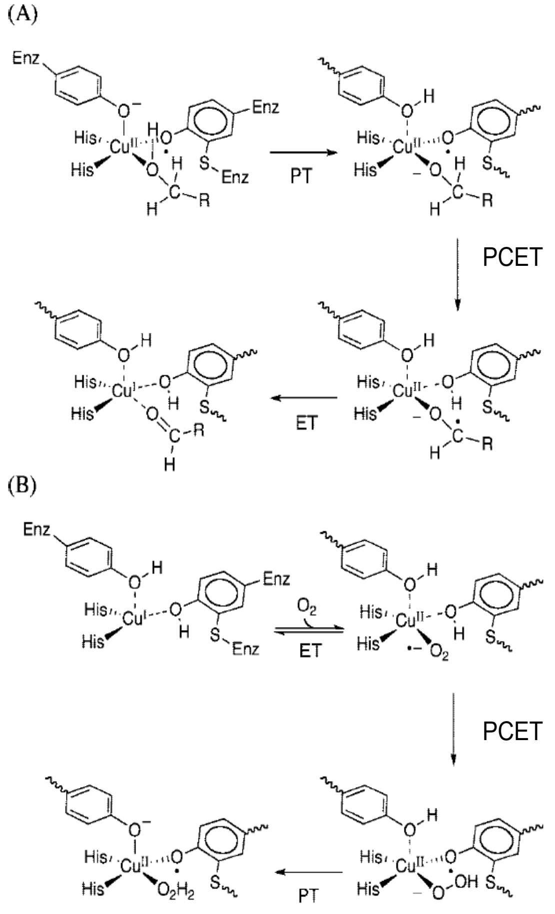

Figure 8.3: Working mechanism for galactose oxidase. (A) The reductive half-reaction involves three steps: i) PT: Proton transfer from substrate, RCH_2OH, to an active site base, Tyr495; ii) PCET: to the radical center,; and iii) ET: Electron transfer to Cu(II). (B) The oxidative half reaction also involves three steps: i) electron transfer from Cu(I) to coordinated oxygen, giving metal bound superoxide; ii) Hydrogen atom transfer (HAT) or PCET: The metal bound superoxide abstracts a hydrogen atom from the hydroxyl group of the Tyr272, producing hydroperoxide and Tyr•272; and iii) A proton is transferred from Tyr495 to the metal bound hydroperoxide, producing hydrogen peroxide and reoxidized enzyme. From Humphreys [9].

The three-dimensional GAOX (PDB: 1GOG) size is 8.4 nm x 6.2 nm x 6.4 nm (as determined using Pymol). The isoelectric point (pI) is 12 [10]. Fig 8.4 shows the electrostatic surface potential distribution of galactose oxidase at pH 7.0.

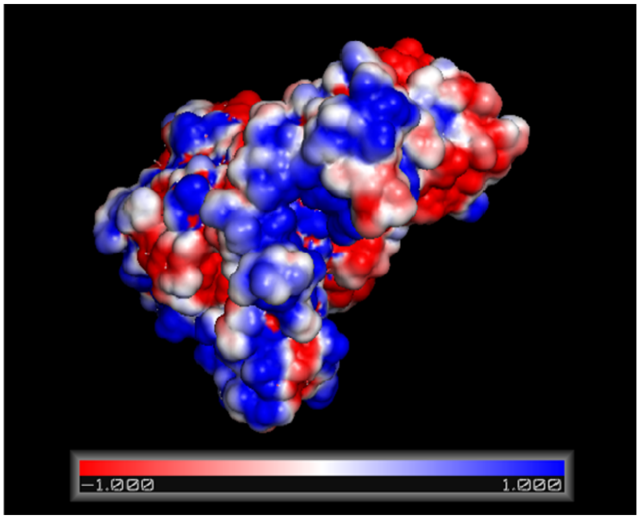

Figure 8.4: Electrostatic potential of galactose oxidase from *Dactylium dendroides* (PDB: 1GOG) at pH 7.0. Positive surface charge is shown in blue and negative surface charge in red. Electrostatic calculations were carried out using Adaptive Poisson-Boltzmann Solver (APBS) after conversion of the PDB file to the PQR file through PDB2PQR Server [11] and visualized with Pymol.

Kondakova et al [5] used macroporous silica with a specific surface area of 80 m^2/g and a total volume of 1.2 cm^3/g and a pore size of 40 to 60 nm (based on other literature [12]) to immobilize GAOX and studied the applicability of the immobilized GAOX for analytical determination of galactose-containing carbohydrate (raffinose). GAOX was immobilized on the silica support by physical adsorption or covalent attachment, but the authors did not address if there was leaching of the enzyme immobilized by physical adsorption. Galactose oxidase was chosen for the present study. Immobilization of galactose oxidase on mesoporous silica has not been explored so far. The mesopore size may allow applications of galactose oxidase which cannot be achieved with macroporous silica. For example, the pore size comparable to the size of the enzyme or the curvature of the pore may change the substrate specificity of the enzyme, which may lead to new applications of galactose oxidase. Two mesoporous silicas were used in the present study and GAOX was immobilized by physical adsorption. Leaching of enzyme was tested and enzyme activity between free and immobilized enzyme compared. In addition, thermal stability between free and immobilized enzyme was compared. Based on the results of the leaching tests, enzyme immobilization by covalent attachment was also studied.

8. 2 Experimental Section

8.2.1 Chemicals

Galactose Oxidase from *Dactylium dendroides* (EC number: 1.1.3.9, lyophilized powder, ≥ 3,000 units/g solid, Sigma-Aldrich), tetraethyl orthosilicate (98%(GC), Aldrich), poly(ethylene glycol)-*block*-poly(propylene glycol)-*block*-poly(ethylene glycol) (Pluronic® P-123, Sigma-Aldrich), D-(+)-Galactose (≥99%, Sigma-Aldrich), and cyanuric chloride (99%, Sigma-Aldrich) were used as received. Milli-Q water (18.2 MΩ cm) was used throughout.

8.2.2 Experimental details

Synthesis and characterization of silica particles. SBA-15 particles were synthesized as follows: 4.0 g Pluronic P123 was added to 144 mL 1.7 M HCl solution and the solution was stirred for 4 hours at 40 °C. 8.0 g TEOS was then added dropwise (the mass ratio of TEOS/P123 = 2) and the mixture was stirred for another 2 hours. The resultant gel was kept at 100°C for 48 hours under static condition. The experiments for systematic characterization by X-ray diffractometry, TEM, and nitrogen adsorption/desorption were performed similarly as for rod-shaped SBA-15 (Section 6.1.). The pore size distribution was determined from the adsorption branch of the nitrogen adsorption isotherm using the BJH method with the statistical film thickness curve for macroporous silica [13]. SEM images were obtained on an Inspect S at CEN of DTU. Silica particles for SEM observation were coated with gold by sputtering. The synthesis procedure and characterization for SBA-15-TMB are described in Section 6.2.

Oxidation of galactose oxidase. As noted, GAOX takes three forms. In order to obtain a homogeneous sample of active enzyme, before use galactose oxidase was oxidized with 50 mM $K_3[Fe(CN)_6]$ and purified with on a Econo-Pac 10DG column (Bio-Rad), eluted with sodium acetate buffer (pH 4.5).

Immobilization of enzyme. 1 mL of oxidized galactose oxidase in sodium acetate buffer pH 4.5 was added to the pre-determined amount of silica particles in an eppendorf tube and stirred for 3h. The mixture was centrifuged and the particles washed and re-suspended in sodium acetate buffer (pH 4.5). The adsorbed amount was determined from the absorbance using an extinction coefficient of 1.05×10^5 M^{-1} cm^{-1} for the enzyme [9]. Covalent attachment of galactose oxidase to SBA-15-TMB was accomplished through surface amino groups of galactose oxidase on the amino-functionalized SBA-15-TMB using cyanuric chloride (CC) linker. The covalent attachment of enzyme onto amino-functionalized silica walls using cyanuric chloride was illustrated in Fig. 2.3 in chapter 2 (step a and a', where "TsT" represents Trichloro-s-triazine; cyanuric chloride). Specifically, SBA-15-TMB was first functionalized with amino groups (detailed in Section 6.4.1). The aminated supports (50 mg) were then suspended in acetone (3.125 ml), to which cyanuric chloride (25 mg) was added. The mixture was stirred gently for 3 h at room temperature under nitrogen, then transferred to a centrifuge tube, and acetone removed by centrifugation. The activated supports were transferred to an eppendorf tube and washed well with acetone. 1 mL of enzyme was then added and stirred for 2 h at 4ºC. The mixture was centrifuged and the solid supports thoroughly washed with water and stored at 4ºC [5][14].

Enzyme activity measurements. Catalytic activity of galactose oxidase was measured using a Clark-type electrode (YSI 5300A Biological Oxygen Monitor). The experimental set-up is described in Section 5.2.2. The sample solution was stirred at 480 rpm. The electrode was calibrated in air-saturated (0.252 mM O_2) [15] distilled water. In each measurement, air bubbles were excluded before the start of the measurement. 50 µl of free or immobilized enzyme (stored on ice) was injected into a 3 ml reaction mixture of air-saturated 5-400 mM galactose and 1 mM $K_3[Fe(CN)_6]$ in buffer (pH 7.0) at 25 °C through the access slot using a syringe. As noted in section 8.1, galactose oxidase takes three forms. There is a possibility of interconversion between active (Fig. 8.2 A) and inactive form (Fig. 8.2 B) [6]. To avoid this, hexacyanoferrate (III) was included in the mixture to re-activate the inactivated enzyme during the activity assays.

Thermal stability. The thermal stability of GAOX immobilized on SBA-15 was examined by heating GAOX immobilized SBA-15 for 30 min at 50-70 °C. The solution was left to cool to room temperature, and the catalytic activity then determined. The free enzyme was treated similarly as a reference. The detailed procedure is similar to that for HRP described in chapter 7.

8.3 Results and Discussion

8.3.1 Synthesis and characterization of SBA-15

Two types of mesoporous silicas were used. One was SBA-15 synthesized by the conventional method (called SBA-15). The other one was SBA-15 synthesized using TMB (called SBA-15-TMB). SBA-15-TMB is described in detail in Section 6.2. Figure 8.5 shows XRD patterns of the samples used. Note that SBA-15 has a hexagonally ordered pore structure while SBA-15-TMB contains larger but disordered pores.

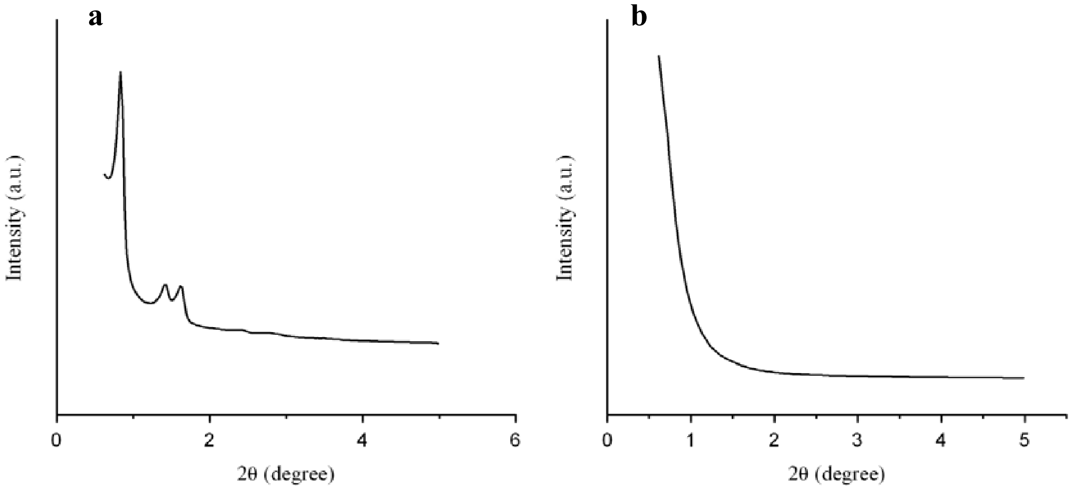

Figure 8.5: Powder XRD patterns of SBA-15 samples used for GAOX immobilization. (a) SBA-15 with a hexagonally ordered pore structure. The three peaks at 2θ = 0.84, 1.41, and 1.62° can be indexed as (100), (110), and (200) reflections associated with p6mm hexagonal symmetry. (b) SBA-15-TMB with disordered structures. There is no peak above 2θ = 0.6°. For details, see section 6.2.2.

Figure 8.6 shows SEM and TEM images of the samples used. The SBA-15 particles are agglomerated and have a width of 400 nm to 600 nm and a length of 700 nm to 1 μm. In the TEM image (Fig. 8.6 (b)), it is noted that ordered channels are running in parallel. Agglomerated structures are observed for SBA-15-TMB particles (Fig. 8.6 (c) and (d)), and the particles do not have a well defined morphology. SBA-15-TMB has a foam-like structure with large pores.

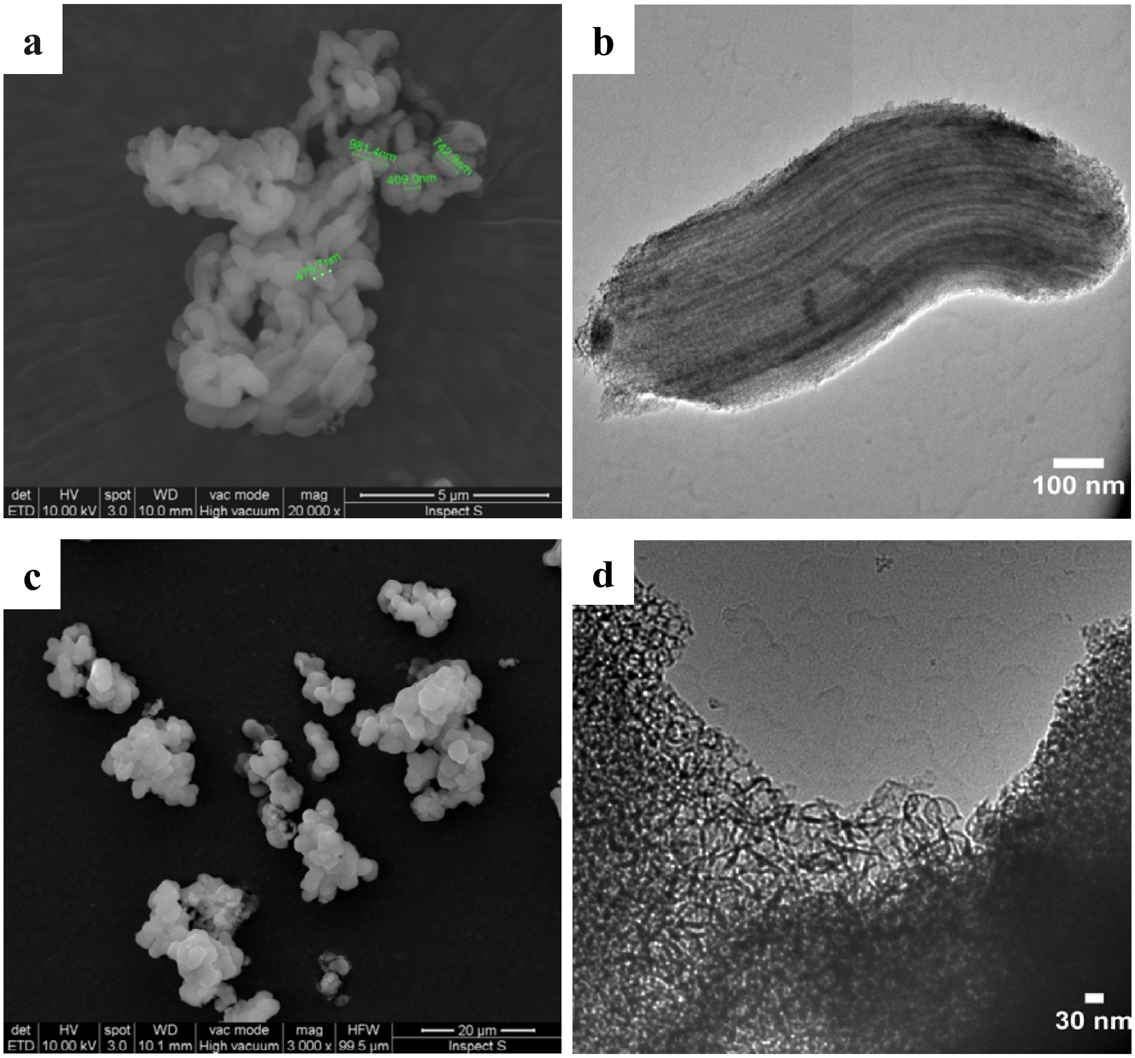

Figure 8.6: SEM and TEM micrographs of SBA-15 used for GAOX immobilization. (a) and (b) SBA-15, (c) and (d) SBA-15-TMB. The SEM image (a) reveals that the SBA-15 particles are aggregated. The TEM image (b) shows that ordered channels are running in parallel. (c) The SBA-15-TMB does not have a well-defined morphology. TEM image (d) shows that the SBA-15-TMB has a disordered foam-like structure with large pores. For details, see section 6.2.2. Scale bars: (a) 5 µm (b) 100 nm (c) 20 µm and (d) 100 nm.

From the XRD patterns, microscopic images and nitrogen adsorption measurements (Table 8.1), SBA-15 is found to be rod-shaped particles with hexagonally ordered pores. The pore size matches the dimensions of GAOX (8.4 nm x 6.2 nm x 6.4 nm). Based on the characterization and synthesis procedure, SBA-15-TMB has a foam-like structure consisting of large spherically disordered pores (cells) with a BJH pore diameter of 23 nm, interconnected by windows of a smaller opening of 8.8 nm, determined by the BJH method (For details, see section 6.3.2). It should be noted that the BJH method underestimates the pore size by around 20% compared to the more accurate BdB-FHH method [16] (section 6.2.2).

Table 8.1: Physical Characteristics of Silica Particles Used in This Study.

Sample	S_{BET} (m^2/g)	V_{tot} (cm^3/g)	D_p (nm)	D_w (nm)
SBA-15	840	1.26	9.5	-
SBA-15-TMB	810	2.12	23.1	8.8

S_{BET}: Total surface area, V_{tot}: Total pore volume, D_p: Pore diameter, determined by the BJH method from the adsorption branch, D_w: Window diameter, determined by the BJH method from the desorption branch of the nitrogen adsorption isotherm.

8.3.2 Immobilization of GAOX onto silica particles

Oxidized Galactose oxidase was adsorbed to SBA-15 and SBA-15-TMB silica particles. To check the enzyme stability under stirring conditions, the solution containing only free oxidized GAOX was stirred for 3 h. As shown in Fig. 8.7, oxidized GAOX was stable during immobilization.

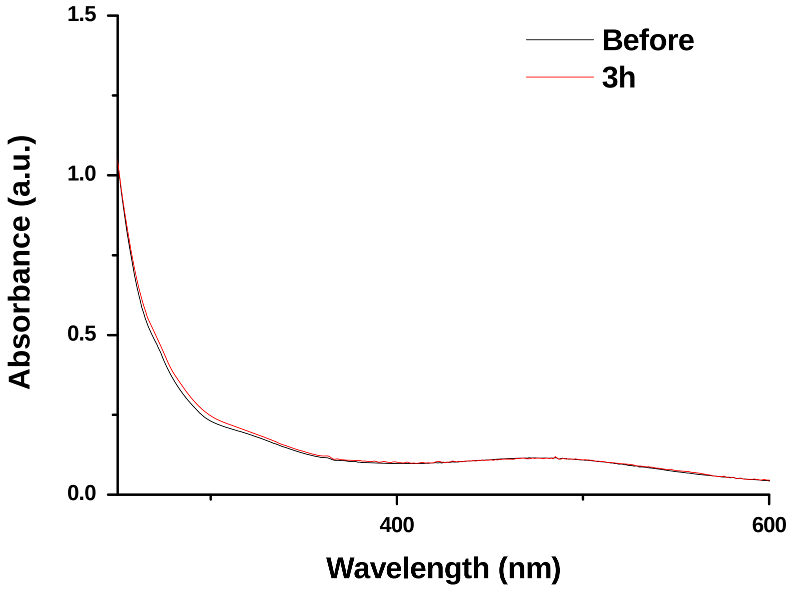

Figure 8.7: Absorption spectra of oxidized galactose oxidase before and after 3 hours of stirring.

The mixture of particles and GAOX solution was stirred for 3 hours. When the initial ratio of protein to particles of 125 µg protein per mg particles in the solutions was used, similar amounts of GAOX was found to be adsorbed onto both types of particles, i.e. about 62 µg protein per mg particles for SBA-15 and 58 µg protein per mg particles for SBA-15-TMB. However, if the initial ratio of protein to particles is higher (e.g., 250 µg protein/mg particles), the observations are somehow surprising. Almost no GAOX was adsorbed on the SBA-15 after 3 h stirring, while the estimated GAOX amount adsorbed onto SBA-15-TMB was about 89 µg protein per mg particles. It is difficult to explain this difference when the initial ratio is higher because protein adsorption is very complex, especially in adsorption to porous material. Possible causes are: (1) different pore structures of the two samples and (2) GAOX has a high pI of 12 as noted in section 8.1. The entrance of the pores are similar in size (9.5 nm for SBA-15 vs. 8.8 nm for SBA-15-TMB), but the pore structure is different (hexagonally ordered cylinder vs. cage-type pores). When the immobilization of GAOX to silica particles was performed using sodium acetate buffer (pH 4.5), GAOX must be positively charged. Lateral repulsion between protein molecules could be strong at pH 4.5. These two facts may be relevant to the observed difference.

It is very challenging to identify the exact location of immobilized enzyme, which could be either inside the pores or outside the particle surfaces or both. In previous studies, nitrogen adsorption measurements were used to support that the enzymes are indeed located inside the pores, because nitrogen adsorption was dramatically reduced after immobilization of the enzyme [17][18]. However, as described below this method is not completely reliable.

Figure 8.8 compares the nitrogen adsorption isotherms obtained for the particle samples before and after immobilization of enzyme. The surface area and pore volume of the SBA-15 particles are both decreased significantly, after the stirring of the particles even in the pure buffer solution (i.e. no enzyme) for 3 hours (Table 8.2). The presence of enzyme in the buffer solution causes a further decrease in both the surface area and volume (Table 8.2). The former is likely due to loss of the micropores in SBA-15 particles by stirring. This was evidenced also by a previous study that the microporosity of SBA-15 is largely lost after the material was stirred in deionized water at room temperature [19] The micropores are lost or smoothed due to the dissolution of the silica with a positive radius of curvature at the entrance of micropores and the subsequent redeposition of the solubilized silica inside the micropores. Thus, we offer the following suggestions to explain the present data shown in Fig. 8.8 and Table 8.2.

(a) The adsorbed amounts of nitrogen at the relative pressure (P/P_0) $\cong 0$ are different for the three samples. The difference between the samples before and after stirring of SBA-15 in pure buffer solution (i.e., SBA-15_before vs. SBA-15_buffer) is most likely attributed to the loss of micropores and/or the changes in the interactions between nitrogen molecules and the pores

(b) The difference in surface area and total pore volume between the samples treated with pure buffer and enzyme-containing buffer (SBA-15_buffer vs. SBA-15_GAOX) is relatively small. This may indicate that immobilized GAOX is located only outside the particle surfaces, but it should be noted that the amount of GAOX adsorbed (ca 45 µg protein per mg particles) was small. Such small enzyme amounts should therefore not cause significant further decrease in the surface area and total volume of the pores.

(c) Since the adsorbed protein also shares a portion (ca. 5 % by wt) of the total weight for the protein-SBA-15 conjugated samples, the exact amount of adsorbed nitrogen could not be precisely calculated. This makes it difficult to compare the values of the surface area and volume of the pores obtained for the pure particle samples and for the protein-SBA-15 conjugated samples.

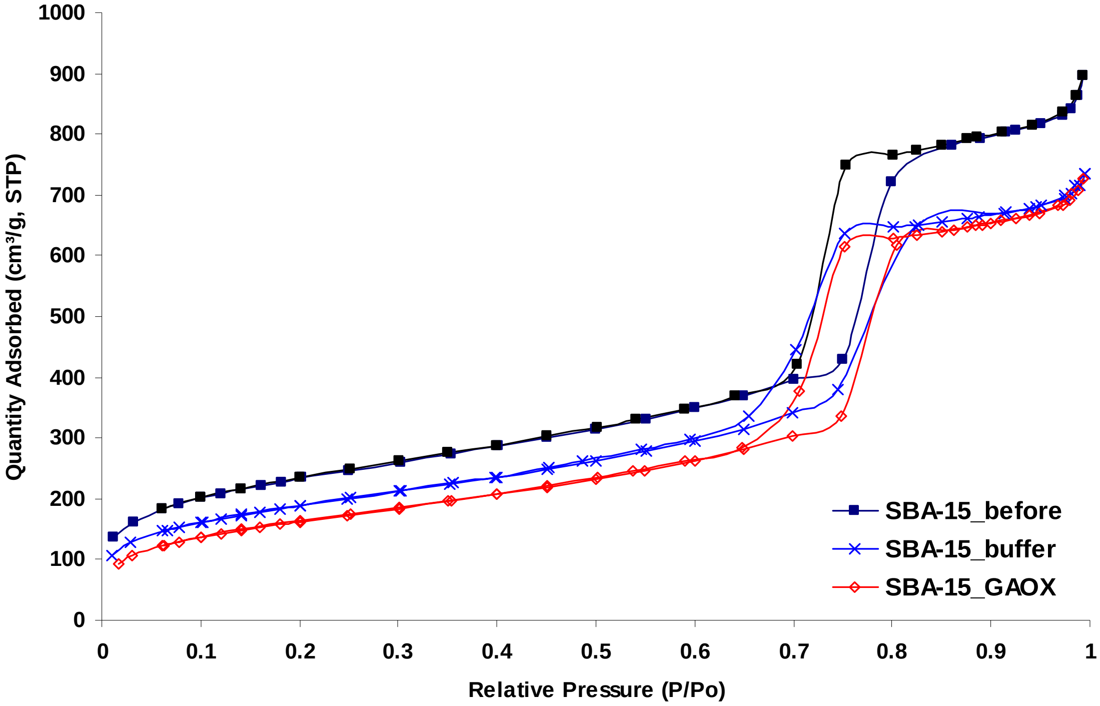

Figure 8.8: Nitrogen adsorption isotherms of SBA-15 before and after GAOX immobilization. SBA-15_before: SBA-15 before the immobilization (calcined SBA-15), SBA-15_buffer: sample after stirring SBA-15 alone in a buffer solution. SBA-15_GAOX: the conjugate of SBA-15 and GAOX. The samples of SBA-15_buffer and SBA-15_GAOX were degassed at 40 °C under vacuum for 12 hours before recording the isotherms.

Table 8.2: Comparison of Surface Area and Total Pore Volume of SBA-15 Samples before and after Stirring in a Buffer Solution or Immobilization with GAOX

Sample	S_{BET} (m^2/g)	V_{tot} (cm^3/g)
SBA-15	840	1.26
SBA-15-buffer	682	1.05
SBA-15-GAOX	592	1.03

S_{BET}: Total surface area, V_{tot}: Total pore volume

8.3.3 Catalytic activity of immobilized Galactose oxidase

(1) SBA-15-GAOX. Immobilization of enzyme via physical adsorption or ionic binding is relatively weak. As a consequence enzyme leaching could occur during activity measurements. To test possible enzyme leaching, the SBA-15-GAOX conjugate was stirred at 475 rpm at room temperature, i.e. similar experimental conditions to those used for the activity measurements. The results show that there is no detectable leaching. This is further supported by the fact that the supernatants obtained from the leaching test experiments show no enzyme activity.

As described in the experimental section, the catalytic activity of galactose oxidase was estimated by measuring dioxygen consumption. Figure 8.9 shows an example of the decrease of dioxygen concentration in solution over the time course.

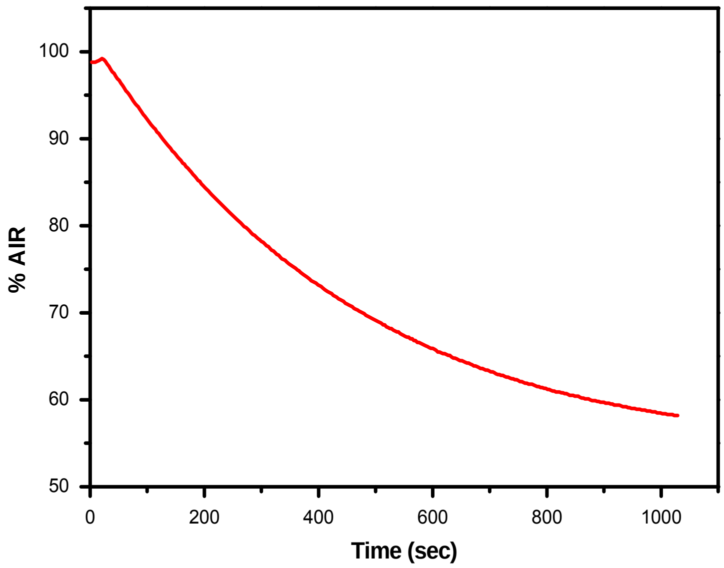

Figure 8.9: Dioxygen consumption by immobilized enzyme, SBA-15-GAOX. The 100 % AIR corresponds to the concentration of dissolved dioxygen in air-saturated distilled water.

To determine catalytic constants of free and immobilized enzyme, the initial reaction rate was obtained over a range of substrate concentrations. Figure 8.10 shows typical Michaelis-Menten plots for the free and immobilized enzyme samples. The solid lines show the theoretical fittings based on the Michaelis-Menten equation (eq.3.11), from which the apparent Michaelis constant (K_M) and apparent turnover number (k_{cat}) are obtained and summarized in Table 8.3. As described in Section 3.2, k_{cat}/K_m is a measure of the catalytic efficiency. After the immobilization, this enzyme retains ca. 70 % catalytic efficiency.

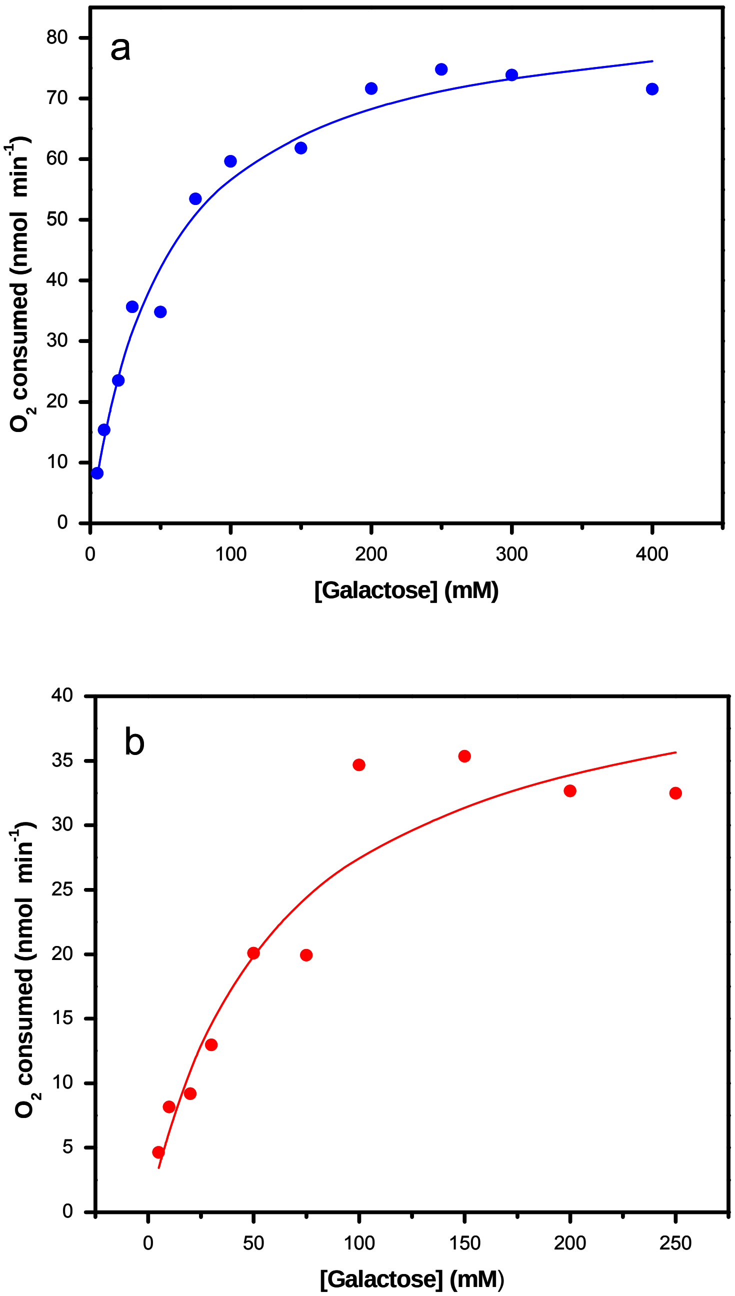

Figure 8.10: Plots of initial velocity versus galactose substrate concentration for (a) free and (b) immobilized GAOX. Free or immobilized enzyme was mixed with solutions containing galactose in different concentrations and 1 mM $K_3[Fe(CN)_6]$ in 100 mM Phosphate Buffer (pH 7.0). Fitting (solid line) was obtained using the Michaelis-Menten rate constant form. The amounts of free and immobilized GAOX used were 0.18 nmol and 0.11 nmol, respectively.

Table 8.3: A Comparison of K_M, k_{cat}, and k_{cat}/K_m of Free and Immobilized GAOX at 25 ºC.

GAOX status	K_M (mM)	k_{cat} (s^{-1})	k_{cat}/K_M
Free	50	7.9	0.16
Immobilized	59	6.7	0.11

(2) SBA-15-TMB-GAOX. In contrast to SBA-15-GAOX, significant enzyme leaching during catalysis was observed for SBA-15-TMB-GAOX. The catalytic activity of the supernatants from the leaching test experiments could reach up to 63 % of that for the immobilized enzyme before the leaching test.

To prevent the enzyme leaching, immobilization was improved by covalent attachment of enzyme onto the silica particles. The covalently immobilized GAOX retains catalytic activity (Fig. 8.11). However, the precise amount of GAOX in SBA-15-TMB could not be obtained due to the overlapping absorbance of the cyanuric chloride with the enzyme. The supernatants obtained from the leaching test experiments had no enzyme activity (data not shown), indicating that leaching was prevented.

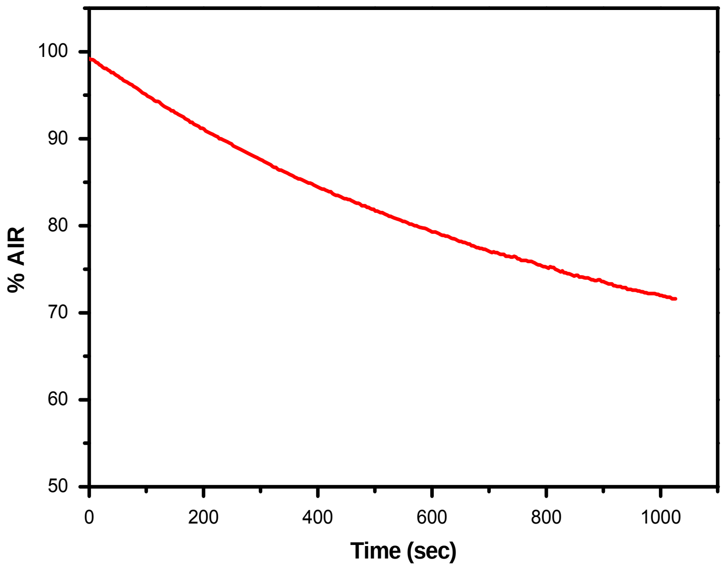

Figure 8.11: Oxygen consumption by the enzyme covalently attached to SBA-15-TMB. The 100 % AIR corresponds to the concentration of dissolved oxygen in air-saturated distilled water.

8.3.4 Thermal Stability

The thermal stability of oxidized GAOX immobilized on SBA-15 (SBA-15-GAOX) was examined by heating the solution of SBA-15-GAOX for 30 min at 50-70 °C. The solution was left for cooling to room temperature and the catalytic activity then determined at 25°C. The free enzyme was treated similarly. This follows the procedure used for the thermal stability test of HRP.

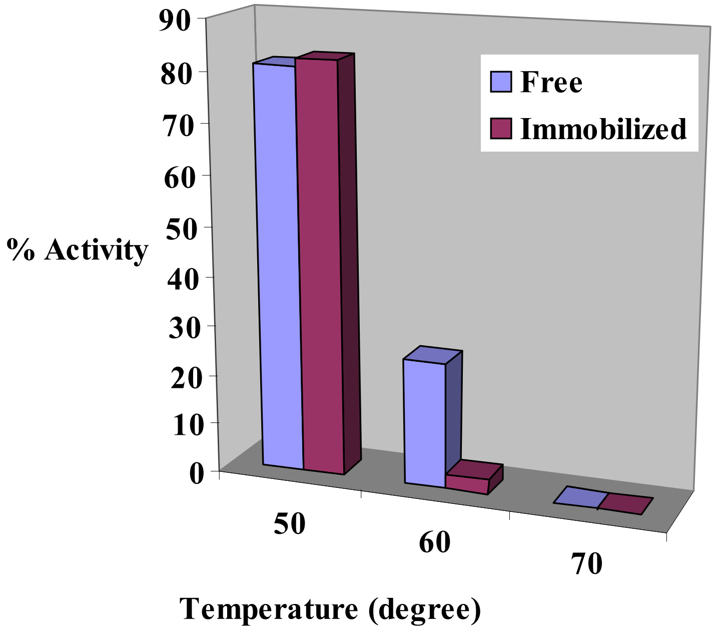

Figure 8.12: Comparison of the catalytic activity between free GAOX and immobilized GAOX (SBA-15-GAOX) after subjection to heat treatment at 50-70 °C. The initial velocity at 25°C before the heat treatment is defined as 100% activity.

Figure 8.12 shows the results. Both free and immobilized enzyme lost activity completely after subjection to heating at 70 °C for 30 min. For the heat treatment at 60 °C, the activity of immobilized enzyme decreased even more significantly than that for the free enzyme. It is known that the transition temperature for thermal inactivation of intracellular galactose oxidase is around 60 °C [20]. The intracellular form of this enzyme is more stable than its extracellular form, because the former contains more carbohydrate. GAOX used in the present study is in the extracellular form. HRP has shown more thermally resistant in its immobilization state (see Chapter 7), but this is not the case for GAOX.

There are many reports in which some enzymes immobilized on mesoporous silica are found to be more thermally resistant than the free enzymes in solution [21][22][23]. However, a few reports also show that immobilization of chloroperoxidase on mesoporous silica did not enhance its thermal stability [24]. Another example reported by

Hisamatsu *et al*. [17] is more complicated. α-Amylase immobilized onto SBA-15 did not show enhanced thermal resistance, but thermal stability of this enzyme is significantly improved when it was immobilized onto folded-sheet mesoporous silica (FSM). The exact reasons are not clear, but the authors attributed the different thermal resistance observed to the difference in hydrophilicity of various mesoporous materials. Covalent attachment could be one of the effective means to reduce unfolding of the enzyme in the immobilized state by reducing conformational flexibility and thermal vibrations [25]. It would thus be interesting if covalently immobilized GAOX in SBA-15-TMB is more thermally resistant. Unfortunately, these experiments could not been attempted due to limited time of the PhD study. This issue will be in focus in future work.

References

[1] J. A. D. Cooper, W. Smith, M. Bacila and H. Medina. Galactose Oxidase from *Polyporus circinatus. J. Biol. Chem.* 234:445, 1959.

[2] E. Çevik, M. Şenel and M. F. Abasıyanık. Construction of Biosensor for Determination of Galactose with Galactose Oxidase Immobilized on Polymeric Mediator Contains Ferrocene. *Current Applied Physics*. 10:1313-1316, 2010.

[3] S. K. Sharma, Suman, C.S. Pundir, N. Sehgal, and A. Kumar. Galactose Sensor Based on Galactose Oxidase Immobilized in Polyvinyl Formal. *Sens. Actuators, B*, 119:15–19, 2006.

[4] Z. Bílková, M. Slováková, A. Lyčka, D. Horák, J. Lenfeld, J. Turková and J. Churá cˇek. Oriented Immobilization of Galactose Oxidase to Bead and Magnetic Bead Cellulose and Poly(HEMA-co-EDMA) and Magnetic Poly(HEMA-co-EDMA) Microspheres. *J. Chromatogr. B*, 770:25–34, 2002.

[5] L. Kondakova, V. Yanishpolskii, V. Tertykh, and T. Buglova. Galactose Oxidase Immobilized on Silica in an Analytical Determination of Galactose-containing Carbohydrates. *Anal.*, 23:97-101, 2007.

[6] J. W. Whittaker. The Radical Chemistry of Galactose Oxidase. *Arch. Biochem. Biophys.* 433:227–239, 2005.

[7] M. S. Rogers, E. M. Tyler, N. Akyumani, C. R. Kurtis, R. K. Spooner, S. E. Deacon, S. Tamber, S. J. Firbank, K. Mahmoud, P. F. Knowles, S. E. V. Phillips, M. J. McPherson, and D. M. Dooley. The Stacking Tryptophan of Galactose Oxidase: A Second-Coordination Sphere Residue that Has Profound Effects on Tyrosyl Radical Behavior and Enzyme Catalysis. *Biochemistry*. 46:4606-4618, 2007.

[8] M. J. McPherson, M. R. Parsons, R. K. Spooner, and C. M. Wilmot, Galactose Oxidase. In *Handbook of Metalloproteins,* Online. John Wiley & Sons, Ltd., 2006.

[9] K. J. Humphreys, L. M. Mirica, Yi. Wang, and J. P. Klinman. Galactose Oxidase as a Model for Reactivity at a Copper Superoxide Center. *J. Am. Chem. Soc*. 131:4657–4663, 2009.

[10] W. J. Sung and Y. H. Bae. Glucose Oxidase, Lactate Oxidase, and Galactose Oxidase Enzyme Electrode Based on Polypyrrole with Polyanion/PEG/Enzyme Conjugate Dopant. *Sens. Actuators, B*, 114:164–169, 2006.

[11] T. J. Dolinsky, J.E. Nielsen, J.A. McCammon, and N.A. Baker. PDB2PQR: An Automated Pipeline for the Setup, Execution, and Analysis of Poisson-Boltzmann Electrostatics Calculations. *Nucleic Acids Res.*, 32:W665-W667, 2004.

[12] O. V. Lomako, I. I. Menyailova, L. A. Nakhapetia, L. I. Kozlovska, and N. A. Rodioxova. Immobilization of β-Glucosidase on an Inorganic Carrier. *Acta Biotechnol.*, 2:179-185, 1982.

[13] M. Jaroniec, M. Kruk, and J. P. Olivier. Standard Nitrogen Adsorption Data for Characterization of Nanoporous Silicas. *Langmuir*. 15:5410-5413, 1999.

[14] K. M. R. Kallury, W. E. Lee, and M. Thompson. Enhanced Stability of Urease Immobilized onto Phospholipid Covalently Bound to Silica, Tungsten, and Fluoropolymer Surfaces. *Anal. Chem.* 65:249-2487, 1995.

[15] C. D. Borman, C. G. Saysell, and A. G. Sykes. Kinetic Studies on the Reactions of Fusarium Galactose Oxidase with Five Different Substrates in the Presence of Dioxygen. *JBIC*, 2:480–487, 1997.

[16] W. W. Lukens, P. Schmidt-Winkel, D. Y. Zhao, J. Feng and G. D. Stucky. Evaluating Pore Sizes in Mesoporous Materials: A Simplified Standard Adsorption Method and a Simplified Broekhoff−de Boer Method. *Langmuir*, 15:5403, 1999.

[17] K. Hisamatsu, T. Shiomi, S. Matsuura, T. Y. Nara, T. Tsunoda, F. Mizukami, and K. Sakaguchi. a-Amylase Immobilization Capacities of Mesoporous Silicas with Different Morphologies and Surface Properties. *J Porous Mater*. Published online: 29 January 2011.

[18] E. Webera, D. Sirima, T. Schreiberb, B. Thomasb, J. Pleiss, M. Hungerb, R. Glaserc, and V. B. Urlacher. Immobilization of P450 BM-3 Monooxygenase on Mesoporous Molecular Sieves with Different Pore Diameters. *J. Mol. Catal. B: Enzym.*, 64: 29–37, 2010.

[19] A. Galarneau, M. Nader, F. Guenneau, F. D. Renzo, and A. Gedeon. Understanding the Stability in Water of Mesoporous SBA-15 and MCM-41. *J. Phys. Chem. C*, 111: 8268–8277, 2007.

[20] M. H. Mendonca and G. T. Zancan. Role of Carbohydrate Content on the Properties of Galactose Oxidase from *Dactylium dendroid*. *Arch. Biochem. Biophys.*, 266: 427-434, 1988.

[21] Y. Urabe, T. Shiomi, T. Itoh, A. Kawai, T. Tsunoda, F. Mizukami, and K. Sakaguchi. Encapsulation of Hemoglobin in Mesoporous Silica (FSM)—Enhanced Thermal Stability and Resistance to Denaturants. *Chem Bio Chem*, 8:668, 2007.

[22] C.H. Lee, J. Lang, C.W. Yen, P.C. Shih, T.S. Lin, and C.Y. Mou, Enhancing Stability and Oxidation Activity of Cytochrome *c* by Immobilization in the Nanochannels of Mesoporous Aluminosilicates. *J. Phys. Chem.* B, 109: 12277-12286, 2005.

[23] E. Terrés, M. Montiel, S. Le Borgne and E. Torres. Immobilization of Chloroperoxidase on Mesoporous Materials for the Oxidation of 4,6-Dimethyldibenzothiophene, a Recalcitrant Organic Sulfur Compound Present in Petroleum Fractions. *Biotechnol Lett*. 30:173-9, 2008.

[24] Y-J. Han, J. T. Watson, G. D. Stucky, and A. Butler. Catalytic Activity of Mesoporous Silicate-Immobilized Chloroperoxidase. *J. Mol. Catal. B: Enzym.*, 17:1–8, 2002.

[25] U. Hanefeld, L. Gardossib and E. Magner. Understanding Enzyme Immobilisation. *Chem. Soc. Rev.*, 38:453–468, 2009.

9. Photophysical properties of light harvesting complex 2 confined in SBA-15

In Chapters 7 and 8, we have focused on the catalytic activity and stability of two enzymes HRP and galactose oxidase immobilized onto the mesoporous silica, SBA-15. In this chapter, the focus is on photophysical properties of a photosynthetic membrane protein complex (i.e., the light harvesting complex 2 (LH2)) confined in mesoporous silica. In nature, light-harvesting complexes are embedded in lipid membranes and closely packed [1]. One of the structural features of mesoporous silica such as MCM-41 and SBA-15 is that the materials contain structurally ordered pores. This feature could allow molecules to be assembled in the pores in ordered and dense-packing fashion. To some extent, confinement of LH2 in a nanoscale environment offered by mesoporous host materials could therefore mimic local environments in the cell membranes.

Most membrane proteins are “more hydrophobic” and tend to aggregate in aqueous solution, and LH2 is one of such proteins. To prevent membrane proteins from molecular aggregation, detergents are often used for preparation of homogenous protein solutions. However, the presence of detergent could complicate the characterization of membrane proteins confined in mesoporous silica.

The work presented in this chapter was carried out mainly at Department of Chemical Physics, Lund University. Fluorescence spectroscopy and microscopy serve as major tools for the characterization of LH2 complex located in mesoporous silica. Both steady-state and time-resolved fluorescence spectroscopic measurements were performed. The steady-state fluorescence spectroscopic measurements were carried out under controlled temperatures ranging from room temperature to liquid-nitrogen temperature.

9.1 Light harvesting complex 2

Photosynthesis is associated with many complicated processes. The primary reactions occur at the photosynthetic center where solar energy is converted into chemical energy. The reaction center (RC) receives light from the sun in a flux of only one photon per second [2]. Light harvesting complexes are needed to gather and transfer solar energy to the reaction center. The light harvesting complexes and reaction center are both embedded in the lipid membrane, and the light harvesting complexes are arranged in a way to surround the reaction center (Fig. 9.1). The light harvesting complexes LH1 and LH2 thus gather light and serve as antennae. The excitation energy is transferred to the reaction center, where chemical charge separation is initiated. The proton gradient across the membrane drives the synthesis of ATP from ADP by ATPase, and chemical energy can be stored in the ATP form.

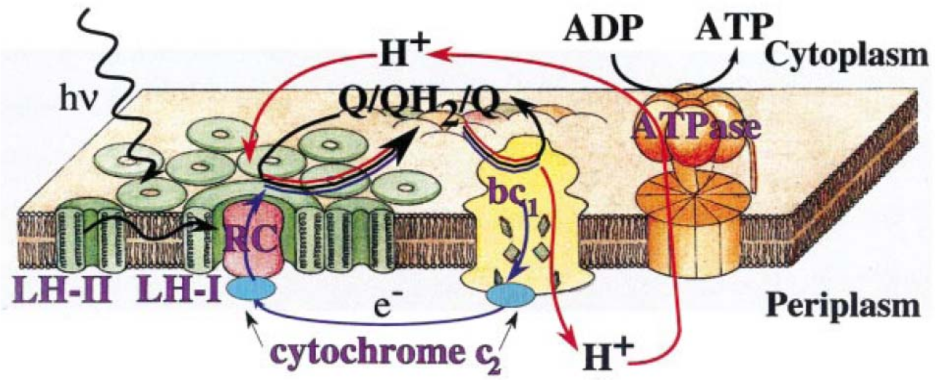

Figure 9.1: Schematic representation of the photosynthetic apparatus in the intracytoplasmic membrane of purple bacteria. From Hu et al [3].

LH2 consists of bacteriochlorophylls (BChl) *a* (Fig. 9.2 (a)), carotenoid (Car) molecules (Fig. 9.2 (b)), and α and β polypeptides (Fig. 9.3).

(a) Bacteriochlorophyll *a*

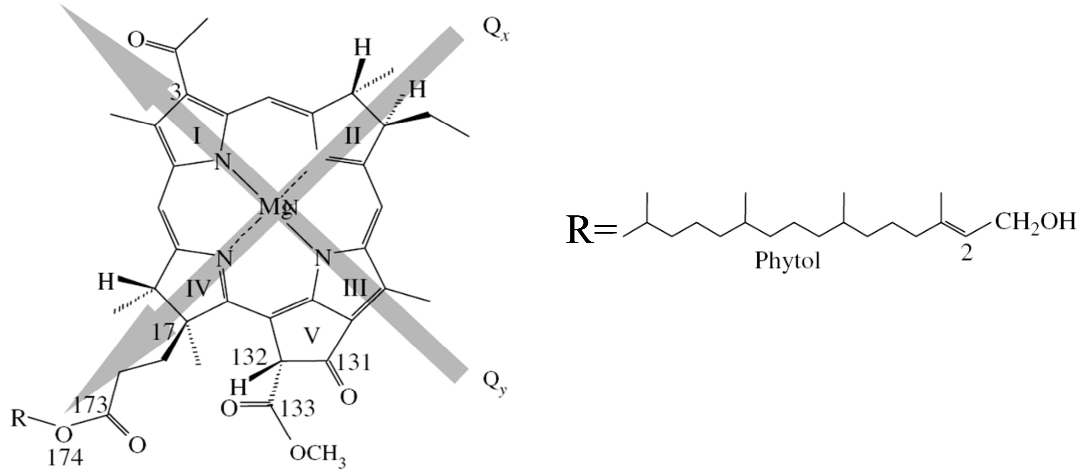

(b) Carotenoids

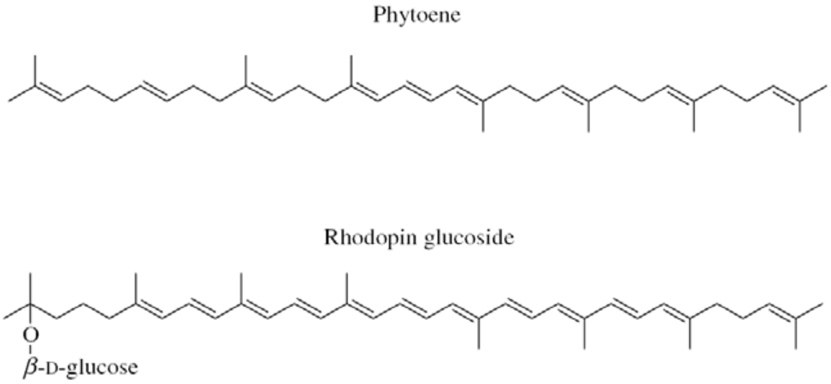

Figure 9.2: Structures of the bacteriochlorophylls a (BChl a) (a) and carotenoids (b). BChl a is composed of a bacteriochlorin macrocycle and an esterifying alcohol, phytol in the case of *Rps. Acidophila* strain 10050. The grey arrows denote the direction of the Qx and Qy transition dipoles within the molecular frame of the bacteriochlorin ring. Carotenoid molecules are built from the C40 molecule, phytoene. The carotenoid molecule in *Rps. Acidophila* strain 10050 is rhodopin glucoside. Qx and Qy are labels for the two BChl a absorption bands at 590 nm and 800 or 850 nm, respectively. The “Qx” and “Qy” are the nomenclature used in the 4-orbital theory developed by Gouterman [4]. The names refer to both the bands and a pair of excited states of the transitions [4]. More details of Qx and Qy are provided in Appendix 3 referring to the absorption spectra of BChl a. From Cogdell et al [5].

In this project, LH2 from *Rps. Acidophila* strain 10050 was used. The α and β heterodimer (α and β polypeptide pairs) in *Rps. Acidophila* binds to three bacteriochlorophylls and one carotenoid molecule, which form a single module. Nine such modules are circularly arranged to form a ring (Fig. 9.3 B). The α and β polypeptides are located inside and outside the ring, respectively (Fig. 9.3 A).

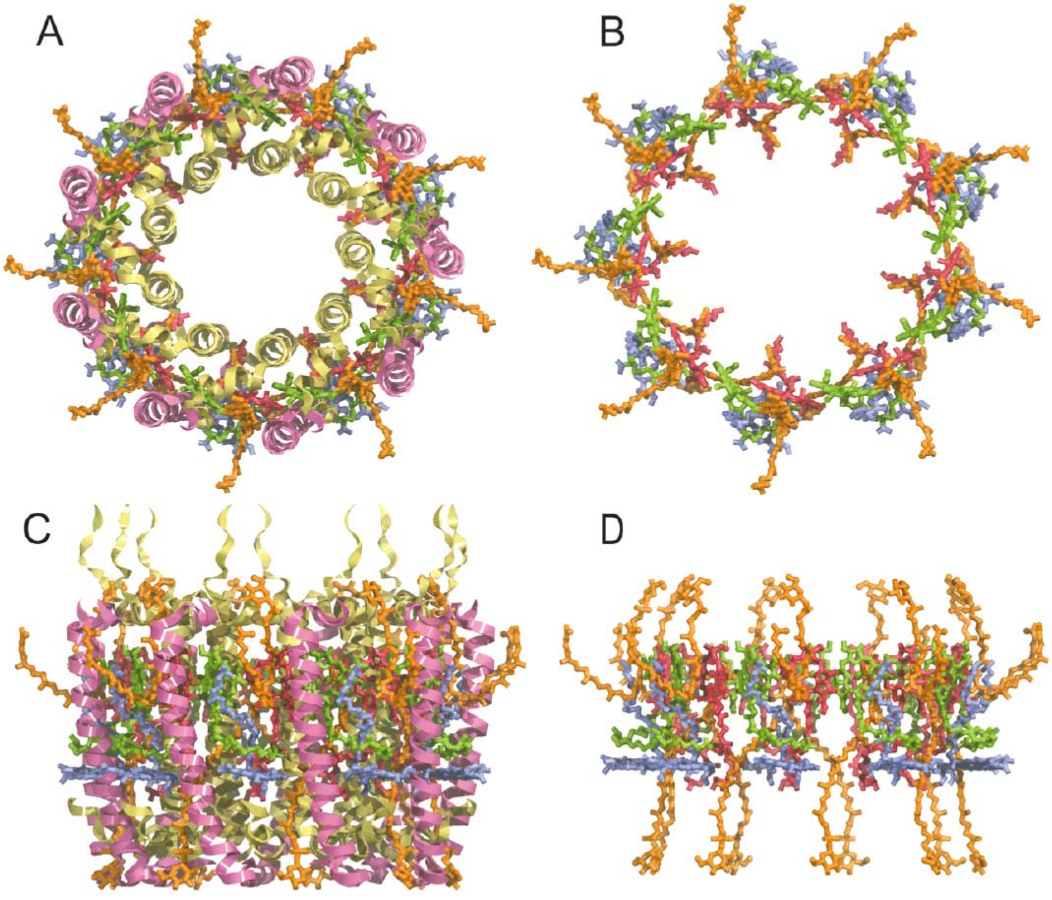

Figure 9.3: A schematic representation of the LH2 complex: (A) and (B) View into the membrane surface; (C) and (D) View along the membrane surface. The α and β polypeptides are drawn as light-green and purple ribbons, respectively. Bacteriochlorophylls are shown separately in (B) and (D): α-B850 (red) and β-B850 (green); B800 (blue) and carotenoid (rhodopin glucoside) (orange). The cytoplasmic surface is at the bottom of (C) and (D), the periplasmic surface at the top. From Papiz et al [6].

The nine BChl *a* molecules are arranged parallel to the plane of the membrane. The BChl *a* molecules absorb light at the maximum wavelength of 800 nm and are thus called B800 BChl *a* (Fig. 9.4). The remaining 18 BChl *a* molecules in the ring, called B850 BChl *a*, are arranged perpendicular to the plane of the membrane and absorb light at around 850 nm (Fig. 9.4). The carotenoid (car) pigments absorb light in the region 450-540 nm (Fig. 9.4). This is the result of transitions from the ground state (S_0) to the second singlet excited state (S_2) [7]. The absorption peaks at 800 and around 850 nm are associated with transitions from the ground state to the lowest excited singlet Q_y states of the B800 BChl *a* and B850 BChl *a* molecules, respectively [7]. LH2 contains both hydrophilic and hydrophobic regions. The hydrophilic region is exposed to the cytoplasm or periplasm, while the hydrophobic region is embedded in the membrane.

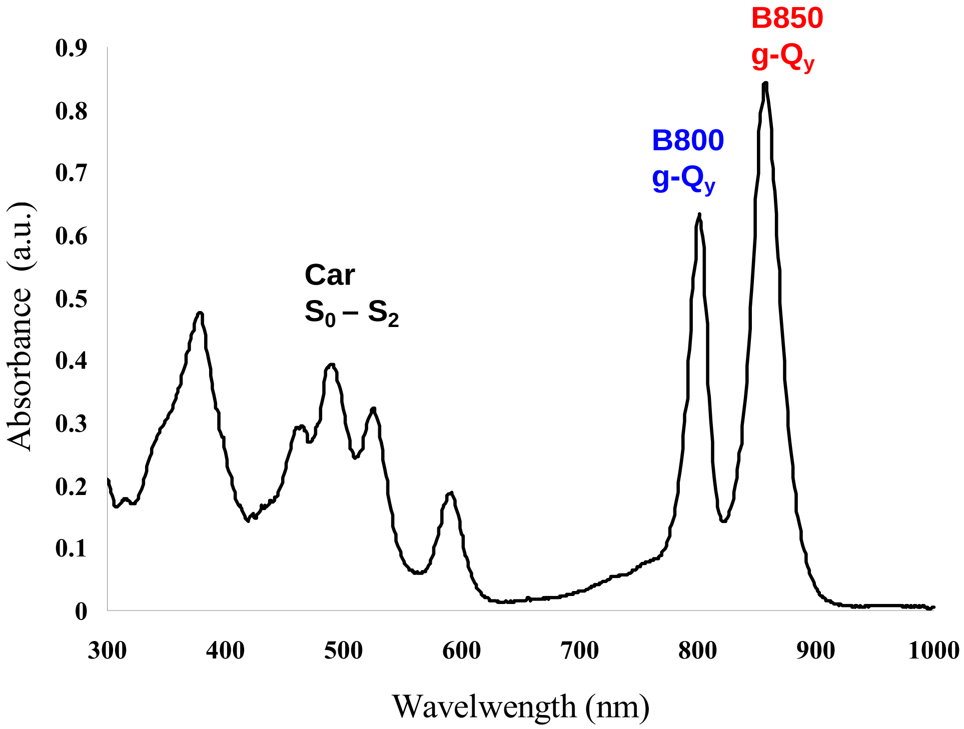

Figure 9.4: Absorption spectrum of LH2. The absorption maxima at 800 and around 850 nm are associated with Q_y transition (g-Q_y, transition from the ground state to the lowest excited singlet Q_y states) of the B800 BChl a and B850 BChl a molecules, respectively. The peak in the region 450-540 nm is associated with the transitions from the ground state, S_0 to the second singlet excited state S_2 of the carotenoids.

One of the features of the LH2 complex is the dense packing of the B850 BChls *a*. The interaction between B850 BChls molecules is strong. When dipole-dipole interaction is strong, excitation energy is delocalized. Exciton notions are used to describe such delocalization. An exciton is a collective excited state, and the excitation energy is delocalized over the BChl ring system. Energy transfer in the bacterial photosynthetic unit is directed by an energy gradient going from LH2 via LH1 to RC, i.e. B800 -> B850 -> B875 (LH1) -> RC. The B800 -> B850 energy transfer takes place in 0.7-0.9 ps at room temperature [8].

A surfactant, lauryl dimethylamine N-oxide (LDAO) was used to prevent aggregation of LH2. LDAO is a zwitterionic or non-ionic surfactant (Fig. 9.5).

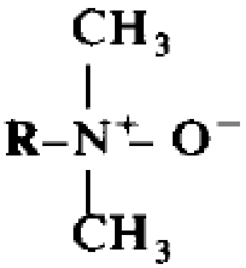

$R{-}N^{+}(CH_3)_2{-}O^{-}$

R = $CH_3(CH_2)_{10}CH_2$-

Figure 9.5: Chemical formula of lauryl dimethylamine N-oxide (LDAO).

In the LH2 solution with LDAO, LDAO surrounds the hydrophobic part of LH2. In the case of LH2 from photosynthetic bacteria *Rhodobacter spheroides* 2.4.1 (strain), the detergent-stabilized LH2 has a shape like an oblate plate, while LH2 alone has a cylindrical structure [9].

9.2 Experimental Section

9.2.1 Chemicals

Tetraethyl orthosilicate (98% (GC), Aldrich), poly(ethylene glycol)-*block*-poly(propylene glycol)-*block*-poly(ethylene glycol) (denoted as Pluronic® P-123, Sigma-Aldrich), Trisma base (Primary Standard and Buffer, ≥99.9%), N,N-Dimethyldodecylamine N-oxide solution (lauryl dimethylamine N-oxide (LDAO), 30% solution), were used as received. Other agents were at least of analytical grade. Milli-Q water (18.2 MΩ cm) was used throughout.

9.2.2 Experimental details

Synthesis of silica particles. The rod-shaped SBA-15 (SBA-rod) was synthesized as follows [10]. 2.4 g P123 and 0.027 g NH_4F were dissolved in 84 ml 1.3 M aqueous HCl solution at room temperature. The solution was transferred to a bottle and incubated in a water bath at a constant temperature (20 °C). After 1 h, a mixture of 5.5 ml tetraethyl orthosilicate (TEOS) and 1.2 ml (1.0 g) 1,3,5-triisopropylbenzene (TIPB) was added. The solution was then stirred for 24 h, keeping the bottle mouth open. The product was then heated at 100°C with the mouth of the bottle closed for 2 days. The synthesized material was isolated by filtering, washing with water and drying at 60°C. The synthesis procedure and characterization for spherical SBA-15 particles with small (SBA-sph-s) and large pores (SBA-sph-l) are described in Section 6.3.

Characterization of silica particles. X-ray diffraction (XRD) patterns of the mesoporous silica material were collected on a PANalytical's X'Pert PRO X-ray diffractometer using Cu Kα as radiation. The diffractograms were recorded in the 2θ range of 0.6° to 5°. SEM images were obtained on an Inspect S or a Helios EBS3 instrument. Silica particles for SEM observation were coated with gold by sputtering. TEM images were obtained using a Tecnai T20 instrument operated at 200 kV. Nitrogen isotherms were measured at 77 K using a Micromeritics ASAP 2020 system. The calcined SBA-15 samples were degassed under vacuum at 200 °C (SBA-rod). For spherical SBA-15 samples, calcined samples were degassed at 200 °C for 13 h (SBA-sph-l) or at 80 °C for 3 h (SBA-sph-s). The specific surface area of the sample was calculated using the BET method [11]. A NLDFT model developed for silica exhibiting cylindrical pores was used for pore size determined by NLDFT method. Characterization by XRD, SEM and TEM was carried out at the Center for Electron Nanoscopy (CEN) of DTU. Nitrogen adsorption measurements were carried out by Bodil Fliis Holten, at the Centre for Catalysis and Sustainable Chemistry, DTU Chemistry.

Adsorption of LH2. 7 µl LH2 from a stock solution was diluted using 2.5 ml 25 mM Tris buffer (pH 8.5) containing 0.1% LDAO. 1 ml of the resultant LH2 solution was mixed with 1 mg silica particles, stirred at 4 °C for 3-3.5 hours and centrifuged. The supernatant was then mixed with 1 mg fresh silica particles, stirred at 4°C for 3-3.5 hours and centrifuged. The LH2-SBA-15 was washed and suspended in a 25 mM Tris buffer (pH 8.5). Absorbance of the solution was measured with a UV-vis spectrophotometer (HP8453, Hewlett Packard).

Ellipsometry. The adsorption of LH2 to a flat silica substrate was monitored by an automated Rudolph thin film ellipsometer, type 43603-200E, equipped with a thermostat. The silica surface was prepared as described by Wahlgren and Arnebrant [12]. The adsorption experiment was performed using 3 ml of 25 mM Tris buffer (pH 8.5) in a cuvette while stirring at around 100 rpm. The silica surface was mounted vertically in the cuvette. The temperature of the cuvette was maintained at 25°C. For adsorption experiment of a mixture of LH2 and LDAO, a stock solution of the mixture of LH2 and LDAO was prepared (0.64 mg/ml LH2 and 1 % w/v LDAO). At a given time, a portion of the stock solution was added to the cuvette which contained 3 ml Tris buffer at start (t = 0). The cuvette was rinsed with the buffer at a flow rate of 20 ml min^{-1}. The adsorbed amount was calculated according to de Feijter [13] using dn/dc = 0.15 (where dn/dc is refractive index increment of the adsorbed material and c is concentration). Most of the ellipsometric measurements were carried out by Professor Marie Wahlgren at Department of Food Technology, Lund University. I prepared the samples and carried out part of the measurements.

Fluorescence spectroscopic measurements at room temperature. Fluorescence spectra at room temperature were obtained as follows. The LH2 solution or the solution of the conjugate of LH2-silica particles was excited at 800 nm. The fluorescence emission was detected with a N_2-cooled CCD detector (HORIBA Jobin Yvon). The spectra obtained were corrected for the wavelength dependent sensitivity of the detector. Fluorescence is related to the energy level (E) of molecules and $\Delta E = hc\tilde{\nu}$ where h represents Plank's constant, c speed of light, $\tilde{\nu}$ wavenumber, i.e., the energy difference is proportional to the wavenumber. It is therefore useful to convert the fluorescence spectra, $I(\lambda)$ (λ is the wavelength) into wavenumber scale. The fluorescence spectra, $I(\lambda)$, were converted to wavenumber scale using the relation, $I(\tilde{\nu}) = \lambda^2 I(\lambda)$ [14], and weighted by $\tilde{\nu}^{-3}$. This, so-called transition dipole moment representation, should be used to extract reliable electronic transition energies and related parameters [15].

Fluorescence spectra at low temperatures. Fluorescence spectra at low, i.e., cryogenic temperatures were obtained using a cryostat. A few drops of LH2 solution or LH2-silica particle solution were deposited onto a glass slide and dried at room temperature. Figure 9.6 shows the set–up of the fluorescence measurement at low temperatures. The fluorescence emission was detected with a N_2-cooled CCD detector (HORIBA Jobin Yvon). The sample was excited at 750 nm with a Continuous Wave (CW) Ti:Sapphire laser (Spectra Physics Model 3900S). The samples were cooled by liquid nitrogen. The temperature was controlled with a temperature controller (Lake Shore 331 temperature controller). Photographs of the set–up are shown in appendix A4. The fluorescence spectra obtained in wavelength representation was converted to wavenumber ($\tilde{\nu}$) scale and weighted by $\tilde{\nu}^{-3}$ as noted.

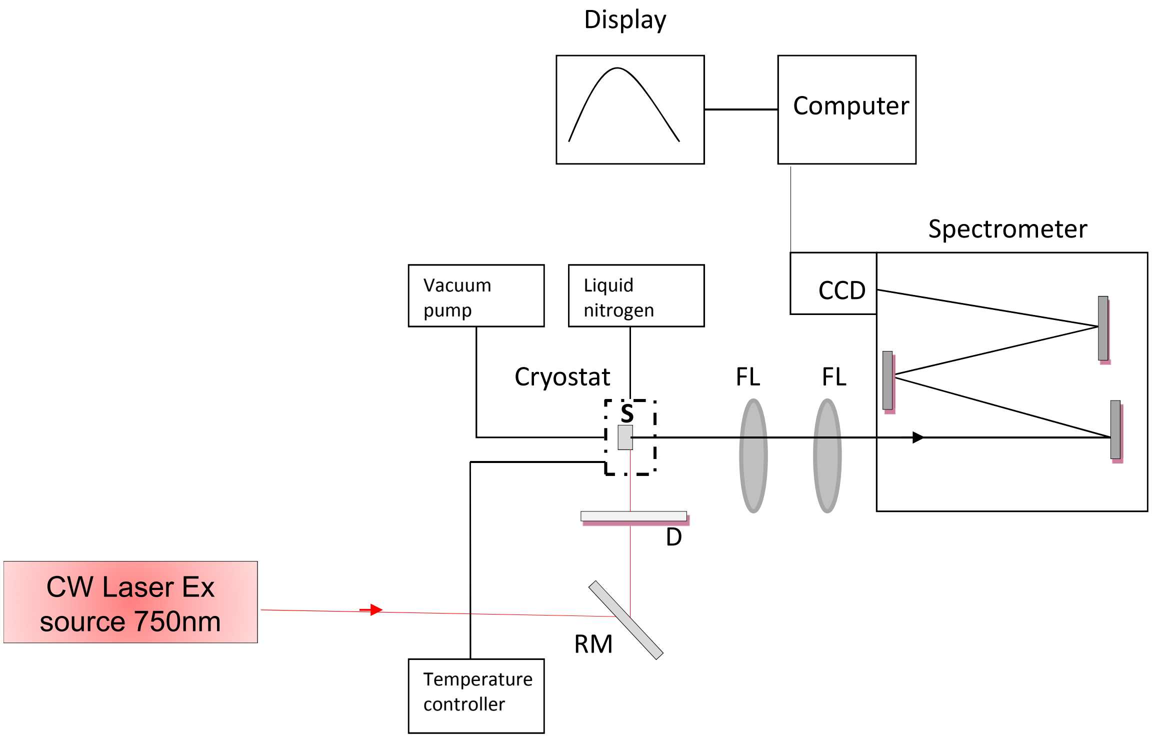

Figure 9.6: Schematic illustration of set–up for fluorescence measurements at low temperatures. Excitation beam (red line) and emission beam (black line), S = Sample, D = Diaphragm, FL = Focusing lens, RM = Reflecting mirror are shown.

Wide-field fluorescence microscopy. A sample was prepared by depositing a drop of LH2 solution or suspension of LH2-SBA-15 conjugate on a cover glass and drying by spin-coating. Fluorescence microscopy was performed using an oil immersion objective lens. Dinitrogen was supplied over the cover glass to prevent photobleaching. The sample was excited at 800 nm with a CW laser. Images were recorded with a CCD camera (PhotonMax). The layout for fluorescence microscopy is shown in Fig. 9.7.

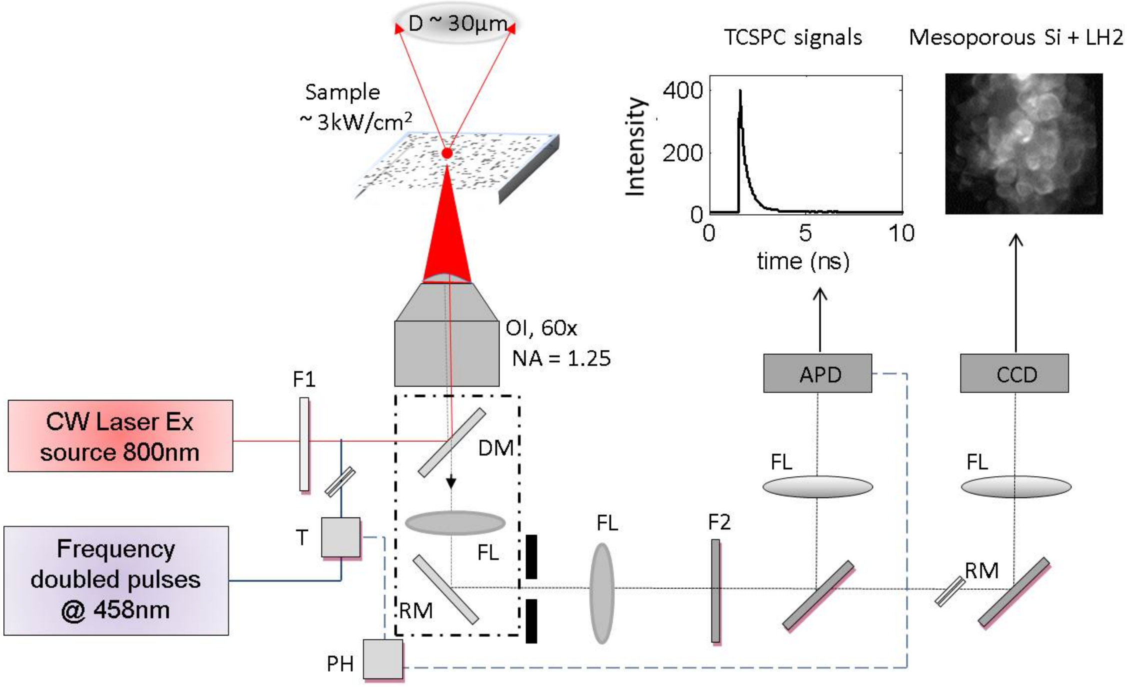

Figure 9.7: Experimental setup for wide-field microscopy and for Time Correlated Single Photon Counting (TCSPC): CCD = Charged Coupled Device camera, F1 = Excitation filter (800nm), F2 = Cut-off filter (830nm), D = Diameter of excitation at sample plan, DM = Dichroic mirror, FL = Focusing lens, OI = Oil immersion objective lens, RM = Reflecting mirror and T = pulse Trigger. This microscopy setup is also used for TCSPC with replacement of CW excitation light with pulsed 458nm laser, APD = Avalanche PhotoDiode and with addition of T = Pulse Trigger and PH = PicoHarp. The inset shows the TCSPC signals obtained from the APD and a microscopic image of silica particles with LH2 inside the pores.

Lifetime measurements. The samples were excited at 458 nm using a pulsed laser. All emission was collected. The set-up was similar to that of wide-field microscopy (Fig. 9.7). Emitted light was detected by an avalanche photodiode (APD) and pulses from APD counted by PicoHarp 300. All decay curves were fitted with MATLAB. These calculations were performed by the Ph.D student, Sumera Tubasum, at Department of Chemical Physics at Lund University.

Fluorescence measurements at room or low temperatures, sample observation with wide-field microscopy, and lifetime measurements were carried out together with the help of Ph.D student, Sumera Tubasum, at Department of Chemical Physics at Lund University.

9.3 Results and Discussion

9.3.1 Synthesis and characterization of SBA-15

Different mesoporous silicas were synthesized and used in this project part: short rod-like SBA-15, spherical SBA-15 with small pore size, and spherical SBA-15 with large pore size, (hereafter referred to as “SBA-rod”, “SBA-sph-s”, “SBA-sph-l”). SBA-sph-s and SBA-sph-l are described in detail in Section 6.3.

Figure 9.8 shows powder XRD patterns of three samples. SBA-rod had a well ordered structure (Fig. 9.8 (a)). Three main peaks are observed at $2\theta = 0.80$, 1.37, and 1.55° for the calcined material, respectively, corresponding to (100), (110), and (200) reflections. The particles are thus proven to have a hexagonally (*p6mm*) ordered pore structure. For SBA-sph-s, there is a single weak peak (Fig. 9.8 (b)), indicating that the pores are less ordered. No peak is found for SBA-sph-l with a disordered structure (section 6.3).

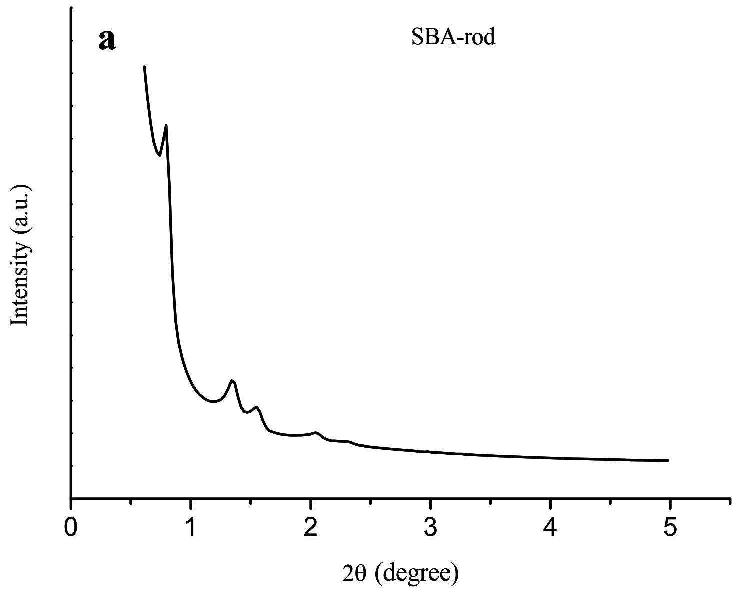

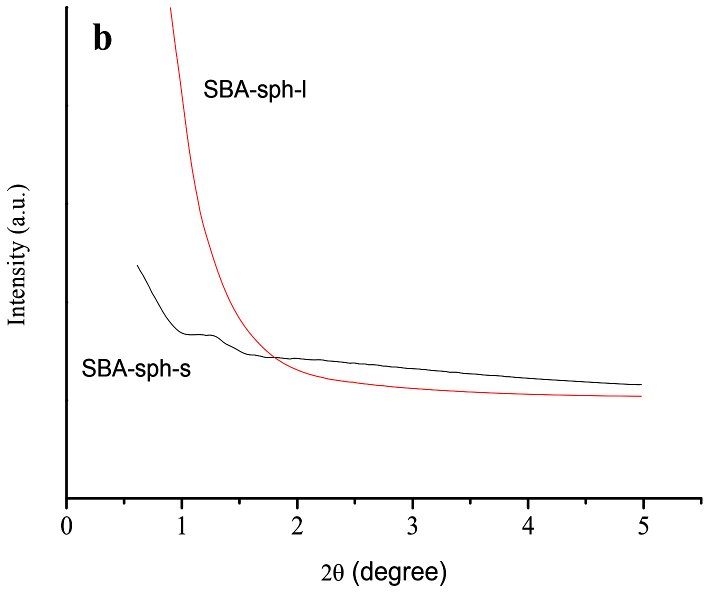

Figure 9.8: Powder XRD patterns of SBA-15 samples. (a) SBA-rod and (b) SBA-sph-s (black curve) and SBA-sph-l (red curve). (a) SBA-rod has a hexagonally ordered pore structure. The three peaks at 2θ = 0.80, 1.37, and 1.55° can be indexed as (100), (110), and (200) reflections associated with p6mm hexagonal symmetry. (b) SBA-sph-s shows a single weak peak, indicating that pores are less ordered and randomly arranged. (c) SBA-sph-l has a disordered structure. There is no peak above 2θ = 0.6°. For details, see section 6.3.

Fig. 9.9 (a) shows a SEM image of SBA-rod where rod-shaped particles are agglomerated. The particle size of SBA-rod is in the range from several hundred nm to ca. 1 μm. Honeycomb patterns are observed in the TEM images (Fig. 9.9 (b) and (c)), which is consistent with the XRD data. The particles of SBA-sph-s are spherical with the size of 4-6 μm (Fig. 9.9 (d)). For the spherical silica particles with large pore (SBA-sph-l), the morphology of some particles is non-spherical and of irregular shape (Fig. 9.9 (e), for details, see Section 6.3). The size of particles with spherical shape is 2 to 5 μm. TEM images (Fig. 9.9 (f)) show that the pores are disordered and the material has a foam-like structure. The particles were ground before adsorption experiments, which could break the grain boundaries.

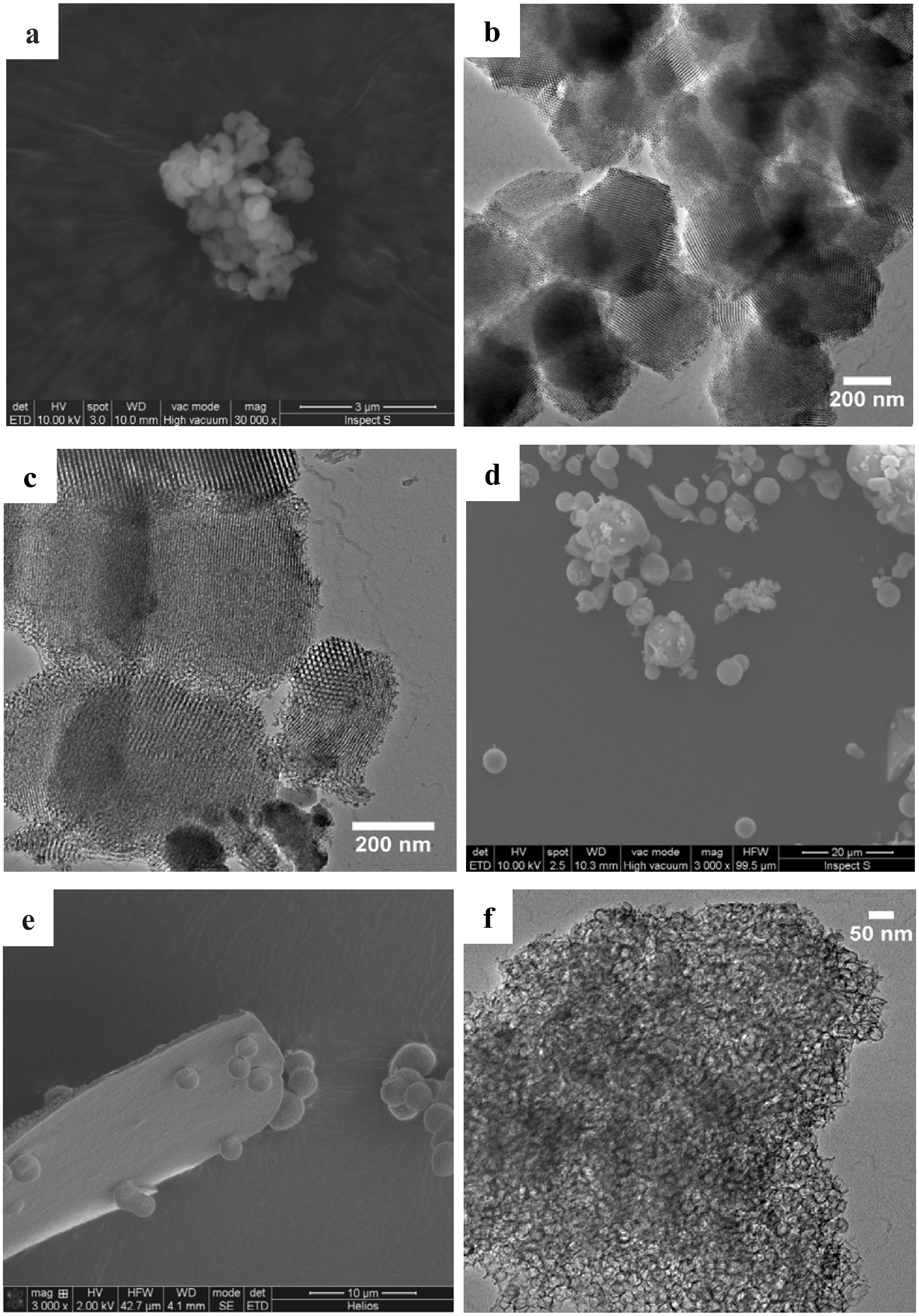
a
det HV spot WD vac mode mag 3 µm
ETD 10.00 kV 3.0 10.0 mm High vacuum 30 000 x Inspect S
b
200 nm
c
200 nm
d
det HV spot WD vac mode mag HFW 20 µm
ETD 10.00 kV 2.5 10.3 mm High vacuum 3 000 x 99.5 µm Inspect S
e
mag HV HFW WD mode det 10 µm
3 000 x 2.00 kV 42.7 µm 4.1 mm SE ETD Helios
f
50 nm

Figure 9.9: SEM and TEM images of SBA-15 samples used (a)-(c) SBA-rod, (d) SBA-sph-s, and (e) and (f) SBA-sph-l. The SEM image (a) reveals that the SBA-rod particles are aggregated. The TEM image (c) shows characteristic two-dimensional hexagonal pore arrays. The SEM images (d) and (e) shows spherical SBA-15 particles with small (SBA-sph-s) and large pores (SBA-sph-l), respectively. The TEM image (f) reveals that the SBA-sph-l has a disordered foam-like structure with large pores. For details, see section 6.3. Note: The long object in (e) is considered to be dust. Scale bars: (a) 3 μm, (b) 200 nm, (c) 200 nm (d) 20 μm (e) 10 μm and (f) 50 nm.

Physical properties of the samples based on the nitrogen adsorption isotherms are summarized in Table 9.1. Note that the pore diameter of SBA-15 with hexagonal arrays of cylindrical pores can be determined by the NLDFT method. The pore diameter of SBA-rod, determined by BJH method, is included for comparison. SBA-sph-l has a MCF-like structure, i.e. a three-dimensional pore structure consisting of large spherical pores (cells) interconnected by windows of a smaller opening (section 6.3.2). The pore diameter, D_p, of the SBA-sph-l corresponds to the diameter of "cells" and D_w represents the diameter of the windows. It is noted that the BJH method could underestimate the pore size of MCF by around 20% compared to the more precise BdB-FHH method [16] (Section 6.2.2).

Table 9.1: Physical Characteristics of SBA-15 Used in This Study.

Sample	S_{BET} (m^2/g)	V_{tot} (cm^3/g)	D_p (nm)	D_w (nm)
SBA-rod	522	1.34	10.7^a 9.4^b	-
SBA-sph-s	853	0.67	3.7^a	-
SBA-sph-l	491	1.34	17.3^a	5.8^c

SBET: Total surface area, V_{tot}: Total pore volume, D_p: Pore diameter, D_w: Window diameter, [a] Determined by BJH method from the adsorption branch, [b] Determined by the NLDFT method, [c] Determined by the BJH method from the desorption branch.

From the results obtained by XRD, TEM, and N_2 adsorption, SBA-rod has ordered hexagonal arrays of cylindrical pores, while SBA-sph-s has a less ordered structure with small pore size. Based on the characterization and synthesis procedure, SBA-sph-l has a foam-like structure consisting of large spherical disordered pores (cells) interconnected by smaller openings (For details, see section 6.3.2).

9.3.2 Adsorption of LH2 onto mesoporous silica particles

Adsorption of LH2 from Tris buffer with 0.1% LDAO onto SBA-rod (mesoporous SBA-15 with hexagonal arrays of cylindrical pores) was achieved by two steps. In the first step, almost no absorption decrease was observed (Fig. 9.10, 1st_3h), indicating that LH2 was not adsorbed onto the particles. In the second step, the supernatant from the 1st step that contains LH2 was mixed with another batch of silica particles. As seen in Fig. 9.10 (2nd_3h), decrease of absorption was now observed, indicating that LH2 was adsorbed to the particles.

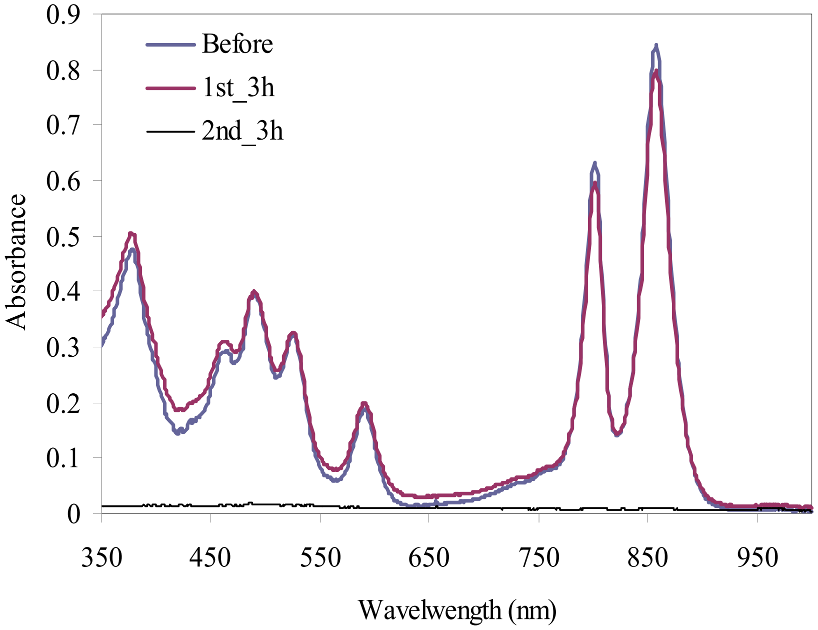

Figure 9.10: Adsorption experiment of LH2 solution (LH2 in 25 mM Tris buffer with 0.1%LDAO) to SBA-rod. Before: Absorbance of LH2 in 25 mM Tris-HCl buffer (pH 8.5) with 0.1% LDAO at start, 1st_3h: supernatant after 3h stirring of LH2 solution and silica particles (1st step), 2nd_3h: supernatant after ca. 3h stirring of the supernatant from 1st step, and fresh silica particles.

The observations could be associated with detergent molecules preventing adsorption of LH2 to silica particles in the 1st step. For example, in the field of capillary electrophoresis (CE) protein separation, non-ionic or zwitterionic detergents have been used for coating fused-silica capillary in order to prevent proteins being attached to capillary walls (capillary shielding) [17]. The free detergent molecules in the supernatant after the 1st step are likely to be decreased due to the adsorption to the pores of the silica particles during the 1st step. This decrease in free detergent molecules could have allowed LH2 to be adsorbed to silica particles in the 2nd step. If we use lower concentration of LDAO in the 1st step, the adsorption of LH2 to silica particles may be achieved in one step. However, lower concentration of LDAO may induce aggregation of LH2 through the hydrophobic region.

9.3.3 Adsorption of LH2 to flat silica substrate

Compared to the cases for HRP and galactose oxidase (Chapters 7 and 8), adsorption of LH2 onto mesoporous silica is complicated by the presence of surfactant in the solution. Adsorption of proteins to silica materials is related to a variety of fields and has been extensively studied. One of the effective techniques for studying adsorption of proteins at liquid-solid interfaces is ellipsometry. In the present case, adsorption of LH2 to a flat silica surface was studied by *in situ* ellipsometry [18]. Although a planar silica substrate instead of porous silica was used in the measurements, useful information could still be obtained. Adsorption of LH2 from a mixture of LH2 and LDAO to the silica substrate was monitored by changing the LH2 and LDAO concentrations in the tested solution (Fig. 9.11). At a given time, a portion of the stock solution of the mixture of LH2 and LDAO was added to the tested solution so that the LH2 and LDAO concentration were adjusted (Table 9.2). The major observations are briefly summarized as follows.

Adsorption was observed at t = 3600 s. As the adsorbed amount is in between what has been measured for the pure components (ca. 4.8 mg/m^2 for LH2 alone and ca. 1.0 mg/m^2 for LDAO alone, data are included as appendix A5), it is most likely that a mixture of LH2 and LDAO is adsorbed on the silica substrate in the form of a LH2/LDAO complex or as a complex and free surfactant molecules. It should be noted that at this point, the concentration of LH2 and LDAO is approximately the same as that (a mixture of 0.064 mg/ml LH2 and 0.1% w/v LDAO) used for the adsorption to mesoporous silica. As noted, there was little adsorption of LH2 to mesoporous silica from a mixture of LH2 and 0.1% LDAO in the first step. This different adsorption behaviour may be due to different surface properties of flat silica and mesoporous silica, SBA-15, such as a different degree of hydrophilicity of the surfaces. Alternatively, it may be assumed that in adsorption to mesoporous silica, surfactant aggregates (micelles) formed at pore walls have blocked the entrance of LH2 from the solution of LH2 and 0.1% LDAO.

Table 9.2: Change in the Concentration of the Mixture with Time in the Adsorption Study by Ellipsometry.

Time (sec)	Amount of stock solution*[1] added (µl)	Total amount of stock solution added (µl)	Total volume of solution in the cuvette (µl) after the addition	Degree of dilution	Conc. of LH2 (mg/ml, upper row) and LDAO (% w/v, lower row) after addition
0	3	3	3003*[2]	1001	6.4×10^{-4} mg/ml 0.10×10^{-3} %
1800	27	30	3030	101	0.0063 mg/ml 0.010 %
3600	270	300	3300	11	0.058 mg/ml 0.091 %
6200	300	600	3600	6	0.11 mg/ml 0.16 %
8000	250	850	3850	4.53	0.14 mg/ml 0.22 %

1. The concentration of stock solution (a mixture of LH2 and LDAO) was 0.64 mg/ml LH2 and 1 % LDAO. 2. The cuvette contained 3 ml Tris buffer before the addition of stock solution at start (t = 0).

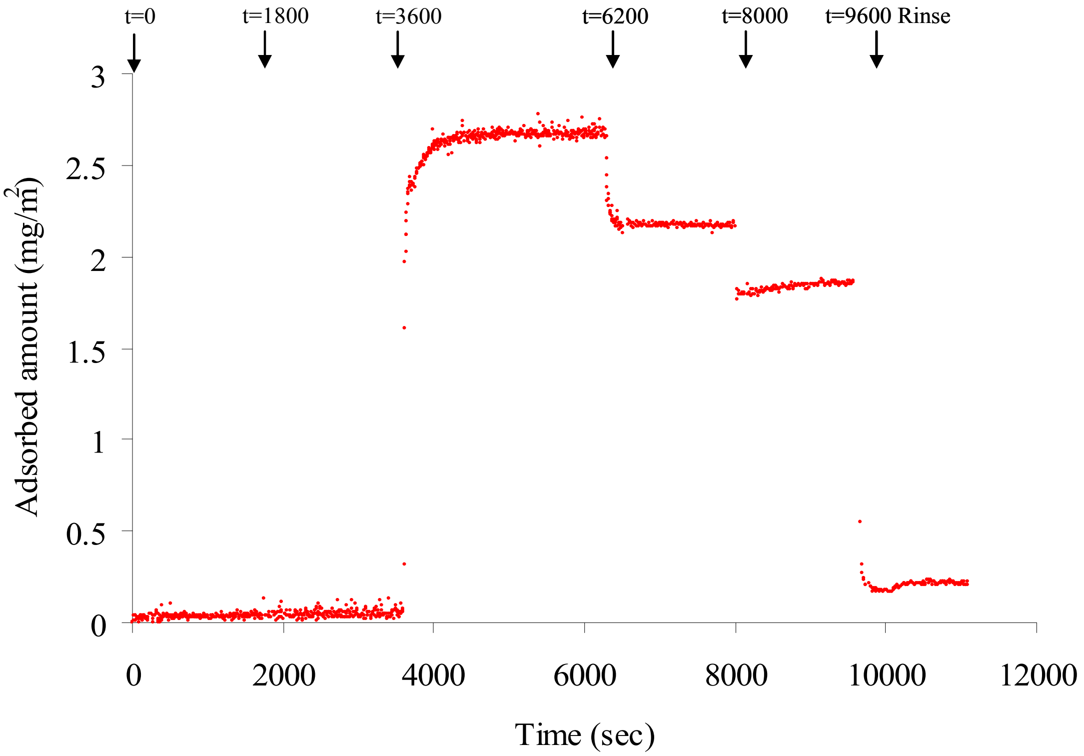

Figure 9.11: Adsorption of LH2 and LDAO mixture onto flat silica substrate in Tris buffer (pH 8.5). At an indicated time, a certain amount of stock solution (LH2 and LDAO mixture) was added to attain a desired concentration.

At t = 6200 sec, further stock solution was added, resulting in a decrease in the adsorbed amount. The decrease is attributed to the displacement of LH2 by LDAO. This observation agrees with the fact that when LH2 adsorbed to mesoporous silica was treated with Tris buffer with 0.1% LDAO, adsorbed LH2 was released into the solution. LDAO therefore seems to adsorb to hydrophilic silica more strongly than LH2/LDAO complex or LH2 alone.

At t = 9600 sec, the substrate was rinsed with a flow of Tris buffer. Significant decrease in the adsorbed amount was found. Surfactants adsorb reversibly to silica surfaces [19]. It is likely that LDAO that is a small surfactant molecule also shows reversible adsorption to the silica surface. It was therefore concluded that the adsorbate before rinsing is dominated by LDAO.

From the study of adsorption to mesoporous silica and flat silica, it is still not clear whether or not LH2 is adsorbed to silica surface with the hydrophobic part surrounded by LDAO. In addition, the location of LH2 is not clear at this stage although in terms of the dimension of LH2 (~ 6 nm in height and ~ 8 nm in diameter) [20], LH2 can be accommodated inside the pores of SBA-rod.

9.3.4 Location of LH2 in the mesoporous particles

To identify the adsorption location of LH2 in the mesoporous materials, we *first* compare experimental observations for the adsorption of LH2 onto spherical silica particles with different pore sizes by UV-Vis measurements (Fig. 9.12). The small-pore silica particles (SBA-sph-s) have an average pore diameter of ca. 3.7 nm, which appears to be too small to accommodate LH2 inside the pores. The SBA-sph-l particles have a pore size of 17.3 nm. The larger pores (cells) are interconnected by smaller openings (or windows) of 5.8 nm. After the 2nd adsorption attempt, little decrease in absorbance of the supernatant was observed for the SBA-sph-s case (Fig. 9.12, top), indicating that only very small amount of LH2 was adsorbed to the silica particles. In contrast, significant decrease in absorbance of the supernatant was observed for SBA-sph-l (Fig. 9.12, bottom). However, the UV-Vis measurements do not provide direct envidence regarding the location of LH2 molecules, although the significant difference in the apparent adsorbed amount was detected.

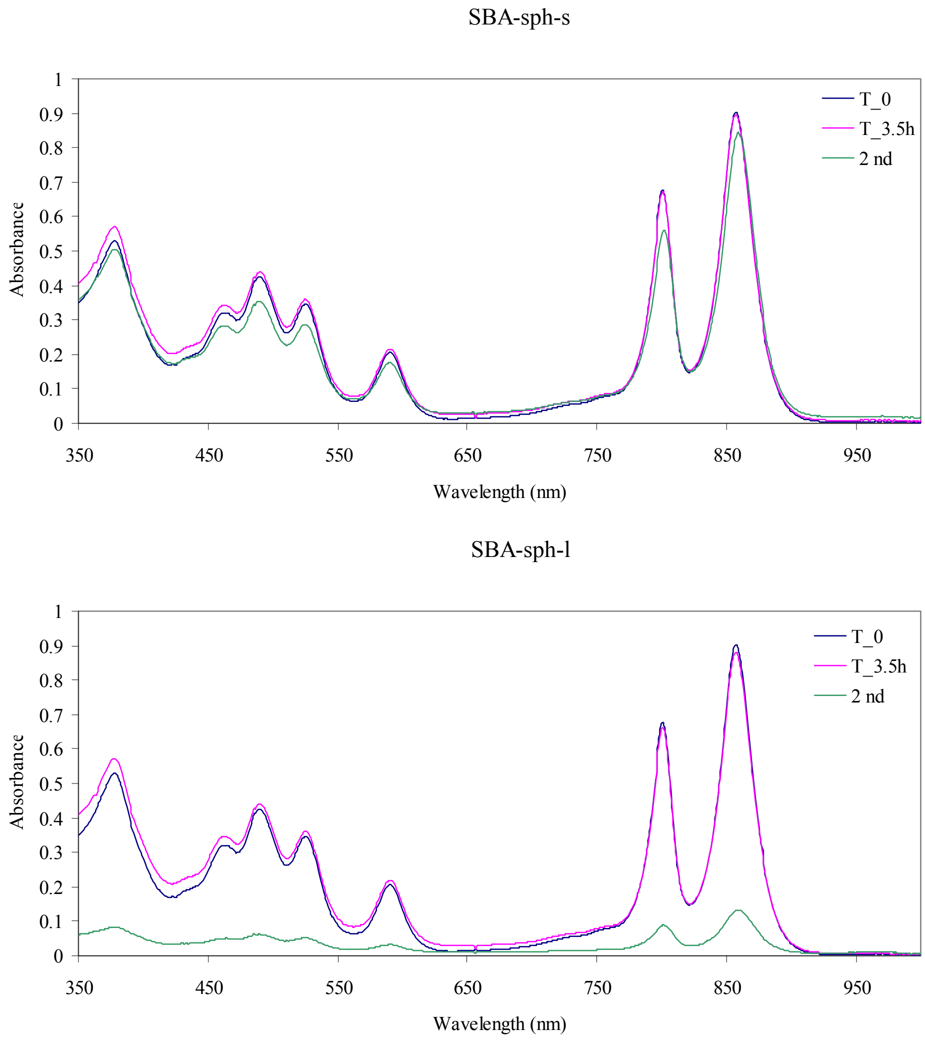

Figure 9.12: Adsorption experiment of LH2 solution (LH2 in 25 mM Tris buffer with 0.1%LDAO) to spherical SBA-15 with small (SBA-sph-s, top panel) or large pores (SBA-sph-l, bottom panel). T_0: Absorbance of LH2 in 25 mM Tris-HCl buffer (pH 8.5) with 0.1% LDAO at start; T_3.5h: supernatant after 3.5 h stirring of LH2 solution and silica particles (1st step); and 2 nd (2 nd step): supernatant after 3.5 h stirring of the supernatant from the 1st step, and fresh silica particles.

To further investigate the location of LH2 adsorbed to the spherical SBA-15 particles, the samples after adsorption experiments were imaged by fluorescence microscope (Fig. 9.13). In the case of SBA-sph-s, very few particles with fluorescence were found (Fig. 9.13 (a)), which is consistent with the result obtained from the adsorption experiments. The image shown in Fig. 9.13 (b) indicates, however, that LH2 was most likely located inside the pores in the large-pore SBA-15 particles. Moreover, the image reveals that

LH2 was mainly located close to the entrances of the pores, but not deep inside the pores. With the microscopy resolution at the level of 0.5 to 1μm, the result suggests that LH2 does not penetrate deeper than 1 μm into the pores. This is likely associated with the structural features of SBA-sph-l. As noted, the particles have foam-like structures consisting of large spherically disordered pores (cells) interconnected by smaller openings. The size of the small openings is only 5.8 nm, and these small openings could thus prevent LH2 penetrating deep inside the pores.

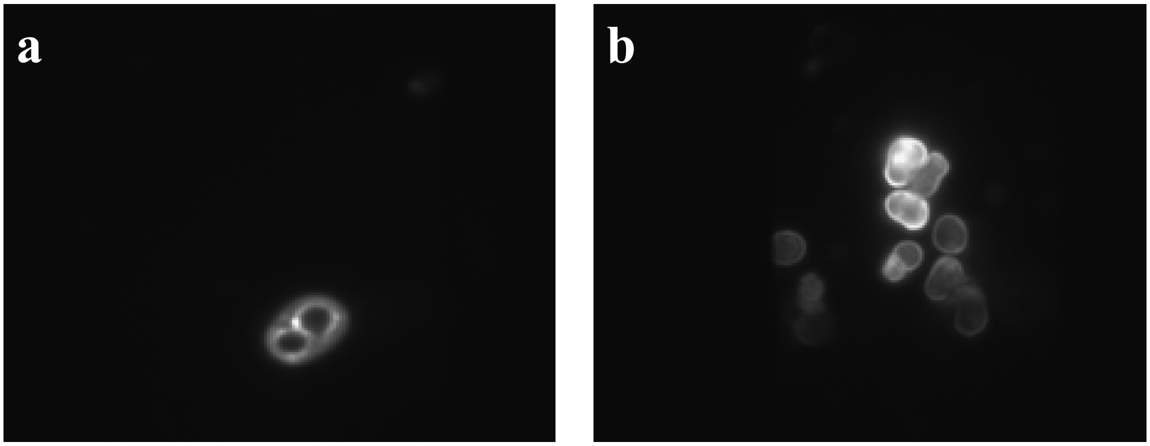

Figure 9.13: Fluorescence microscopic images of the samples after adsorption of LH2 solution (LH2 in 25 mM Tris buffer with 0.1%LDAO) to (a) spherical SBA-15 with small pores (SBA-sph-s) or to (b) spherical SBA-15 with large pores (SBA-sph-l). For the sample of spherical SBA-15 with small pores (a), very few particles with fluorescence were observed, while many particles with fluorescence were observed for the sample of spherical SBA-15 with large pores (b). The image (b) indicates that LH2 was most likely located inside the pores.

9.3.5 Steady-state fluorescence spectra

Figure 9.14 shows fluorescence spectra of free LH2 (in 25 mM Tris-HCl buffer (pH 8.5) with 0.1% LDAO) and of the LH2-particle conjugates including LH2-SBA-sph-l and LH2-SBA-rod. These spectra were recorded at room temperature. Surprisingly, there is little difference in the emission spectra obtained for the three samples, except for a very slightly larger bandwidth in the spectrum for the LH2-SBA-rod sample. All the spectra are notably asymmetric in the band wings, with a slower fall-off on the low-frequency side of the maximum than on the high-frequency side. Such effects could reflect strong electronic-vibrational coupling to high-frequency nuclear modes ("quantum modes", [21]) either locally or in the solvent and protein environment. We shall re-address this issue in Section 9.3.6 and in Appendix A6.

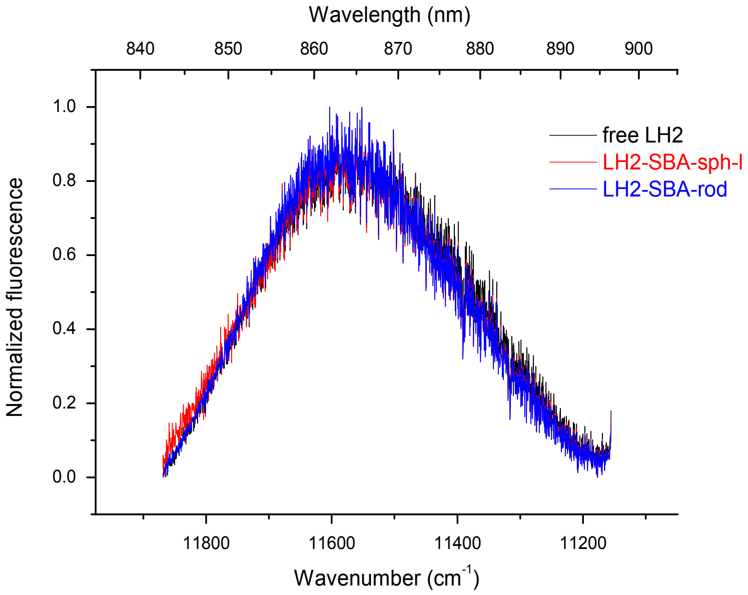

Figure 9.14: Normalized fluorescence spectra ($I(\tilde{\nu})/\tilde{\nu}^3$) of free LH2 in 25 mM Tris-HCl buffer (pH 8.5) with 0.1% LDAO (black) and the conjugates of LH2 and SBA, LH2-SBA-sph-l (red) and LH2-SBA-rod (blue). The conjugate samples were prepared by the adsorption of LH2 in buffer with 0.1% LDAO to LH2-SBA-sph-l or SBA-rod.

9.3.6 Fluorescence spectra at low temperatures

For all three types of samples, more fluorescence spectra were acquired at different temperatures ranging from room temperature (298 K) to liquid-nitrogen temperature (77 K). These data were analyzed in more detail, and organized in two ways as compared in Figs. 9.15 and 9.16.

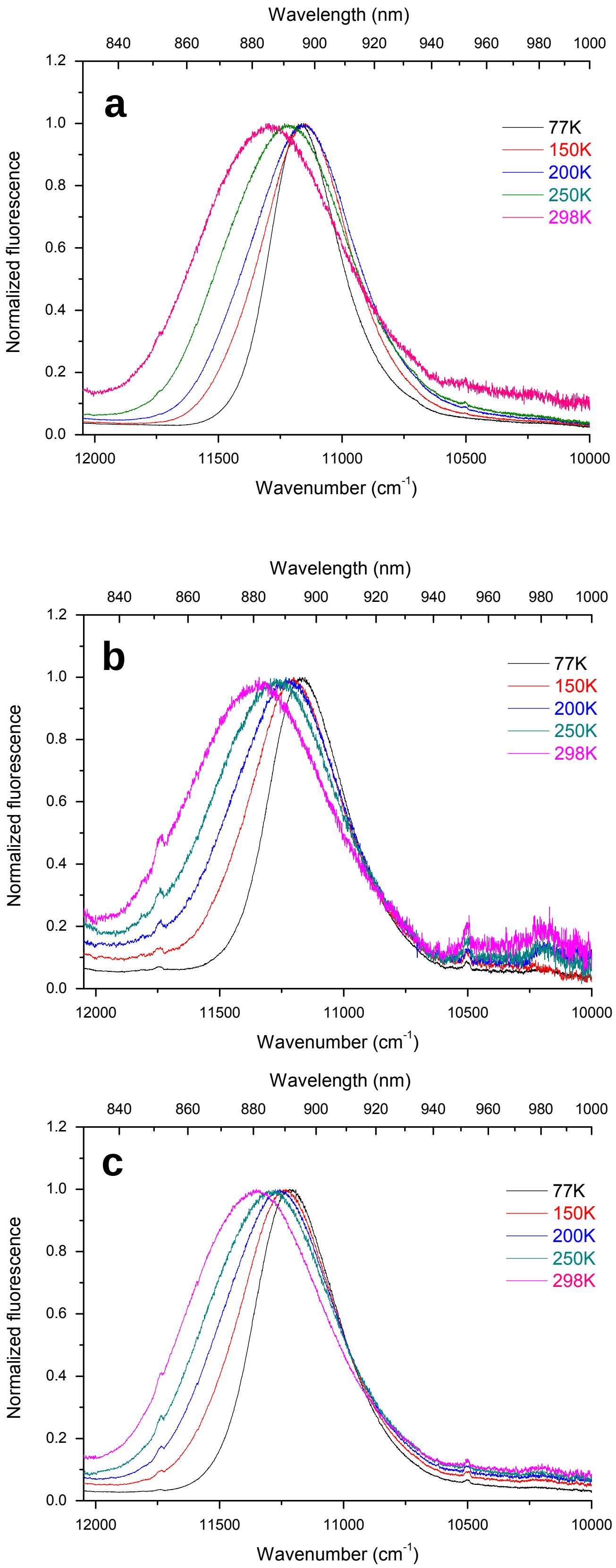

Figure 9.15: Normalized fluorescence spectra ($I(\tilde{\nu})/\tilde{\nu}^3$) at different temperatures. (a) Free LH2 (b) conjugate of LH2 and SBA-sph-l and (c) conjugate of LH2 and SBA-rod.

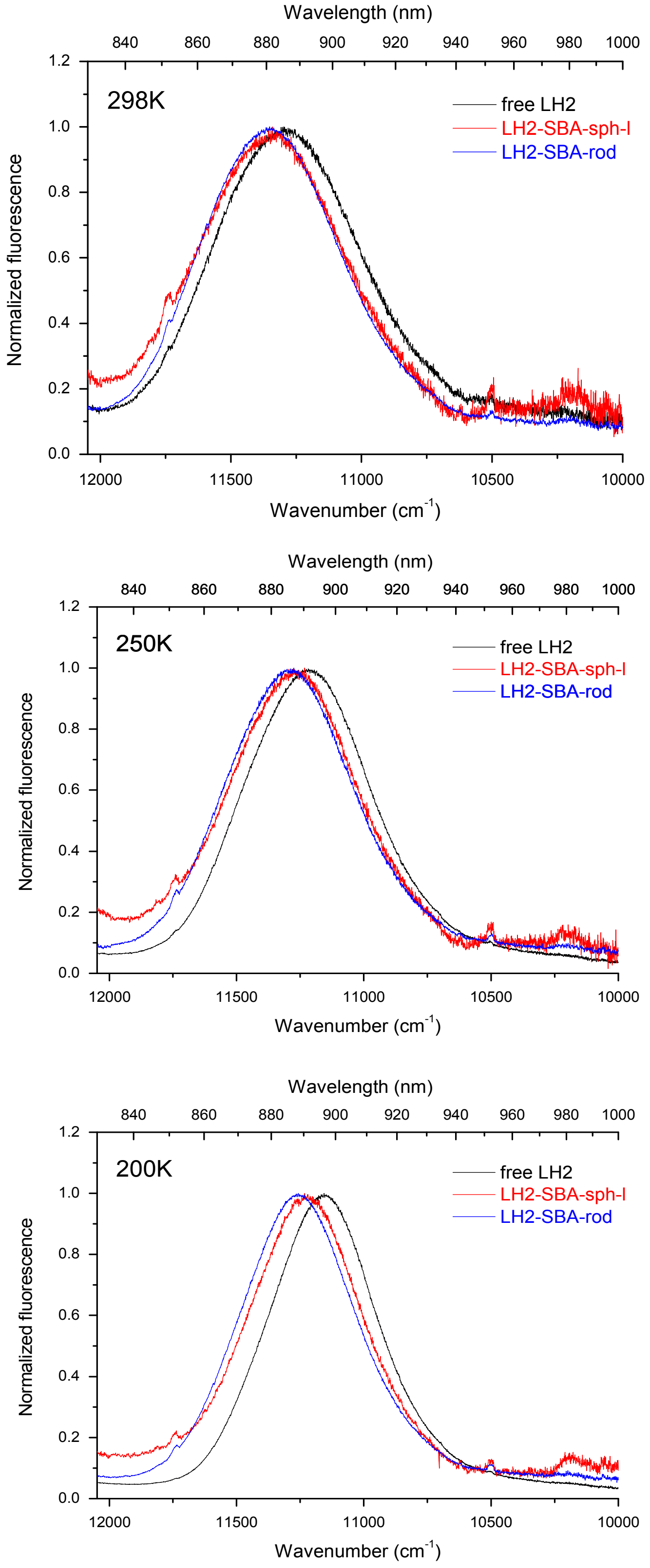

Figure 9.16: Normalized fluorescence spectra $(I(\tilde{\nu})/\tilde{\nu}^{3})$ at different temperatures, 298K, 250K, 200K, 150K, and 77K.

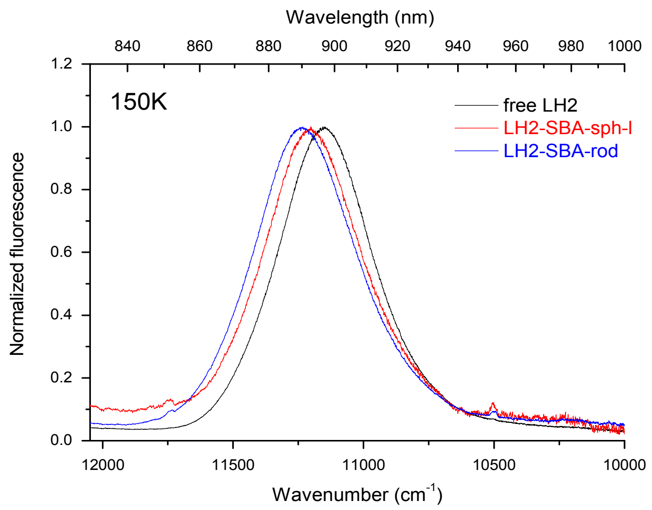

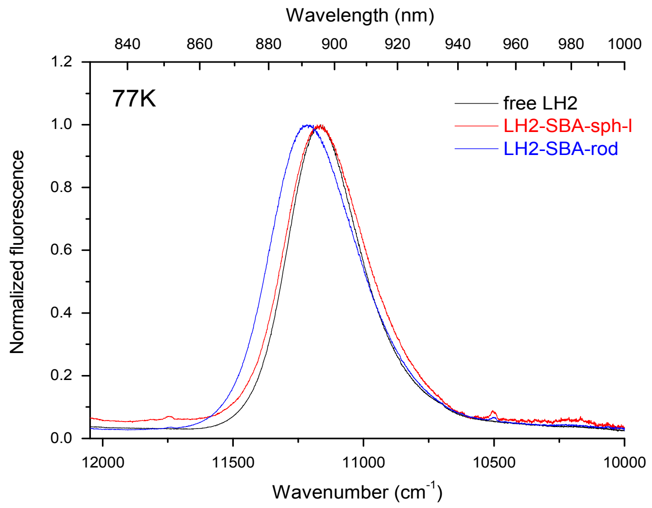

Disregarding multiple, excitonic transitions, the temperature dependence of the spectra of all the three samples, i.e. free LH2, LH2-SBA-sph-1 and LH2-SBA-rod shows the following features:

- The fluorescence bands seem to differ little between free and pore-confined LH2. Although small, the differences are, however, systematic as disclosed by further bandshape analysis, cf. below and Appendix A6.
- The spectra are asymmetric in the band wings with a slower fall-off in the low-frequency branch of the spectrum than in the high-frequency branch. As noted, this could reflect strong electronic-vibrational coupling to local or solvent high-frequency nuclear

modes, Appendix A6. The importance of high-frequency mode coupling is substantiated by the increasing apparent asymmetry as the temperature is lowered.

- Significant band narrowing is observed as the temperature is lowered. This is expected as nuclear vibrational excitation is attenuated when the temperature is lowered for transitions with strong electronic-vibrational coupling (Appendix A6, refs., e.g. [22]). Ideally the bandwidth should follow a $\sqrt{T}$-dependence at high temperatures and be independent of temperature at low temperatures (a $\sqrt{\coth\left(\hbar\omega_{eff}/2k_BT)\right)}$ dependence where k_B is Boltzmann's constant, T the temperature, $\hbar$ Planck's constant divided by 2π and ω_{eff} a average vibrational frequency of all the nuclear modes reorganized). This is detailed in Appendix A6.
- The $\sqrt{T}$-dependence of the peak width based on Gaussian bandshape analysis, Appendix A6 is shown in Fig.9.17. The ideal dependence is followed approximately considering the asymmetry features noted and the possibly composite nature of the transition which involves a number of single-centre LH2 chromophores.
- The coupling parameters (E_R) are in the range 400-500 cm^{-1} or about 50-60 meV. Such values are indicative of transitions screened from the outer environment but with notable coupling to low-frequency protein nuclear modes.
- The T-dependence of the band width tails off in the T- range 150-200 K. This suggests that vibrational frequencies (from $\hbar\omega_{eff} \approx k_BT$) in the range 150-200 cm^{-1} dominate the transition. The values are, interestingly specific to the local – film and pore-confined environment, cf. below.
- Immediate inspection of the fluorescence spectra discloses little difference, but the bandshape analysis gives a slightly more detailed view. The band width, i.e. the coupling strength follows the order LH2 < LH2-SBA-sph-1 < LH2-SBA-rod in most of the temperature range. Secondly, although the absolute band width values differ little, the transition temperatures appear slightly different, cf. above, with those for pore-confined LH2 systematically higher than those for free LH2. In other words, nuclear motion of slightly higher frequencies seem to dominate increasingly as LH2 is trapped in the pore confinement.

- There is, finally a shift of the band maximum towards lower frequencies as the temperature is lowered, Fig. 9.18. The shift follows roughly the same order as for the band width, LH2 > LH2-SBA-sph-1 > LH2-SBA-rod. Temperature dependent peak shifts are not inherent in the simplest models for optical electronic transitions. The shifts can be caused by gradual "freezing out" of part of the vibrational motion (lower "polaron trapping" energy difference) as the temperature is lowered, or by redistribution among the single-centre chromophores that contribute to the overall optical fluorescence bands. We do not here pursue these issues further.

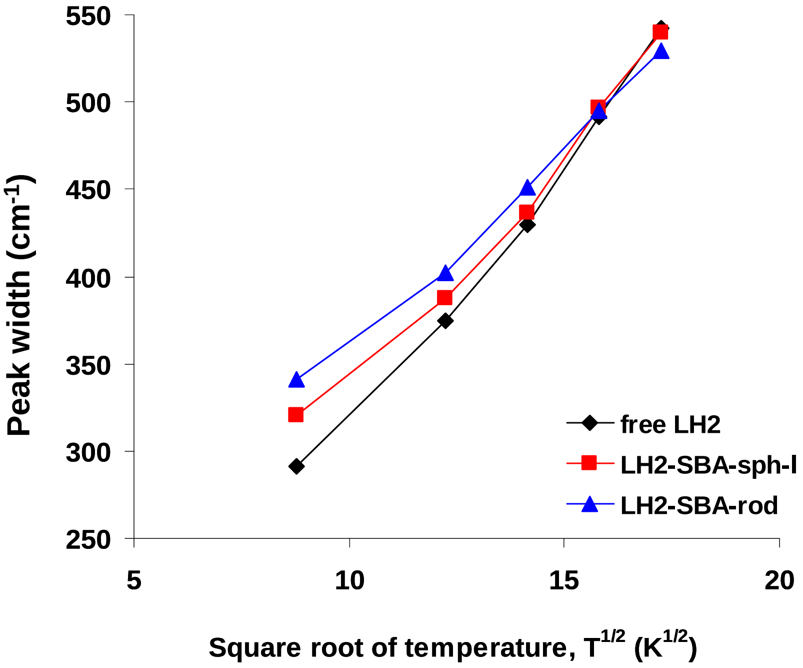

Figure 9.17: Temperature dependence of the bandwidth of the fluorescence spectra of free LH2 (black), LH2-SBA-sph-I (red), and LH2-SBA-rod (blue). The data are obtained by Gaussian bandshape analysis, cf. Appendix A.6 of the fluorescence spectra shown in Figs. 9.15 and 9.16.

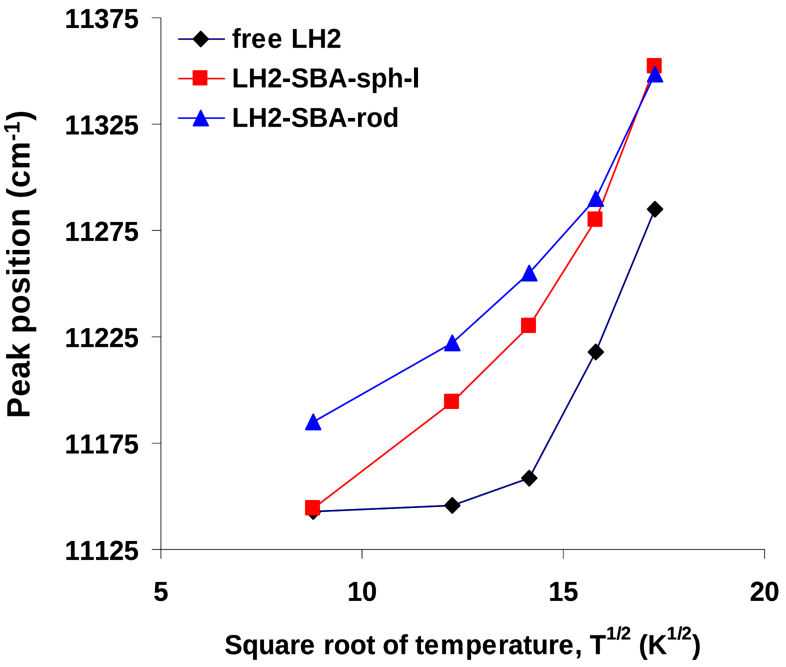

Figure 9.18: Temperature dependence of the peak position of the fluorescence spectra for free LH2 (black), LH2-SBA-sph-I (red), and LH2-SBA-rod (blue), obtained by Gaussian bandshape analysis.

9.3.7 Comparison of fluorescence lifetime

The time-resolved fluorescence spectra were recorded and are used to evaluate the fluorescence kinetics of free LH2 and the LH2-SBA conjugates. Figure 9.19 shows an example of such spectra.

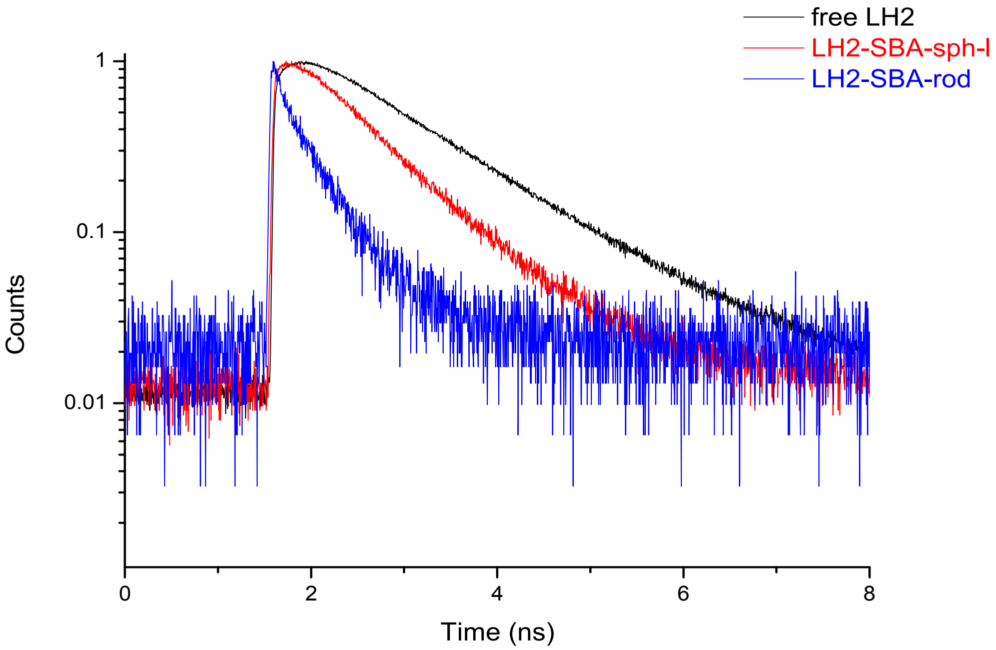

Figure 9.19: Normalized fluorescence decays of free LH2 (black) and LH2-SBA-sph-l (red), and LH2-SBA-rod (blue). The data were recorded at room temperature and at an excitation density of 3.22 x 1011 photons/(pulse·cm^2) and 5.57 x 10^{-4} photons/(pulse· LH2 ring) [23]. The samples were excited at 458 nm using a pulsed laser.

It is known that for the lifetime of LH2 when the excitation power exceeds a threshold value, excitation annihilation occurs, which leads to a decrease in lifetime [24]. The data were recorded at room temperature and at an excitation density of 3.22 x 10^{11} photons/(pulse·cm^2) and 5.57 x 10^{-4} photons/(pulse· LH2 ring) [23], which is below the threshold value at which excitation annihilation occurs [25]. The fluorescence decay of free LH2 and LH2-SBA-sph-l can be fitted with a single exponential with a time constant of 1.1 ns for free LH2 and 0.69 ns for LH2-SBA-sph-l, whereas the fluorescence decay of LH2-SBA-rod is biexponential with time constants of τ_1 = 0.077 ns and τ_2 = 0.39 ns, respectively. The lifetime (1.1 ns) of free LH2 is consistent with the result of detergent solubilized LH2 from *Rps. acidophila* [25].

The simplest expectation is that the fluorescence lifetime depends on the refractive index according to the equation (in Chapter 4), namely, $\tau \sim 1/n^2$ (where τ is the lifetime and n is the refractive index). The refractive index of water and SBA-15 is 1.33 and 1.15, respectively [26]. The lifetime of LH2 in mesoporous SBA is therefore expected to be 1.47 ns. The obtained lifetime is thus shorter than this value.

To interpret the results, additional detailed study is desirable. For example, use of streak camera allows us to measure fluorescence decay both in wavelength and time. Such data can be used to study time-dependent spectral relaxation. However, additional detailed study using e.g. streak camera was unfortunately not possible due to instrument fault and limited time of study. Nonetheless, some possible reasons for the shorter lifetimes of the LH2-SBA conjugates can be identified. For example, some quenching molecules such as oxidized pigments in the pores may have caused quenching of the fluorescence. There was different life times between different LH2-SBA conjugates. This could be due to different arrangements of LH2 molecules in the particles. As described in the characterization of the samples, SBA-rod has ordered hexagonal arrays of cylindrical pores, while the pores of SBA-sph-l are disordered and with a MCF type structure, i.e., a three-dimensional pore structure consisting of large spherical pores (cells) interconnected by smaller openings. The following arrangement of LH2 in the particles could therefore be speculated. For the LH2-SBA-rod conjugate, LH2 is located inside the ordered cylindrical pores. This could lead to homogeneous distribution or regular arrangement of LH2 and to dense packing of LH2 in the particles. For the LH2-SBA-sph-l conjugate, LH2 is located in the disordered pores and some pores may not be filled with LH2 due to small 5.8 nm openings (windows) that interconnect large spherical pores (cells). This could lead to inhomogeneous distribution or less organized arrangement of LH2 and to less dense packing of LH2 in the particles, where LH2 molecules are mainly located close to the entrance of the pores as observed in the fluorescence microscopy image. Regular arrangement and dense packing of LH2 in the SBA-rod particles may have led to efficient quenching, resulting in fast fluorescence decay. In contrast, random arrangement or inhomogeneous distribution of LH2 in SBA-sph-l particles may have led to less efficient quenching. As noted, further studies are needed to clarify to which extent the above interpretation is reasonable.

References

[1] S. Bahatyrova, R. N. Frese, C. A. Siebert, J. D. Olsen, K. O. van der Werf, R. van Grondelle,. R. A. Niederman, P. A. Bullough, C. Otto and C. N. Hunter. The Native Architecture of a Photosynthetic Membrane. *Nature*, 430:1058–1062, 2004.

[2] D. Voet and J. G. Voet, *Biochemisty*, page 632. John Wiley & Sons, Inc., 2nd edition, 1995.

[3] X. Hu, T. Ritz, A. Damjanovic, F. Autenrieth, and K. Schulten. Photosynthetic Apparatus of Purple Bacteria. *Quarterly Reviews of Biophysics*, 35: 1–62, 2002.

[4] Gouterman, 1961: M. Gouterman. Spectra of Porphyrins. *J. Mol. Spectrosc.*, 6:138163, 1961.

[5] R. J. Cogdell1, A. Gall and J. Köhler. The Architecture and Function of the Light-Harvesting Apparatus of Purple Bacteria : From Single Molecules to In Vivo Membranes. *Quarterly Reviews of Biophysics*. 39:227–324, 2006.

[6] M. Z. Papiz, S. M. Prince, T. Howard, R. J. Cogdell, and N. W. Isaacs. The Structure and Thermal Motion of the B800–850. *J. Mol. Biol.*, 326:1523–1538, 2003.

[7] A. Macpherson, J. B. Arellano, N. J. Fraser, R. J. Cogdell and T. Gillbro. Efficient Energy Transfer from the Carotenoid S2 State in a Photosynthetic Light-Harvesting Complex. *Biophys. J.*, 80:923–930, 2001.

[8] J. T. M. Kennis, A. M. Streltsov, S. I. E. Vulto, T. J. Aartsma, T. Ž. Nozawa, and J. Amesz. Femtosecond Dynamics in Isolated LH2 Complexes of Various Species of Purple Bacteria. *J. Phys. Chem. B*, 101:7827-7834, 1997.

[9] X. Hong, Yu-X. Weng, and M. Li. Determination of the Topological Shape of Integral Membrane Protein Light-Harvesting Complex LH2 from Photosynthetic Bacteria in the Detergent Solution by Small-Angle X-Ray Scattering. *Biophys. J.*, 86:1082–1088, 2004.

[10] L. Cao, T. Man and M. Kruk, Synthesis of Ultra-Large-Pore SBA-15 Silica with Two-Dimensional Hexagonal Structure Using Triisopropylbenzene as Micelle Expander. *Chem. Mater.*, 21:1144–1153, 2009.

[11] S. Brunauer, P. H. Emmett, and E. Teller. Adsorption of Gases in Multimolecular Layers. *J. Am. Chem. Soc.*, 60:309–319, 1938.

[12] M. Wahlgren and T. Arnebrant. Adsorption of β-Lactoglobulin onto Silica, Methylated Silica, and Polysulfone. *J. Colloid Interface Sci.*, 136: 259–265, 1989.

[13] J. A. De Feijter, J. Benjamins and F. A. Veer, Ellipsometry as a Tool to Study the Adsorption Behavior of Synthetic and Biopolymers at the Air-Water Interface. *Biopolymers*, 17:1759, 1978.

[14] J. R. Lakowicz. *Principles of Fluorescence Spectroscopy.* Springer, 3rd edition, 2006.

[15] G. Angulo, G. Grampp, and A. Rosspeintner. Recalling the Appropriate Representation of Electronic Spectra. *Spectrochim. Acta Pt. A.*, 65:727, 2006.

[16] W. W. Lukens, P. Schmidt-Winkel, D. Y. Zhao, J. Feng and G. D. Stucky, Evaluating Pore Sizes in Mesoporous Materials: A Simplified Standard Adsorption Method and a Simplified Broekhoff−de Boer Method. *Langmuir*, 15:5403, 1999.

[17] H. Stutz. Protein Attachment onto Silica Surfaces – A Survey of Molecular Fundamentals, Resulting Effects and Novel Preventive Strategies in CE. *Electrophoresis*. 30:2032-61, 2009.

[18] M. C. Wahlgren and T. Arnebrant, The Concentration dependence of adsorption from a mixture of β-lactoglobulin and sodium dodecyl sulfate onto methylated silica surfaces. *J. Colloid Interface Sci*., 148: 201-206, 1992.

[19] M. Wahlgren and T. Arnebrant. Interaction of Cetyltrimethylammonium Bromide and Sodium Dodecyl Sulfate with β-Lactoglobulin and Lysozyme at Solid Surfaces. *J. Colloid Interface Sci.*, 142: 503-511, 1991.

[20] A. Schubert, A. Stenstam, W. J. D. Beenken, J. L. Herek, R. Cogdell, T. Pullerits, and V. Sundström. In Vitro Self-Assembly of the Light Harvesting Pigment-Protein LH2 Revealed by Ultrafast Spectroscopy and Electron Microscopy. *Biophys. J* ., 86: 2363–2373, 2004.

[21] J. Ulstrup and J. Jortner. The Effect of Intramolecular Quantum Modes on Free Energy Relationships for Electron Transfer Reactions. *J. Chem. Phys.*, 63:4358, 1975.

[22] A. M. Kuznetsov and J. Ulstrup. Electron Transfer in Chemistry and Biology : An Introduction to the Theory. Wiley, 1st edition, 1999.

[23] S. Tubasum, 2011: S. Tubasum. 2011, Personal communication, Lund University, Sweden.

[24] T. G. Monger and W. W. Parson. Singlet-Triplet Fusion in *Rhodopseudomonas Sphaeroides* Chromatophores. A Probe of the Organization of the Photosynthetic Apparatus *Biochim. Biophys. Acta*, 460:393–407, 1977.

[25] T. Pflock, M. Dezi, G. Venturoli, R. J. Cogdell, S. Oellerich, J. Köhler and S. Oellerich. Comparison of the Fluorescence Kinetics of Detergent-Solubilized and Membrane-Reconstituted LH2 Complexes from *Rps. Acidophila* and *Rb. Sphaeroides*. *Photosynth Res.*, 95:291–298, 2008.

[26] M. H. Bartl, S. W. Boettcher, K. L. Frindell, and G. D. Stucky. 3-D Molecular Assembly of Function in Titania-Based Composite Material Systems. *Acc.Chem. Res.*, 38: 263, 2005.

10. Concluding summary

Two metalloenzymes (HRP and GAOX) and a photosynthetic membrane protein-pigment complex (LH2) were immobilized on mesoporous silica materials. Catalytic kinetics, stability, and photophysical properties were investigated and compared between free enzymes or protein-pigment complex, and the proteins in the pore-confined state.

Focus in the study of HRP was on catalytic kinetics and stability. The Michaelis constant (K_M) at room temperature was similar for free and immobilized enzymes. However, at room temperature the maximum velocity (V_{max}) of the immobilized enzyme was significantly lower than that for the free enzyme. Diffusion is one of the rate-limiting factors for the lower activity of the immobilized enzyme. Much better thermal and environmental stability were shown by the immobilized enzyme. Different stability patterns of immobilized HRP toward denaturing agents were observed. Free and immobilized HRP displayed almost the same activity profile on exposure to GdmCl, with a drop to ~60% up to 1 to 2 M GdmCl, followed in either case by a plateau in the 1.5 - 4 M GdmCl concentration range and a further drop to almost complete denaturation at 4 to 5 M GdmCl. This pattern resembles three-state unfolding, as observed for sequential protein domain unfolding [1]. In comparison, HRP immobilized in SBA-15 pores exhibited significantly improved resistance to urea exposure compared with the free enzyme, with only ~20% denaturation at 5 M urea, where the free enzyme activity has dropped to < 10%. The bound enzyme activity has dropped to 16% only at 10 M urea. The observed effects of heat or denaturing agents were all largely reflected in the turnover rate, V_{max}, with relatively small effects on K_M. Mechanisms of the attenuated enzyme activity and increased stability to heat and urea based on hydration forces and folding properties in the confined space were discussed.

In the study of GAOX, physical adsorption of galactose oxidase on the mesoporous silica with hexagonally ordered pores of a pore size comparable to the size of galactose oxidase did not lead to enzyme leaching. The immobilized enzyme was catalytically active, but about 30% less efficient than the free enzyme. The immobilized enzyme did not show any enhanced resistance to heat. In contrast, physical adsorption of enzyme onto the mesoporous silica with a cage-like structure resulted in significant leaching of enzyme. Covalent attachment of enzyme via cyanuric chloride linker successfully prevented the enzyme leaching, and the immobilized enzyme retained catalytic activity. The effects of denaturants were not examined to time restrictions.

The study of LH2 showed, first that LH2 is adsorbed into the pores of mesoporous SBA-15. The fluorescence spectra of pore-confined LH2 appeared, secondly rather similar to those of free LH2 in solution, indicative that the molecular and electronic structures of the LH2 molecule is largely preserved inside the pores. The temperature dependence of the spectra in the range 77-298 K combined with spectral bandshape analysis, however, pointed to small but systematic differences between free and pore-confined LH2, most clearly by slightly stronger electronic-vibrational coupling strengths (reorganization energies) for the latter than for the former.

The lifetime measurement of free and pore-confined LH2 presented finally other interesting results although further investigation is needed. Free LH2 in solution and LH2 confined in a disordered pore structure with large spherical pores (MCF-type mesoporous silica) showed monoexponential fluorescence decay, while LH2 confined in hexagonally ordered pores (rod-shaped SBA-15) showed biexponential fluorescence decay. As a temporary interpretation, the faster decay time for the conjugates of LH2 and SBA-15 than for free LH2 may have been caused by quenching of the fluorescence in the solid state local confinement. The different life time between the conjugates of LH2 and SBA-15 may be attributed to the difference in the arrangement and packing of LH2 in the pores. Hexagonally ordered mesopores allow dense packing and/or regular arrangement of LH2, which may have resulted in more efficient fluorescence quenching. In contrast, the disordered pore structure consisting of cells interconnected by smaller windows caused less dense packing and irregular arrangement of LH2. This may have resulted in less efficient fluorescence quenching.

Mesoporous silica extends the use of enzymes beyond the natural environments and properties of the enzyme (e.g. heat susceptibility, and denaturation under harsh conditions) such as shown in the present study and also in the literature [2] and [3]. Enhanced thermal or environmental stability depends, however, on the specific enzymes immobilized. In addition to the role as a support of enzymes, mesopores also offer openings for studying biomolecules in unique environments different from bulk solution. Huang et al [4] recently reported advantages of mesoporous materials in studies of biomolecules at cryogenic temperatures because pore-confined water remains in a liquid state at sub-freezing temperatures. These same environments offered other observations in the fluorescence behaviour of pore-confined LH2, as noted most clearly with small but notable spectral bandshape differences and different fluorescence decay patterns both specific to the particular local environment.

Many studies on the use of mesoporous silica in life sciences, biotechnology, etc. have already been reported. The present study revealed in new ways possible involvements of pore-confined water in the stability and structural flexibility of proteins in the pores. We have seen that different pore structure, size and ordering can lead to different properties of the biomolecules immobilized. Many studies on pore size dependent property changes have been undertaken, but not many studies of the effect of different pore structure and ordering are reported. Many opportunities to explore the use of mesoporous silica in novel contexts of biological science both in fundamental studies and application purposes still seem to remain.

References

[1] N. H. Andersen, T. J. Jensen, A. Nørgaard, J. Ulstrup. Sequential Unfolding of the Two-Domain Protein *Pseudomonas Stutzeri* Cytochrome c_4. *J. Inorg. Biochem.,* 88:316–327, 2002.

[2] H. Takahashi, B. Li, T. Sasaki, C. Miyazaki, T. Kajino, and S. Inagaki. Catalytic Activity in Organic Solvents and Stability of Immobilized Enzymes Depend on the Pore Size and Surface Characteristics of Mesoporous Silica. *Chem. Mater.*, 12:3301–3305, 2000.

[3] Y. Urabe, T. Shiomi, T. Itoh, A. Kawai, T. Tsunoda, F. Mizukami, and K. Sakaguchi. Encapsulation of Hemoglobin in Mesoporous silica (FSM)—Enhanced Thermal Stability and Resistance to Denaturants. *Chem Bio Chem*, 8:668, 2007.

[4] Y.-W. Huang, Y.-C. Lai, C.-J. Tsai, and Y.-W. Chiang. Mesopores Provide an Amorphous State Suitable for Studying Biomolecular Structures at Cryogenic Temperatures. *PNAS,* 108:14145–14150, 2011.

Appendix

A.1 Set-up of fluorescence measurement at room temperature

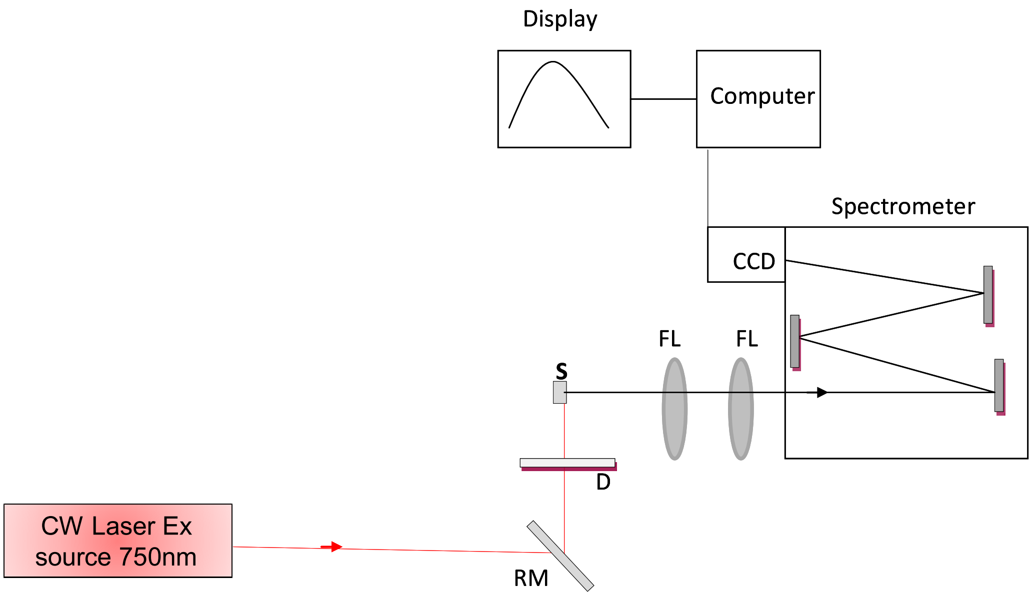

Figure A.1: Schematic illustration of fluorescence measurement set–up at room temperature. Excitation beam (red line) and emission (black line), S = Sample, D = Diaphragm, FL = Focusing lens, RM = Reflecting mirror are shown.

As noted in Section 5.3.1, this set-up was used for the measurements of fluorescence spectra at room temperature in the latter period of my external stay at Lund University.

A.2 Lineweaver-Burk and Michaelis-Menten plots

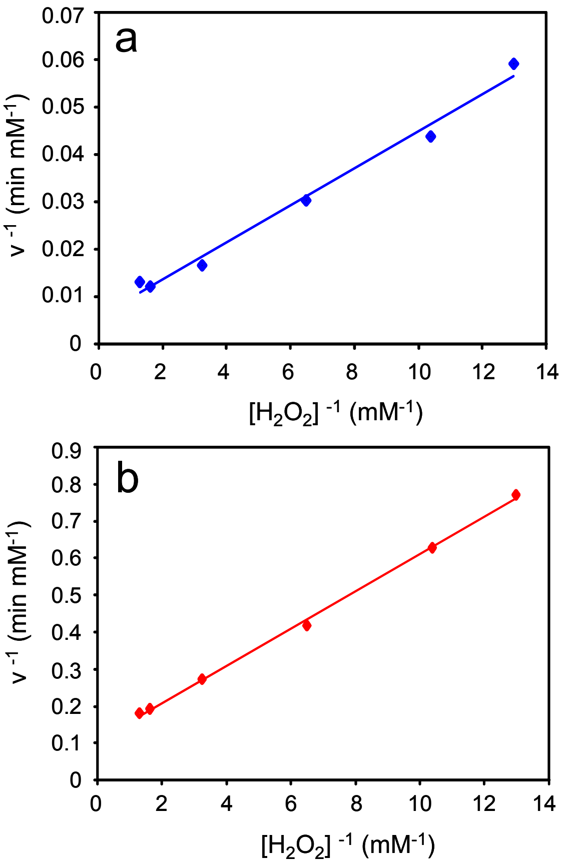

Figure A.2.1: Lineweaver-Burk plots of (a) free and (b) immobilized HRP. Free or immobilized enzyme was mixed with solutions containing 2.4 mM 4-AAP, 86 mM phenol, hydrogen peroxide in different concentrations, and 25 mM phosphate buffer (pH 7.4).

The catalytic constants (K_M and V_{max}) were determined by two methods: (1) transformation of data to linear form and use of linear regression (Figure A.2.1), and (2) direct nonlinear curve fitting of the Michaelis-Menten form, e.q. (3.11) (Figure A.2.2).

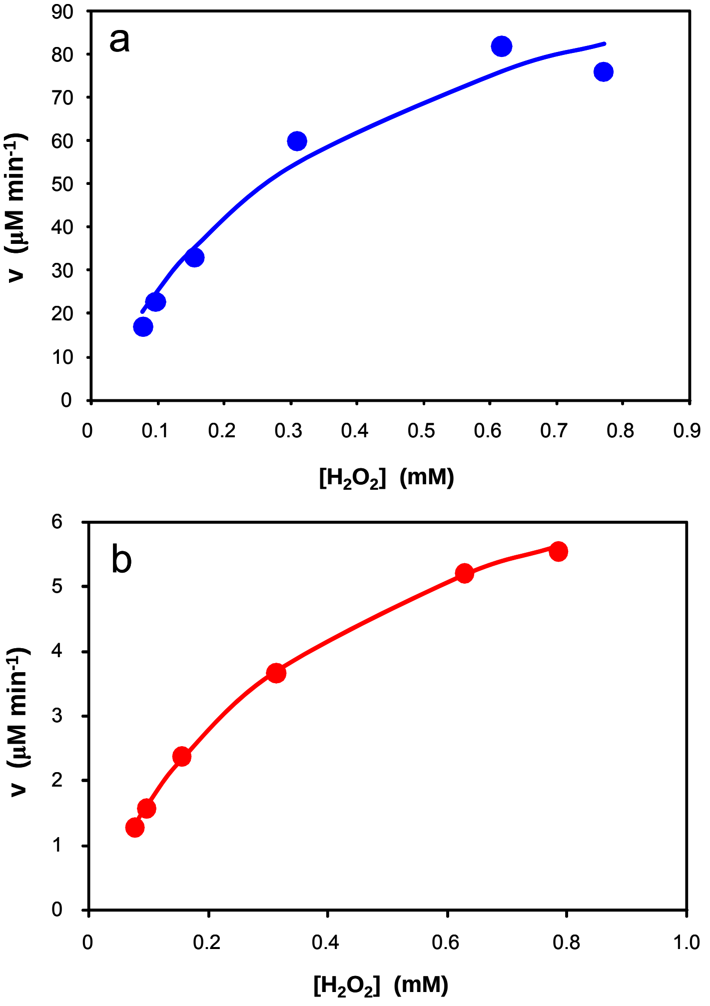

Figure A.2.2: Plots of initial velocity versus substrate concentration for (a) free and (b) immobilized HRP. Free or immobilized enzyme was mixed with solutions containing 2.4 mM 4-AAP, 86 mM phenol, hydrogen peroxide in different concentrations, and 25 mM phosphate buffer (pH 7.4). Fitting (solid line) was obtained using the Michaelis-Menten rate constant form.

A.3 The absorption spectra of BChl a (The concept of Q_x and Q_y)

Figure A3.1 shows the absorption spectrum of BChl a in 7: 2 (v/v) acetone : methanol. Since BChl a is a porphyrin derivative (Fig. A3.2), the electronic transitions in the spectra of BChl a can be understood by the four-orbital theory of Gouterman, developed for porphyrins [1][2][3].

Four electronic states are associated with the electronic transitions shown in the absorption spectrum of Fig. A3.1 involving the two highest occupied molecular orbitals (HOMO and HOMO-1) and the two lowest unoccupied molecular orbitals (LUMO and LUMO-1). The transitions from HOMO and HOMO-1 to LUMO are called Q bands (in the visible to near IR region [3]) and the transitions from HOMO and HOMO-1 to LUMO-1 are called B (Soret) bands in the UV. Each electronic transition is accompanied by a unique "transition dipole moment" with different strength and orientation. The two arrows in Fig. A3.2 indicate directions of the two polarization axes, x and y. The transition to the lowest energy state has the transition dipole moment in the y-direction. This y-polarized transition is called the Q_y transition. The other low-energy transition has the transition dipole moment in the x-direction. This x-polarized transition is called the Q_x transition. The same holds true for the B_x and B_y transitions.

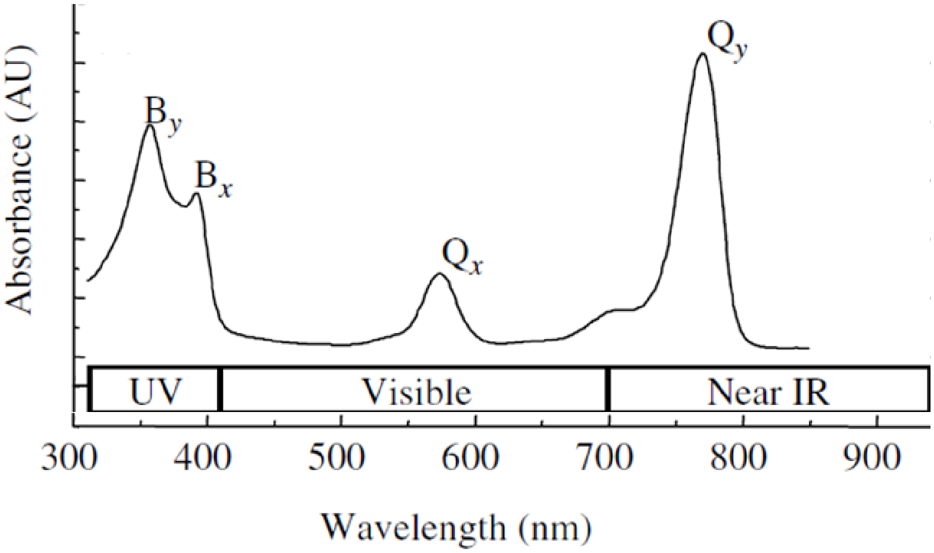

Figure A.3.1: The room-temperature absorption spectrum of monomeric BChl a from *Rps. Acidophila* in 7: 2 (v/v) acetone :methanol. The Soret (B_x and B_y) bands are shown in the UV and Q (Qx and Qy) bands in the visible (590 nm) to near IR region (772 nm). From Cogdell et al [4].

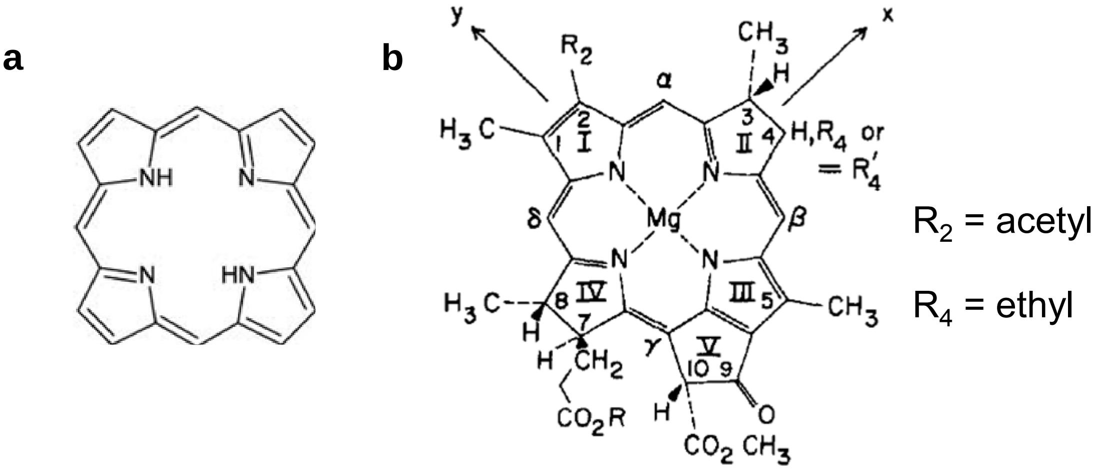

Figure A.3.2: The structures of porphyrin (a) and bacteriochlorophyll a (b). From [5] and [3].

A.4 Set-up for fluorescence measurements at low temperatures

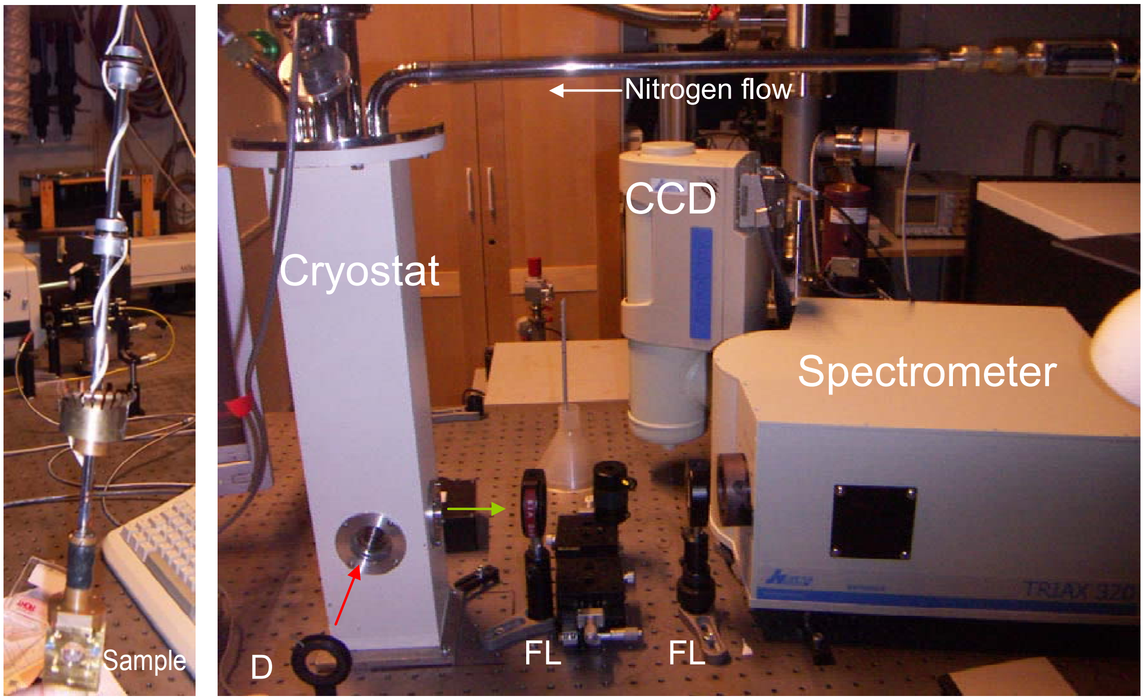

Figure A.4: Set–up for fluorescence measurements at low temperatures. Left picture shows a sample holder. Right picture includes excitation beam (red line) and emission beam (green line), where D and FL denote Diaphragm and Focusing lens, respectively.

Figure A.4 shows the set–up used for the fluorescence measurements from room temperature to cryogenic temperatures. The sample holder (left picture) is inserted in the cryostat, which is connected to the flow of liquid nitrogen. The temperature of the cryostat is controlled with a temperature controller (not shown in the picture).

A.5 Adsorption of LH2 to a flat silica substrate

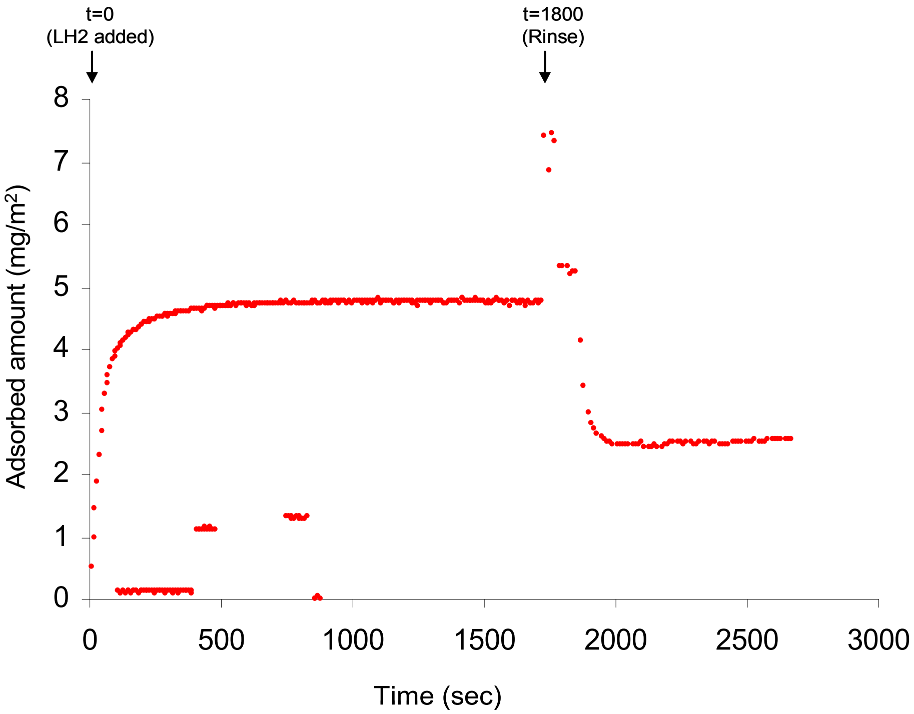

Figure A.5: Adsorption of LH2 onto a flat silica substrate in Tris buffer (pH 8.5). At t = 0 s, 8.4 μl LH2 stock solution was added to 3 ml Tris buffer (pH 8.5) in a cuvette. The concentration of LH2 is the same as that used for the adsorption experiment in Fig. 9.12. At t = 1800 s, the cuvette was rinsed with buffer.

Figure A.5 shows an adsorption experiment of LH2 alone (without surfactant, LDAO) to a flat silica substrate. After addition of LH2 at t = 0 s, LH2 was adsorbed on the silica substrate. LH2 was desorbed by rinsing with buffer at t = 1800 s, but about half amount was retained on the substrate. In the case of adsorption of a mixture of LH2 and LDAO (Fig. 9.12), most of the adsorbed substances were desorbed from the substrate due to rinsing. As noted in section 9.3.3, surfactants adsorb reversibly to silica surface. In contrast, proteins often adsorb irreversibly on the solid surface with respect to the dilution. The desorbed LH2 is likely to be LH2 adsorbed on the silica substrate as a second layer (multilayer adsorption) [6].

A.6 Bandshape analysis

The fluorescence spectral data for free LH2 and LH2 confined in either SBA-sph-1 or in SBA-rod nanoscale environment offer a case for comparison between the three environments based on spectral bandshape analysis. We provide here a few observations to support the data in Chapter 9 and the conclusions offered in Chapters 9 and 10.

Assessment of differences between free and pore-confined LH2 is here based on a simplified view and a simple Gaussian analysis to provide the intensity, band maximum, and bandwidth. We consider only a single optical transition. In view of the composite chromophoric electronic interactions in the large LH2 protein complex, this consideration is “generic” but the outcome still offers observations of some importance to the assessment of the differences between the different local and bulk LH2 environments.

The physical basis of the bandshape analysis is strong electronic-vibrational coupling involving both local LH2 nuclear and protein or solvent motion. These features are reflected particularly in the spectral bandwidth which we focus on. The coupling is taken to be represented by a Gaussian bandshape close to the maximum ([7][8]). Asymmetry arises in the band wings with a slower fall-off on the low-frequency side than on the high-frequency side. This is caused by high-frequency local and solvent motion and is more pronounced the lower the temperature. For the sake of simplicity, asymmetry is not incorporated in the present parametric fitting. The fittings were undertaken by Ph.D. student Sumera Tubasum, Department of Chemical Physics, Chemical Center, Lund University.

The bandshape function $F(\nu)$ close to the band maximum is ([7][8])

$$F(\nu) = F_0 \frac{1}{\Delta_{fluor}} \exp\left[-\frac{\left(h\nu - h\nu_{\max}\right)^2}{\left(\Delta_{fluor}\right)^2} \right] \qquad \text{(A1)}$$

Δ_{fluor} is the Gaussian band width, ν_{max} the frequency at the maximum, and h Planck's constant. F_0 can here be regarded as a constant and all spectra are normalized with respect to the band maximum intensity. $F(\nu)$ is related to the measured fluorescence intensity, $I_{fluor}(\nu)$, as $F(\nu) \sim \nu^{-3} I_{fluor}(\nu)$ ([9]). This conversion was taken into account in the bandshape analysis.

The bandwidth can be given the following approximate form ([7] [8])

$$\Delta_{fluor} \approx \sqrt{\left(2E_R\hbar\omega_{eff}\right)\coth\left(\hbar\omega_{eff}/2k_BT\right)} \tag{A2}$$

where ω_{eff} is the effective nuclear vibrational frequency of all the nuclear modes reorganized in the electronic transition, E_R the nuclear reorganization (free) energy that accompanies the transition (the Stokes shift), k_B Boltzmann's constant, T the temperature, and $\hbar = h/2\pi$. Δ_{fluor} takes the following forms in the high- and low-temperature limits

$$\Delta_{fluor}^{high-T} = \sqrt{4E_Rk_BT} \;\; ; \;\; \Delta_{fluor}^{low-T} = \sqrt{2E_R\hbar\omega_{eff}} \tag{A3}$$

i.e. Δ_{fluor} is proportional to $\sqrt{T}$ at high temperature and independent of T at low temperature. This reflects a transition from classical thermal nuclear motion at high T and nuclear tunnelling at low T.

The band maximum is independent of T in the formalism represented by eqs.(A1)-(A3) but a red-shift with increasing T can be expected as high-frequency nuclear motion represented by the band asymmetry is increasingly thermally excited, gradually lifting the asymmetry features.

The analysis in Chapter 9 (Fig. 9.17) with focus on the band width, is based on eqs.(A1)-(A3).

References

[1] Gouterman, 1961: M. Gouterman. Spectra of Porphyrins. *J. Mol. Spectrosc.*, 6:138163, 1961.

[2] Gouterman and Wagniere, 1963: M. Gouterman and G. H. Wagniere. Spectra of Porphyrins Part II. Four Orbital Model. J. Mol. Spectrosc., 11:108-127, 1963.

[3] Hanson, 1988: L. K. Hanson. Theoretical Calculations of Photosynthetic Pigments. Photochem. Photobiol., 47:903-921, 1988.

[4] Cogdell, 2006: R. J. Cogdell1, A. Gall and J. Köhler. The Architecture and Function of the Light-Harvesting Apparatus of Purple Bacteria : From Single Molecules to In Vivo Membranes. *Quarterly Reviews of Biophysics*. 39:227–324, 2006.

[5] http://www.doitpoms.ac.uk/tlplib/liquid_crystals/printall.php. Web page, November 4, 2011.

[6] Wu, 1993: H. Wu, Y. Fan, J. Sheng, S.-F. Sui. Induction of Changes in the Secondary Structure of Globular Proteins by a Hydrophobic Surface. Eur Biophys J, 22:201-205, 1993.

[7] A. M. Kuznetsov and J. Ulstrup. Electron Transfer in Chemistry and Biology : An Introduction to the Theory. Wiley, 1 edition, 1999.

[8] A. M. Kjaer and J. Ulstrup. Solvent Bandwidth Dependence and Band Asymmetry Features of Charge-Transfer Transitions in N-Pyridinium Phenolate. *J. Am. Chem. Soc.*, 109:1934-1942, 1987.

[9] G. Angulo, G. Grampp, and A. Rosspeintner. Recalling the appropriate representation of electronic spectra. *Spectrochim. Acta Pt. A.*, 65:727, 2006.

Publications and Presentations

I. International Journals

(1) H. Ikemoto, Q. Chi, and J. Ulstrup
Stability and Catalytic Kinetics of Horseradish Peroxidase Confined in Nanoporous SBA-15. *J. Phys. Chem.* C **2010**, *114*, 16174–16180.

(2) H. Ikemoto, S. Tubasum, T. Pullerits, J. Ulstrup, and Q. Chi
Fluorescence Spectroscopic Characterization of Light Harveting Complex II Confined in Nanoscale Environments. In preparation.

(3) H. Ikemoto, J. Ulstrup, and Q. Chi
Enzyme Catalysis of Galactose Oxidase Immobilized in Mesoporous Silica. In preparation.

II. Oral Presentations in the Conference and Symposium

Second International Conference on Multifunctional, Hybrid and Nanomaterials: Catalytic Kinetics and Stability of Horseradish Peroxidase Confined in Nanoporous SBA-15, 6-10 March **2011**, Strasbourg, France.

DTU Chemistry PhD School Symposium: Encapsulation of Proteins in Mesoporous Silica, 4-5 November **2010**, Gentofte, Denmark.

III. Poster Presentations in the Conference and Symposium

DTU Chemistry PhD School Symposium: Catalytic Kinetics and Stability of Enzyme Immobilized in Mesoporous silica, 4-5 November **2010**, Gentofte, Denmark.

PhD NANO 2010 - Workshop for Doctoral Students in Nanoscience and Nanotechnology: Catalytic Kinetics and Stability of Enzyme Confined in Mesoporous Silica, 28-29 October **2010**, Gothenburg, Sweden.

Joint meeting between Nano•DTU, Nano-Science Center, NanoTUM and TU/e NanoDay 2009: Encapsulation of Biological Molecules in Mesoporous Silica, 6 May **2009**, Lyngby, Denmark.